



Damage Identification in Civil Engineering Infrastructure under Operational and Environmental Conditions

Elói João Faria Figueiredo

2010

FACULTY OF ENGINEERING
OF THE
UNIVERSITY OF PORTO

Damage Identification in Civil Engineering Infrastructure under Operational and
Environmental Conditions

A dissertation submitted in satisfaction of the requirements of the degree
Doctor of Philosophy in Civil Engineering

by

Elói Figueiredo

Committee in charge:

Vitor Abrantes Almeida, Chair

Joaquim A. Figueiras, Advisor

Charles R. Farrar, Advisor

Carlos da Silva Rebelo

Jorge Mascarenhas Proença

Rui Carneiro Barros

Elsa de Sá Caetano

2010

Copyright

Elói Figueiredo, 2010

All rights reserved.

To my mom, dad, and brother

TABLE OF CONTENTS

TABLE OF CONTENTS	i
LIST OF FIGURES	v
LIST OF TABLES	xv
NOTATION	xvii
ABSTRACT	xxi
RESUMO	xxiii
ACKNOWLEDGEMENTS	xxv
1. INTRODUCTION	1
1.1 SHM BACKGROUND	1
1.1.1 <i>Historical Perspective</i>	1
1.1.2 <i>Statistical Pattern Recognition Paradigm</i>	3
1.1.3 <i>Hierarchical Structure of Damage Identification</i>	5
1.1.4 <i>Economic and Safety Considerations</i>	6
1.2 CURRENT STATUS AND MOTIVATION	7
1.3 OBJECTIVE AND ORGANIZATION OF THIS DISSERTATION	7
1.4 ORIGINAL CONTRIBUTIONS AND EXTENSION OF KNOWLEDGE.....	8
2. CIVIL INFRASTRUCTURE: THE BRIDGE CASE	11
2.1 BRIDGE DISASTERS: CAUSES AND CHALLENGES	11
2.2 SHM APPLICATION: LIMITATIONS DUE TO OPERATIONAL AND ENVIRONMENTAL VARIABILITY....	16
2.3 SUMMARY	21
3. STATISTICAL PATTERN RECOGNITION PARADIGM	23
3.1 INTRODUCTION.....	23
3.2 FEATURE EXTRACTION	23
3.2.1 <i>Modal Parameters</i>	24
3.2.2 <i>First Four Statistical Moments</i>	25

3.2.3	<i>Auto-regressive Model</i>	26
3.2.4	<i>Auto-regressive Model with Exogenous Inputs</i>	30
3.2.5	<i>State-space Reconstruction and Time Series Modeling</i>	31
3.2.5.1	State-space Representation.....	31
3.2.5.2	Embedology and Multivariate Auto-regressive Model.....	32
3.2.5.3	Multivariate Embedding Approach.....	35
3.2.6	<i>Principal Component Analysis</i>	35
3.2.7	<i>Time-frequency Analysis</i>	37
3.2.8	<i>Holder Exponent</i>	38
3.2.9	<i>Correlation Procedures</i>	39
3.2.10	<i>Probability Density Function</i>	41
3.3	MACHINE LEARNING ALGORITHMS FOR DATA NORMALIZATION	42
3.3.1	<i>Auto-associative Neural Network</i>	43
3.3.2	<i>Factor Analysis</i>	44
3.3.3	<i>Singular Value Decomposition</i>	46
3.3.4	<i>Mahalanobis Squared Distance</i>	47
3.4	STATISTICAL MODELING FOR FEATURE CLASSIFICATION	47
3.4.1	<i>Cluster Analysis</i>	48
3.4.2	<i>Statistical Process Control</i>	49
3.4.3	<i>Outlier Detection based on Central Chi-square Hypothesis</i>	51
3.4.4	<i>Outlier Detection from Residual Errors</i>	52
3.4.5	<i>Receiver Operating Characteristic Curves</i>	53
3.5	SUMMARY AND CONTRIBUTIONS	54
4.	VALIDATION ON A LABORATORY TEST STRUCTURE	59
4.1	INTRODUCTION AND OVERVIEW	59
4.2	EXPERIMENTAL PROCEDURE	60
4.3	NUMERICAL SIMULATION	64
4.4	STATIONARY PROPERTIES OF THE DATA SETS	69

4.5	FEATURE EXTRACTION	71
4.5.1	<i>Basic Statistics</i>	71
4.5.1.1	Probability Density Function	71
4.5.1.2	Normal Probability Plot.....	72
4.5.1.3	First Four Statistical Moments	73
4.5.1.4	Conclusions	74
4.5.2	<i>Modal Parameters</i>	75
4.5.3	<i>Auto-regressive Models</i>	78
4.5.3.1	Appropriate Model Order	78
4.5.3.2	AR Residual Errors	80
4.5.3.3	AR Parameters.....	86
4.5.3.4	Conclusions	88
4.5.4	<i>Time-frequency Analysis</i>	88
4.5.5	<i>Holder Exponent</i>	100
4.5.6	<i>Principal Component Analysis</i>	102
4.5.7	<i>Correlation Coefficients</i>	103
4.6	STATISTICAL MODELING FOR FEATURE CLASSIFICATION.....	105
4.6.1	<i>Cluster Analysis</i>	106
4.6.2	<i>Statistical Process Control</i>	108
4.6.3	<i>Outlier Detection based on State-space Reconstruction</i>	112
4.6.4	<i>Outlier Detection based on Machine Learning Algorithms</i>	119
4.6.5	<i>Outlier Detection based on Central Chi-square Hypothesis</i>	125
4.7	SUMMARY AND CONCLUSIONS.....	133
4.8	CONTRIBUTIONS.....	138
5.	ALAMOSA CANYON BRIDGE	139
5.1	INTRODUCTION AND OVERVIEW.....	139
5.2	OPERATIONAL EVALUATION AND DATA ACQUISITION.....	140
5.3	FEATURE EXTRACTION	147

5.3.1	<i>Modal Parameters</i>	147
5.3.2	<i>Auto-regressive Models</i>	152
5.3.2.1	Linear Assumption	152
5.3.2.2	Appropriate Model Order.....	154
5.3.2.3	AR Parameters	155
5.3.2.4	AR Residual Errors.....	158
5.3.3	<i>Dimension of a Dynamical System</i>	163
5.4	STATISTICAL MODELING FOR FEATURE CLASSIFICATION	164
5.4.1	<i>Modal Parameters</i>	165
5.4.2	<i>AR Parameters</i>	167
5.5	SUMMARY AND CONCLUSIONS	170
5.6	CONTRIBUTIONS	173
6.	CONCLUSIONS, CONTRIBUTIONS, AND FUTURE RESEARCH	175
6.1	CONCLUSIONS AND CONTRIBUTIONS.....	175
6.2	FUTURE RESEARCH.....	177
	REFERENCES	181

APPENDIX A – SHMTools Software

LIST OF FIGURES

Figure 1.1. SPR paradigm for SHM.	3
Figure 1.2. Hierarchical structure of damage identification.	5
Figure 2.1. Collapse of the Silver Bridge on December 17, 1967, that killed 46 people, USA.	12
Figure 2.2. Collapsed north section of the Minneapolis I-35W Bridge, Minnesota, USA [28].	13
Figure 2.3. Tsing Ma and Ting Kau Bridges in Hong Kong, China [36].	14
Figure 2.4. Hintze Ribeiro Bridge collapse in 2001, Portugal [39].	15
Figure 2.5. First mode shape of one simply supported span of the Alamosa Canyon Bridge, New Mexico, USA, during two distinct times of the day: (a) in the morning (7.75 Hz); and (b) in the afternoon (7.42 Hz).	18
Figure 2.6. Vertical cut used to simulate a fatigue crack in a mid-span plate girder of the I-40 Bridge, New Mexico, USA.	19
Figure 2.7. Settlement-related damage scenario at Z-24 Bridge, Switzerland [60].	20
Figure 3.1. Schematic representation (for $m=3$) of the MAR model approach.	34
Figure 3.2. Network architecture of the AANN.	43
Figure 3.3. Linear factor model.	45
Figure 3.4. Singular spectra $\theta_{\mathbf{x}}$ and $\theta_{\mathbf{M},j}$	47
Figure 3.5. Traditional representation of the Hierarchical Clustering.	48
Figure 3.6. MSD-based algorithm combining feature extraction, data normalization, and statistical modeling for feature classification.	52
Figure 3.7. Distributions from the undamaged and damaged conditions.	53
Figure 3.8. Example of a ROC curve; the diagonal line divides the ROC space into two parts and represents a classifier that performs random classifications.	54
Figure 4.1. Basic dimensions of the three-story test bed structure. (All dimensions are in cm.)	61
Figure 4.2. Acceleration time series of various state conditions: (a) Channel 2; (b) Channel 3; (c) Channel 4; and (d) Channel 5.	63
Figure 4.3. Structural details of the sources of simulated operational and environmental changes: (a) mass-loading added at the base; and (b) nonlinearity source.	64
Figure 4.4. Shear-building model of the test structure.	65
Figure 4.5. Numerical (NM) and experimental (Exp) mode shapes of the baseline condition: (a) second; (b) third; and (c) fourth mode shapes.	66

Figure 4.6. Correlation between numerical and experimental mode shapes: (a) MAC; and (b) COMAC values.....	67
Figure 4.7. Responses from Channel 5 due to the measured experimental excitation at Channel 1 (State#1): (a) experimental time series; and (b) time series derived from the numerical model.....	67
Figure 4.8. ACFs of the experimental and numerical responses.....	68
Figure 4.9. PSDs obtained from experimental and numerical time responses.....	68
Figure 4.10. Box plots of the first four statistical moments of all 10 time series from Channel 5.....	70
Figure 4.11. Box plots of the skewness and kurtosis of all 10 time series from Channel 1.....	70
Figure 4.12. Box plots of the ACFs, for the first 15 coefficients, of all time series from Channel 5: (a) State#1; and (b) State#14.....	70
Figure 4.13. PDFs estimated from acceleration time series from Channel 5 of two undamaged (State#1 and 7) and two damaged (State#14 and 17) states using a kernel density estimator.....	72
Figure 4.14. Normal probability plots of four state conditions at Channel 5: (a) State#1; (b) State#7; (c) State#14; and (d) State#17.....	73
Figure 4.15. First four statistical moments based on one acceleration time series from Channel 2-5 of each state condition: (a) mean; (b) standard deviation; (c) skewness; and (d) kurtosis.....	74
Figure 4.16. CMIF for one FRF from Channel 5 of State#1.....	75
Figure 4.17. Curve fitting example on the FRFs from Channel 2-5 for the selected frequency range between 25-80 Hz (State#1).....	75
Figure 4.18. Natural frequencies estimated based on one test of each state condition.....	77
Figure 4.19. Natural frequency deviations of all state conditions from the baseline condition (State#1).....	77
Figure 4.20. AR order estimation based on one time series of Channel 5 from the baseline condition (State#1) using four different techniques: (a) AIC; (b) PAF; (c) RMS; and (d) SVD.....	79
Figure 4.21. AIC functions estimated using time series from Channels 2-5.....	79
Figure 4.22. Comparison of the measured and predicted time series from the baseline condition at Channel 5 using: (a) AR(5); (b) AR(15); and (c) AR(30) models.....	80
Figure 4.23. Residual-error histograms along with the superimposed Gaussian distribution based on one time series from the baseline condition at Channel 5: (a) AR(5); (b) AR(15); and (c) AR(30) models.....	81

Figure 4.24. Log PSDs of the residual errors based on one time series from the baseline condition at Channel 5: (a) AR(5); (b) AR(15); and (c) AR(30) models.	81
Figure 4.25. ACFs of one acceleration time series at Channel 5 from: (a) State#1; (b) State#7; (c) State#14; and (d) State#17.	82
Figure 4.26. ACFs of the residual errors at Channel 5 from State#1, 7, 14, and 17 using: (a) AR(5); (b) AR(15); and (c) AR(30) models.	83
Figure 4.27. Lag plots of the original time series from Channel 5: (a) State#1; (b) State#7; (c) State#14; and (d) State#17.	84
Figure 4.28. Lag plots of the AR(5) model residual errors from Channel 5: (a) State#1; (b) State#7; (c) State#14; and (d) State#17.	84
Figure 4.29. Lag plots of the AR(15) model residual errors from Channel 5: (a) State#1; (b) State#7; (c) State#14; and (d) State#17.	84
Figure 4.30. Lag plots of the AR(30) model residual errors from Channel 5: (a) State#1; (b) State#7; (c) State#14; and (d) State#17.	85
Figure 4.31. RMS of the residual errors using 8177- (original) and 2044-points (grouped).	86
Figure 4.32. AR parameter amplitudes for all the 17 state conditions at Channel 5 using: (a) AR(5); (b) AR(15); and (c) AR (30) models.	87
Figure 4.33. Amplitude of the third parameter of all the state conditions at Channel 5 from the three AR models.	87
Figure 4.34. AR(15) parameters, in concatenated format, from one test (Channel 2-5) of each state condition.	88
Figure 4.35. STFT analysis of signal from State#1, Channel 4: (a) time-frequency-amplitude representation; and (b) time-frequency representation.	91
Figure 4.36. STFT analysis of signal from State#10, Channel 4: (a) time-frequency-amplitude representation; and (b) time-frequency representation.	92
Figure 4.37. STFT analysis of signal from State#14, Channel 4: (a) time-frequency-amplitude representation; and (b) time-frequency representation.	93
Figure 4.38. STFT analysis; individual spectrograms in concatenated format, Channel 4: (a) time-frequency-amplitude representation; and (b) time-frequency representation.	94
Figure 4.39. CWT of time series from State#1, Channel 4: (a) time-frequency-amplitude representation; and (b) time-frequency representation.	95
Figure 4.40. CWT of time series from State#10, Channel 4: (a) time-frequency-amplitude representation; and (b) time-frequency representation.	96

Figure 4.41. CWT of time series from State#14, Channel 4: (a) time-frequency-amplitude representation; and (b) time-frequency representation.	97
Figure 4.42. Details of the WT coefficients based on time series from Channel 4 for: (a) State#1; and (b) State#14.	99
Figure 4.43. Detection of singularities: (a) original entire time series from Channel 4 of State#10; and (b) AR(15) residual errors.	100
Figure 4.44. WT of the time series from State#10, Channel 4.	100
Figure 4.45. Singularities detection at Channel 4 using on time series from State#10: (a) portion of the time series; (b) Holder exponent function; (c) AR(5) residual errors; (d) AR(15) residual errors; and (e) AR(30) residual errors.	101
Figure 4.46. Projection of the AR(5) parameters onto the first: (a) two; and (b) three principal components.	102
Figure 4.47. Projection of the AR(15) parameters onto the first: (a) two; and (b) three principal components.	103
Figure 4.48. Projection of the AR(30) parameters onto the first: (a) two; and (b) three principal components.	103
Figure 4.49. Correlation coefficients between Channel 1 and Channel 1-5 ($r_{1,1:5}$) along with correlation coefficients between Channel 5 and Channel 1-5 ($r_{5,1:5}$).	104
Figure 4.50. Correlation coefficients of pair of channels for all state conditions (State#1-17): (a) Channel 5 and 1; (b) Channel 5 and 2; (c) Channel 5 and 3; and (d) Channel 5 and 4. .	104
Figure 4.51. Binary classification (undamaged and damaged conditions) using AR(15) parameters from one time series of each state condition at Channel 5 (<i>DataSet2007</i>).	106
Figure 4.52. Cluster tree of the state conditions in Figure 4.51 (<i>DataSet2007</i>).	107
Figure 4.53. Binary classification (undamaged and damaged conditions) using AR(15) parameters from one time series of each state condition at Channel 5 (<i>DataSet2009</i>).	107
Figure 4.54. Cluster tree of the state conditions in Figure 4.53 (<i>DataSet2009</i>).	108
Figure 4.55. The Shewhart X-Bar control charts of the mean of the grouped AR(15) residual errors; outliers are represented by crosses.	110
Figure 4.56. Number of outliers falling outside the control limits defined based on data from the baseline condition (State#1); the horizontal dashed line corresponds to the maximum number of outliers among the undamaged states (State#5).	111
Figure 4.57. Number of outliers falling outside the control limits defined based on data from all undamaged state conditions (State#1-9); the horizontal dashed line corresponds to the	

maximum number of outliers among the undamaged states (State#5); in overlap format one can see the log-scale version of the figure.....	111
Figure 4.58. Singular values obtained from the state-space reconstructions of the undamaged and damaged structural state conditions at Channel 5, where the bold line represents the baseline condition (State#1).....	113
Figure 4.59. AIC function of the MAR model for increasing order $p=1,2,\dots,25$ (Channel 5).	114
Figure 4.60. Predicted trajectory of the baseline condition (black dots) along with the predicted trajectories from test conditions (gray dots) at Channel 5 for $m=3$: (a) State#1; (b) State#1 and 7; (c) State#1 and 10; and (d) State#1 and 14.	115
Figure 4.61. Feature extraction at Channel 5 for $m=3$: (a) plot of d^2 from all state vectors from the undamaged (State#1-9) and damaged state conditions (State#10-17), in concatenated format, along with one-sided threshold (horizontal dashed line); and (b) number of outliers, or d^2 values beyond the threshold, along with the average sum-of-square MAR errors (ϵ).....	116
Figure 4.62. Relative distances between the undamaged and damaged conditions as a function of the embedding dimension m ; Dm is the distance between the mean of both d^2 distributions; $Dout$ is the distance between the minimum number of outliers among the damaged state conditions and the maximum number of outliers among the undamaged state conditions.	117
Figure 4.63. Outlier detection and feature extraction per structural condition in the four accelerometers (Channel 2-5) for $m=12$; number of outliers along with the average sum-of-square MAR errors (ϵ) in log scale.	118
Figure 4.64. Number of outliers along with the average sum-of-square MAR(p) errors (ϵ) in log scale per structural state condition: (a) based on a global embedding (Channel 2-5, $M=12$ and $p=7$); and (b) based on a semi-global embedding (Channel 4-5, $M=12$, and $p=8$).....	119
Figure 4.65. Average AIC function for four independent AR(p) models of increasing order p using baseline-based time series (State#1) from the four accelerometers (Channel 2-5).	120
Figure 4.66. ROC curves: (a) linear scale; and (b) log scale to highlight the differences between curves.	122
Figure 4.67. DIs calculated based on feature vectors from the undamaged (black) and damaged (gray) state conditions along with thresholds defined by the 95% cut-off value over the training data: (a) AANN-; (b) FA-; (c) MSD-; and (d) SVD-based algorithms.	124

Figure 4.68. Distance between the mean of the DI distributions of the undamaged and damaged state conditions along with the number of Type II errors as a function of the number of factors: (a) AANN-; and (b) FA-based algorithms.	125
Figure 4.69. Comparison of the behavior of the CIC as a function of model order using: (a) 4096-point; and (b) 1024-point time series.	127
Figure 4.70. Estimated PDF for each variable, or AR(15) parameter, of the original undamaged feature vectors from Channel 5.	127
Figure 4.71. Four theoretical chi-square distributions, χ_m^2 , along with PDFs of the DIs from undamaged condition and assuming AR(p) models of increasing order $p=m=5, 15, 30, \text{ and } 50$	128
Figure 4.72. Correlation coefficients between the theoretical chi-square distributions, χ_m^2 , and PDFs of the DIs from the undamaged condition for increasing AR(p) model order $p=m=1, 2, \dots, 50$	128
Figure 4.73. ROC curves for AR(p) models of varying order $p=5, 10, \dots, 50$ at: (a) Channel 2; (b) Channel 3; (c) Channel 4; and (d) Channel 5.	129
Figure 4.74. True-detection rate for fixed false-alarm rate equals to 0.1 at Channels 2-5.	130
Figure 4.75. Percentage of Type I and Type II errors for varying AR model order $p=1, 2, \dots, 50$ assuming a level of significance equals to 10%; (a) Channel 2; (b) Channel 3; (c) Channel 4; and (d) Channel 5.	131
Figure 4.76. PDFs based on the DIs of all tests from undamaged and damaged conditions along with a threshold (vertical dashed line) defined by the 90% confidence interval of the χ_{15}^2 distribution when using AR(15) parameters as damage-sensitive features and 50% of the entire undamaged data sets to establish the normal condition.	132
Figure 5.1. Alamosa Canyon Bridge near to Truth or Consequences, New Mexico, USA, in 2008.	140
Figure 5.2. Schematic representation of the accelerometers and driving point (DP) locations.	141
Figure 5.3. Attachment of the accelerometers to the bridge: (a) on the bottom of the steel girders; and (b) on the deck surface.	142
Figure 5.4. An impact being applied adjacent to the driving point (in 2008).	143
Figure 5.5. Picture of the area underneath the first span with the data acquisition system (in 2008).	143
Figure 5.6. Response caused by a hammer impact (time08_3): (a) force; and (b) acceleration time series at node 15.	145
Figure 5.7. FRFs in overlaid format (time08_3).	145
Figure 5.8. Transverse cracking on the surface of the deck pavement (in 2008).	146

Figure 5.9. Variability in the modal parameters along with the differential temperature across the deck during the 24-hour test in 1996: (a) first natural frequency; and (b) first damping ratio.	148
Figure 5.10. Variability in the modal parameters along with the differential temperature across the deck during the 24-hour test in 1997: (a) first natural frequency; and (b) first damping ratio.	148
Figure 5.11. Modal parameters of all tests in 1996, 1997, and 2008: (a) natural frequencies; and (b) damping ratios.	150
Figure 5.12. First mode shape for the maximum and minimum natural frequencies observed in: (a) 1996; (b) 1997; and (c) 2008.	151
Figure 5.13. SDOF system.	152
Figure 5.14. Free vibration responses caused by two impulse forces (I_1 and $I_2 = I_1 \times 2$).....	153
Figure 5.15. AR model analysis: (a) estimated parameters based on responses caused by I_1 and I_2 ; and (b) responses estimated using parameters from the response caused by I_1	153
Figure 5.16. Normalized 13-average AIC, RMS, SVD, and PAF functions during the 24-hour test in 1996 (node 15).	154
Figure 5.17. Normalized 11-average AIC, RMS, SVD, and PAF functions during the 24-hour test in 1997 (node 15).	154
Figure 5.18. Normalized 20-average AIC, RMS, SVD, and PAF of the tests performed in 2008 (node 15).	155
Figure 5.19. Error bar (two standard deviations) with AR(25) parameters estimated at node 15 during the 24-hour test in 1996 along with the outlier-free means (dots).	156
Figure 5.20. Error bar (two standard deviations) with AR(25) parameters estimated at node 15 during the 24-hour test in 1997 along with the outlier-free means (dots).	156
Figure 5.21. Error bar (two standard deviations) with AR(25) parameters estimated at node 15 during the tests in 2008 along with the outlier-free means (dots).	156
Figure 5.22. Outlier-free means of the AR parameters estimated in 1996, 1997, and 2008.	157
Figure 5.23. Force time series for linearity check using tests performed in 2008: (a) low force level, time08_1; and (b) high force level, time08_2.....	158
Figure 5.24. Average of the AR(25) parameters for linearity check using time08_1 and time08_2 tests performed in 2008 at node 15.	158
Figure 5.25. Measured and predicted acceleration time series at 17:52 (1996) using an AR(25) model with the 24-hour-average parameters of 1996: (a) full time series; and (b) windowed time series.....	159

Figure 5.26. Measured and predicted acceleration time series at 18:00 (1997) using an AR(25) model with the 24-hour-average parameters of 1996: (a) full time series; and (b) windowed time series.	159
Figure 5.27. Measured and predicted acceleration time series at 17:20 (2008) using an AR(25) model with the 24-hour-average parameters of 1996: (a) full time series; and (b) windowed time series.	160
Figure 5.28. RMS of the AR(25) residual errors from the tests performed in 1996, 1997, and 2008.	160
Figure 5.29. RMS of the AR(25)-ARX(15,10) residual errors from the tests performed in 1996, 1997, and 2008.	161
Figure 5.30. RMS of the AR(25) residual errors from the tests performed in 1996, 1997, and 2008; horizontal dashed line corresponds to the maximum value of 1997.	162
Figure 5.31. RMS of the AR(25)-ARX(15,10) residual errors from the tests performed in 1996, 1997, and 2008; horizontal dashed line corresponds to the maximum value of 1997.	162
Figure 5.32. Differential temperature across the deck along with the RMS of the AR(25) residuals, with parameters estimated at 21:10, for each test at node 15 during the 24-hour test in 1996.	163
Figure 5.33. Differential temperature across the deck along with the RMS of the AR(25) residual errors, with parameters estimated at 22:00, for the 24-hour tests in 1997 at node 15.	163
Figure 5.34. Averaged singular spectra at node 15 in 1996, 1997, and 2008.	164
Figure 5.35. Outlier detection of feature vectors composed of natural frequencies using the MSD-based algorithm; threshold defined based on 99% confidence interval of a χ_6^2	166
Figure 5.36. Outlier detection of feature vectors composed of natural frequencies using the SVD-based algorithm; threshold equals to 99% cut-off value over the DIs from the training data.	166
Figure 5.37. Outlier detection of feature vectors composed of natural frequencies using the AANN-based algorithm; threshold equals to 99% cut-off value over the DIs from the training data assuming: (a) one factor; and (b) two factors.	167
Figure 5.38. Outlier detection of feature vectors composed of natural frequencies using the FA-based algorithm; threshold equals to 99% cut-off value over the DIs from the training data assuming: (a) one factor; and (b) two factors.	167
Figure 5.39. Outlier detection of feature vectors composed of AR(25) parameters using the MSD-based algorithm; threshold defined based on 99% confidence interval of a χ_{25}^2	169

Figure 5.40. Outlier detection of feature vectors composed of AR(25) parameters using the SVD-based algorithm; threshold equals to 99% cut-off value over the DIs from the training data	169
Figure 5.41. Outlier detection of feature vectors composed of AR(25) parameters using the AANN-based algorithm; threshold equals to 99% cut-off value over the DIs from the training data assuming: (a) one factor; and (b) two factors.	169
Figure 5.42. Outlier detection of feature vectors composed of AR(25) parameters using the FA-based algorithm; threshold equals to 99% cut-off value over the DIs from the training data assuming: (a) one factor; and (b) two factors.....	170
Figure 5.43. Estimated PDF of the DIs from the training data along with the theoretical χ_{25}^2 , when using the MSD-based algorithm.	170

LIST OF TABLES

Table 3.1.	Accuracy of binary classification.	53
Table 3.2.	Feature extraction techniques along with potential detectable type of damages.	55
Table 4.1.	Data labels of the 17 structural state conditions.	62
Table 4.2.	Experimental along with numerical natural frequencies and damping ratios for State#1 (baseline condition).	66
Table 4.3.	Experimental natural frequencies and damping ratios of all state conditions.	76
Table 4.4.	Number and percentage of Type I and Type II errors for each algorithm.	124
Table 4.5.	Number of Type I and Type II errors.	133
Table 5.1.	Summary description of the data sets from the 24-hour test in July/August, 1996.	144
Table 5.2.	Summary description of the data sets from the 24-hour test in July, 1997.	144
Table 5.3.	Summary description of the data sets measured in September, 2008.	145
Table 5.4.	Daily average temperature and humidity records at Truth or Consequences, New Mexico.	146
Table 5.5.	Maximum and minimum values of the first natural frequency and damping ratio observed in 1996, 1997, and 2008.	149
Table 5.6.	Values of the first natural frequency and damping ratio observed in 1996, 1997, and 2008 at 10:00 (morning) and 17:20 (afternoon).	149
Table 5.7.	Correlation coefficients of the AR parameter curves in Figure 5.22.	157

NOTATION

All symbols used in this dissertation are defined when they first appear in the text. For the reader's convenience, this section contains only the principal meanings of the commonly used acronyms and symbols. Some symbols denote more than one meaning, but their meaning should be clear when read in context.

Abbreviations

AANN	Auto-associative neural network
ACF	Auto-correlation function
AIC	Akaike information criterion
AR(p)	Auto-regressive model of order p
ARX(a,b)	Auto-regressive model with exogenous inputs (a auto-regressive and b exogenous input terms)
BMS	Bridge management system
CIC	Consistent information criterion
CMIF	Complex mode indicator function
COMAC	Co-ordinate modal assurance criterion
CWT	Continuous wavelet transform
DI	Damage indicator
FA	Factor analysis
FHWA	Federal Highway Administration
FRF	Frequency response function
MAC	Modal assurance criterion
MAR(p)	Multivariate auto-regressive model of order p
MSD	Mahalanobis squared distance
NBI	National Bridge Inventory
NBIS	National Bridge Inspection Standards
NDT	Non-destructive testing
NI	National Instruments
NTSB	National Transportation Safety Board
PAF	Partial auto-correlation function
PCA	Principal components analysis
PDF	Probability density function
PSD	Power spectral density
RFP	Rational-fraction polynomial
RMS	Root mean square

ROC	Receiver operating characteristics
SDOF	Single-degree-of-freedom
SHM	Structural health monitoring
SPC	Statistical process control
SPR	Statistical pattern recognition
STFT	Short-time Fourier transform
SVD	Singular value decomposition
USA	United States of America
WT	Wavelet transform

Roman Symbols

d^2	Mahalanobis squared distance
e	Residual error value
\mathbf{e}	Vector of residual errors
$E[\]$	Expectation operator
\mathbf{E}	Matrix of residual vectors
\mathbf{D}	Damping matrix
$i, j, \text{ and } k$	Indices
\mathbf{K}	Stiffness matrix
m	Feature vector dimension or embedding dimension
n	Number of feature vectors
N	Time series size or number of observations
N_t	Total number of observations used in fitting auto-regressive models
\mathbf{M}	State matrix
p	Number of regressive model parameters (or model order)
r_{xz}	Correlation coefficient between x and z
R_{xx}	Auto-correlation function of x
R_{xz}	Cross-correlation function between x and z
\mathbf{s}	Response time series
t	Time variable
\mathbf{v}	Response time series
x	Variable
\bar{x}	Sample average of x
\mathbf{x}	Feature vector (or vector of variables)
\mathbf{X}	Matrix of feature vectors from the training data (normal condition)

z	Variable
\bar{z}	Sample average of z
\mathbf{z}	Feature vector (or vector of variables)
\mathbf{Z}	Matrix of feature vectors from the test data

Greek Symbols

α	Level of significance
β	Vector of exogenous parameters
ε	Sum-of-square of errors
Λ	Matrix of factor loadings
μ	Population mean
Σ	Covariance matrix
σ	Population standard deviation
σ^2	Population variance
τ	Time lag
ϕ	Vector of auto-regressive parameters (or mode shape vector)
Φ	Matrix of mode shapes
χ_m^2	Central chi-square distribution with m degrees of freedom

ABSTRACT

Damage Identification in Civil Engineering Infrastructure under Operational and Environmental
Conditions

by

Elói Figueiredo

Doctor of Philosophy in Civil Engineering

Faculty of Engineering of the University of Porto, 2010

Joaquim A. Figueiras¹ and Charles R. Farrar²

Real-world structures are subjected to operational and environmental condition changes that impose difficulties for detecting and identifying structural damage. In fact, the author believes that separating changes in sensor readings caused by damage from those caused by changing operational and environmental conditions is one of the biggest challenges for transitioning structural health monitoring (SHM) technology from research to practice. The SHM process is posed in the context of the statistical pattern recognition (SPR) paradigm, where vibration-based methods are applied to detect damage in civil infrastructure. Even though this paradigm intends to pave the way for data-based models applicable to systems of arbitrary complexity, the bridge structures are the focus of this dissertation.

The objective of this dissertation is to review, develop, and apply several SHM statistical procedures for feature extraction and statistical modeling for feature classification capable of detect damage on structures under unmeasured operational and environmental variations. In the feature extraction step, the auto-regressive (AR) model is focus of special attention due to its simplicity of application and capability to detect damage. Additionally, a novel algorithm for feature extraction is presented that uses the state-space reconstruction to infer the geometrical structure of a deterministic dynamical system from observed time series of a system response at multiple locations. The unique contribution of this algorithm is that it uses a multivariate auto-regressive model of a baseline condition to predict the state space, where the model encodes the embedding vectors rather than scalar time series. Moreover, four machine learning algorithms are presented to remove the effects of operational and environmental variations on the extracted features. These algorithms are desirable because they develop a functional relationship that models how changing operational and environmental conditions

¹ Full Professor, Faculty of Engineering of the University of Porto, Portugal

² Director of the Engineering Institute, Los Alamos National Laboratory, United States of America

influence the underlying distribution of the damage-sensitive features, without direct measurement of the factors such as temperature and humidity.

The applicability of the SHM-SPR, along with the reviewed and proposed statistical procedures, is first demonstrated in a base-excited three-story frame structure tested in laboratory environment to obtain standard data sets from an array of sensors under several structural state conditions. Tests were performed with varying stiffness and mass conditions with the assumption that these sources of variability are representative of changing operational and environmental conditions (e.g. changing mass might represent varying live loads and changing temperature will influence stiffness properties on a structure). Damage is simulated through nonlinear effects introduced by a bumper mechanism that induces a repetitive, impact-type nonlinearity. This mechanism intends to simulate, for instance, the cracks that open and close under dynamic loads or loose connections that rattle.

Finally, the applicability of the SHM-SPR paradigm is demonstrated in 12-year span data from the real-world undamaged Alamosa Canyon Bridge, near to Truth or Consequences, New Mexico. Herein, the AR models and machine learning algorithms are focus of special attention. The former because their applicability on civil infrastructure is still limited, and the latter because they might be useful for real-world applications, in situations where the operational and environmental variations cannot be measured.

RESUMO

Identificação de Dano em Infra-estruturas de Engenharia Civil sob Condições Operacionais e Ambientais

por

Elói Figueiredo

Doutoramento em Engenharia Civil

Joaquim A. Figueiras³ e Charles R. Farrar⁴

As estruturas estão sujeitas a alterações operacionais e ambientais que impõem dificuldades na detecção de danos estruturais. De facto, o autor acredita que, a separação das alterações nas respostas estruturais causadas por danos das alterações causadas por variações de natureza operacional e ambiental é um dos maiores desafios para a transição da monitorização da integridade estrutural (SHM) da investigação para a prática. Assim, o processo de SHM é integrado no contexto do paradigma de reconhecimento de padrões (SPR), onde métodos estatísticos baseados em vibração estrutural são aplicados para detecção de danos em infra-estruturas de engenharia civil. Mesmo embora o paradigma tem como objectivo abrir caminho a métodos estatísticos aplicáveis a sistemas de complexidade arbitrária, as pontes serão alvo de especial atenção nesta dissertação.

O objectivo desta dissertação é o de rever, desenvolver e aplicar vários métodos estatísticos para a extracção de características (ou parâmetros da resposta estrutural) e para classificação das mesmas no contexto do paradigma SHM-SPR, capaz de detectar danos em estruturas sob condições operacionais e ambientais variáveis. Na fase de extracção de características é dado ênfase ao modelo auto-regressivo devido à sua capacidade e simplicidade de aplicação. Além disso, um novo algoritmo baseado no conceito de *state-space reconstruction* é proposto para inferir a estrutura geométrica de um sistema dinâmico e determinístico observado através de respostas estruturais em forma de séries temporais. A contribuição original deste algoritmo reside na utilização de um modelo auto-regressivo multi-variável do estado inicial, onde o modelo incorpora vectores ao invés de escalares. Uma hipótese é testada em que o modelo multi-variável não consegue prever o estado inicial quando o dano está presente. Além disso, quatro algoritmos de aprendizagem são apresentados para remover os efeitos das variações operacionais e ambientais sobre os dados de respostas estruturais. Esses algoritmos são desejáveis porque eles desenvolvem uma relação funcional entre as variações operacionais e ambientais e a distribuição das características.

³ Professor Catedrático, Faculdade de Engenharia da Universidade do Porto, Portugal

⁴ Director do *Engineering Institute, Los Alamos National Laboratory*, Estados Unidos da América

A aplicabilidade do paradigma SHM-SPR, e dos vários métodos revistos e propostos, é verificada previamente num modelo reduzido de laboratório de três pisos. Esta estrutura é usada para obter respostas estruturais através da simulação de diversas condições operacionais e ambientais e também de dano. Testes foram realizados com diferentes condições de rigidez e de massa, com o pressuposto de que estas fontes de variabilidade são representativas da evolução das condições operacionais e ambientais (por exemplo, alteração da massa simula acções variáveis e a mudança de temperatura pode influenciar propriedades de rigidez de uma estrutura). O dano é simulado através de efeitos não lineares introduzidos por um mecanismo constituído por uma coluna suspensa e por um batente. Este mecanismo tem como objectivo simular, por exemplo, fendas que abrem e fecham devido a acções dinâmicas ou ligações aparafusadas soltas.

Finalmente, a aplicabilidade do paradigma SHM-SPR é testada em respostas estruturais, de três períodos distintos dentro de um intervalo de 12 anos, recolhidas de um vão da ponte *Alamosa Canyon Bridge*, perto de *Truth or Consequences*, Novo México, Estados Unidos da América. Os modelos auto-regressivos e os algoritmos de aprendizagem são foco de atenção especial. Os primeiros porque a sua aplicabilidade em pontes é ainda limitada e os últimos porque eles são úteis em aplicações reais, onde as variações operacionais e ambientais não podem ser medidas.

ACKNOWLEDGEMENTS

I would like to give special thanks to my advisors, Joaquim Figueiras and Chuck Farrar. Their constant support, advice, and commitment to my research have been invaluable. I would like to thank Gyuhae Park for his one-to-one guidance that gave me while working at Los Alamos National Laboratory (LANL) and Mike Todd as my host while working at the University of California, San Diego (UCSD). Also, a special thanks to Keith Worden from the University of Sheffield for his collaboration and lessons.

Thanks to my friends and collaborators at LANL/UCSD including Stuart Taylor, Eric Flynn, Kevin Farinholt, David Mascarenas, Greg Jarmer, Samory Kpotufe, Eric Moro, and Dustin Harvey. Also, a special thanks to Kathie Womack on behalf of the technical staff members at LANL.

Thanks to my friends and collaborators at Faculty of Engineering of the University of Porto including José Santos, Lino Maia, and Américo Dimande.

A special thanks to my forever professors and friends Luís Juvandes, Arlindo Begonha, Ana Maria Sarmiento, and Rui Carneiro Barros.

I would like to acknowledge support through the four-year PhD Fellowship SFRH/BD/29460/2006 given by the *Fundação para a Ciência e a Tecnologia* (FCT). Also, I would like to acknowledge support through the UCSD Jacobs School of Engineering Fellowship for the six-month period of studies at that institution and *Fundação Luso-Americana* (FLAD) for the institutional research grant number 036/2009 to reinforce the capacity of action of research collaboration on SHM between the Engineering Institute and the Laboratory for the Concrete Technology and Structural Behaviour.

Lastly but most importantly, I would like to thank my family and Rute for their constant support throughout the entire PhD program, especially for their comprehension during my period of studies in the USA.

1. INTRODUCTION

1.1 SHM Background

The process of implementing a damage detection strategy for aerospace, civil, and mechanical infrastructure is referred to as structural health monitoring (SHM). Here damage is defined as changes to the material and/or geometric properties of these systems, including changes to the boundary conditions and system connectivity, which adversely affect the system's current or future performance. The goal of SHM is to improve the safety and reliability of aerospace, civil, and mechanical infrastructure by detecting damage before it reaches a critical state. To achieve this goal, technology is being developed to replace qualitative visual inspection and time-based maintenance procedures with more quantifiable and automated damage assessment processes. These processes are implemented using both hardware and software with the intent of achieving more cost-effective condition-based maintenance. A more detailed discussion on SHM can be found in [1, 2]. Nevertheless, throughout this chapter, a general overview of the SHM for civil infrastructure, with special emphasis on bridges, will be presented.

1.1.1 *Historical Perspective*

The damage detection in the past was mainly performed based on visual inspection methods, with occasional application of conventional non-destructive testing (NDT) techniques such as ultrasonic and acoustic emission (e.g. tap tests on train wheels). However, vibration-based damage detection methods have received considerable attention during the last 40 years. A brief review of the SHM historical evolution using vibration-based structural damage identification is given below. However, the author recommends Doebling et al. [3] and Sohn et al. [4] for a review of literature on this subject.

The most successful application of damage detection using vibration-based methods has been reported for rotating machinery. The shorter lifetime, controlled operational and environmental variability along with well-defined damage types permitted one to build up large data sets, from both undamaged and damaged conditions, and to pave the way for application of pattern recognition algorithms. In the broad sense, a pattern recognition algorithm simply assigns estimated spectra to types of damage. A relative recent state of the art review on monitoring rotating machinery was made by Randall [5, 6].

The aerospace industry has pioneered the transition of SHM from research to practice in a variety of civilian and defense applications. In early 1980s, the development of the space shuttle motivated the aeronautics community to implement vibration-based methods. The Shuttle Modal Inspection System was developed to detect fatigue damage in the fuselage panels, typically covered with a thermal protection system making the visual inspection difficult. This system has been used successfully to detect and locate damage in hidden components using analytical and measured modal correlation procedures [1]. Another successful SHM application in the aerospace industry is the rotorcraft Health and Usage Monitoring System that were developed in early 1990s. These systems were initially installed in the rotor drive train and gearbox components for early failure detection. Well-defined operational conditions (e.g. the variation in rotor speed) provide the basis to correlate vibration spectrum changes with component degradation. Even though it was initially implemented to increase flight safety, it has been commercially developed for economic benefits, such as increasing mission reliability, downtime reduction, and customization of maintenance actions [7].

During the 1970s and 1980s, the oil industry also made attempts to detect damage on a global basis in offshore platforms using vibration-based methods. These methods were mainly based on inverse modeling approaches, where analytical models are adjusted with measured natural frequencies. The operational and environmental variability present in those structures such as platform machine noise, difficult access for measurement, changing mass caused by rise and fall of sea levels as well as liquid storage, and boundary condition changes were the main reasons that the damage detection procedures were not successful [1].

The civil engineering community has also studied vibration-based damage-detection methods for bridges since the early 1980s. Those methods were fundamentally based on inverse modeling approaches, using modal parameters as well as derived quantities such as mode-shape curvatures and a dynamic flexibility matrix [1]. However, the operational and environmental variability present significant difficulties to detect damage in such large-scale structures. Even though there is still a long way to go for a successful real-world SHM application, regulatory requirements are driving current research and development of vibration-based bridge monitoring systems. In the United States of America (USA), the Long-Term Bridge Performance Program was included in the latest highway legislation. This program attempts to provide quantitative data for network and bridge level management and, ultimately, to improve the safety assessment of the nation's bridges [8]. Furthermore, in eastern Asian countries, the construction companies need to certify, periodically, the bridge structure condition. (Special attention on SHM for bridges and challenges are discussed in more detail in Chapter 2.)

In a general sense, all the examples given above make use of two complementary approaches, namely inverse problem or pattern recognition techniques. The former tries to identify damage by relating the measured data from the structure to physics-based numerical models (e.g. finite element models). A

summary of these inverse modeling approaches for damage identification can be found in Doebling et al. [3]. The latter one is a data-based (or data-driven) modeling approach, where data from a damaged state condition is assigned to a known type of damage. Basically, the identification of damage requires data comparison between two state conditions, the baseline and damaged conditions. The later approach will be the focus of this dissertation.

1.1.2 Statistical Pattern Recognition Paradigm

The author believes that all approaches to SHM as well as all traditional NDT techniques can be cast in the context of a pattern recognition problem. Thus, the statistical pattern recognition (SPR) paradigm for the development of SHM solutions can be described as a four-step process as illustrated in Figure 1.1 [1].

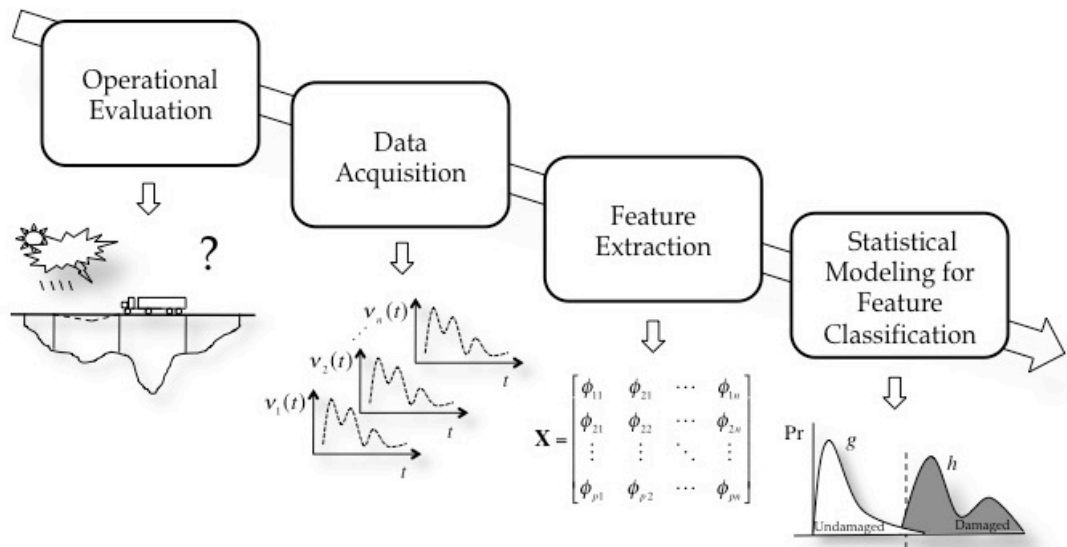


Figure 1.1. SPR paradigm for SHM.

A necessary first step to developing SHM capability is to perform an operational evaluation. This part of the SHM solution process attempts to answer four questions regarding the implementation of a SHM system: (i) What are the life safety and/or economic justifications for monitoring the structure? (ii) How is damage defined for the system being monitored? (iii) What are the operational and environmental conditions under which the system of interest functions? (iv) What are the limitations on acquiring data in the operational environment? Operational evaluation defines, and to the greatest extent possible quantifies, the damage that is to be detected. It also defines the benefits to be gained from deployment of the SHM system. This process also begins to set limitations on what will be monitored and how to perform the monitoring as well as tailoring the monitoring to unique aspects of the system and unique features of the damage that is to be detected.

The data acquisition portion of the paradigm involves selecting the excitation methods; the sensor types, numbers, and locations; and the data acquisition/storage/processing/transmittal hardware. The

actual implementation of this portion of the SHM process will be application-specific. A fundamental premise regarding data acquisition and sensing is that these systems do not measure damage. Rather, they measure the response of a system to its operational and environmental loading or the response to inputs from actuators embedded with the sensing system. Depending on the sensing technology deployed and the type of damage to be identified, the sensor readings may be more or less directly correlated to the presence and location of damage. Data interrogation procedures (feature extraction and statistical modeling for feature classification) are the necessary components of a SHM system that convert the sensor data into information about the structural condition. Furthermore, to achieve successful SHM, the data acquisition system will have to be developed in conjunction with these data interrogation procedures.

A damage-sensitive feature is some quantity extracted from the measured system response data that is correlated with the presence of damage in a structure. Ideally, a damage-sensitive feature will change in some consistent manner with increasing damage level. Identifying features that can accurately distinguish a damaged structure from an undamaged one is the focus of most SHM technical literature [3, 4]. Fundamentally, the feature extraction process is based on fitting some model, either physics- or data-based, to the measured response data. The parameters of these models, or the predictive errors associated with them, become the damage-sensitive features. An alternative approach is to identify features that directly compare the sensor waveforms or spectra of these waveforms measured before and after damage. Many of the features identified for impedance-based and wave propagation-based SHM studies fall into this category [9, 10, 11, 12].

The portion of the SHM process that has received the least attention in the technical literature is the development of statistical models to enhance the damage detection process. Statistical modeling for feature classification is concerned with the implementation of algorithms that analyze the distributions of the extracted features in an effort to determine the structural condition. The algorithms used in statistical model development usually fall into three general categories: (i) group classification; (ii) regression analysis; and (iii) outlier detection. The appropriate algorithm to use will depend on the ability to perform supervised or unsupervised learning. Here, supervised learning refers to the case where examples of data from damaged and undamaged conditions are available. Unsupervised learning refers to the case where data are only available from the undamaged condition. Note that for high capital expenditure structures, such as most civil infrastructure, the unsupervised learning algorithms are often required because only data from the undamaged condition are available.

Inherent in the data acquisition, feature extraction, and statistical modeling portions of the SHM process are data normalization, cleansing, fusion, and compression [2]. As it applies to SHM, data normalization is the process of separating changes in sensor reading caused by damage from those caused by varying operational and environmental conditions [13]. Data cleansing is the process of selectively choosing data to pass on to, or reject from, the feature selection process. Data fusion is the

process of combining information from multiple sensors in an effort to enhance the fidelity of the damage detection process. Data compression is the process of reducing the dimensionality of the data, or the features extracted from the data, in an effort to facilitate efficient storage of information and to enhance the statistical quantification of these parameters. These four activities can be implemented in either hardware or software and usually a combination of the two approaches is used.

1.1.3 Hierarchical Structure of Damage Identification

The damage identification should be as detailed as possible in order to describe the damage impacts on the system. In a broad sense, developments on damage identification can be broken down into three areas, namely damage detection, damage diagnosis, and damage prognosis. Nonetheless, damage diagnosis can be subdivided in order to better characterize the damage in terms of location, type, and severity. Thus, even though the original guidelines of Rytter [14] assumed a four-step process, the hierarchical structure of damage identification can be established into a five-step process (Figure 1.2) that answers the following questions [15]:

1. Is the damage present in the system (detection)?
2. Where is the damage (localization)?
3. What kind of damage is present (type)?
4. What is the extent of damage (severity)?
5. How much useful lifetime remains (prognosis)?

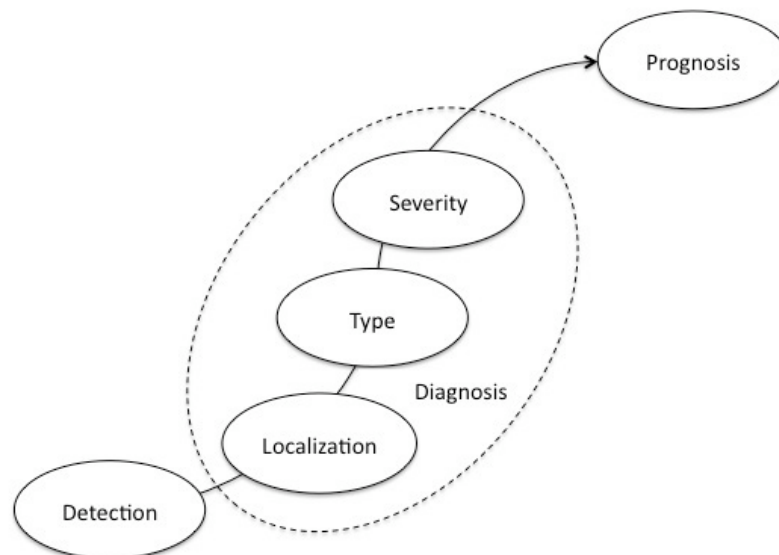


Figure 1.2. Hierarchical structure of damage identification.

The answers to the questions above can be made only in a sequential way, e.g., the answer to the severity of damage can only be made with *a priori* knowledge of the type of damage. When applied in an unsupervised mode, statistical algorithms are typically used to answer questions regarding the detection and localization of damage. When applied in a supervised learning mode and coupled with

analytical models, the statistical algorithms can be used to better determine the type of damage, the severity of damage, and remaining useful lifetime. Note that damage prognosis at step five cannot be accomplished without an understanding of the damage accumulation process. See [16] for further discussion on the concept of damage prognosis.

1.1.4 Economic and Safety Considerations

The ability to transition SHM from research to practice depends highly on the economical and/or life safety benefits it can provide. Besides the ultimate goal to prevent catastrophic failures and the usefulness to evaluate the bridge performance, as with any investment, the SHM system must prove to be a way of reducing the overall life-cycle maintenance costs related to a structure.

For new bridges, currently the initial investment of a SHM system ranges between 0.5 and 3% of the total bridge construction cost. Additionally, every year the maintenance and data management typically add 5-20% of the SHM system cost. Therefore, over the first 10 years of a medium-size bridge, the SHM system may require an investment in the order of 2-5% of the total construction cost [17].

In the light of the previous cost estimates, a SHM system must be designed as an integrated system that can be developed during the construction stage as well as over the bridge lifetime. Note that for the construction stage, the SHM system can potentially be used to supervise the construction and thus put pressure on the contractors to deliver a high-quality product as well as to support the construction of new lightweight structures. Note that many failures occur during construction and the SHM system can be used to minimize these risks.

An overview of the motivation to deploy SHM systems on bridges is well stated by Ko and Ni [18]. Even though the main goal of SHM systems is for early damage identification and, ultimately, to prevent catastrophic failures, from a more general perspective, SHM systems for bridges might be designed to:

- (i) provide structural monitoring during the construction stage with the potential benefit of reducing manufacturing costs and to permit lightweight structures by fully exploit the material strength;
- (ii) validate design assumptions to measure the actual structural response as well as to improve design specifications for future structures;
- (iii) detect anomalies and/or damage at early stages;
- (iv) reduce and/or support visual inspections;
- (v) provide the owners with a real-time tool to support the decision-making process:
 - a. reduce unnecessary *ad hoc* maintenance;
 - b. extend the structures' lifetime by preventive maintenance;
 - c. reduce downtime costs;

- d. traffic management and control.
- (vi) after extreme events (e.g. earthquakes and blast loading) the SHM systems can be used for condition assessment regarding the integrity of the structure;
- (vii) finally, the ultimate goal to deploy SHM systems in the bridge structures will always be to prevent catastrophic failures.

1.2 Current Status and Motivation

In real-world structures, the separation of changes in sensor readings caused by damage from those caused by changing operational and environmental conditions is one of the biggest challenges for transitioning SHM technology from research to practice. Even though those challenges affect almost every structure, the civil infrastructure, and specially the bridges, is the focus of this dissertation.

Currently, in the SHM field, there are two well-known approaches to separate those changes. The first approach consists of measuring the factors related to operational and environmental variations such as live loads, temperature, wind speed, and/or moisture levels, as well as the structural response at different locations. Then, the normal condition can be parameterized as a function of different operational and environmental conditions. With such parameterized model, novelty detection procedures can be used to detect when the measured structural response deviates from the normal condition that corresponds to the appropriate operational and environmental conditions. The second approach, and the one used in this dissertation, attempts to establish the existence of damage for cases when measures of the operational and environmental factors that influence the structure's dynamic response cannot be measured. Thus, this approach intends to eschew the measure of operational and environmental variations and physics-based models such as finite element analysis and, therefore, pave the way for data-based models applicable to systems of arbitrary complexity.

Fundamentally, this dissertation poses the SHM process in the context of the SPR paradigm. Essentially, the motivation of this dissertation is to contribute to steps three and four of this paradigm, specially the development of vibration-based damage detection procedures in an unsupervised mode, which use observed structural response data to detect damage in the civil infrastructure in the presence of unmeasured operational and environmental variability. Actually, the author believes that vibration-based damage detection procedures will not be feasible without robust algorithms that are capable of normalizing the effect of operational and environmental variations in the measured data. Thus, data normalization algorithms, derived from the machine learning field, will be the focus of this dissertation.

1.3 Objective and Organization of this Dissertation

The objective of this dissertation is to review, develop, and apply several SHM statistical procedures for feature extraction and statistical modeling for feature classification, in the context of the SPR

paradigm, capable of detect damage on structures under unmeasured operational and environmental factors. To test their performance, the procedures are first applied on standard data sets measured from a laboratory three-story frame structure and then on response data from a real-world structure – The Alamosa Canyon Bridge. The three-story structure intends to validate SHM statistical procedures in order to bridge the gap between laboratory experiments and real-world structures. Note that even though this procedure might be applied to civil infrastructure of arbitrary complexity, in this case the procedures are specially posed in the context of bridge applications.

In the hierarchical structure of damage identification, this dissertation addresses the need for robust incipient vibration-based damage-detection procedures. Therefore, this dissertation is mainly concerned with detection of damage in the structures. Even though locating and assessing the severity of damage are important in terms of estimating the residual lifetime of the structures, the reliable detection of damage existence must precede these more detailed damage descriptions.

For several years the monitoring systems have been installed on bridges around the world without any damage detection strategy. Thus, in order to have a glimpse on the state of the art in monitoring applications on bridges as well as the motivation behind them, Chapter 2 performs a literature review on several bridge disasters over the recent history and the reactive actions taken by the authorities to mitigate future accidents. Additionally, it points out several limitations and challenges for implementing of effective SHM systems to detect damage on a global basis under operational and environmental variations. Chapter 3 summarizes several feature extraction techniques and statistical algorithms for feature classification that have been widely used in different engineering fields. Machine learning algorithms are presented to remove the effects of the operational and environmental variability from the features. Furthermore, a novel algorithm for feature extraction based on state-space reconstruction from time series is presented. Chapter 4 tests and applies the described statistical procedures on standard data sets from a base-excited three-story frame structure under simulated operational and environmental conditions. To the extent possible, all SHM research should be validated using data from real-world structures. Thus, in Chapter 5 the SHM-SPR paradigm is applied on vibration data from the Alamosa Canyon Bridge. Finally, Chapter 6 summarizes the main conclusions and contributions of this dissertation as well as points out future research topics.

1.4 Original Contributions and Extension of Knowledge

A considerable number of research projects have been funded to improve the damage identification in two independent but complement areas: sensing system development and signal processing. This dissertation is a contribution at the signal processing level, with special emphasis on the feature extraction techniques and statistical modeling development for feature classification. Nevertheless, the author recommends further reading for a discussion of recent developments in SHM-related sensing

technology [19]. The following content attempts to highlight some of the original contributions of this dissertation at the signal processing level.

In Chapter 3, the feature extraction techniques and machine learning algorithms are summarized using the same nomenclature for easier understanding. In Section 3.2.5, a novel algorithm is proposed for feature extraction in structures under varying operational and environmental conditions. It uses the state-space reconstruction to infer the geometrical structure of a deterministic dynamical system from observed response time series at multiple locations. The unique contribution is the use of a multivariate auto-regressive (MAR) model of the baseline condition to predict the state space, where the model encodes the embedding vectors rather than scalar time series. Notice that most of the techniques described in Chapter 3 have been incorporated into a software package called *SHMTools*. This package is presented in Appendix A as the beginning of a larger effort to collect and archive proven approaches to support the SHM process. The package provides a set of functions organized into modules according to the three primary steps of the SHM-SPR paradigm: data acquisition, feature extraction, and statistical modeling for feature classification. A modular function design and a set of standardized parameter formats make it easy to assemble and test customized SHM process.

Throughout the last 15 years many studies have proposed both feature extraction and statistical model for feature classification algorithms. However, most of the studies generally restrict their performance to specific damage-sensitive features and statistical modeling algorithms. Thus, Chapter 4 contributes to the SHM field by verifying the performance of a variety of statistical procedures to detect damage under simulated operational and environmental conditions by using standard data sets from a laboratory frame structure. Although several machine learning algorithms have been reported in the literature, there is no study that has compared these algorithms on a common set of data to assess their relative performance. Therefore, the study reported herein intends to provide such a comparison. Moreover, another study is carried out to highlight the importance of the still complex issue of estimating the appropriate auto-regressive (AR) model order. Additionally, an attempt is made to correlate the optimal AR model order to the classification performance using an information criterion technique.

Finally, in Chapter 5 the applicability of the AR models to extract damage-sensitive features on real-world response data from one simply supported span of the Alamosa Canyon Bridge is demonstrated. Moreover, the machine learning algorithms are applied, to remove changes in the sensor readings caused by operational and environmental variability, using real-world data from three distinct periods, namely in 1996, 1997, and 2008. To the author knowledge, no other researchers have examined bridge SHM data over that long of a time span.

2. CIVIL INFRASTRUCTURE: THE BRIDGE CASE

For more than 40 years, several structural monitoring systems have been installed on bridges around the world. However, in the last decade, the number of implemented SHM systems in bridges has increased considerably. Note that here SHM is distinguished from structural monitoring, because the former assumes *a priori* a strategy for damage identification.

In the last decade, the USA and China have played an important role in the SHM community. The USA have been the driving force in development of sensing and data acquisition technology while China has led the deployment of SHM technology in real-world civil infrastructure [20]. Nonetheless, one should note that important contributions have also been made in Europe as will be shown throughout this chapter.

Despite enormous developments in technology, the number of real-world examples from long-time application is still limited to gain enough knowledge of their performance. Thus, SHM for civil infrastructure, particularly bridges, is still a challenge [21]. Upon a historic perspective on several bridge disasters, this chapter gives the big picture of the motivation behind some real-world SHM systems on bridges. Additionally, it points out some of the limitations and shortcomings for effective successful implementation with particular focus on the effects of operational and environmental variations on the damage detection process.

2.1 Bridge Disasters: Causes and Challenges

In the USA, it is speculated that the first bridge construction boom started along with the road construction program mandated by the Federal Highway Act of 1956 [22]. During that time, the whole emphasis was centered on the construction of new bridges rather than on routinely inspections or preventive maintenance of the existing ones. In 2002 more than 800 of the 1100 long-span bridges (those with spans of 100 m or longer) in the National Bridge Inventory (NBI) were classified as fracture-critical [23]. The Federal Highway Administration (FHWA) stated in 2005 that 28% of their 595 000 bridges were rated deficient [21]. (Note that, normally, this assessment is based on visual field inspections and/or preliminary NDT.) Besides these warning reports, several catastrophic bridge failures have occurred in the USA. Actually, the safety and/or deterioration of the existence bridges came up in the late 1960s when the pin-connected link suspension US Highway 35 Silver Bridge

suddenly collapsed on December 17, 1967, and killed 46 people (Figure 2.1). This catastrophic event prompted the FHWA to establish the National Bridge Inspection Program in 1970. This program required the bridges to be inspected every two years and the creation of the NBI database. Despite the efforts to inspect the bridges, in June 1983 the Mianus River Bridge on I-95 collapsed killing three people. This disaster caused more concerns regarding fatigue and fracture-critical bridges. The National Transportation Safety Board (NTSB) determined the disaster as a result of undetected anomalies in the pin and hanger assembly by the inspection and maintenance program. In 1987 and 1989, the scour-induced failures at the Schoharie Creek Bridge in New York and at the Hatchie River Bridge in Tennessee, respectively, pushed the need to design bridge piers to resist scour and also the initiation of the underwater bridge inspection program [22]. Realizing the need to inspect the bridges for scour, the FHWA issued a technical advisory in 1988 revising the National Bridge Inspection Standards (NBIS) to require evaluation of all bridges for susceptibility to damage resulting from scour. Actually, scour is statistically considered the most common cause of highway bridge failures in the USA [24]. From 1961 to 1976, 46 out of 86 major bridge failures were a result of scour near piers. Note that more bridge failures during that period were caused by scour than by earthquakes, wind, structural, corrosive, accidental, and construction-related failures [25]. A glimpse on bridge scour research and evaluations can be found in the references [26, 27].



Figure 2.1. Collapse of the Silver Bridge on December 17, 1967, that killed 46 people, USA.

In 2007, the Minneapolis I-35W Bridge over the Mississippi River, Minnesota, collapsed during the rush hour killing 13 people (Figure 2.2). Later, the NTSB determined that the probable cause of the collapse was the inadequate load capacity of the gusset plates at one node along with additional weight

on the bridge [28]. Curious the fact that, in 2005, the bridge was rated as “structural deficient” according to the NBI database and, in 2006, subsequent report found cracking and fatigue problems [29]. In the same year, in a lower advertized event, a heavy truck collapsed the 40-year-old Harp Road Bridge in a rural southwest Washington. The reasons to the non-fatality accident were related to live load caused by the truck that was much higher than the design capacity of the bridge.



Figure 2.2. Collapsed north section of the Minneapolis I-35W Bridge, Minnesota, USA [28].

In spite of these facts, real-world field SHM applications on bridges in the USA are still limited to few deployments. For instance, in response to the I-35W Bridge collapse, a SHM system was incorporated in the new I-35W Saint Anthony Falls Bridge. The main targets of the system were to support the construction stage, structure monitoring, and bridge security. The system includes a wide range of sensors such as vibrating wire strain gauges, thermistors (to measure ambient and gradient temperature), linear potentiometers (to measure joint movements), accelerometers, concrete corrosion, humidity sensors, and SOFO (French acronym of Surveillance d’Ouvrages par Fibres Optiques) long-gauge fiber optic deformation sensors [30]. In New Orleans, a monitoring system has been installed on the Huey P. Long Bridge over the Mississippi River, Jefferson Parish. The system is composed of an array of over 800 vibrating wire and full-bridge resistance strain gauges designed to measure axial and bending load effects on the truss structure. The system was completed with tiltmeters and temperature sensors [31]. The Commodore Barry Bridge that spans the Delaware River is another example of a long-span bridge with an integrated SHM system in the USA [32].

In China, several bridge disasters have kept the attention of the authorities for efficient regulation codes as well as better maintenance programs. For instance, on January 4, 1999, the collapse of the three-year-old pedestrian Rainbow Bridge, Qijiang county, killed 49 people. Investigations into the collapse showed that the steel was of poor quality and that the accident resulted from dereliction of duty by several government officials [33]. Since 2000, the Ministry of Science and Technology along

with the National Natural Science Foundation of China have intensely supported research programs to develop SHM systems [34]. At the present day, hundreds of SHM systems have been implemented into civil infrastructure, such as bridges, buildings, highways, high-speed railway, and offshore structures. The recently constructed long-span cable-supported bridges in Hong Kong, namely the Tsing Ma Bridge, the Kap Shui Bridge, and the Ting Kau Bridge (Figure 2.3), are equipped with the Wind and Structural Health Monitoring System (WASHMS) installed and operated by the Hong Kong Highways Department to ensure road user comfort and safety [35, 36]. The WASHMS consists of roughly 800 sensors in seven major types: anemometers, temperature sensors, dynamic weigh-in-motion sensors, accelerometers, displacement transducers, level sensing stations, strain gauges, video cameras, and GPS systems. The structural responses measured are vibration of cables and main girders, displacement of expansion joints, temperature of box girders, strain of main girders and towers, cable forces, and global position at the top of towers and center of girder spans. The operational and environmental factors measured are the air temperature, wind velocity at top of towers and above bridge deck, and traffic weight. For further reading, the application of SHM technology on bridges in China has been extensively reported in the literature [37, 38].



Figure 2.3. Tsing Ma and Ting Kau Bridges in Hong Kong, China [36].

In Portugal, the Hintze Ribeiro Bridge disaster boosted the owners and authorities for regular bridge inspections and to deploy SHM systems on bridges capable to anticipate disasters. The collapse of the centenary bridge (Figure 2.4), that killed 59 people, was later related to streambed scouring caused by illegal sand extraction, which compromised the integrity of the foundations of the pillars [39]. This disaster pushed the authorities to realize the need of periodic underwater bridge inspections. As a proactive measure to prevent that type of disasters, the SHM system integrated in the Leziria Bridge, Carregado, incorporates sonars to monitor the streambed around two piers. Besides, in the last decade, the authorities and owners have carried out several inspections in the existence bridges and installed

SHM systems on new ones. Real-world examples of SHM systems are the overpasses of the Metro do Porto railway system, D. Luiz I Bridge, Sorraia Bridge, and the already mentioned Leziria Bridge.



Figure 2.4. Hintze Ribeiro Bridge collapse in 2001, Portugal [39].

In the rest of the world, several disasters have happened over the years. For instance, in South Korea, on October 21, 1994, the collapse of the Seongsu Bridge, Seoul, killed 31 people. Further investigations into the disaster concluded that the central section of the structure sheared off during the morning rush hour and fell into the river. It was determined that the structure failure was caused by no-properly welded joints of trusses supporting the bridge concrete slab [39]. In Canada, Quebec, on September 30, 2006, five people were dead when part of the Concorde Boulevard overpass collapsed into the Highway 19. The collapse was related to shear failure in one of the abutments. Later, from the Inquiry Commission's view, no single entity or person was responsible for the collapse, rather it resulted from a sequential chain of causes, namely, inappropriate code standards, defects and lapses during the design and construction, and management during its useful life. The Commission also strongly recommended proper management programs to better face aging infrastructure [40]. Nevertheless, several implementations of long-term SHM systems on bridges have been widely reported. For long-span bridges, the most famous examples are the Great Belt Bridge in Denmark, the Confederation Bridge in Canada, the Akashi Kaikyo Bridge in Japan, and the Seohae Bridge in Korea. Further information on several SHM case studies is available in the International Society for Structural Health Monitoring of Intelligent Infrastructures website [41]. Furthermore, several companies have given the first steps to install SHM systems on bridges. For instance, in Switzerland, the SMARTTEC SA is involved in the SHM process for more than a decade, having participated in more than 250 SHM projects worldwide. See [42] for further reading on some of the lessons learned from those projects.

At the same time the SHM process evolves and matures under long-term research programs supported mainly by public funding, currently, many bridge owners around the world have adopted the so-called

Bridge Management Systems (BMSs) to build inventories and inspection history databases. Basically, these systems are essentially visual-inspection-based decision-support tools developed to analyze engineering and economic factors and to assist the authorities in determining how and when to make decisions regarding maintenance, repair, and rehabilitation of structures in a systematic way [21]. In the early 1990s several software packages were developed to assist in managing bridges, such as PONTIS and BRIDGIT in USA, DANBRO in Denmark [43], and GOA in Portugal [44]. To date, the structural condition assessment of these systems essentially relies on weighted indices based on visual inspections and/or preliminary NDT technologies. Note that these systems are currently described as part of the Asset Management process [45, 46].

2.2 SHM Application: Limitations Due to Operational and Environmental Variability

Among several others, current procedures in SHM for bridges have a considerable number of limitations and prevailing uncertainties due to non-stationary variability sources associated with operational and environmental conditions. Varying operational conditions include live loads such as traffic loads, speed of operation, and changing excitation sources. Varying environmental conditions are frequent result of the temperature, humidity, wind, rainfall, and snow. Note that other sources of variability exist at the experimental level such as instrumentation, random noise, estimation methods, vibration source, etc.

For the last three decades, several studies have investigated the effects of operational and environment conditions as well as damage on dynamic characteristics. In a global basis, when the damage is substantial, such as loss of a primary element of the structure, these procedures have some success to identify damage. However, the operational and environmental variability present in the bridges can often impose changes in the structure response, and mask the changes caused by damage such as concrete cracking, yielding of steel elements, or material deterioration related to aging [47]. Actually, those changes have made the physics-based model approach to detect damage in civil infrastructure a challenge. In other to understand the challenge associated to damage detection under those sources of variations, this section summarizes some real-world examples of measured variability on the dynamic characteristics, with special emphasis on the modal parameters. Additionally, the vulnerability of the boundary conditions to change due to environmental conditions (especially the temperature) is also addressed.

Kim et al. [48] studied the effect of vehicle mass on the dynamic characteristics of three different bridges (three-span suspension bridge, five-span continuous steel box girder bridge, and simply supported plate girder bridge). The natural frequencies were estimated using ambient vibration tests with traffic-induced vibration as source to excite the structures. The authors concluded that for the middle and long-span bridges, the differences could be hardly detected. Actually, in the case of the long-span suspension bridge, where the mass ratio of heavy vehicles to superstructure is about 0.38%,

the mass of vehicles does not have influence on the measured natural frequencies. However, for the short-span bridges whose mass is relatively small compared to traffic mass, the differences become distinguishable. In the case of the simply supported plate girder bridge (46 m), where the mass ratio of heavy traffic to the superstructure is about 3.8%, the measured natural frequencies could change up to 5.4%.

In a study to verify the possible variation in the dynamic properties of a long-span cable-supported bridge under routine traffic conditions, Zhang et al. [49] noted from a 24-hour ambient vibration monitoring that the natural frequencies, of the bridge's modes up to 2 Hz, could exhibit as much as 1% change within a day.

In Irvine, California, a three-span post-tensioned box girder concrete bridge was monitored with accelerometers for a five-year period. The bridge was opened to traffic in 1998 and the monitoring started in 2002. Soyoz and Feng [50] found variations over that period in the first natural frequency in the order of +/-10% comparing to those obtained in the beginning of the monitoring. The authors input those significant variations to changes in the mass of the bridge caused by traffic and environmental effects. To investigate the influence of the vehicle mass, the authors carried out a parametric study using 10 standard passenger vehicles. It was concluded that the vehicles changed the total mass of the bridge in the order of 10% and the fundamental natural frequency of the bridge in the order of 5%. Additionally, over the five-year monitoring it was observed a 5% decrease in the first natural frequency. Furthermore, based on the identified modal parameters and using a neural network-based identification method, it was observed a 2% decrease in the superstructure stiffness. The authors also believe that in the context of the FHWA's Long-Term Bridge Performance Program, the stiffness values can be used to support or partially replace the visual inspections for condition assessment.

Based on a three-year continuous monitoring of the concrete three-cell box girder Westend Highway Bridge in Berlin, Rohrmann et al. [51] noted that the natural frequencies are, approximately, linearly dependent on the measured temperature in the range -9 to 27°C, and that the frequencies of the first 12 modes vary between 0.75×10^{-2} and 4.3×10^{-2} Hz per 1°C change in bridge temperature. Also, it was shown that the higher modes are generally more sensitive than the lower ones. Based on results from traffic, the authors also pointed out that additional mass due to traffic is irrelevant to input changes on the natural frequencies. Additionally, the effect of the Young's modulus of concrete and asphalt was investigated with a dynamic model. It was observed that the effect of temperature on the Young's modulus of asphalt is significant. During the winter time, the Young's modulus of the asphalt coincides with the concrete. In contrast, during the summer time the asphalt layer loses its strength completely for asphalt temperature over 50°C.

In the case of highway bridges, numerous investigations indicate that the temperature can cause modal variability that might reach 5-10% [18]. In a nine-span monitoring program, Roberts and Pearson [52]

found that normal environmental changes could account for changes in natural frequencies between 3-4% during the year. Askegaard and Mossing [53] found that a three-span footbridge exhibits normal frequency variations of 10% over the year.

Based on experimental data obtained from the Alamosa Canyon Bridge, in New Mexico, Farrar et. al [54] noted that natural frequencies were found to vary approximately 5% during a 24-hour time period. Those changes at that time and one year later were correlated with surface temperature differentials across the deck, but were uncorrelated with absolute air temperature. Additionally, in 2008, a study carried out in one simply supported span at the end of the same bridge, the author found an asymmetrical variation in the first mode shape that changed throughout the day, as shown in Figure 2.5. This asymmetry along the longitudinal axis was correlated with the time of day and associated solar heating. These thermal effects were more pronounced because of the north-south orientation of the bridge. If not properly accounted for, such changes in the dynamics response characteristics can potentially result in false indications of damage. Notice that if the mode in Figure 2.5a was considered to be the baseline condition, a classification algorithm would identify the mode in Figure 2.5b as some form of an outlier. This outlier could inappropriately be labeled as damaged if the environmental variability associated with this feature was not taken into account in the outlier detection process.

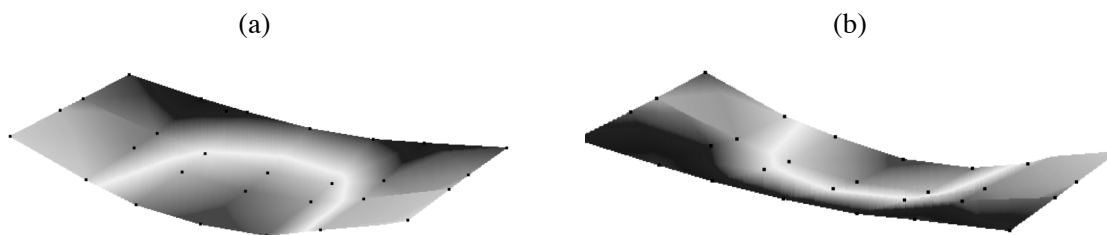


Figure 2.5. First mode shape of one simply supported span of the Alamosa Canyon Bridge, New Mexico, USA, during two distinct times of the day: (a) in the morning (7.75 Hz); and (b) in the afternoon (7.42 Hz).

Xia et al. [55] investigated the relation between dynamic properties and the environmental factors, temperature and humidity, in a laboratory reinforced concrete slab. The study indicated that the natural frequencies of three bending modes decreased 0.13-0.23% for 1°C of increasing temperature and decreased 0.03% for 1% of increasing relative humidity.

Sohn and Farrar [56] successfully identified the location of plastic hinges at the bottom of a column using acceleration time series, but also claimed that further investigation into the influence of environmental effects was needed, because the authors were not able to distinguish changes caused by damage from changes in the environment when both were present at the same time.

Farrar et al. [57] performed vibration tests on the I-40 Bridge over Rio Grande, in New Mexico, USA, in order to investigate if modal parameters could be used to identify damage in the structure. Cuts in four increase level stages were made in a mid-span plate girder to simulate the formation of fatigue

cracks (Figure 2.6). Intuitively, the natural frequencies should decrease as the damage level increases. However, for the fundamental natural frequency, it was observed that the magnitude increased for the first two levels of damage and decreased for the other two levels. Later investigation concluded that the ambient temperature of the bridge played a major role in the variation of the bridge's dynamics characteristics.



Figure 2.6. Vertical cut used to simulate a fatigue crack in a mid-span plate girder of the I-40 Bridge, New Mexico, USA.

In Switzerland, under of the European SIMCES project, the post-tensioned concrete box girder Z-24 Bridge was monitored during almost one year before it was artificially damaged. (Note that this project was only possible because the bridge needed to be demolished.) The monitoring system was composed of sensors to measure air temperature, wind, humidity, bridge expansion, soil temperatures at the boundaries, and concrete temperatures. Based on the continuous monitoring, the authors found strong correlation between temperature and natural frequencies. However, they found no relation between others environmental factors and modal parameters. Furthermore, it was claimed that “moisture absorption” does not significantly change the mass of the bridge based on the assumption that bridge hardly absorbs water and besides every bridge has a draining system to reduce the amount of water on the bridge [58]. In 2001, for the same bridge, Peeters et al. [59] performed a study addressing the influence of the excitation source and the effect of temperature on the modal parameters. The authors concluded that ambient excitation yielded comparable results to the use of shakers. This was a very important conclusion, because it validates the ambient vibration tests to estimate the modal parameters in continuous monitoring. The authors speculated that, for one-year monitoring, differences in the natural frequencies ranging from 14-18% must be explained by normal environmental changes. Additionally, the authors found a bilinear behavior, with turning point at 0°C , to describe the relationship between natural frequencies and temperature. The authors attributed such

behavior to the asphalt layer that during cold periods contributes significantly to stiffen the bridge. Finally, data-based models were used to first establish the correlation between the natural frequencies and temperature, and then to detect damage. Note that in this case the damage was simulated using settlement systems at the piers as shown in Figure 2.7 [60].



Figure 2.7. Settlement-related damage scenario at Z-24 Bridge, Switzerland [60].

Alampalli [61] tested several structures including a 1/6-scale model highway bridge, an abandoned fracture-critical highway bridge, and an in-service highway bridge. The first two bridges were tested under intact and simulated-damage conditions. Note that for obvious reasons it was not possible to introduce damage on the in-service bridge. The damage-scenarios were based on currently observed fatigue damages in bridges: (i) a gusset-plate weld crack; (ii) a longitudinal-stiffener bottom weld crack; and (iii) a crack in weld and base material at a cover-plate toe. The results indicated that natural frequencies, in conjunction with modal shapes, might be used to identify the existence of damage (especially when it changes significantly the structure condition) or deterioration. Furthermore, cross-diagnosis using multiple features is important for such detection. On the other hand, damping ratios were more sensitive to testing and estimation methods rather than to detect damage. However, the author highlighted difficulties to locate damage using those modal parameters, referring that operational conditions affect the modal parameters and are critical in establishing a baseline condition.

In another study based on tests performed on a two-steel girder concrete-deck bridge located over Mud Creek on Van Duesen Road, in Claverack, New York, Alampalli [62] performed saw cuts across the bottom flanges of both main girders. After careful examination of the data sets, the modal results from the damaged condition were split into two groups, namely, above- and below-freezing temperatures. Comparing the first three natural frequencies from the damaged condition above-freezing temperature and the ones from the undamaged condition measured at similar operational and environmental effects, the author concluded with high certainty that the structure has suffered stiffness loss due to the

simulated damage, reflected in 8.2, 2.6, and 4.2% averaged reduction in the first three natural frequencies, respectively. However, for the damaged condition above- and below-freezing temperatures, comparison of the same frequencies suggests different conclusions. The authors noted that the first three natural frequencies increase in average 67, 43, and 58%, respectively, between above- and below-freezing temperatures. Further investigation indicated frozen supports as the probable cause of the significant increase in the structural stiffness.

As shown above, boundary conditions might also change due to varying environmental conditions, especially the temperature, and radically modify the structural system. In a laboratory study, Woon and Mitchell [63] carried out an experimental investigation on a rectangular steel plate to verify the effect of two different boundary conditions (clamped and free plate) along with temperature changes on the natural frequency variability. Besides the fact that the natural frequencies of the plate decrease as temperature increases, it was observed that shifts are significantly higher in the clamped plate than in the free plate, which indicates that certain boundary conditions may amplify the variability caused by changing temperature due to induce of different thermal stresses. Furthermore, the authors concluded that the percent shift in natural frequency (relative to the warm reference frequency) is approximately the same for each mode. Actually, this is a clear indication that the temperature affects the Young's modulus of the plate.

As part of the general discussion on the limitations of using modal parameters for damage detection in the presence of changing boundary conditions, Cawley [64] compared the effect of crack formation at the fixed end of the cantilever beam to the varying length of a beam on the natural frequency. The varying length of the beam was intended to simulate the sensitivity of the natural frequency to the boundary conditions. He demonstrated that the resonance-frequency change caused by a crack, which was a 2% cut through the depth of the beam, is 40 times smaller than that caused by a 2% increase in the length of the beam.

Final note to other sources of variability that often the damage detection process needs to deal with. In a long-term monitoring, the sensors and data acquisition systems are themselves vulnerable to humidity and temperature. It is current to observe the drifting phenomenon in the measured responses not caused by structural behavior [65]. Another source of variability that needs to be addressed carefully, when using data-based methods for damage detection, is the consistency of the experimental techniques. For instance, it is well known that the modal testing, especially on ambient vibration testing, produces variable results when repeated because of inevitable noise caused by electrical disturbance, operator errors, and test environment [62].

2.3 Summary

Several bridge disasters around the world have been associated with lack of visual inspections and inappropriate maintenance programs. At the same time, the community and authorities have claimed

that the visual inspections are insufficient to characterize the health of the structures. This limitation has motivated the implementation of SHM systems to better quantify the condition of the structures.

However, the limitations and challenges caused by operational and environmental variability make full implementation of SHM for bridges more difficult than any monitoring of a well defined mechanical structure, such as the rotating machinery. Irrespectively of the structural-type bridge, the effect of operational and environmental conditions on the dynamical characteristics (especially the modal parameters) is real even though the sensitive (linear or non-linear) can be different for each case. The studies have confirmed that the temperature plays the major role on the modal parameters variability, and so most of the studies were focused on the relationship between the temperature and modulus of elasticity. On the other hand, even though not consensual, other studies have reported that concrete absorbs considerable amount of moisture that increases the mass of the bridges. Even though the degree of influence of the traffic loading on modal parameters has been related to the mass ratio of the vehicles to the superstructure, several studies have reported significant changes associated to the traffic loads. It was also noted that often when the temperature drops at freezing level, it might change the boundary conditions and, consequently, change the (quasi-) linear relationship between the temperature and natural frequencies. Besides, it was also shown that often changes caused by the operational and environmental variations are greater than those changes caused by damage. Thus, establish the baseline condition and determining sensitivity of the damage-sensitive features (e.g. natural frequencies) to operational and environmental effects are critical for SHM successful application.

As such, the author believes that vibration-based damage identification procedures will not be feasible without robust algorithms capable of normalizing such effects caused by operational and environmental variations in the measured data. In that regard, machine learning algorithms present in this dissertation can play an important role to detect damage under operational and environmental variations, because they model the effect of those variations on the extraction damage-sensitive features. Note that these algorithms do not require the measure of the operational and environmental factors such as temperature and traffic. Rather, they rely only on measured structural responses. Furthermore, those algorithms might be also important to support, or even replace, the traditional visual inspection techniques.

3. STATISTICAL PATTERN RECOGNITION PARADIGM

3.1 Introduction

In Chapter 1, the SHM process was posed in the context of the SPR paradigm. It was mentioned that this paradigm might be broken down into four steps. Even though the first two steps, namely operational evaluation and data acquisition, are discussed later, this chapter is only concerned with the discussion of the remainder steps, namely feature extraction and statistical modeling for feature classification. Thus, several statistical models for discrete time series are presented as well as examples of their application in civil infrastructure. Additionally, in order to enhance the damage detection process, machine learning algorithms for data normalization are presented to separate changes in the features caused by operational and environmental variability from changes caused by damage.

3.2 Feature Extraction

A damage-sensitive feature was described as some quantity extracted from the measured system response data that is correlated with the presence of damage in a structure. Moreover, damage was defined as changes to the material and/or geometric properties of these systems, including changes to the boundary conditions and system connectivity, which adversely affect the system's current or future performance.

Ideally, changes in the extracted damage-sensitive features are correlated with the level of damage present in the structure. However, in real-world structures, operational and environmental variations can mask the damage-related features as well as change the correlation between the magnitude of the features and the damage level. Furthermore, currently damage that manifests itself by a local reduction in stiffness tends to cause the structure to respond as a linear system before and after damage. Thus, to overcome this drawback, "intelligent" feature extraction procedures are usually required [66]. Therefore, the goal of this section is to briefly review the theory behind of some of the widely used feature extraction techniques, in different engineering fields, based on time and frequency domain analysis as well as on time-frequency domain analysis. It is shown that the appropriate sort of feature to use, is damage-specific, and so, each feature has its advantages and disadvantages regarding its sensitive to a particular type of damage.

Generally, the data measured from SHM systems are in the form of time series, where observations have some dependence. To understand the nature of this underlying dependence, regression models are presented, including discussion of several techniques to determine the appropriate model order. These models are specially relevant in SHM because, for linear stationary systems, their parameters are constant and do not dependent on the amplitude of the response. Moreover, the AR models are normally used to model the linear phase and so, along with the Holder exponent, they are potentially sensitive to detect damage in the form of nonlinearities over time. Based on the assumption that many “real-world” damage modes induce transitions from linear to nonlinear response in a system and that the operational and environmental variations usually manifest themselves as linear effects on measured data, a novel algorithm to extract features based on the state-space reconstruction is proposed. The first four statistical moments are also presented as features for type of damage that introduces changes into the normally assumption. Other features regarding global changes in the signal are described, such as modal parameters and correlation procedures. Spectral analysis comprises one class of techniques for time series analysis, but it is not the main focus of this dissertation. Nonetheless, the short-time Fourier transform (STFT) and wavelet transform (WT) are also described in order to extract damage-sensitive features from signals. Finally, the principal component analysis (PCA) is described as a feature extraction technique, even though it can also be used in the context of data normalization.

Notice that this section intends to summarize the mathematical formulation, present several applications, and highlight some advantages and disadvantages of the feature extraction techniques used by the author, rather than showing all possible techniques.

3.2.1 Modal Parameters

Modal parameters as damage-sensitive features were widely used in early SHM studies [3]. The motivation behind this approach is that modal parameters (natural frequencies, mode shapes, and modal damping ratios) extracted from experimental data are function of the physical properties of the structure (mass, damping, and stiffness). Therefore, any changes in the physical properties caused by structural damage will result in changes in the modal parameters. The theory behind the modal parameters has been extensively discussed in the literature among the community. Therefore, the author recommends further reading [67].

The applicability of the modal parameters as damage-sensitive features was discussed in Section 2.2, where it was shown that operational and environmental variability can cause changes in the modal parameters and mask the changes resulting from damage. Additionally, it was shown in many cases that modal parameters do not have the required sensitivity to small defects in a structure. Nonetheless, a real-world bridge application as well as a review on structural damage detection through changes in the natural frequencies can be found in [58, 68]. However, one should be aware that many studies

using these features only investigate numerical models or simple laboratory structures, and, therefore, they do not include the effects of the operational and environmental variability on the modal parameters.

3.2.2 First Four Statistical Moments

The first four statistical moments (mean, standard deviation, skewness, and kurtosis) are often computed when examining raw time series data. It should be noted that many classical statistical tests depend on the assumption of normality, and when time series data have significant skewness and kurtosis diverges from three, the normality assumption is no longer valid. A brief review on the first four moments is given here for completeness.

When a random variable x is measured in terms of deviations from its mean, its expectation yields moments about the mean also referred to as central moments. The k^{th} central moment of the probability distribution of x is defined as

$$\mu_k = E(x - \mu_x)^k, \quad (3.1)$$

where $\mu_x = E(x)$ is the mean of x . The mathematical operator E is the expectation of the random variable x , i.e., in simple terms, the expectation operator calculates the mean of a random quantity. Thus, the first central moment of a standard normal distribution is zero, because the first moment of a symmetric distribution about the mean is zero.

The variance is the second central moment. The variance of a random variable is a measure of the dispersion from the mean, and is defined as

$$\sigma_x^2 = E(x - \mu_x)^2. \quad (3.2)$$

The square root of the variance is called the standard deviation and is denoted as σ_x . While the mean describes the central tendency of the data, the standard deviation describes the spread about the mean.

The third statistical moment is a measure of the asymmetry of a probability distribution function (PDF). The normalized third statistical moment is called the skewness, and is defined as

$$S_x = \frac{E(x - \mu_x)^3}{\sigma_x^3}, \quad (3.3)$$

where a positive skewness means that the right tail is longer and the area of the distribution is concentrated below the mean. On the other hand, a negative skewness means that the left tail is longer and the area of the distribution is concentrated above the mean. The skewness of a standard normal distribution is zero.

The fourth statistical moment is a measure of the relative amount of data located in the tails of a probability distribution. The kurtosis is the normalized fourth statistical moment and is defined as

$$K_x = \frac{E(x - \mu_x)^4}{\sigma_x^4}, \quad (3.4)$$

The kurtosis of a standard normal distribution is three, where a kurtosis greater than three indicates a “peaked” distribution that has longer tails than a standard normal distribution. This means that there are more cases far from the mean. Kurtosis less than three indicates a “flat” distribution with shorter tails than a standard normal distribution. This property implies that fewer realizations of the random variable occur in the tails than would be expected in a normal distribution.

It is well known that a zero-mean Gaussian input to a linear system will always elicit a zero-mean Gaussian response [69]. Thus, for instance, when a Gaussian input is known, the statistical moments can be used as damage-sensitive features to detect deviations from the normal assumption. Farrar et al. [70] used the skewness and kurtosis to detect nonlinearities associated with damage in an eight-degree-of-freedom system. Soon et al. [71] applied the statistical moments as damage-sensitive features on residual errors derived from AR models. In another study, Mattson and Pandit [72] used statistical moments of AR residuals for damage localization.

3.2.3 Auto-regressive Model

The linear stationary models are an important class of stochastic models. In fact, the AR models have received special attention in the SHM community for feature extraction. For a time series s_1, s_2, \dots, s_N the AR(p) model of order p is given by

$$s_i = \sum_{j=1}^p \phi_j s_{i-j} + e_i, \quad (3.5)$$

where s_i is the measured signal and e_i is an unobservable random error at discrete time index i . The unknown AR parameters, ϕ_j , can be estimated by using the least-squares technique or the Yule-Walker equations [73].

In SHM, an AR model can be used as a damage-sensitive feature extractor based on two approaches: (i) using the residual errors e_i ; and (ii) using the parameters ϕ_j . The first approach consists of using the AR model, with parameters estimated from the baseline condition, to predict the response of data obtained from a potentially damaged structural condition. The residual error, which is the difference between the measured and the predicted signal, is calculated at time i as follows

$$e_i = s_i - \hat{s}_i, \quad (3.6)$$

where \hat{s}_i is the prediction observation at the i^{th} sampling instant. For the baseline condition, the residual errors are generally assumed to be independent and normally distributed with zero mean and variance σ^2 , $e_i \sim N(0, \sigma^2)$. This approach is based on the assumption that damage will introduce either linear deviations from the baseline condition or nonlinear effects in the signal and, as a result, the linear model developed with the baseline data will no longer accurately predict the response of the damaged structure. As a consequence, the residual errors associated with the damaged structure will increase. Note that for a fitted AR(p) model, the residual errors can only be computed for $i > p$ time points. The second approach consists of fitting an AR model to signals from the undamaged and damaged structural conditions. In this approach, the AR parameters are used directly as damage-sensitive features, and some form of a multivariate classifier can be used to distinguish between the damage classes. Notice that the parameters should be constant when obtained from times series of a time-invariant structural system.

As will be discussed later in Section 3.3, an AR model can also be used for data normalization by encoding the operational and environmental effects in its parameters. The procedure would be similar to the first approach discussed above. However, in this case, the AR model will be established based on the mean of the parameters estimated on time series from several operational and environmental conditions. For n time series from the same number of conditions, the parameters are equal to

$$\bar{\phi}_j = \frac{1}{n} \sum_{i=1}^n \phi_j^i \quad \text{for } j=1,2,\dots,p. \quad (3.7)$$

Therefore, the AR model of Equation (3.5) defined for varying operational and environmental conditions can be rewritten as follows

$$s_i = \sum_{j=1}^p \bar{\phi}_j s_{i-j} + e_i. \quad (3.8)$$

The appropriate AR model order is initially unknown. A high-order model may better fit the data, but may not generalize well to other data sets. On the other hand, a low-order model will not necessarily capture the underlying physical system dynamics. Model order estimation remains a very complex issue and various techniques to address this problem have been proposed. Based on the mathematical formulation, the techniques can be classified into three major categories [74]. The first category requires an *a priori* estimate of the model parameters in order to find the optimal order. The final prediction error, criterion auto-regressive transfer function [75], the Akaike information criterion (AIC), and partial auto-correlation function (PAF) have attracted much attention in the literature. The root mean square (RMS) error is a heuristic one to estimate the model order. Second, there are techniques that do not require an *a priori* estimate of the model parameters. This category is generally

based on the singular value decomposition (SVD) of the data covariance matrix. Another category of techniques, but not reported in this dissertation, includes Bayesian approaches which estimate the model order and model parameters, simultaneously, at the cost of more computational complexity. Note that often those techniques cannot be automated and require subjective interpretation [76]. A brief description of some techniques included in the first two categories is given for completeness.

The AIC has been used to assess the generalization performance of linear models [77, 78]. This technique simply computes a statistics that is the sum of two terms as follows

$$AIC(p) = N_t \ln(\varepsilon) + 2p, \quad (3.9)$$

where $\varepsilon = SSE/N_t$ is an average sum-of-square errors, N_t is the number of data points used in fitting the model, and p is the number of parameters in the model. It clearly represents a trade-off between the fit of the model and the model complexity. The first term is related to how well the model fits the data, i.e., if the model is too simple the residual errors increase. On the other hand, the second term is a penalty factor related to the complexity of the model, which increases as the number of parameters grows. The AR model with the lowest AIC value gives the optimal order p . Thus, the AIC criterion penalizes models with unrealistic large p . Note that the bias-corrected version, AICc, might also be used [79]. This version incorporates a penalty term that is relevant for small sample sizes. However, the AIC has also been reported to be too strict in model order estimation [80], yielding excessive model orders. In order to obtain an asymptotically unbiased estimate of the model order, Ciftcioglu [81] proposed a consistent information criterion (CIC) in the form of

$$CIC(p) = N_t \ln(\sigma_e^2) + 2p \ln(N_t), \quad (3.10)$$

where σ_e^2 is the variance of the residuals. For practical applications, this procedure attempts to eliminate the excessive model order convergence and, consequently, it might yield reduction in the model order estimation. Note that the form of the criterion in Equation (3.10), to some extent, corresponds to the Bayesian information criterion based on Bayesian modification of the AIC.

The PAF has also been used effectively in order to estimate the AR model order by Box & Jenkins [82]. The PAF is defined by fitting AR models of successively increasing order p to the measured data and then plotting the amplitude of the last estimated parameter, ϕ_{pp} , as a function of the model order.

Thus, the AR model of Equation (3.5) can be rewritten as follows

$$s_i = \sum_{j=1}^p \phi_{pj} s_{i-j} + e_i. \quad (3.11)$$

For an AR model of a noise-free order- p process, the PAF coefficients, ϕ_{kk} , will be non-zero for $k \leq p$ and zero for $k > p$. For real-world structures with noise in the measurements, the partial auto-

correlation coefficients of an actual $AR(p)$ will not be exactly zero after lags greater than p , but will assume small random values. As a result, it is necessary to define upper and lower bounds such that the coefficients will be considered zero if they fall within these limits. The idea is to look for the points of the PAF that are essentially zero. An approach based on the standard deviation error, σ_ϕ , is defined as follows

$$\sigma_\phi[\phi_{kk}] = \frac{1}{\sqrt{N_t}}, \quad k \geq p+1, \quad (3.12)$$

where the estimated partial auto-correlation coefficients of order $p+1$ and higher are approximately independently distributed. Placing a confidence interval for statistical significance is helpful for this purpose. For example, assuming an approximate 95% confidence interval, the limits are placed at $\pm 2\sigma_\phi$.

A heuristic technique to establish the appropriate AR model order is by means of the RMS of the AR residuals for varying order p . For each model order, the RMS of the residuals becomes

$$RMS(p) = \sqrt{\frac{1}{N_t} \sum_{i=1}^{N_t} (s_i - \hat{s}_i)^2}. \quad (3.13)$$

In this case, plotting the $RMS(p)$ for varying the model order p , the optimal model order will be at the convergence point of the RMS error values. The convergence point can be defined when the RMS error between two consecutive orders decrease below a pre-established percentage.

Finally, an estimation of the optimal AR model order can also be given by using the SVD technique. In linear algebra, the SVD is a factorization of a rectangular matrix \mathbf{M} defined as follows

$$\mathbf{M} = \mathbf{U}\mathbf{\Lambda}\mathbf{V}^T, \quad (3.14)$$

where the matrix $\mathbf{\Lambda}$ contains the singular values sorted in descending order on the diagonal and zeros for the off-diagonal terms. The matrices \mathbf{U} and \mathbf{V} are both orthogonal, i.e., $\mathbf{U}^T\mathbf{U} = \mathbf{V}^T\mathbf{V} = \mathbf{I}$. The SVD is used to determine the effective rank of a matrix \mathbf{M} by counting the non-zero singular values. In order to conduct the AR order analysis, Equation (3.5) can be written as

$$\begin{Bmatrix} s_{p+1} \\ s_{p+2} \\ \vdots \\ s_N \end{Bmatrix} = \begin{bmatrix} s_1 & s_2 & \cdots & s_p \\ s_2 & s_3 & \cdots & s_{p+1} \\ \vdots & \vdots & \cdots & \vdots \\ s_{N-p} & s_{N-p+1} & \cdots & s_{N-1} \end{bmatrix} \begin{Bmatrix} \phi_p \\ \phi_{p-1} \\ \vdots \\ \phi_1 \end{Bmatrix} \quad (3.15)$$

or

$$\mathbf{s} = \mathbf{M}\boldsymbol{\phi}, \quad (3.16)$$

where \mathbf{s} and \mathbf{M} contain the measured signal data and $\boldsymbol{\phi}$ contains the AR parameters. One can also express Equation (3.15) in the form of

$$\begin{Bmatrix} s_{p+1} \\ s_{p+2} \\ \vdots \\ s_N \end{Bmatrix} = \phi_p \begin{Bmatrix} s_1 \\ s_2 \\ \vdots \\ s_{N-p} \end{Bmatrix} + \phi_{p-1} \begin{Bmatrix} s_2 \\ s_3 \\ \vdots \\ s_{N-p+1} \end{Bmatrix} + \dots + \phi_1 \begin{Bmatrix} s_p \\ s_{p+1} \\ \vdots \\ s_{N-1} \end{Bmatrix} \quad (3.17)$$

or, in an obvious notation,

$$\mathbf{s}_{p+1} = \phi_p \mathbf{s}_1 + \phi_{p-1} \mathbf{s}_2 + \dots + \phi_1 \mathbf{s}_p. \quad (3.18)$$

Hence, the SVD counts how many of the \mathbf{s} -vectors (the columns of \mathbf{M}) are linearly independent and therefore needed for an accurate model, which in turn defines the number of necessary AR parameters.

As highlighted above, the AR models have been used in SHM to extract damage-sensitive features from time series data, either using the model parameters or residual errors. For instance, in order to discriminate time series from two different conditions, Soon et al. [71] applied AR models to measured strain data from a Norwegian surface-effects fast patrol boat with fiber-optic strain gages. The residual errors between the measured and predicted time series were used as damage-sensitive features. Regression models have been also used in the Ting Kau Bridge [18]. In this case, the regressive model was used to fit sequences of the first natural frequency.

3.2.4 Auto-regressive Model with Exogenous Inputs

The auto-regressive model with exogenous inputs (ARX) can also be used in SHM as feature extraction technique when the input is known. In this case, for an output time series s_1, s_2, \dots, s_N and an input time series v_1, v_2, \dots, v_N , the ARX(a, b) model with a auto-regressive terms and b exogenous input terms is given by

$$s_i = \sum_{j=1}^a \phi_j s_{i-j} + \sum_{k=0}^{b-1} \beta_k v_{i-k-\tau} + e_i, \quad (3.19)$$

where ϕ_j and β_k are, respectively, the auto-regressive and exogenous input parameters, e_i is assumed a white-noise residual error, and τ is the number of input observations that occurs before the input affects the output. This model permits to reproduce the input/output relationship of s and v . The model orders can be estimated using the AIC or minimum description length [83]. The parameters can be estimated using the least-squares technique.

Besides the capability to extract damage-sensitive features, and as will be discussed later in Section 3.4, this technique can also be used for statistical modeling. Peeters et al. [59] used the ARX model to establish the relationship between temperature time series (input) and sequence of natural frequencies (output) estimated from accelerations time series. Based on the previous example, this technique can be used for statistical modeling for feature classification as follows: (i) ARX model is used to fit data from the normal condition (undamaged condition with operational and environmental variations); and (ii) for new data, the ARX model is used to predict new temperature and natural frequencies; when the predicted natural frequencies fall beyond established confidence intervals, the structure is assumed to be damaged or at least the structural response has suffered statistically significant changes. On the other hand, for those cases where the operational and environmental factors are unknown, Soon et al. [84] proposed a novel time series analysis to locate damage sources, in a mechanical system running under operational and environmental effects, where the residual errors obtained from a combination of AR-ARX model are defined as the damage-sensitive features. Further discussion of this algorithm to normalize the measure data with respect to varying operational and environmental conditions can be found in [85].

3.2.5 *State-space Reconstruction and Time Series Modeling*

A novel algorithm for nonlinear time series is presented to extract features in systems under varying operational and environmental conditions. This section summarizes the use of the state-space reconstruction to infer the geometrical structure of a deterministic dynamical system from observed time series of a system response at multiple locations. The unique contribution of this algorithm is that it uses a MAR model of a baseline condition to predict the state space, where the model encodes the embedding vectors rather than scalar time series. A hypothesis test is established that the MAR model will fail to predict future response if damage is present in the test condition.

3.2.5.1 *State-space Representation*

The dynamics of linear multi-degree-of-freedom system is given by the well-known second order differential equation

$$\mathbf{M}\ddot{\mathbf{q}}(t) + \mathbf{D}\dot{\mathbf{q}}(t) + \mathbf{K}\mathbf{q}(t) = \mathbf{f}(t), \quad (3.20)$$

where \mathbf{M} , \mathbf{D} , and \mathbf{K} are the mass, damping, and stiffness matrices of the system, respectively, \mathbf{f} is the input force vector, and $\mathbf{q}(t)$ is the vector of the responses of each degree-of-freedom in the system. The general state space description for a linear time-invariant, continuous-time dynamical system is

$$\begin{aligned} \dot{\mathbf{x}}(t) &= \mathbf{A}\mathbf{x}(t) + \mathbf{B}\mathbf{u}(t) \\ \mathbf{y}(t) &= \mathbf{C}\mathbf{x}(t) \end{aligned} \quad (3.21)$$

where $\mathbf{x}(t) = [\mathbf{q} \quad \dot{\mathbf{q}}]^T$ is the state vector (commonly position and velocity), \mathbf{u} is a vector representing the input, and \mathbf{y} is a vector representing the observed output. The matrices \mathbf{A} , \mathbf{B} and \mathbf{C} determine the relationships between the input, output, and the state variables, and are referred to as the state, input, and output matrices, respectively. The state-space representation of Equation (3.21) can then be expressed as

$$\begin{aligned}\dot{\mathbf{x}}(t) &= \begin{bmatrix} \mathbf{0} & \mathbf{I} \\ -\mathbf{M}^{-1}\mathbf{K} & -\mathbf{M}^{-1}\mathbf{D} \end{bmatrix} \mathbf{x}(t) + \begin{bmatrix} \mathbf{0} \\ \mathbf{M}^{-1} \end{bmatrix} \mathbf{f}(t), \\ \mathbf{y}(t) &= [\mathbf{I} \quad \mathbf{0}] \mathbf{x}(t)\end{aligned}\quad (3.22)$$

where \mathbf{I} is the identity matrix. Of course, if the system is nonlinear, a similar formulation may be defined, although additional terms would appear on the right-hand side.

3.2.5.2 Embedology and Multivariate Auto-regressive Model

An alternative way to describe this physical-based state-space representation is to build a similar model directly from data. This approach is referred to as state-space reconstruction. For data obtained discretely in time from measured observations of a dynamic system response, the continuous-domain evolution described by ordinary differential equations, e.g. system in Equation (3.22) becomes a map

$$\mathbf{x}_{i+1} = G(\mathbf{x}_i; \mathbf{f}), \quad (3.23)$$

where the mapping G describes the evolution rule for the system. Since only measured data are available and the form of G is not generally known, recourse is made to reconstructing the dynamics via the embedding theorem of Takens [86], which provides the conditions under which a state space can be reconstructed from an observed time series, including even a single time-sampled representation (i.e., \mathbf{x} reduces to a scalar time series, say \mathbf{s}). One method commonly implemented to convert observations into state vectors uses delay time reconstruction. Assuming a single observed time series s_1, s_2, \dots, s_N , where indices are time-based, one can reconstruct an m -dimensional state vector in the form of delayed versions of the time series

$$\mathbf{x}_i = (s_i, s_{i+\tau}, \dots, s_{i+(m-1)\tau}), \quad (3.24)$$

where $i = 1, \dots, n$ and $n = N - (m-1)\tau$. The time delay embedding depends on two parameters, the embedding dimension m and the lag or delay time τ , which have to be chosen properly in order to yield an equivalent representation of the original state space. Note that $m \geq 2D + 1$, where D is the unknown dimension of the original state space. Thus, the trajectory matrix (or vector space) \mathbf{X} is defined as

$$\mathbf{X} = \begin{bmatrix} \mathbf{x}_1 \\ \mathbf{x}_2 \\ \vdots \\ \mathbf{x}_n \end{bmatrix}. \quad (3.25)$$

A straightforward way to verify the influence of the embedding parameters on the state-space reconstruction is by examining the convergence of topological properties. However, this approach carries more computational efforts when an embedding dimension is higher than the minimal for appropriate representation of the attractor. Therefore, some techniques have been proposed to find suitable estimates of those parameters [87, 88]. Broomhead and King [89] proposed the SVD on a trajectory matrix of w -dimensional state vectors ($w > m$) to estimate the embedding dimension m and also defined a criterion for the choice of the window length, w , because it determines the form of the singular spectrum. The goal of this approach is to obtain a basis for the embedding space such that the attractor can be modeled with invariant geometry in a subspace with fix dimension, i.e., the number of linearly independent vectors that can be constructed from the trajectory matrix in the embedding space. The set of vectors $\{\mathbf{s}_k \in R^n\}$ are supposed to give a set of linearly independent vectors in R^n with orthonormal basis $\{c_k \mid k = 1, 2, \dots, w\}$. Therefore, a natural choice for the embedding dimension m is the point of convergence of the singular spectrum. Note that this approach assumes unit lag.

In the context of state-space reconstruction, the MAR(p) model of order p is defined as follows

$$\mathbf{x}_i = \bar{\mathbf{x}} + \sum_{j=1}^p \mathbf{x}_{i-j} \Gamma_j + \mathbf{e}_{x,i}, \quad (3.26)$$

where \mathbf{x}_i and $\mathbf{e}_{x,i}$ are the i^{th} predicted state vector and additive Gaussian noise vector, respectively, $\bar{\mathbf{x}}$ is the mean vector of the variables, and Γ_j is an m -by- m matrix containing constant coupling parameters. Notice that the prediction can only be performed for $i > p$.

The approach presented for feature extraction is based on the assumption that when some source of damage affects the dynamical properties of a system, a MAR model with parameters estimated from the baseline system cannot accurately predict the attractor of the damaged system. Basically, this approach can be summarized in the following steps. First, as shown in Figure 3.1, a time series $s(t)$ from the baseline condition is embedded into a state space in order to establish the baseline and assumed undamaged vector space \mathbf{X} . Then, the MAR parameters Γ_j are determined through the multivariate least-squares technique. Second, and for a similar input, the baseline MAR model is used to predict any new test vector space \mathbf{Z} from an unknown system condition in the form of

$$\hat{\mathbf{z}}_i = \sum_{j=1}^p \mathbf{z}_{i-j} \Gamma_j, \quad (3.27)$$

where the residual errors are given by $\mathbf{e}_{z,i} = \mathbf{z}_i - \hat{\mathbf{z}}_i$. Assuming that Γ_j contains the underlying information of the baseline system, a hypothesis test is established that the MAR model will fail to predict the attractor if damage is present and the dynamical properties of the new system have changed. Therefore, the residuals increase, and the system \mathbf{Z} is said to correspond to a different class, under the damage hypothesis test. In this approach, the visualization of the predicted states, MAR parameters, and, in a very generalized form, the residual errors can be used as damage-sensitive features.

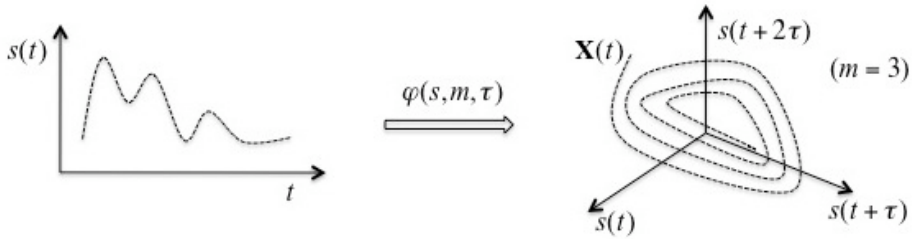


Figure 3.1. Schematic representation (for $m=3$) of the MAR model approach.

One may think of the trajectory as exploring on average an m -dimensional ellipsoid [89]. Thus, the accuracy of the predicted states can be statistically quantified using the Mahalanobis metric (d^2) in Equation (3.55), where \mathbf{z}_i is the potential outlier state vector. The covariance matrix Σ and mean vector $\bar{\mathbf{x}}$ are established for the baseline system. (Note that the number of variables is equal to the embedding dimension m .) Once the Mahalanobis equation is established to incorporate the underlying distribution of the baseline vector space \mathbf{X} , the d_i^2 will increase for new state vectors when their coordinates statistically differ from the pre-defined variance along the axes (or variables) of the system.

Finally, the order of the MAR model is initially an unknown. As shown in Section 3.2.3, the AIC is a measure of the goodness of fit of an estimated statistical model that balance the trade-off between fitting accuracy and number of adjustable parameters. In the context of MAR model as it applies to state-space reconstruction, Equation (3.9) can be rewritten as follows

$$AIC(p) = N_t \ln(\varepsilon) + 2N_p, \quad (3.28)$$

where $N_p = pm^2$ is the number of estimated parameters, $N_t = (n-p)m$ is the number of predicted state vectors, ε is the average sum-of-square MAR errors,

$$\varepsilon = \frac{1}{N_t} \sum_{i=1}^{n-p} \sum_{j=1}^m (\mathbf{z}_j - \hat{\mathbf{z}}_j)_i^2. \quad (3.29)$$

The optimal order p for the MAR(p) model is given by the one having the lowest AIC value.

3.2.5.3 Multivariate Embedding Approach

A multivariate embedding to reconstruct the state space of the structure can be extended from the univariate case in Equation (3.24) in the form of

$$\mathbf{x}_i = \left\{ s_i^1, s_i^2, \dots, s_i^l, s_{1+\tau_1}^1, s_{1+\tau_2}^2, \dots, s_{1+\tau_l}^l, \dots, s_{i+(m_1-1)\tau_1}^1, s_{i+(m_2-1)\tau_2}^2, \dots, s_{i+(m_l-1)\tau_l}^l \right\}, \quad (3.30)$$

where l corresponds to the number of sensor channels. This approach permits one to combine structural response data measure at multiple locations into a global attractor. Note that the approach presented to the univariate case from Equations (3.24)-(3.29) is still valid for the multivariate one, where $M = m_1 + m_2 + \dots + m_l$ is the global embedding dimension. Even though this global embedding approach destroys localization information associated with each discrete sensor response, it takes into account all available sensor network information simultaneously to produce a low-dimensional feature set for discrimination that encapsulates the full observation space.

3.2.6 Principal Component Analysis

PCA is a classical linear technique of multivariate statistics for mapping multidimensional data into lower dimension with minimal loss of information [90, 91]. A brief description of this dimensionality reduction technique is given as follows. Let $\mathbf{X} \in \mathfrak{R}^{n \times d}$ be a feature data matrix with n cases and d variables. The matrix \mathbf{X} can be decomposed as follows

$$\mathbf{X} = \mathbf{T}\mathbf{U}^T = \sum_{i=1}^d \mathbf{t}_i \mathbf{u}_i^T, \quad (3.31)$$

where \mathbf{T} is called the scores matrix and \mathbf{U} is a set of d orthogonal vectors \mathbf{u}_i also called the loadings matrix. The orthogonal vectors can be obtained by decomposing the covariance matrix Σ of the data matrix \mathbf{X} in the form of

$$\Sigma = \mathbf{U}\Lambda\mathbf{U}^T, \quad (3.32)$$

where Λ is a diagonal matrix containing the ranked eigenvalues λ_j , and \mathbf{U} is the matrix containing the corresponding eigenvectors. The eigenvectors associated with the higher eigenvalues are the principal components of the data matrix and they correspond to the dimensions that have the largest variability in the data.

Basically, this technique permits one to perform an orthogonal transformation by retaining only the significant eigenvectors (principal components) m ($< d$). More precisely, choosing only the first m eigenvectors, the final data matrix can be rewritten without significant loss of information in the form of

$$\mathbf{X} = \mathbf{T}_m \mathbf{U}_m^T + \mathbf{E} = \sum_{i=1}^m \mathbf{t}_i \mathbf{u}_i^T + \mathbf{E} \quad (3.33)$$

and

$$\mathbf{E} = \mathbf{X} - \hat{\mathbf{X}}, \quad (3.34)$$

where \mathbf{E} is the residual matrix and $\hat{\mathbf{X}}$ is the estimated matrix of \mathbf{X} using m principal components. The simplest method to assess the importance of a particular component is to take the ratio $\zeta_i = \lambda_i / \text{trace}(\Lambda)$ or to plot each eigenvalue as a sequence from largest to smallest.

In the SHM field, PCA might be used for four primary purposes: (i) evaluation of patterns; (ii) feature visualization; (iii) feature cleansing; and (iv) feature selection. The evaluation of patterns in the data is achieved through a linear mapping of data from the original feature space into a transformed feature space, where the eigenvectors are orthogonal to each other and, as a consequence, they are uncorrelated. One can extract a line, plane, or hyperplane that characterize the data. Furthermore, it is a useful graphical technique to take the scores of the first two or three components and to perform scatter plots to identify clusters or outliers. Basically, the scores are the projection of the data onto the new coordinate system, where it is simply scores plotted against each other. The loadings plot gives information on which variables are responsible for patterns found in the scores. This plot is simply the loadings of a principal component plotted against the loadings of another principal component. Feature cleansing is a process used to discard those linear combinations of the data that have small contributions to the overall variance, i.e., the principal components with low eigenvalues. This process can be achieved by reversing the projection back to the original feature space using only the principal components with higher eigenvalues. Feature selection is the process of choosing a subset of \mathbf{X} by constructing a matrix \mathbf{X}' composed of coordinates on the first m principal components, whose dimension is smaller than the original matrix. However, note that mapping the data into a lower dimension space may result in a loss of some information that can be necessary to discriminate the undamaged and damaged conditions. Additionally, note that PCA simply performs a coordinate rotation to align the transformed axes with the directions of maximum variance. Thus, there is no guarantee that those directions will preserve good features for discrimination.

Several examples of PCA applied to feature extraction can be found in the literature. For instance, Soon et al. [71] applied the PCA for feature visualization. The original data matrix was composed of

the first four statistical moments extracted from time series. The authors were able to discriminate the structural conditions by projecting the original data matrix onto the first two principal components.

One should note, as will be discussed later in Section 3.3, that PCA might also be cast in the context of data normalization, as proposed by Yan et al. [92, 93], to separate changes in the features caused by operational and environmental conditions from changes caused by damage. Additionally, a numerical application of PCA to separate changes in the sensor readings can be found in [94].

3.2.7 Time-frequency Analysis

The time-frequency representation of the signals is used to track the evolution of the frequency components of a signal over time [95]. For a stationary system, the frequency content should not change over time. However, often nonlinearities introduced into the systems can result in a non-stationary system. Therefore, if damage manifests itself as a nonlinearity, a signal from a damaged system can be time-variant and, as a consequence, the frequency content may change with respect to time in a manner that it might be correlated with damage.

The STFT and WT are two techniques currently applied to detect changes in the time series that are associated with the non-stationary response characteristics. The WT stands as an alternative approach to the well-known STFT. While Fourier analysis consists of decomposing a signal into harmonic functions of various frequencies, wavelet analysis consists of decomposing a signal into the shifted and scaled versions of the original mother wavelet [96].

Mathematically, the Fourier transform [67] is the integral over time of the signal $s(t)$ multiplied by a complex exponential in the form of

$$G(\omega) = \int_{-\infty}^{+\infty} s(t)e^{-i\omega t} dt, \quad (3.35)$$

where $G(\omega)$ describes the system response in the frequency domain. The STFT is used to determine the frequency content of small segments (or windows) of a signal over time. Basically, the Fourier transform algorithm is applied to a window and is used to calculate related spectral quantities for this window. This process is repeated using a moving window where the data windows are allowed to overlap. This technique maps a signal into a function of both time and frequency domain. The limitation of this technique is that for a given sampling rate, the frequency resolution of the STFT is determined by the time length or period of the window.

On the other hand, the WT has been developed to overcome the resolution limitations of the STFT. Recall that in STFT analysis the time and frequency resolutions are determined by the length of the window, and it yields a time-frequency representation of the signal that has constant resolution in time and frequency. However, wavelet analysis uses a different window technique with variable-sized

length. Actually, the wavelet analysis allows the use of long time interval for more precise low-frequency information and shorter time interval to better capture the time varying nature of the high-frequency information [96]. As a consequence, wavelets analysis can have a good time and poor frequency resolution at high frequencies, and good frequency and poor time resolution at low frequencies.

The continuous wavelet transform (CWT) is defined by convolving the signal $s(t)$ with scaled and shifted versions of the wavelet function ψ , as follows

$$W(a, b) = \int_{-\infty}^{+\infty} s(t) \frac{1}{\sqrt{a}} \psi \left* \left(\frac{t-b}{a} \right) dt. \quad (3.36)$$

This process produces WT coefficients, W , which are a function of two parameters: scale a and position b . The scale parameter, a , is correlated with the frequency and it dilates or compresses the wavelet function. In terms of frequency, low frequencies (high scales) correspond to global information of a signal. High frequencies (low scales) correspond to a detailed view of a signal that usually lasts a relatively short time [97]. The position parameter, b , intends to move the wavelet function along the time signal as a moving window. The resulting coefficients W estimated at different scales and positions provide both frequency and time information about the signal being analyzed. Note that a wavelet function is a waveform with finite duration and an average value of zero. There are many wavelet functions available [96], however the type of wavelet to use depends on the signal to be analyzed.

The major advantage of the wavelets is the ability to perform local analysis. In the SHM field, this ability makes the wavelets useful in detecting damage in the form of nonlinearities related to discontinuities in the signal caused by transient processes, such as cracks that open and close under dynamic loading or loose connections that rattle. See [12] for an example of wavelet-based active sensing for delamination detection in composite structures.

3.2.8 Holder Exponent

Mathematically, the Holder exponent is a measure of the signal's regularity. Because singularity points have no continuous derivatives, they can be identified when the Holder exponent suddenly drops to a value of zero or below [98]. Basically, the Holder exponent γ can be obtained in time by

$$\gamma = \frac{\log|W(a, b)|}{\log(b)}. \quad (3.37)$$

In SHM, the Holder exponent can be used to identify damage that introduces discontinuities into the measured dynamic response data. Basically, this technique indicates the presence of singularities and identifies when they occur over time. Therefore, drops in the Holder exponent can be used as damage-

sensitive features. Examples of capturing the time-varying nature of the Holder exponent for systems excited by non-stationary random signals with underlying discontinuities and to a harmonically excited mechanical system that contains a loose part are described in [98]. In real-world civil infrastructure, it can potentially be used to identify singularities associated with cracks that open and close during dynamic loading or loose connections that rattle.

3.2.9 Correlation Procedures

Correlation is a statistical technique used in signal processing for analyzing the relationship between two or more signals. The cross correlation is a standard technique of estimating the degree to which two different signals are correlated. Considering two random variables x and z , the cross correlation function R_{xz} at delay, or time lag, τ is defined as

$$R_{xz}(\tau) = \frac{E[(x_t - \mu_x)(z_{t+\tau} - \mu_z)]}{\sigma_x \sigma_z}, \quad (3.38)$$

where μ_x and μ_z are the means of the corresponding variables, E is the expected value, and t is an integer for a discrete-time process. The standard deviations of the variables, σ_x and σ_z , in the denominator serve to normalize the range of the correlation, and for a stationary process, the correlation values are in the range $[-1, 1]$. A coefficient equal to 1 indicates perfect correlation, i.e., the variables overlap when they are shifted by τ , and -1 indicates perfect anti-correlation where the variables are completely out of phase when shifted by τ .

Auto-correlation function (ACF) is the correlation of a signal with itself and for the variable x is defined as

$$R_{xx}(\tau) = \frac{E[(x_t - \mu_x)(x_{t+\tau} - \mu_x)]}{\sigma_x^2}. \quad (3.39)$$

The ACF is used to find out repeating patterns within the responses, such as the presence of periodic signals buried under noise. As a general rule, it is sufficient to compute the auto-correlation for values of $\tau \leq N/4$, where N is the number of data points in the signal [99].

A particular case of the correlation function in Equation (3.38) is the correlation coefficient for τ equals to zero and is given in the form of

$$r_{xz} = \frac{E[(x_t - \mu_x)(z_t - \mu_z)]}{\sigma_x \sigma_z}. \quad (3.40)$$

Note that for m variables, one can define the covariance (or correlation for standardized variables) matrix Σ with a dimension of m -by- m .

Another correlation technique is the so-called modal assurance criterion (MAC) [100, 101]. It has been a common technique of comparing numerical and experimental mode shapes. In the context of damage identification, this technique may be used to detect the presence of damage in the structure. In this case, one must replace the numerical and experimental modes by modes estimated from undamaged and damaged conditions. For two sets of measured mode shapes Φ_b and an Φ_d , the MAC values are defined for the mode shape $\phi_{b,j}$ and $\phi_{d,k}$ as

$$MAC(j,k) = \frac{|\phi_{b,j}^T \phi_{d,k}|^2}{(\phi_{b,j}^T \phi_{b,j})(\phi_{d,k}^T \phi_{d,k})}, \quad (3.41)$$

The MAC value is bounded between zero and one. The mode shapes are correlated if MAC value is close to one and totally uncorrelated if it is zero. A second type of MAC, called the co-ordinate MAC or COMAC, may be used for damage localization. The MAC in Equation (3.41) computes the correlation between two modes for all the measurement locations or nodes. On the other hand, the COMAC determines the correlation at nodes i for all the mode shapes l in the form of

$$COMAC(i) = \frac{\left[\sum_{j=1}^l |\phi_{b,j}(i) \phi_{d,j}(i)| \right]^2}{\sum_{j=1}^l [\phi_{b,j}(i)]^2 \sum_{j=1}^l [\phi_{d,j}(i)]^2}. \quad (3.42)$$

The COMAC value is also bounded between zero and one. If the modal displacements at node i of all mode shapes are similar, the COMAC value is one. On the other hand, errors or deviations between mode shapes of different sets may give COMAC values less than one.

The correlation coefficients and MAC values can also be used as data fusion techniques to combine data from single and multiple sensors [15]. Actually, in a study carried out to detect damage in a bridge under operational and environmental variations, Alampalli [61] successfully applied MAC values to perform cross-correlation of multiple features in order to use them as damage-sensitive features.

Another way to check the existence of correlation or patterns in the data is by means of the lag plot technique. For a time series \mathbf{s} , the lag plot consists of plotting the values s_i versus $s_{i-\tau}$, where τ is the lag. If the underlying data are not random, it is possible to identify a trend or pattern in the lag plot. Lag plots can be generated for any arbitrary lag, however the most commonly used lag is one. Furthermore, the lag plot can also be used to identify the existence of outliers. Note that cluster around a straight line with a positive slope is an indication of positive auto-correlation in the observations.

3.2.10 Probability Density Function

A common technique to verify the underlying distribution of the data is to estimate its PDF using non-parametric density estimators. In statistics, the histogram and the kernel density estimators are two non-parametric techniques used to estimate an unobservable underlying PDF of a random variable. Although the former is the oldest and most widely used form of density estimation, the kernel density estimator is a generalization and improvement over histograms. Given data from a sample of a population, the kernel density estimator allows one to draw inferences about the entire population being studied. More details about this estimator can be found in the references [71, 102]. For completeness, a brief description is given as follows. Considering a series with N observations s_1, s_2, \dots, s_N , the estimated density distribution is given by

$$\hat{f}(s) = \frac{1}{Nh} \sum_{i=1}^N K\left(\frac{s - s_i}{h}\right), \quad (3.43)$$

where K is the kernel function and h is the bandwidth, also called the smoothing parameter. Even though there are many choices among kernels, it is common to take the standard Gaussian function with zero mean and unit variance as follows

$$K(s) = \frac{1}{\sqrt{2\pi}} e^{-\frac{1}{2}s^2}. \quad (3.44)$$

One of the most important factors for a good kernel density estimator is the choice of the smoothing parameter h . The quality of the kernel estimate depends less on the shape of the kernel function than on the value of its bandwidth. A value h that is too small or too large is not useful, because small values of h lead to spiky estimates and the kernel density estimate is said to be under-smoothed. On the other hand, large values of h lead to flat estimates and the kernel density estimate is said to be over-smoothed. In the SHM field, the definition of this parameter tends to be crucial because damage often manifests itself as small changes in the tails of the distribution. Several techniques to estimate the optimum value for h can be found in the references [103].

As an example of application, in the Tsing Ma Bridge, strain/stress PDFs of deck components have been estimated as part of the long-term SHM. It is expected that when the measured strain/stress distribution varies due to structural damage or loading condition, the estimated PDFs will also change accordantly [18].

A final consideration is made regarding the verification of normality distribution of the data. The normal probability plot might be used to graphically verify whether the measured data is from a normal distribution. The plot is linear if the data come from a normal distribution. On the other hand, if the data are related to another probability distribution, it introduces curvature into the plot [104].

This technique follows the same procedure for feature extraction as described for the PDF case. However, in this case, the indication of damage is given by deviations from a Gaussian distribution.

3.3 Machine Learning Algorithms for Data Normalization

Currently, there are two well-known approaches to separate changes in damage-sensitive features caused by changing operational and environmental conditions from those changes caused by damage. The first approach consists of measuring the parameters related to operational and environmental variations such as live loads, temperature, wind speed, and/or moisture levels, as well as the structural response at different locations. Then, the features corresponding to the normal condition can be parameterized as a function of these operational and environmental conditions. Herein normal condition refers to those state conditions acquired under varying operational and environmental effects when the structure is undamaged. The second approach consists of applying machine learning algorithms to “learn” the influence of the operational and environmental conditions from the response data. This approach intends to eschew the measure of operational and environmental variations and pave the way for data-based models applicable to systems of arbitrary complexity.

In SHM, the aim of the machine learning algorithms is to enhance the damage detection in the presence of varying operational and environmental conditions under which the system response is measured. Several statistical methods have been reported in the literature related to the data normalization procedure [92, 93, 105, 106, 107, 108, 109]. However, herein only reference is made to algorithms based on the auto-associative neural network (AANN), factor analysis (FA), Mahalanobis squared distance (MSD), and SVD. These algorithms are designed and developed in such a way that their performance is improved based on the analysis of normal condition data (i.e. they “learn” from data acquired under operational and environmental conditions and when the structure is thought to be undamaged.) Basically, the machine learning algorithms develop a functional relationship that models how changing operational and environmental conditions influence the underlying distribution of the damage-sensitive features [110]. When subsequent features are analyzed with these algorithms and the new set of features are shown not to fit into an appropriate distribution, they might be more confidently classified as outliers or, potentially, features from a damaged structure, because the varying operational and environmental conditions have been incorporated into the classification procedure.

Even though these algorithms have different underlying mathematical formulations, they are implemented in a common sequence of steps; first, each algorithm is trained and its parameters are adjusted using feature vectors extracted from the normal condition, i.e., time series data collected under different operational and environmental conditions when the structure is assumed to be undamaged; second, in the test phase all the machine learning algorithms (with exception of the MSD-based one) will transform each input feature vector into an output feature vector of the same

dimension. However, the elements of the new feature vector should be nearly invariant for the normal condition, assuming the test data are representative of the normal condition data. All the algorithms assume a training matrix composed of feature vectors extracted from the undamaged condition, $\mathbf{X} \in \mathfrak{R}^{m \times n}$, with m -dimensional feature vectors from n different operational and environmental conditions and a test matrix, $\mathbf{Z} \in \mathfrak{R}^{m \times k}$, where k is the number of feature vectors extracted potentially from the damaged condition. Note that here a feature vector represents some property of the system at a given time. Traditionally, the modal parameters have been used in the civil engineering field as features that characterize the global condition of the structure. However, for instance, the AR parameters and residual errors as well as statistical moments can also be used as damage-sensitive features. For completeness, the four algorithms will be briefly described.

3.3.1 Auto-associative Neural Network

The AANN is trained to characterize the underlying dependency of the identified features on the unobserved operational and environmental factors by treating that unobserved dependency as hidden intrinsic variables in the network architecture. As shown in Figure 3.2, the AANN architecture consists of three hidden layers: the mapping layer, the bottleneck layer, and de-mapping layer. The mapping layers consist of hyperbolic tangent sigmoid transfer functions (N). On the other hand, the bottleneck and output layers are formed with linear transfer functions (L). The number of nodes in each layer as well as the number of input features is problem specific. This type of network is also related to nonlinear principal component analysis, where the target outputs are simply the inputs of the network. More details on the AANN, including the number of nodes to use, can be found in the references [107, 111].

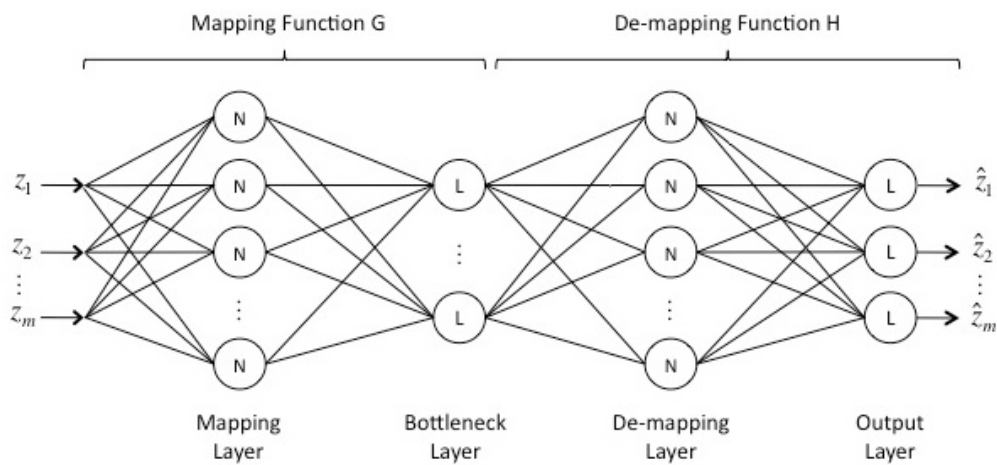


Figure 3.2. Network architecture of the AANN.

In the context of data normalization for SHM, the AANN is first trained to learn the correlations between features from the training matrix \mathbf{X} . The network should be able to quantify the unmeasured

sources of variability that influence the structural response. This variability is represented at the bottleneck output, where the number of nodes (or factors) should correspond to the number of unobserved independent variables that influence the structural response (e.g. temperature and humidity). Second, assuming the network is trained for the normal condition data, the errors will grow when the features are fed to the network come from the damaged condition. For the test matrix \mathbf{Z} , the residual errors matrix \mathbf{E} is given by

$$\mathbf{E} = \mathbf{Z} - \hat{\mathbf{Z}}, \quad (3.45)$$

where $\hat{\mathbf{Z}}$ corresponds to the estimated feature vectors that are the output of the network. If a feature vector j ($j = 1, 2, \dots, k$) is related to the undamaged condition, then $\mathbf{z}_j \approx \hat{\mathbf{z}}_j$. On the other hand, if the features come from the damaged condition, the neural network should not be able to predict the targets, the residual errors increase, thereby indicating an abnormal condition in the structure. Notice that the technique presented here is a mixture of two different learning approaches, i.e., supervised learning is used to obtain the operational and environmental conditions dependency albeit without direct measure of these conditions, while unsupervised learning is used to detect damage. It is re-emphasized that a key issue is to appropriately define the number of nodes in the bottleneck layer, which depends on the independent sources of variability present in the measurements.

Several studies have used the AANN to remove the effects of the operational and environmental variability and to detect damage [112]. For instance, Li et al. [113] applied the AANN as a signal pre-processing tool to distinguish temperature and wind effects on the modal parameters from other environmental factors. Oh et al. [114] proposed a kernel principal component analysis, as an AANN-derived data normalization algorithm, and applied it to data obtained from Yeongjong Suspension Bridge in Korea.

3.3.2 Factor Analysis

Kullaa [115] proposed to use the FA technique in SHM in order to eliminate the effects of operational and environmental variations from the measured data. Statistically, FA is a multivariate technique used to describe the linear correlation among a number of observed dependent variables (features) m in terms of a small number of unobserved independent variables (or factors) f ($< m$) as shown in Figure 3.3. Mathematically, for one feature vector \mathbf{z} of dimension $m \times 1$, the linear factor model can be written as

$$\mathbf{z} = \Lambda \boldsymbol{\xi} + \mathbf{e}, \quad (3.46)$$

where Λ is a $m \times f$ matrix of factor loadings, $\boldsymbol{\xi}$ is a $f \times 1$ vector of factor scores, and \mathbf{e} is a $m \times 1$ vector of unique factors (or error terms). The factors scores are independent with zero mean and unit variance. In a matrix form, the model can be written as

$$\begin{Bmatrix} z_1 \\ z_2 \\ \vdots \\ z_m \end{Bmatrix} = \begin{bmatrix} \lambda_{11} & \lambda_{12} & \cdots & \lambda_{1f} \\ \lambda_{21} & \lambda_{22} & \cdots & \lambda_{2f} \\ \vdots & \vdots & \ddots & \vdots \\ \lambda_{m1} & \lambda_{m2} & \cdots & \lambda_{mf} \end{bmatrix} \begin{Bmatrix} \xi_1 \\ \xi_2 \\ \vdots \\ \xi_f \end{Bmatrix} + \begin{Bmatrix} e_1 \\ e_2 \\ \vdots \\ e_m \end{Bmatrix} \quad (3.47)$$

or in the most generic form,

$$z_i = \lambda_{i1}\xi_1 + \lambda_{i2}\xi_2 + \cdots + \lambda_{if}\xi_f + e_i \quad \text{with } i=1,2,\dots,m. \quad (3.48)$$

The elements in Λ are deterministic and are estimated from the training data matrix \mathbf{X} , and so they are parameters in the model. On the other hand, \mathbf{z} , ξ , and \mathbf{e} are unknown and need to be further estimated.

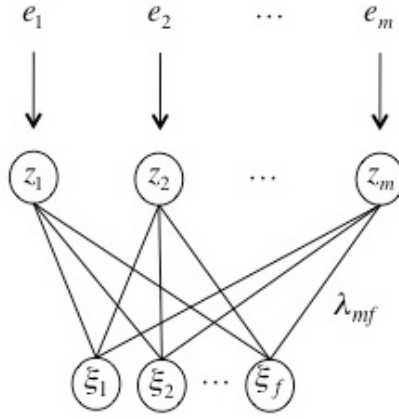


Figure 3.3. Linear factor model.

In order to facilitate computation, it is presented a matrix representation considering n tests (or feature vectors) for the training matrix $\mathbf{X} \in \mathfrak{R}^{m \times n}$ and k tests for the test matrix $\mathbf{Z} \in \mathfrak{R}^{m \times k}$. Note that the training matrix should be composed solely of feature vectors from the undamaged condition, and test matrix might be composed of feature vectors from both undamaged and damaged conditions. In matrix representation, the linear factor model in Equation (3.46) can be rewritten as

$$\mathbf{Z} = \Lambda \Xi + \mathbf{E}, \quad (3.49)$$

where Λ is a $m \times f$ matrix of factor loadings, Ξ is a $f \times k$ matrix of factor scores, and \mathbf{E} is a $m \times k$ matrix of errors. The error variables $i=1,\dots,m$ are assumed to be independent with ψ_i specific variances.

In the context of data normalization, the FA technique can be used as follows. First, the matrices Λ and Ψ , diagonal matrix with the specific variances, are estimated using the covariance matrix $\Sigma \in \mathfrak{R}^{m \times m}$ of the training matrix \mathbf{X} under model assumptions of Equation (3.49)

$$\Sigma = \Lambda\Lambda^T + \Psi. \quad (3.50)$$

Note that the number of factors corresponds to the number of underlying unobserved variables affecting the features, e.g. temperature and humidity. Second, using the test data matrix \mathbf{Z} , with k feature vectors, and given Λ and Ψ from the normal condition, the factor scores Ξ ($f \times k$) might be estimated using the linear regression method for a minimum mean squared error

$$\hat{\Xi} = \Lambda^T (\Psi + \Lambda\Lambda^T)^{-1} \mathbf{Z}. \quad (3.51)$$

Finally, the unique factors ($m \times k$) in Equation (3.49) are computed by

$$\mathbf{E} = \mathbf{Z} - \Lambda\hat{\Xi}. \quad (3.52)$$

In terms of SHM applications, Kullaa [115] successfully applied the FA algorithm to eliminate environmental effects on simulated data to resemble the observations of the Z-24 Bridge.

3.3.3 Singular Value Decomposition

Ruotolo and Surage [116] proposed a data normalization algorithm based on the SVD technique. This algorithm relies on the determination of the rank of a state matrix \mathbf{M} composed of r known independent m -dimensional feature vectors contained in \mathbf{X} , and one potential outlier feature vector \mathbf{z}_j in the form of

$$\mathbf{M} = [\mathbf{X}, \mathbf{z}_j]. \quad (3.53)$$

If the potential outlier comes from the undamaged condition and it is a linear combination of the ones contained in \mathbf{X} , it is expected that the rank will not change and will be equal to r . On the other hand, if the potential outlier feature vector comes from the damaged condition, and it is independent from the others, the rank will be equal to $r + 1$.

However, when dealing with real-world data, noise is often present which can affect the rank of \mathbf{M} and introduce residual singular values [117]. For this purpose, the comparison of two singular spectra is preferred. Basically, a three-step process is adopted to use the SVD as a data normalization algorithm:

- (i) the singular values of the training matrix \mathbf{X} are calculated and stored into the vector $\theta_{\mathbf{X}}$;
- (ii) for each potential outlier \mathbf{z}_j , $j = 1, 2, \dots, k$, the singular values are calculated for \mathbf{M} and stored into a vector $\theta_{\mathbf{M},j}$; if the feature vector \mathbf{z}_j is related to damage in the structure, a plot of the singular values contained in $\theta_{\mathbf{M},j}$ should not overlap with the ones contained in $\theta_{\mathbf{X}}$ as shown in Figure 3.4;

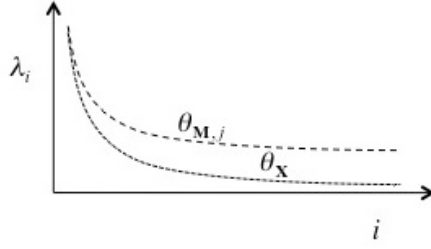


Figure 3.4. Singular spectra $\theta_{\mathbf{X}}$ and $\theta_{\mathbf{M},j}$.

(iii) the residual errors for each feature vector, \mathbf{e}_j , are then given by the difference between $\theta_{\mathbf{X}}$ and $\theta_{\mathbf{M},j}$ in the form of

$$\mathbf{e}_j = \theta_{\mathbf{X}} - \theta_{\mathbf{M},j}. \quad (3.54)$$

Notice this algorithm assumes that when a feature vector comes from the damaged condition and it differs significantly from the ones used in the training data, the singular spectrum $\theta_{\mathbf{M},j}$ deviates from $\theta_{\mathbf{X}}$ and the residuals increase.

3.3.4 Mahalanobis Squared Distance

The Mahalanobis distance differs from the Euclidean distance because it takes into account the correlation between the variables and it does not depend on the scale of the features. Considering the training matrix $\mathbf{X} \in \mathfrak{R}^{m \times n}$, with a multivariate mean vector $\bar{\mathbf{x}} \in \mathfrak{R}^{m \times 1}$ and covariance matrix $\Sigma \in \mathfrak{R}^{m \times m}$, the MSD is defined for each feature vector of the test matrix $\mathbf{Z} \in \mathfrak{R}^{m \times k}$ as

$$d_j^2 = (\mathbf{z}_j - \bar{\mathbf{x}})^T \Sigma^{-1} (\mathbf{z}_j - \bar{\mathbf{x}}), \quad (3.55)$$

where \mathbf{z}_j ($j=1, \dots, k$) is an m -dimensional potential outlier feature vector. In the context of data normalization, the mean vector and covariance matrix should encode all feature vectors extracted from the undamaged condition under different operational and environmental variability (normal condition).

The Mahalanobis distance has been extensively applied in SHM for data normalization. For instance, Manson et al. [112] applied the Mahalanobis distance algorithm to vibration data obtained from a simplified model of a metallic aircraft wingbox to detect damage in the stringer.

3.4 Statistical Modeling for Feature Classification

The development of statistical models to classify the extracted damage-sensitive features is the fourth step of the SHM-SPR paradigm. Even though several statistical modeling algorithms have been proposed in the literature, this section only makes reference to the ones used and/or developed by the author. Herein, the unsupervised learning algorithms are addressed because currently for high capital

expenditure structures, such as most civil infrastructure, only data from the undamaged condition are available. Therefore, first the cluster analysis is presented as a classification technique that groups extracted features into different clusters (i.e. undamaged; damaged level 1, level 2, and so on). Second, within the outlier category of classification algorithms, the statistical process control (SPC) techniques are introduced for random processes in undamaged systems. Third, the machine learning algorithms described in Section 3.3 might also be used for outlier detection. Thus, the MSD-based algorithm is designed and developed in such a way that the d^2 in Equation (3.55) from the normal condition follows a chi-square distribution under certain assumptions. Additionally, in the presence of enough data, an approach is presented to transform residual vectors from the AANN-, FA-, and SVD-based algorithms into scores. Finally, even though the receiver operating characteristic (ROC) curves are not used for classification, they have been used in the machine learning community because of their capabilities to assess the performance of classifiers, where performance is assessed on Type I/Type II error trade-offs.

3.4.1 Cluster Analysis

Data clustering is a common statistical data analysis technique that is used in many fields, such as machine learning, data mining, and pattern recognition [118]. Data clustering is the classification of feature vectors into different groups (also called clusters), so that in each group the feature vectors share some common underlying similarity.

There are many kinds of clustering [119], such as Hierarchical Clustering, which is a way to join feature vectors into different clusters by creating a cluster tree. In this process, clusters at one level are joined at the next higher level by progressively merging clusters. The higher the level in the tree, the smaller number of clusters. In the context of SHM for damage detection, cluster analysis might be applied in order to discriminate undamaged and damaged conditions into two clusters (binary classification), as shown in Figure 3.5 for instance for feature vectors \mathbf{z}_j , with $j = 1, 2, \dots, 6$.

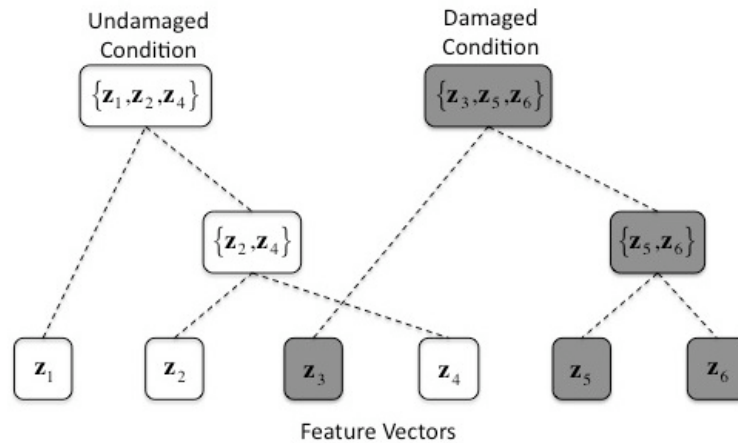


Figure 3.5. Traditional representation of the Hierarchical Clustering.

A relatively recent application of cluster analysis in a continuous monitoring system, for detecting CFRP debonding from a host reinforced concrete structure, can be found in [120].

3.4.2 Statistical Process Control

The SPC techniques may be applied for feature classification in an effort to discriminate the undamaged and damaged conditions. SPC uses control charts for monitoring whether the process is operating in statistical control. The process is said to be in control when the data vary randomly within the control limits (or thresholds). The purpose is to detect any abnormal changes in the process. These changes are observed as abnormal points on the charts resulting from changes in the mean and/or variance of the data. Thus, abnormal conditions might be identified by a statistically significant number of points exceeding the control limits as well as by systematic changes to the data within the control limits (e.g. the data are no longer randomly distributed within the control limits). Control charts often make assumptions of normality (the data have a normal distribution) and independence (data are not correlated) for better performance [99, 121, 122].

Different charts are used depending on the nature of the data. Herein, the Shewhart X-bar control charts are introduced to identify when data points fall outside the control limits (these points are also called “outliers”). A statistically significant number of points outside the control limits indicate that the structure has unusual source of variability that deviates its responses from the baseline condition. On the other hand, if data points fall inside the control limits, the process is said to be in control. (Note that there are cases where all data points fall inside the control limits and the process is not in-control.) A brief description of X-bar control charts is provided below.

Suppose a random variable x that is characterized by a normal probability distribution described by its parameters: mean μ and standard deviation σ . If x_1, \dots, x_n is a sample of size n and \bar{x} is the average of this sample then, based on the central limit theorem, the samples means \bar{x}_i are normally distributed with mean μ and standard deviation $\sigma_{\bar{x}} = \sigma/\sqrt{n}$. Thus, in $100(1-\alpha)\%$ of the cases, the sample mean \bar{x}_i will fall between the following interval

$$\mu - Z_{\alpha/2} \frac{\sigma}{\sqrt{n}} \leq \bar{x}_i \leq \mu + Z_{\alpha/2} \frac{\sigma}{\sqrt{n}}, \quad (3.56)$$

where $Z_{\alpha/2}$ is a parameter related to the confidence interval and α is the desired significant level. The standard deviation of the distribution of the \bar{x}_i values is σ/\sqrt{n} , i.e., the standard deviation of the population divided by the square root of the sample size. It is also commonly referred to the standard error of the mean. Note that the limits are a function of data acquired when the process is thought to be in control and might not necessarily have any direct relationship to the actual process performance.

However, generally the parameters μ and σ corresponding to the underlying process are unknown and they need to be estimated from samples when the process is thought to be in control.

One method to estimate the parameters of the probability distribution is as follows. Suppose that m samples of x with n observations each are available. The best estimator of μ is given by

$$\hat{\mu} = \frac{1}{m} \sum_{i=1}^m \bar{x}_i, \quad (3.57)$$

where \bar{x}_i is the sample average value for the i^{th} sample. The standard deviation can be estimated from either the m standard deviations, or the ranges of the m samples. By using the former one, an estimate of the process standard deviation can be obtained by averaging the m sample standard deviations std_i

$$\hat{\sigma} = \frac{1}{m} \sum_{i=1}^m std_i. \quad (3.58)$$

With these estimates of the process mean and standard deviation, the control charts limits (UCL - upper control limit, CL - centerline, and LCL - lower control limit) can be defined. Setting the control limits requires one to make a trade-off between false-positive and false-negative indications of damage. For instance, 99.73% confidence interval of a normal distribution corresponds to three standard deviations from the mean. Thus, in Equation (3.56), $Z_{\alpha/2}$ is replaced by three and the control limits can be defined as

$$\begin{aligned} UCL &= CL + 3 \frac{\hat{\sigma}}{\sqrt{n}}, \\ CL &= \hat{\mu}, \\ LCL &= CL - 3 \frac{\hat{\sigma}}{\sqrt{n}}. \end{aligned} \quad (3.59)$$

Notice that the quantity plotted is the sample average \bar{x}_i and, therefore, the chart is usually called an X-bar chart.

Several applications have been reported in the literature [123]. Soon et al. [71] applied control charts to examine changes in the mean value and standard deviation of the residual errors derived from AR models. Fugate et al. [124] applied control charts in an unsupervised learning mode to monitor data obtained from a concrete bridge column. In this case, the control limits were developed based on AR residual time series from the baseline condition. Then, for AR residual errors derived from vibration data acquired from the column at progressively increasing damage levels, the existence of damage was identified by counting the number of outliers beyond the control limits. One should notice that in this

experiment the AR residual errors were used as damage-sensitive features and an electro-magnetic shaker was used to generate random signals.

3.4.3 Outlier Detection based on Central Chi-square Hypothesis

Some authors [125] have used the MSD as a distance measure for multivariate statistics outlier detection. In the outlier detection approach presented herein, a hypothesis test is established, where the null hypothesis, H_0 , is the undamaged condition and the alternative hypothesis, H_1 , is presumably the damaged condition. To determine if a feature vector is from a structure in the undamaged condition, a thresholdable, single-dimensional measure of separation between a new feature vector and an existing distribution is established. In SHM, this value is often referred to as damage indicator (DI). In Equation (3.55) if a multivariate feature vector \mathbf{z} is extracted from the undamaged condition and corresponds to a multivariate Gaussian random distribution, then the d^2 , or DI, will be chi-square distributed with m degrees of freedom

$$DI = \chi_m^2. \quad (3.60)$$

Note that as m increases the PDF begins to look more like a normal PDF, as predicted by the central limit theorem. Therefore, multivariate outliers can simply be defined as observations having large DIs. (Note that m is equal to the length of the feature vector.) The assumption of a chi-square distribution is important for outlier detection because it permits a defined cut-off value or threshold, c , for a level of significance, α , in the form of

$$c = \text{inv}F_{\chi_m^2}(1 - \alpha), \quad (3.61)$$

where $F_{\chi_m^2}$ is the cumulative distribution function of the central chi-square distribution. Thus, a feature vector is considered to be a multivariate outlier (the null hypothesis is rejected) when its DI is equal or greater than c . Note that the selection of α carries a trade-off between the Type I error (“false-positive” indication of damage) and the Type II error (“false-negative” indication of damage). Alternatively, in statistical hypothesis testing, the p -value is the probability of obtaining a result at least as extreme as the one that is being tested. For a given DI, the p -value is defined as $p\text{value} = 1 - F_{\chi_m^2}(DI)$. Generally, one rejects the null hypothesis if p -value is less than α .

A schematic representation of this MSD-based algorithm combining feature extraction, data normalization, and statistical classification is shown in Figure 3.6. The approach can be summarized in the following steps. First, the extracted feature vectors from time series are divided into training matrix \mathbf{X} composed solely of undamaged condition data, and test matrix \mathbf{Z} composed of both undamaged and damaged conditions data. The training matrix should be representative of the operational and environmental variations present in the structure. Second, the mean vector and

covariance matrix of \mathbf{X} are computed as parameters for calculating the distances. Third, the d^2 (or DI) for each feature vector of the test data is computed. If DI is below the chosen threshold, c , the null hypothesis is accepted, otherwise it is rejected. Note that this approach assumes that the original features from the undamaged condition follow a multi-dimensional Gaussian distribution $\{f(x_i) | i=1,2,\dots,m\}$ and the features from the damaged condition follow an unknown distribution $h(x_i)$. Recall that the alternative hypothesis is not tested since no assumptions are made regarding the form of structural damage or its effect on the feature vector.

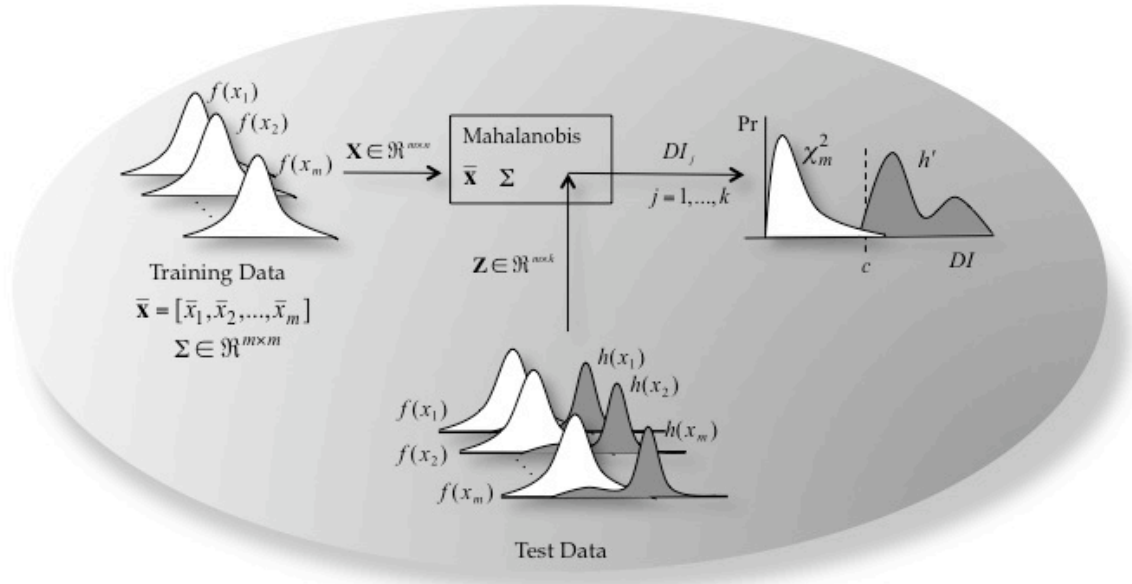


Figure 3.6. MSD-based algorithm combining feature extraction, data normalization, and statistical modeling for feature classification.

3.4.4 Outlier Detection from Residual Errors

The data normalization algorithms presented in Section 3.3, namely based on AANN, FA, and SVD, output a feature vector of residuals with dimension equals to the dimension of the original feature vector. From Equations (3.45), (3.52), and (3.54), it is possible to establish a quantitative measure of damage for each feature vector. Thus, in the absence of another measure, a DI might be adopted in the form of the squared root of the sum-of-square errors (or Euclidean norm) for each residual feature vector. Thus, a DI for each feature vector of \mathbf{Z} is given by

$$DI_j = \|\mathbf{e}_j\| \quad \text{with } j=1,2,\dots,k, \quad (3.62)$$

where k is the total number of vectors in the residual matrix \mathbf{E} . If a feature vector \mathbf{z}_j is related to the undamaged condition, $\mathbf{e}_j \approx \mathbf{0}$ and $DI_j \approx 0$. On the other hand, if a feature vector comes from the damaged condition, the residual errors increase and the DI deviates from zero, thereby indicating an abnormal condition in the structure. Then, it is necessary to establish confidence intervals to take into

account variability and to classify those DIs that significantly deviates from zero. However, often it is not possible to define confidence intervals based on parametric distributions and recursive is made to non-parametric distributions. Another way, and when a considerable number of representative data is available from the undamaged condition, one might simply find thresholds based on values corresponding to a certain percentage of confidence over the training data. Therefore, multivariate outliers can now simply be defined as tests having DIs beyond a specific threshold.

3.4.5 Receiver Operating Characteristic Curves

Assessment of classification performance is a critical aspect of evaluating and comparing models, algorithms, or classifiers. For the two-class problem in SHM (binary classification), in which the two sets of cases are labeled as damaged (or positive, P) and undamaged (or negative, N), for each threshold there are four possible outcomes as summarized in Figure 3.7 and Table 3.1. For a positive outcome, the case can be either true positive (TP) if the observed is positive or false positive (FP) if the observed is negative. On the other hand, for a negative outcome the case can be either false negative (FN) if the observed is positive or true negative (TN) if the observed is negative. The shaded portion of Table 3.1 represents the confusion matrix (also known as contingency table), where the numbers along the major diagonal represent the correct classifications, and the numbers off the diagonal represent misclassifications, also known as Type I (FP) and Type II (FN) errors.

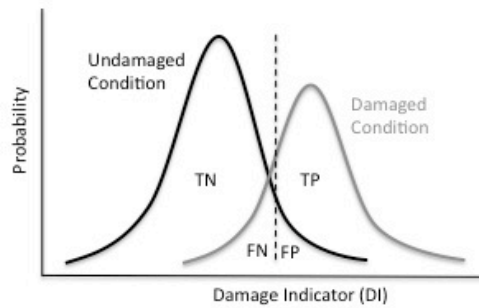


Figure 3.7. Distributions from the undamaged and damaged conditions.

Table 3.1. Accuracy of binary classification.

Outcome	Observed		
	Positive	Negative	Total
Positive	True Positive (TP)	False Positive (FP)	TP+FP
Negative	False Negative (FN)	True Negative (TN)	FN+TN
Total	TP+FN	FP+TN	TP+FP+FN+TN

Receiver operating characteristic (ROC) curves provide a comprehensive and graphical way to summarize the performance of classifiers [126]. The ROC curves were introduced in signal detection

theory by electrical and radar engineers during the World War II for detecting enemy objects in battle fields. Since that the ROC curves have become increasingly common in fields such as finance, atmosphere science, and medicine. In the field of machine learning, these curves have become a standard tool to evaluate the performance of binary classifiers.

The ROC curves focus on the trade-off between *sensitivity* and *1-specificity*. As shown in Figure 3.8, the *sensitivity* is sometimes called the true-positive rate, $TPR=TP/(TP+FN)$, and defines the fraction of true detection. The *1-specificity* is sometimes called false-positive rate, $FPR=FP/(FP+TN)$, and defines the fraction of false alarm. Each point on the ROC curve corresponds to a specific threshold, although the values of thresholds are not evident from the square plot. The diagonal line divides the ROC space into two parts and represents a classifier that performs random classifications. Any point in the upper-left triangle means that the classifier has some understanding of the classes. Moreover, the closer the ROC plot is to the upper-left corner, the higher the overall accuracy of the classifier. On the other hand, any point in the lower-right triangle means that the classifier is performing worse than random, i.e., the classifier has some underlying information about the classes but applies it in the opposite way.

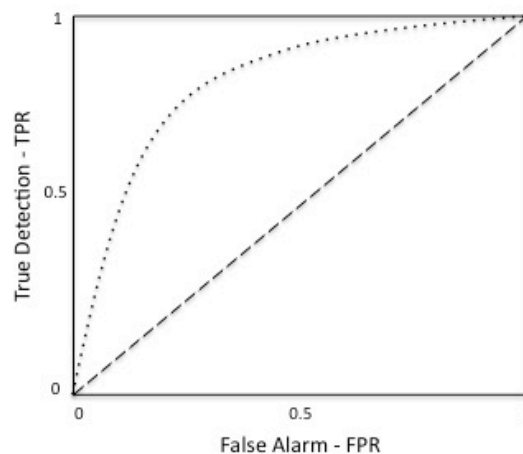


Figure 3.8. Example of a ROC curve; the diagonal line divides the ROC space into two parts and represents a classifier that performs random classifications.

3.5 Summary and Contributions

The major contribution of this chapter is the novel approach for feature extraction that makes use of the state-space reconstruction. The reconstruction of the state space obtained discretely, in time, from measured time series of a dynamic system response can be used when some source of damage affects the dynamical properties of a system. The assumption of this algorithm is that a MAR model with parameters estimated from the baseline system cannot accurately predict the attractor of the damaged system. Thus, the parameters encode the baseline condition and, for linear stationary systems, the amplitude of the excitation will not affect the prediction. This algorithm is appropriate when damage is present in the form of nonlinearities. Furthermore, when the parameters are representative of the

operational and environmental conditions, this algorithm can also be cast in the context of data normalization. In real-world structures, it can potentially be used to detect nonlinearities in the form of loose connections that rattle or cracks that open and close by modeling the response of induced excitations, such as traffic and/or wind.

Nevertheless, other contributions are present in this chapter. Feature extraction techniques along with specific applications were presented, using the same nomenclature for better understanding. The AR model was the focus of special attention, because it is a useful feature extraction technique for civil infrastructure SHM applications based on three main reasons: (i) they are sensitive to damage when it manifests in the form of nonlinearities or transitions between two states; (ii) the extraction of features only depends on response time series data; and (iii) simple and easy implementation.

It was also highlighted that the choice of the appropriate damage-sensitive feature is a damage-specific issue. Unfortunately, it is unlikely to find a feature that performs well under any type of damage and for every type of signal. Thus, in order to provide guidance on that issue, Table 3.2 summarizes some of the feature extraction techniques mentioned in this chapter along with proper scenario, where they might be applied to take advantage of their sensitivity to damage in the structures. Note that settlement can be derived from either piers or abutments and, in parentheses, one can find the type of measurement to be used.

Table 3.2. Feature extraction techniques along with potential detectable type of damages.

Technique/Feature	Type of Damage	Observations
Modal Parameters	Settlement, yielding steel elements, or complete severing of truss elements	When damage changes the global load path (e.g. accelerations)
Mean		When damage introduces permanent deformations (e.g. strains)
Skewness and Kurtosis		When damage introduces changes into the normal distribution (e.g. accelerations)
Correlation Coefficients		When damage imposes permanent deformations (e.g. displacements and strains)
PDF		Changes in the loading path caused by loading conditions or different structural system (e.g. strains)
AR Model		Fatigue cracks or loose connections
STFT and CWT	When damage is characterized by transitions between two state conditions (e.g. accelerations)	
Holder Exponent	When damage is reflected in the form of singularities in the signal (e.g. accelerations)	

Four data normalization algorithms based on AANN, FA, MSD, and SVD were presented to separate changes in the sensor readings caused by damage from changes caused by operational and environmental variations. These algorithms are generally known as machine learning algorithms because they are developed in such a way that their performance is improved based on the analysis of normal condition data. Even though these algorithms have different underlying mathematical formulations, they are implemented in a common sequence of steps. All four algorithms offer some advantages over other parametric data normalization techniques because the operational and environmental variables (e.g. traffic loading and temperature) do not need to be measured to reveal their influence on the structural responses. Actually, the algorithms rely only on features extracted from measured response time series data acquired under varying operational and environmental conditions. However, these algorithms have potential problems if the training data are only characteristic of a limited range of operational and environmental variability. Hence, all sources of variability must be well characterized by the training data in order for the algorithms to accurately learn their influence on the system's response. Thus, one should note that with these algorithms there is no guarantee that they will work effectively when new data correspond to operational and environmental conditions not used in the training phase. Also, if the damage produces changes in the system's dynamic response characteristics that are similar to those produced by the sources of variability, it is not clear that these algorithms will be able to separate changes in the features caused by damage from changes caused by the operational and environmental variability. Thus, the training data should be representative of at least one full cycle to reduce the likelihood of misclassifications. In conclusion, it is the author's belief that these algorithms have a wide application in SHM for the following reasons: (i) applicability for short- and long-term monitoring; (ii) it assumes any kind of input feature vector; (iii) these algorithms do not require a direct measure of the operational and environmental factors; and (iv) they can be updated when new training data become available. Additionally, for the MSD-based algorithm, under certain assumptions, a hypothesis test is established that the algorithm rejects the null hypothesis (undamaged condition) if DI does not follow a chi-square distribution.

The SPC techniques, and particularly the Shewhart X-bar control charts, were presented as a procedure of statistical modeling for feature classification. Those charts allow one to detect any abnormal changes in the monitored process, especially when damage causes changes in the mean and/or variance of the response data. However, the performance of them depends highly on assumption of Gaussian process data. Thus, in a long-term SHM monitoring of civil infrastructure, the applicability of these charts might be conditioned by the existence of external excitation source. Nevertheless, these techniques might potentially be used on NDT and/or in the presence of integrated actuators capable to generate random excitation into the structural elements.

Finally, several feature extraction and statistical modeling procedures described in this chapter have been incorporated into a software package called *SHMTools*. This package is described in Appendix A as the beginning of a larger effort to collect and archive proven approaches to support the SHM process.

4. VALIDATION ON A LABORATORY TEST STRUCTURE

4.1 Introduction and Overview

The goal of this chapter is to apply the SHM-SPR paradigm to standard data sets acquired from a base-excited three-story frame structure tested in a laboratory environment. It should be emphasized that this structure is not a scale model of any prototype system, but rather it was designed as standard test bed for SHM validation studies. For different studies on these data sets, one should see [127, 128, 129].

The data sets are composed of force and acceleration time series measured under different structural state conditions. The damage was simulated through nonlinear effects introduced by a bumper mechanism that induces a repetitive, impact-type nonlinearity. The nonlinearities were intended to produce a small perturbation to an essentially stationary process, causing a nonlinear phenomenon called intermittency [130], i.e., the system alternates between two states in an irregular way. In this case, the irregular behavior is characterized by impacts, whose number depends on the input to the structure and the level of damage introduced by the bumper, which is quantified by the initial bumper gap. This mechanism was intended to simulate a crack that opens and closes under dynamic loads (a so-called ‘breathing’ crack), or loose connections that rattle. Several real-world examples have been published reporting bending and shear cracks that open and close under dynamic loads. For instance, in the prestressed bi-cellular box girder N. S. da Guia Bridge, in Portugal, cracks were measured that open and close 0.12 mm under the loads produced by two vehicles passing side-by-side at 20 km/h [131]. On the other hand, the operational and environmental effects were simulated through different mass and stiffness conditions (non-damage related events), which are indicative of changing system mass caused by varying live loads or changing system stiffness properties caused by changing thermal environments. Those changes were designed to introduce variability in the fundamental natural frequency up to approximately 7% from the baseline condition, which is perfectly within the range normally observed in real-world structures as highlighted in Chapter 2.

In the hierarchical structure of damage identification, this chapter addresses the need for robust incipient damage detection methods. Therefore, it is essentially concerned with determining the existence of damage in the test structure. Even though locating and assessing the severity of damage

are important in terms of estimating the residual lifetime of the structures, the reliable detection of damage existence must precede these more detailed damage descriptions. To achieve that goal, this chapter is mainly focused on the application of the feature extraction, data normalization, and statistical modeling for feature classification procedures described in Chapter 3, i.e. steps three and four of the SHM-SPR paradigm. Nonetheless, a brief overview will be given to the operational evaluation and data acquisition steps of the paradigm. Recall that this approach for damage detection is solely based on signal analysis of the measured acceleration response data, and thus, it does not take into account any physical information about the structure being analyzed or the excitation source.

The layout of this chapter is as follows. Section 4.2 addresses the first two steps of the SHM-SPR paradigm, providing a summary description of the test structure, data acquisition system, experimental procedure, simulated operational and environmental conditions, and the damage scenarios. In Section 4.3, a physics-based numerical model is summarized. This model does not interfere in the damage detection process, rather it is used to validate some assumptions about the system response as well as the measured experimental data. Section 4.4 demonstrates the stationarity property of the data sets. Section 4.5 applies and discusses most of the SHM procedures described in Chapter 3 for feature extraction, with special attention on the AR model. In the statistical modeling for feature classification step, Section 4.6 applies the machine learning algorithms for data normalization and the novel algorithm based on the state-space reconstruction for outlier detection. Notice that those algorithms combine feature extraction (and/or data normalization) and statistical classification (outlier detection). Finally, Sections 4.7 and 4.8 conclude with a general discussion to summarize the main conclusions regarding the effectiveness of the various statistical procedures to identify damage under simulated operational and environmental variations as well as the main contributions of this study.

4.2 Experimental Procedure

The base-excited three-story aluminum frame structure shown along with its basic dimensions in Figure 4.1 is used as a damage detection test bed structure. The structure consists of columns and plates assembled using bolted joints. The structure slides on rails that allow movement in the x -direction only. At each floor, four columns (17.7x2.5x0.6 cm) are connected to the top and bottom plates (30.5x30.5x2.5 cm) forming a (essentially) four-degree-of-freedom system. Additionally, a center column (15.0x2.5x2.5 cm) is suspended from the top floor. This column is used to simulate damage by inducing nonlinear behavior when it contacts a bumper mounted on the next floor. The position of the bumper can be adjusted to vary the extent of impacting that occurs at a particular excitation level.

An electrodynamic shaker provides a lateral excitation to the base floor along the centerline of the structure. The structure and shaker are mounted together on an aluminum baseplate (76.2x30.5x2.5 cm) and the entire system rests on rigid foam. The foam is intended to minimize extraneous sources of

unmeasured excitation from being introduced through the base of the system. A load cell (Channel 1) with a nominal sensitivity of 2.2 mV/N was attached at the end of a stinger to measure the input force from the shaker to the structure. Four accelerometers (Channel 2-5) with nominal sensitivities of 1000 mV/g were attached at the centerline of each floor on the opposite side from the excitation source to measure the system response. Because the accelerometers are mounted at the centerline of each floor, they are insensitive to torsional modes of the structure. In addition, the shaker location and the linear bearings minimize the torsional excitation of the system.

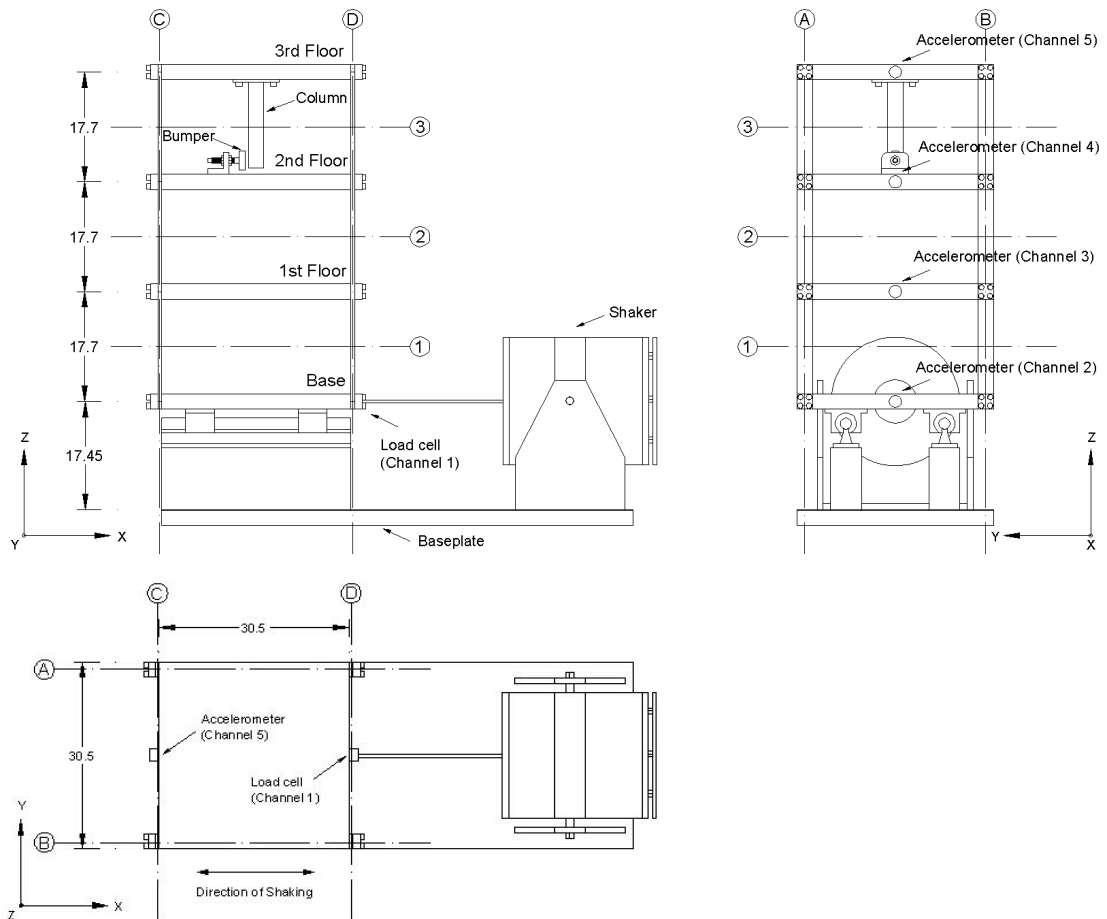


Figure 4.1. Basic dimensions of the three-story test bed structure. (All dimensions are in cm.)

A Dactron Spectrabook data acquisition system was used to collect and process the data. The output channel of this system, which provides the excitation signal to the shaker, is connected to a Techtron 5530 Power Supply Amplifier that drives the shaker. The analog sensor signals were discretized into 8192 data points sampled at 3.125 ms intervals corresponding to a sampling frequency of 320 Hz. These sampling parameters yield time series of 25.6 sec. A band-limited random excitation in the range of 20-150 Hz was used to excite the structure. This excitation signal was chosen in order to avoid the rigid body modes of the structure that are present below 20 Hz. Note that the rigid body modes occur at non-zero frequency because of the presence of (slight) damping and stiffness (caused by the friction between the structure and rails, and to some extent, the stinger of the shaker). These

modes were excluded from the analysis because their frequencies varied significantly even under the normal condition. Furthermore, the rigid body modes often overloaded the sensors, imposing difficulties in accurate measurements of the structure. The excitation level was set to 2.6 V RMS in the Dactron system, which corresponds to, approximately, 20 N RMS measured from the load cell. Force and acceleration time series for 17 different structural state conditions were collected as shown in Table 4.1 along with information that describes the different states. For example, the state condition labeled “State#4” is described as “87.5% stiffness reduction in column 1BD”, which means that there was an 87.5% stiffness reduction (corresponding to a 50% reduction in the column thickness) in the column located between the base and first floor at the intersection of plane B and D. For each structural state condition data were acquired from 10 separate tests. Each test consists of five time series from the same number of sensors. For illustration purposes, Figure 4.2 plots in concatenated format acceleration time series of State#1, 7, 14, and 17 from Channel 2-5, where one can see that the amplitude of the time series is relatively consistent.

Table 4.1. Data labels of the 17 structural state conditions.

Label	State Condition	Description
State#1	Undamaged	Baseline condition
State#2	Undamaged	Added mass (1.2 kg) at the base
State#3	Undamaged	Added mass (1.2 kg) on the 1 st floor
State#4	Undamaged	Stiffness reduction in column 1BD
State#5	Undamaged	Stiffness reduction in column 1AD and 1BD
State#6	Undamaged	Stiffness reduction in column 2BD
State#7	Undamaged	Stiffness reduction in column 2AD and 2BD
State#8	Undamaged	Stiffness reduction in column 3BD
State#9	Undamaged	Stiffness reduction in column 3AD and 3BD
State#10	Damaged	Gap (0.20 mm)
State#11	Damaged	Gap (0.15 mm)
State#12	Damaged	Gap (0.13 mm)
State#13	Damaged	Gap (0.10 mm)
State#14	Damaged	Gap (0.05 mm)
State#15	Damaged	Gap (0.20 mm) and mass (1.2 kg) at the base
State#16	Damaged	Gap (0.20 mm) and mass (1.2 kg) on the 1 st floor
State#17	Damaged	Gap (0.10 mm) and mass (1.2 kg) on the 1 st floor

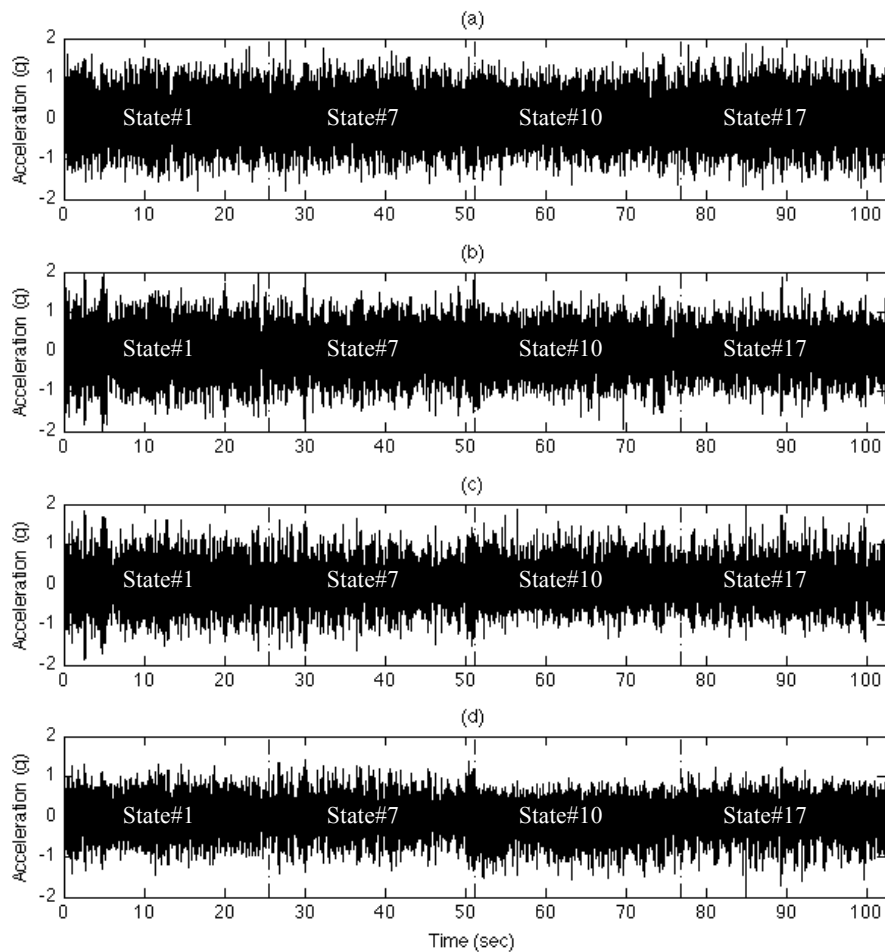


Figure 4.2. Acceleration time series of various state conditions: (a) Channel 2; (b) Channel 3; (c) Channel 4; and (d) Channel 5.

The structural state conditions can be categorized into four main groups. The first group is the baseline condition. The baseline condition is the reference structural state and is labeled “State#1” in Table 4.1. The bumper and the suspended column are included in the baseline, but the spacing between them was maintained in such a way that there were no impacts during the excitation. The second group includes the states with simulated operational and environmental variability. In real-world structures such variability often manifests itself in changes in the stiffness or mass distribution of the structure. In order to simulate those changes, tests were performed with different mass-loading and stiffness conditions (State#2-9). The mass changes consisted of adding a 1.2 kg (approximately 19% of the total mass of each floor) to the first floor and to the base, as shown in Figure 4.3a when the mass is at the base. The stiffness changes were introduced by reducing the stiffness of one or more of the columns by 87.5%. This process was executed by replacing the corresponded column with one that had half the cross sectional thickness in the direction of shaking. Those changes were designed to introduce

variability in the fundamental natural frequency up to approximately 7% from the baseline condition. Recall that as shown in Section 2.2, for instance in the case of highway bridges, numerous investigations indicate that the temperature can cause modal variability in the range of 5-10%. Under the assumption that many “real-world” damage modes induce transitions from linear to nonlinear response in a system, the third group includes the damaged state conditions. Therefore, damage is simulated by a bumper mechanism that creates a repetitive, impact-type nonlinearity. This mechanism was intended to simulate, for instance, a crack that opens and closes under dynamic loads (a so-called ‘breathing’ crack), or loose connections that rattle. As shown in Figure 4.3b, adjusting the gap between the bumper and the suspended column controls the level of damage. Therefore, the gap was varied (0.20, 0.15, 0.13, 0.10, and 0.05 mm) in order to introduce different levels of nonlinearities (State#10-14). The higher the gap, the smaller the level of damage. Finally, to create more realistic conditions, the fourth group includes state conditions with the simulated damage in addition to the mass changes used to simulate operational variations (State#15-17). More details about the test structure as well as data sets can be found in Figueiredo et al. [127].

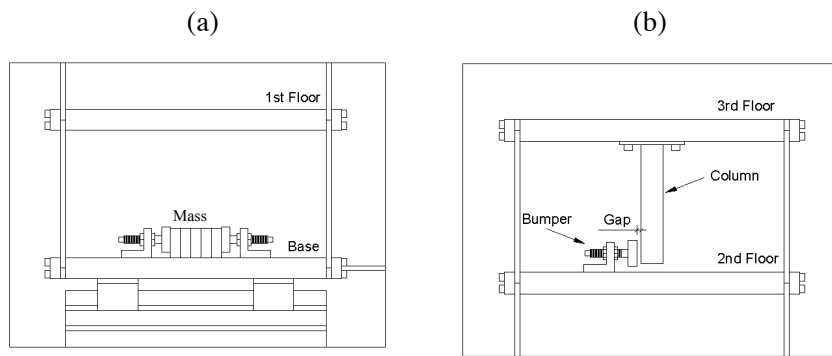


Figure 4.3. Structural details of the sources of simulated operational and environmental changes: (a) mass-loading added at the base; and (b) nonlinearity source.

4.3 Numerical Simulation

A linear physics-based numerical model of the test structure was developed in order to compare the numerical results with the measured experimental data. In general, physics-based numerical models can be used to define the SHM system properties, such as sensor type and location, prior to deploying a monitoring system on real-world structures and to validate SHM systems’ measurements. The test structure is modeled as a shear-building model with four lumped masses at the floors, including the base that slides on rails, as shown in Figure 4.4. An extra story with stiffness k_1 and damping d_1 was included to simulate the friction between the rails and the structure.

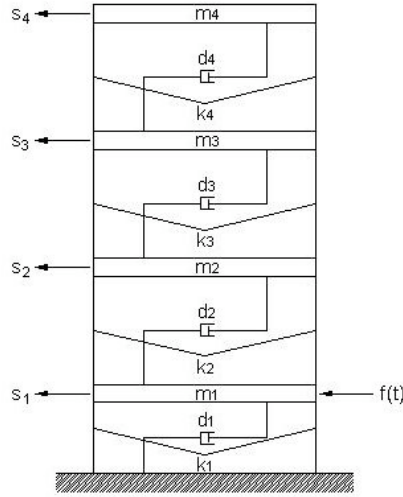


Figure 4.4. Shear-building model of the test structure.

The equations of motion of the shear-building model can be written in matrix notation as follows

$$\mathbf{M}\ddot{\mathbf{s}} + \mathbf{D}\dot{\mathbf{s}} + \mathbf{K}\mathbf{s} = \mathbf{f}(t), \quad (4.1)$$

where the \mathbf{M} , \mathbf{D} , and \mathbf{K} are the mass, damping, and stiffness matrices of the system, respectively, $\mathbf{f}(t)$ is the input vector excitation, and \mathbf{s} the vector of unknown displacements at the nodal coordinates $i = 1, \dots, 4$. The mass and stiffness matrices are given, respectively, by

$$\mathbf{M} = \begin{bmatrix} m_1 & 0 & 0 & 0 \\ 0 & m_2 & 0 & 0 \\ 0 & 0 & m_3 & 0 \\ 0 & 0 & 0 & m_4 \end{bmatrix} \quad \text{and} \quad \mathbf{K} = \begin{bmatrix} k_1 + k_2 & -k_2 & 0 & 0 \\ -k_2 & k_2 + k_3 & -k_3 & 0 \\ 0 & -k_3 & k_3 + k_4 & -k_4 \\ 0 & 0 & -k_4 & k_4 \end{bmatrix}, \quad (4.2)$$

where m_i denotes the mass at the i^{th} floor and k_i denotes the stiffness of the i^{th} story. Note that the masses of the columns are redistributed through the floors and the stiffness of each column is given by $k_c = 12EI/L^3$, where E is the Young's modulus, I is the inertial, and L is the length of the column. The equations of motion can be uncoupled with the modal damping assumption [132, 133], in which \mathbf{D} can be evaluated from the following modal damping matrix

$$\mathbf{D}_n = \begin{bmatrix} 2\xi_1\omega_1M_1 & 0 & 0 & 0 \\ 0 & 2\xi_2\omega_2M_2 & 0 & 0 \\ 0 & 0 & 2\xi_3\omega_3M_3 & 0 \\ 0 & 0 & 0 & 2\xi_4\omega_4M_4 \end{bmatrix}, \quad (4.3)$$

where ξ_i , ω_i , and M_i are the damping ratio, natural frequency, and modal mass, respectively, associated with the i^{th} mode. The damping ratios are estimated from the measured experimental data. The matrices \mathbf{D} and \mathbf{D}_n can be related by

$$\mathbf{D}_n = \Phi^T \mathbf{D} \Phi, \tag{4.4}$$

where Φ is the mode shapes' matrix. As a consequence, the matrix \mathbf{D} is determined by

$$\mathbf{D} = \Phi^{-T} \mathbf{D}_n \Phi^{-1}. \tag{4.5}$$

For the numerical model described above, Figure 4.5 shows the comparison between the numerical and experimental mode shapes. Notice that the first mode is a rigid-body mode and, for convenience, it is not illustrated here. The experimental modal parameters were estimated using the rational-fraction polynomial (RFP) method (as described later in Section 4.5.2). The experimental natural frequencies and damping ratios for the baseline condition (State#1) as well as the numerical natural frequencies are summarized in Table 4.2. Note that the numerical model assumes, for the aluminum, a calibrated Young's modulus equal to 65 GPa and negligible friction between the rails and the structure. The Young's modulus was adjusted to match the numerical and experimental frequencies. This manner, the modulus takes into account not quantified sources of variability like the friction at the base and local geometric imperfections. As shown in the Figure 4.6, the MAC values of the second, third, and fourth mode shapes as well as the COMAC values at each node are very close to one, indicating that the numerical and experimental mode shapes are highly correlated.

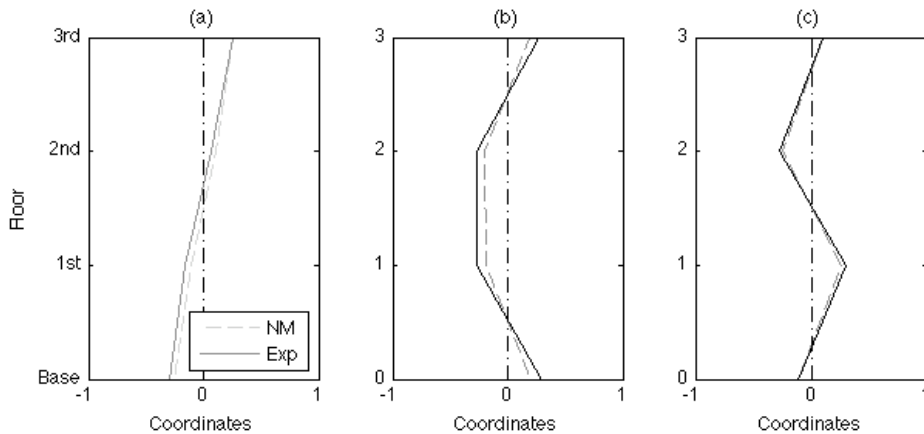


Figure 4.5. Numerical (NM) and experimental (Exp) mode shapes of the baseline condition: (a) second; (b) third; and (c) fourth mode shapes.

Table 4.2. Experimental along with numerical natural frequencies and damping ratios for State#1 (baseline contidion).

Mode Number	Frequency (Hz)		Damping Ratio (%)
	Experimental	Numerical	
2	30.7	29.8 (-2.9 %)	6.3
3	54.2	54.0 (-0.4 %)	2.0
4	70.7	71.6 (+1.3 %)	0.97

Figure 4.7a and b show the experimental and the numerical acceleration responses at the third floor (Channel 5), respectively. The experimental response corresponds to a measured time series response of the baseline condition (State#1) due to the excitation measured at Channel 1. The numerical response corresponds to the acceleration at the same location due to the same experimental excitation. Apparently, the figure indicates that the acceleration amplitudes of both responses are consistent. Nonetheless, two techniques are used for quantitative comparison of both responses, namely, ACF and power spectral density (PSD). By overlapping the numerical and experimental ACFs, this procedure permits to evaluate if the numerical response reasonably characterizes the experimental data. The ACFs shown in Figure 4.8, in an overlap format, indicate that the experimental and numerical responses are correlated.

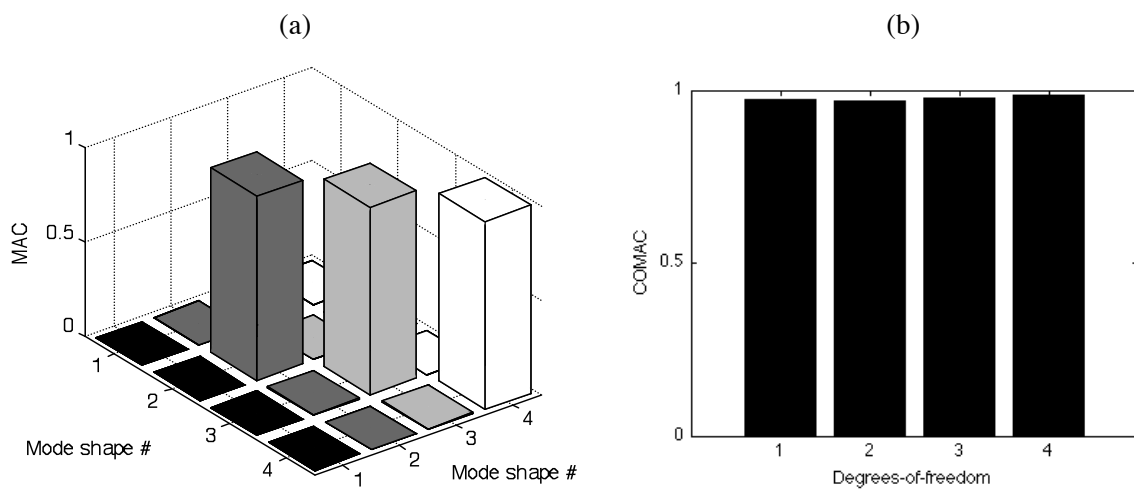


Figure 4.6. Correlation between numerical and experimental mode shapes: (a) MAC; and (b) COMAC values.

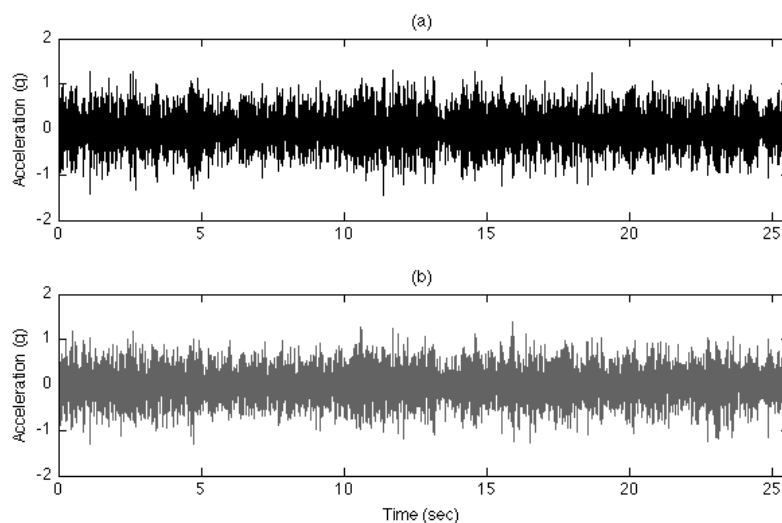


Figure 4.7. Responses from Channel 5 due to the measured experimental excitation at Channel 1 (State#1): (a) experimental time series; and (b) time series derived from the numerical model.

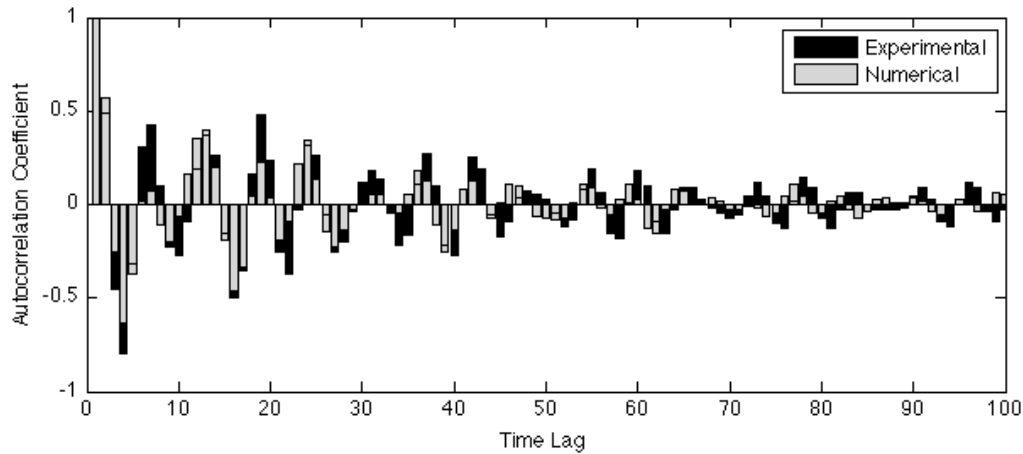


Figure 4.8. ACFs of the experimental and numerical responses.

Another manner to compare the accuracy of the experimental and numerical responses is by means of overlapping the PSDs of both responses, as shown in Figure 4.9. In this case, each PSD is estimated by averaging small spectrum quantities of segments from the original time series. Basically, for each response, the associated time series (8192-point length) is divided into segments according to a moving window of 1024-point length. Each segment is windowed with a Hamming window. The fast Fourier transform is computed in each segment using a moving window with 50% overlap. Finally, the set of spectra is averaged to form the final PSD. In the figure, the numerical estimated PSD seems to fit the experimental one, even though the former has more energy content in the second and less energy in the third natural frequencies. Those differences are likely related to the friction at the base. Recall that, as an approximation, the numerical model assumes negligible friction.

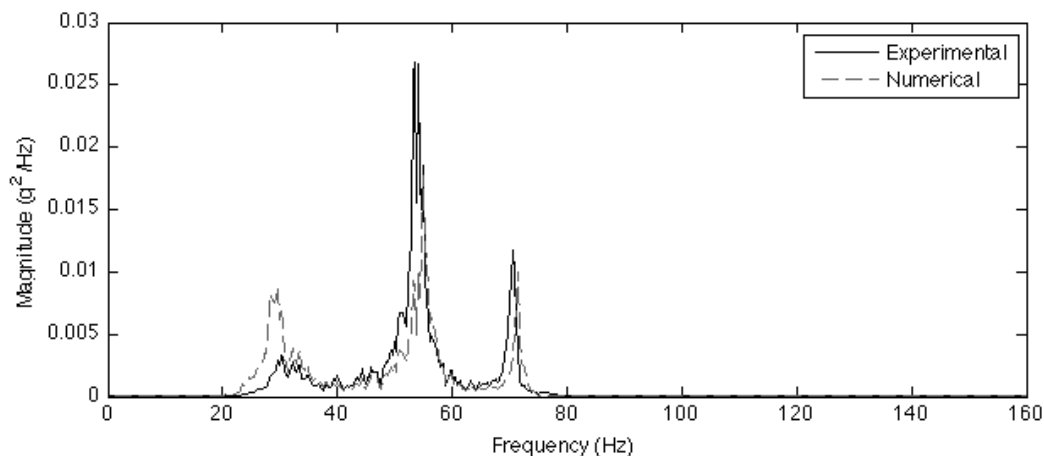


Figure 4.9. PSDs obtained from experimental and numerical time responses.

In conclusion, this section summarized the development of a four-degree-of-freedom physics-based numerical model to confirm that a linear model predicts reasonably the experimental data. The structure was modeled as a shear-building model with four lumped masses at the floors. The damping

matrix was obtained using the results of the experimental modal analysis. The Young's modulus was adjusted so that the numerical natural frequencies agreed with the experimental ones. The numerical model assumed negligible friction between the rails and the structure. Additionally, some statistical techniques, such as MAC, COMAC, ACF, and PSD, were used to show that the numerical model is able to predict with high level of certainty baseline response data. Finally, note that this model was just used to better understand the system behavior of the test structure and it will not be used throughout this chapter as a tool to detect damage.

4.4 Stationary Properties of the Data Sets

Because no explicit mathematical equation can be written for the time series produced by a random excitation, such as the measured data in this study, statistical procedures must be used to define their properties. In statistics, the data from a random process are said to be stationary and (essentially) ergodic when the statistical moments and joint moments are time-invariant and do not change when computed over different time series [134]. In this study, some of the basic statistical properties such as the first four statistical moments (mean, standard deviation, skewness, and kurtosis) as well as the ACFs are used to describe the data. The box plots in Figure 4.10 indicate the degree of dispersion and symmetry in the statistical moments computed over all 10 time series from Channel 5 of each state condition. The bottom and top of each box are the lower and upper quartiles, respectively. (Note that the crossed signs correspond to outliers, i.e., values more than 1.5 times the interquartile range away from the bottom or top of each box.) The scatter highlighted in the mean is related to the arbitrary plot scale and is largely meaningless because the mean is, approximately, zero for all state conditions and cannot be used to scale the figure. Looking at the standard deviation, skewness, and kurtosis, one observes that, although there is variation in the statistics across states (between-class scatter), there is very little variation across the test sequence for a given state (within-class scatter). As, for each state, the statistics do not change significantly across the test sequence, the structural system in each state can be assumed stationary. As highlighted in the figure for the damaged states (State#10-17), the skewness and kurtosis actually prove to be features revealing the presence of nonlinearities (and hence the damage), as indicated by significant departures from the expected values of a Gaussian signal (zero for skewness and three for kurtosis). Furthermore, the skewness and kurtosis of the responses for Channel 1 in Figure 4.11 indicate that this channel is insensitive to the presence of damage. This result in itself is important because it shows that the departures from the Gaussian condition for Channel 5 cannot be blamed on the possibility of non-Gaussian input signals – the between-class scatter on the skewness and kurtosis for the different states of Channel 1 is not significant. As further evidence of stationarity for the various states, the ACFs of the responses for each state are relatively consistent across the sequence of the 10 tests. For illustration purposes, the box plots in Figure 4.12 indicate the degree of dispersion and symmetry in the first 15 auto-correlation coefficients computed over all 10 time series from Channel 5 of State#1 and 14.

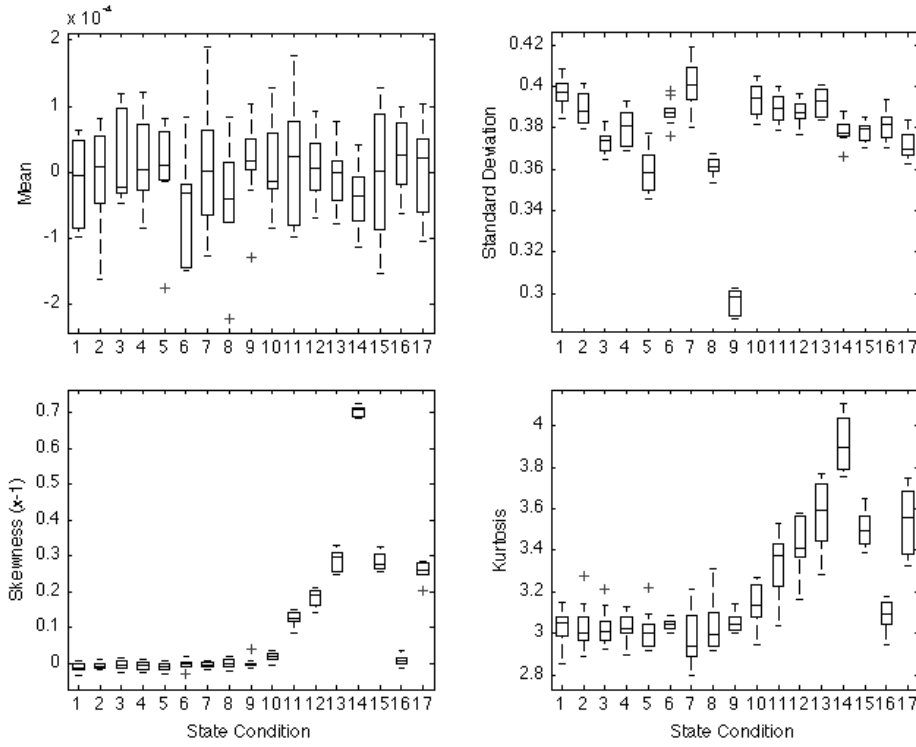


Figure 4.10. Box plots of the first four statistical moments of all 10 time series from Channel 5.

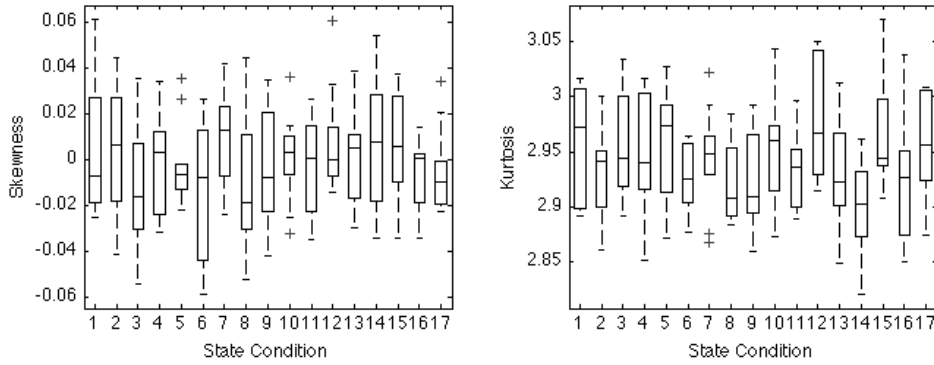


Figure 4.11. Box plots of the skewness and kurtosis of all 10 time series from Channel 1.

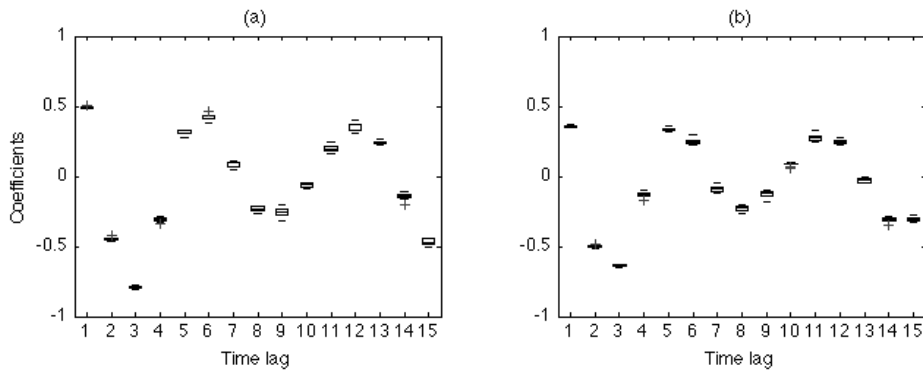


Figure 4.12. Box plots of the ACFs, for the first 15 coefficients, of all time series from Channel 5: (a) State#1; and (b) State#14.

In summary, based on the observations above, it can be assumed that the random processes associated with all channels are at least weakly stationary and may be stationary in the wide sense. Moreover, it was shown that the changes in the statistical moments of the response are not the result of changing inputs. This assumption implies that the statistics of a single time series are representative of the entire time-history ensemble corresponding to a specific state condition. Based on this assumption, throughout the feature extraction section, only one time series from each state condition is used to demonstrate the feature extraction capabilities of each technique.

4.5 Feature Extraction

In Chapter 1, the feature extraction step was posed as the portion of the SHM-SPR paradigm concerned with the calculating of some signature or quantity from the structural response data that can be correlated with damage. In Chapter 3, several feature extraction techniques were presented. Herein, the main goal is to apply all the techniques described and to show that selected features are sensitive to the simulated damage and insensitivity to simulated operational and environmental variations. Note that throughout this section, the AR models are focus of special attention.

4.5.1 Basic Statistics

The features used herein (PDF, normal probability plot, and statistical moments) expect that the damage can introduce significant changes in the statistics of the acceleration time series. The sequence of exposition pretends to show the importance to maximize the structural information in a low-dimensional feature vector.

4.5.1.1 Probability Density Function

The PDF-based features expect that changes in time series caused by damage might imply changes in the shape of the PDFs. Therefore, the non-parametric kernel density estimator is used herein to estimate the PDFs associated to the underlying processes from Channel 5 of four state conditions, namely State#1 (baseline), 7 (stiffness reduction in columns), 14 (gap of 0.05 mm), and 17 (gap of 0.1 mm and 1.2 kg added on the first floor). Recall that this kernel density is useful because no information is given *a priori* regarding the shape of the distribution.

Figure 4.13 shows individual estimates of PDFs from Channel 5 of State#1, 7, 14, and 17, based on the standard Gaussian kernel function given by Equation (3.44) and using a smoothing parameter h that is a function of the number of points in each acceleration time series. The density is estimated at 100 equally spaced points that cover the range of acceleration amplitudes in each time series. Based on the plots, one can observe that there exists a significant difference between PDFs from damaged states (State#14 and 17) and the undamaged ones (State#1 and 7). Besides the baseline data, the figure also suggests that the undamaged states tend to assume an underlying normal distribution. Conversely, as the level of damage increases, the PDFs tend to deviate from the normal distribution.

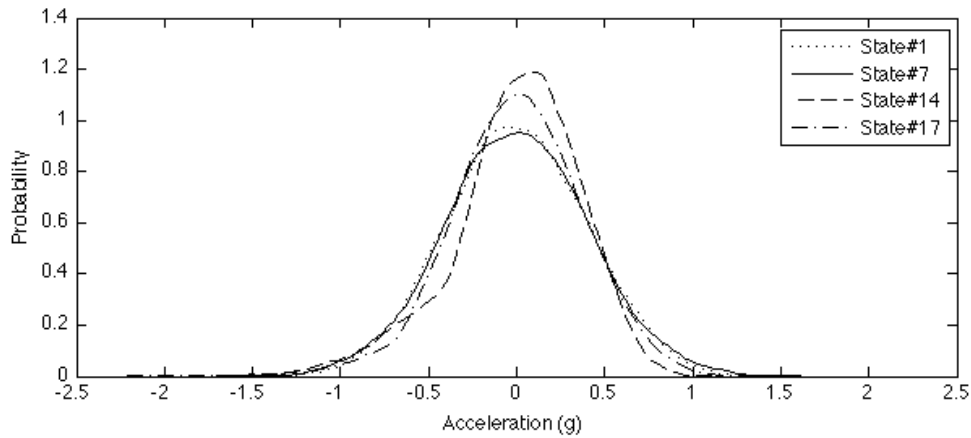


Figure 4.13. PDFs estimated from acceleration time series from Channel 5 of two undamaged (State#1 and 7) and two damaged (State#14 and 17) states using a kernel density estimator.

4.5.1.2 Normal Probability Plot

It was shown in Figure 4.13 that at least the data from the baseline condition (State#1) are normally distributed. Therefore, herein the normal probability plot is applied to graphically verify whether the measured data is from a normal distribution. It is expected that damage might change the normal assumption of the baseline condition. By definition, the normal probability plot is linear when data come from a normal distribution. Otherwise, curvatures are shown in the plot if the data are related to another underlying probability distribution.

Figure 4.14 shows normal probability plots of the same states, i.e., State#1, 7, 14, and 17. The nonlinear scale of the vertical axis corresponds to empirical probability (between zero and one) versus the accelerations data points in the horizontal axis. Recall that all points should fall close to the diagonal dashed line if the data are normally distributed. Therefore, the plots clearly show that data from the baseline condition (State#1) and the state affected by simulated environmental condition (State#7), but without nonlinearities, are normally distributed. Note that in this case the shaker does not have a feedback control mechanism and, as such, it has difficulty in reproducing an accurate Gaussian input. This difficulty manifests itself in the tails of the distribution where slight deviations from the normal assumption can be seen. Nevertheless, the states with the nonlinearities (State#14 and 17) show that an assumption of normality is not justified, as shown by the significant curvature in the tails of the normal probability plot.

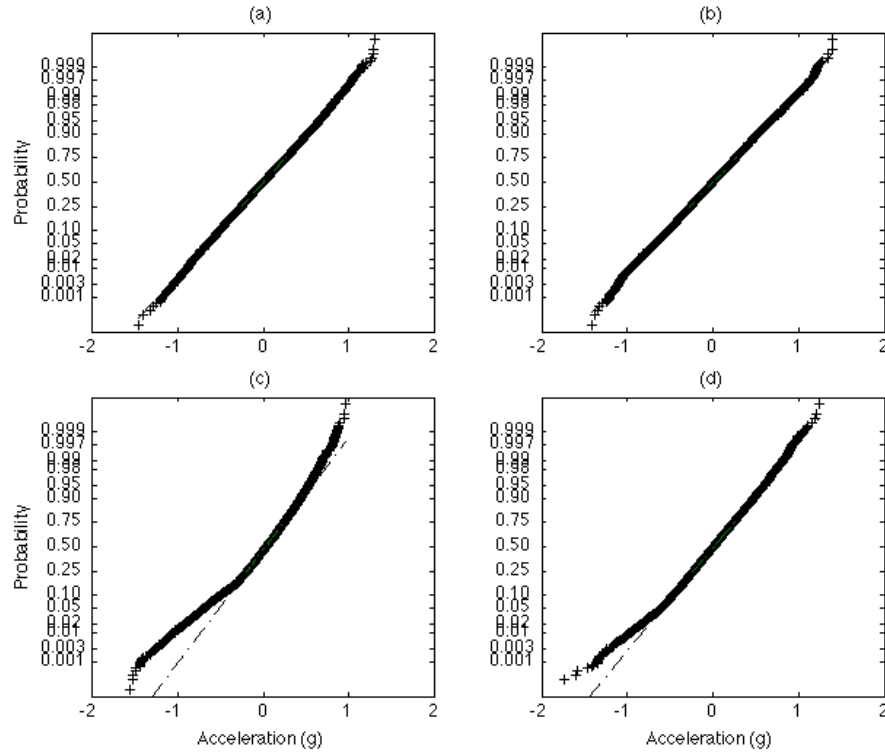


Figure 4.14. Normal probability plots of four state conditions at Channel 5: (a) State#1; (b) State#7; (c) State#14; and (d) State#17.

4.5.1.3 First Four Statistical Moments

The PDFs and normal probability plots highlighted significant changes in the damaged states when comparing with the undamaged ones. However, the assessment was made either in a visual manner or at cost of high-dimensional feature vectors. Therefore, herein the first four statistical moments (mean, standard deviation, skewness, and kurtosis) are used to quantify those changes in a lower dimensional feature vector. For each state condition (State#1-17), Figure 4.15 plots the first four statistical moments of one time series from all accelerometers (Channel 2-5). It is shown that for every channel, the mean and standard deviation does not give any insight about the presence of nonlinearities associated with the damaged state conditions (State#10-17). However, for Channel 4 and 5, the skewness and kurtosis change significantly in the damaged states when compared to the undamaged ones (State#1-9).

It is of interest to note that, among the damaged states, the skewness has an opposite sign for the sensors on either side off the impact device, implying the response from Channel 5 has more values above the mean and the response from Channel 4 has more values below the mean in the damaged state conditions. Moreover, these same damaged states in general have larger kurtosis (larger than 3.2) than the undamaged ones. Note that a kurtosis larger than three means most of the variance is caused by non-frequent extreme deviations from the mean. Actually, these results were expected because

damage is introduced in the form of intermittent singularities into the time series data. However, for both skewness and kurtosis the changes are only significant in the data from Channel 4 and 5, which are on the floors directly above and below the bumper location. This fact points out the challenge to detect and/or locate damage with a sparse array of sensors.

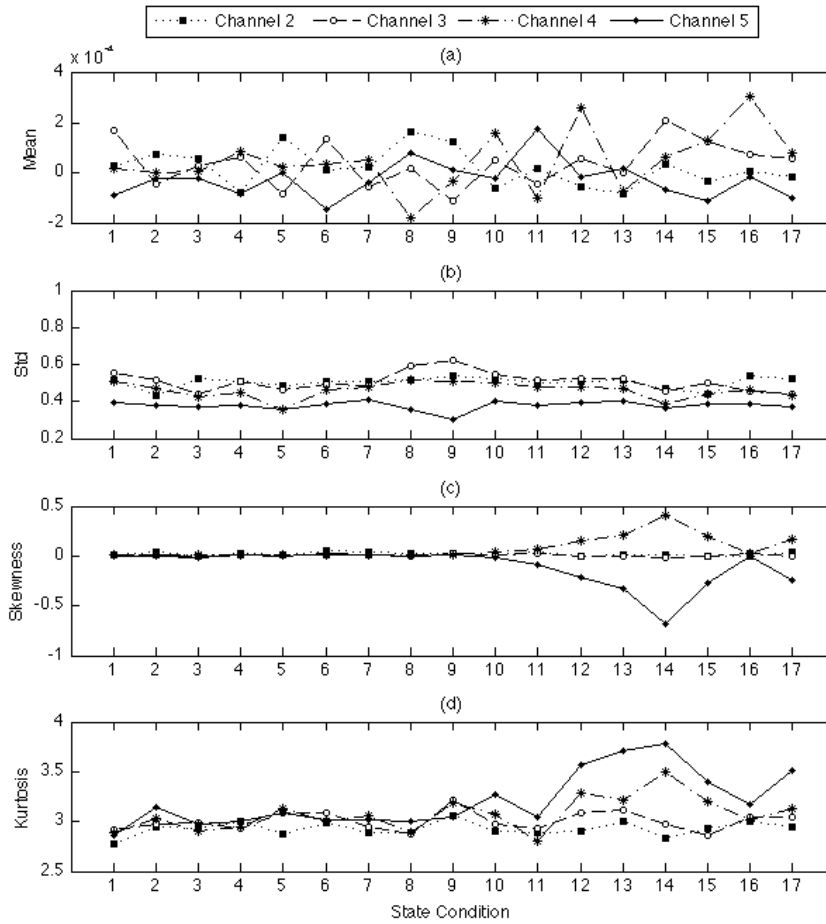


Figure 4.15. First four statistical moments based on one acceleration time series from Channel 2-5 of each state condition: (a) mean; (b) standard deviation; (c) skewness; and (d) kurtosis.

4.5.1.4 Conclusions

The PDFs and normal probability plots showed that damage introduces deviations from the normal distribution. Additionally, the skewness and kurtosis were shown to be useful damage-sensitive features when damage introduces an asymmetry into the response data even in the presence of linear changes caused by simulated operational and environmental variations. However, a high density of sensors throughout the structure might be required to detect damage in a global basis, because the sensors might only be sensitive to damage when located near the source of damage. Actually, the statistical moments showed to be useful because of their low dimension when compared to the dimension of the PDFs and normal probability plots. Thus, the first four statistical moments might be

preferred over the other two techniques, because it permits to detect deviations from the normal condition with a lower dimensional feature vector.

4.5.2 Modal Parameters

The modal parameters estimation is done by curve fitting a parametric form of the frequency response function (FRF), defined in terms of the natural frequencies, modal damping ratios, and mode shapes, to the measured FRFs from one test corresponding to each state condition. The natural frequencies, damping ratios, and modes shapes were estimated using a RFP global curve fitting method [135]. The RFP method is a frequency domain curve fitting that operates directly on the complex FRF. This method performs a least squared error curve fit to all FRFs [100, 136]. Note that the curve fitting is applied to minimize the effects of measurement noise. As shown in Figure 4.16 for State#1, the specified frequency bands, over which the RFP method was applied, were determined by visualizing the imaginary part of the complex mode indicator function (CMIF). By looking at this plot, three frequencies can be clearly identified. Therefore, for all state conditions, the FRFs were curve fit in one window with a frequency band between 25 and 80 Hz, as shown in Figure 4.17.

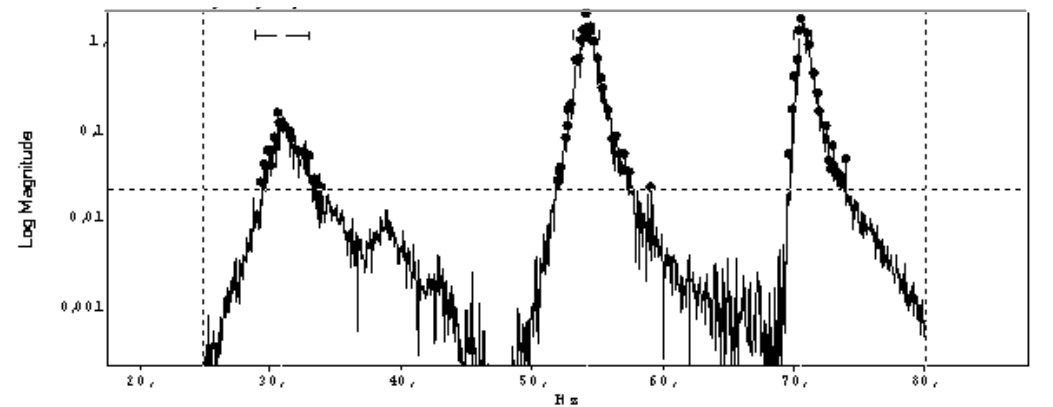


Figure 4.16. CMIF for one FRF from Channel 5 of State#1.

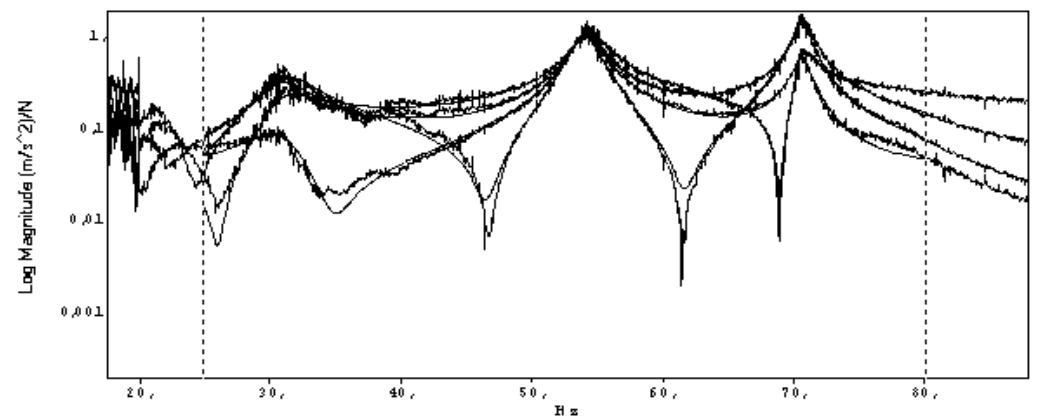


Figure 4.17. Curve fitting example on the FRFs from Channel 2-5 for the selected frequency range between 25-80 Hz (State#1).

Table 4.3 summarizes the estimated natural frequencies and damping ratios corresponding to one test of each state condition. (For completeness, the mode shapes of the baseline condition are plotted in Figure 4.5.) In order to highlight the differences in the natural frequencies from the baseline condition (State#1), Figure 4.18 plots the natural frequencies of all state conditions and Figure 4.19 plots the frequency differences between the baseline condition and the other states. In general, one can observe that the differences decrease for the undamaged state conditions (State#2-9) and increase for the damaged states with no mass or stiffness changes (State#10-14). However, the challenge of this study is to detect damage when the structure is also affected by operational and environmental changes. Thus, it is clear that changes in frequencies associated with the damage introduced for State#15, 16, and 17 are masked by the varying mass and stiffness values associated with these state conditions.

Table 4.3. Experimental natural frequencies and damping ratios of all state conditions.

State Condition	Frequency (Hz)			Damping Ratio (%)		
	2nd	3rd	4th	2nd	3rd	4th
State#1	30.7	54.2	70.7	6.3	2.0	0.97
State#2	30.4	52.9	70.3	6.4	1.5	0.76
State#3	30.9	53.1	68.2	5.5	2.1	0.82
State#4	30.9	51.2	69.2	7.1	2.2	0.55
State#5	30.3	47.0	67.8	7.0	1.8	0.38
State#6	29.7	53.9	65.8	5.3	1.7	1.2
State#7	28.6	54.2	62.2	5.1	1.7	0.72
State#8	30.2	51.1	69.3	5.6	2.2	0.80
State#9	28.9	47.4	68.0	4.6	2.6	0.80
State#10	31.1	54.4	70.9	6.6	2.1	1.0
State#11	31.7	54.5	70.9	7.0	1.9	0.93
State#12	31.8	54.9	71.2	6.3	1.9	1.0
State#13	32.4	55.2	71.4	6.3	1.9	1.0
State#14	33.5	57.6	74.2	7.1	2.2	0.97
State#15	31.6	54.0	71.1	5.4	1.6	0.73
State#16	31.0	53.4	68.3	5.3	2.3	0.82
State#17	32.3	54.4	69.2	5.0	2.2	0.80

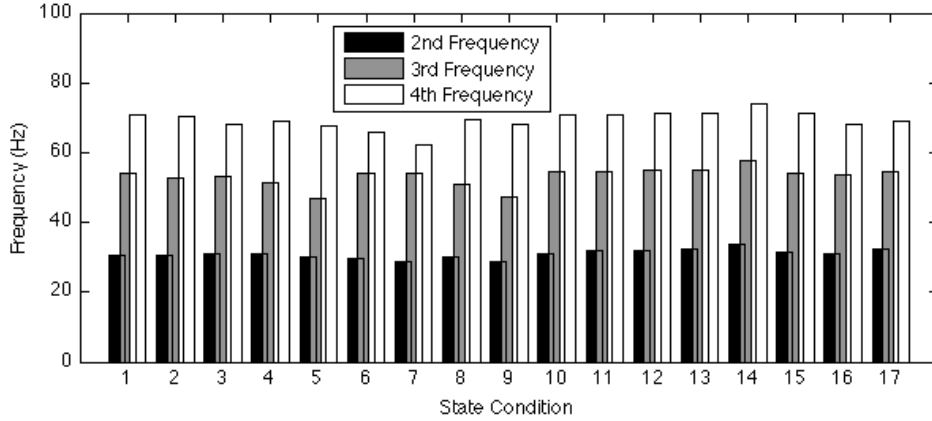


Figure 4.18. Natural frequencies estimated based on one test of each state condition.

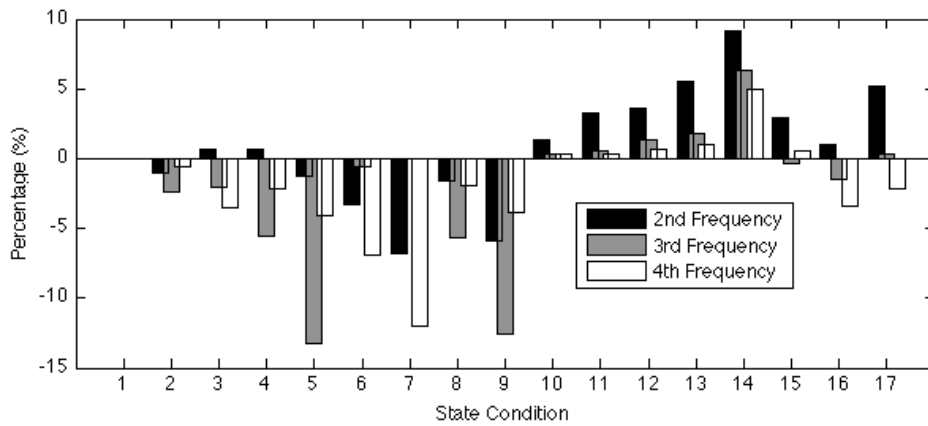


Figure 4.19. Natural frequency deviations of all state conditions from the baseline condition (State#1).

As shown in Table 4.3, the damping ratios do not show signs of consistently increasing or decreasing with the damaged state conditions. Theoretically, the impacts associated with nonlinearities should increase the energy dissipation, which should manifest itself in higher damping. However, damping ratios are empirical values that must be obtained by measurements that assume a linear system. As a consequence, the lack of consistent changes in damping as a function of damage can be justified by the fact that the damping ratios are estimated through the FRF curve fitting process that fits a linear modal model to nonlinear system response data, and so, the damping ratios tend to represent only the linear portion.

In conclusion, some limitations of using modal parameters as damage-sensitive features were demonstrated, specifically the natural frequencies and damping ratios. For the simulated changes, one could not conclude which data are from the damaged states by just examining changes in the natural frequencies when other sources of variability are present that influence the dynamic response characteristics of the structure. However, note that the effects of the temperature were partially simulated in this case, because if the stiffness of the columns were increased (replacing by a thicker

one), the natural frequencies would increase to values similar to those verified for the damaged state conditions (State10-14).

4.5.3 *Auto-regressive Models*

4.5.3.1 *Appropriate Model Order*

The analysis performed to determine the optimal AR model order is divided into two parts. First, one time series from the baseline condition (State#1) of Channel 5 is used. This procedure permits one to apply all the estimation techniques in a more comprehensive manner. Then, a brief extension is performed to the other channels. The plots in Figure 4.20 are produced for Channel 5 based on the four techniques described in Section 3.2.3, namely AIC, PAF, RMS error, and SVD. The specific goal of using multiple techniques is to verify the consistency of them to find the optimal number of parameters needed to fit the data and to detect damage in the form of nonlinearities. Figure 4.20a, b, and c plot, respectively, results from the AIC, PAF, and RMS error techniques obtained by directly fitting AR models of increasing order $p=1,2,\dots,60$ to the measured response data. Figure 4.20d plots the singular values of \mathbf{M} in Equation (3.16). Assuming $p=60$, the matrix \mathbf{M} has a dimension of 8132×60 . Note that the abscissa of the plot is, in some sense, related to the AR model order as indicated by Equation (3.18). From these plots one can point out some facts that compromise the definition of the optimal model order: (i) the AIC function is not minimized in the plotted window; (ii) in the case of the PAF technique, after convergence the coefficients do not stay within the 95% confidence limits; and (iii) for the other two techniques, the point of convergence is not precisely defined. Because of these issues, optimal model order selection still requires interpretation as stated by Al-Smadi [76]. Even though it is not possible to establish a unique solution, the results suggest that the optimal order is possibly in the range of 15 to 30. Additionally, it was confirmed that the AIC, PAF, and RMS error techniques suffer from the fact that all parameters of the models corresponding to different model orders first must be estimated in order to calculate these values. On the other hand, the SVD technique does not require prior estimation of the model parameters, which reduces the computational effort associated with this technique compared to the others. Even though the SVD technique gives an upper bound solution, the lower computational efforts can be an advantage for implementation on embedded hardware.

Based on this analysis, three AR models, namely AR(5), AR(15), and AR(30), are used throughout this section in order to indicate the influence of the model order on the damage detection process under operational and environmental variations. These values were chosen so the first is unequivocally too small, while the second and third bound the plausible range of model orders suggested by these four techniques.

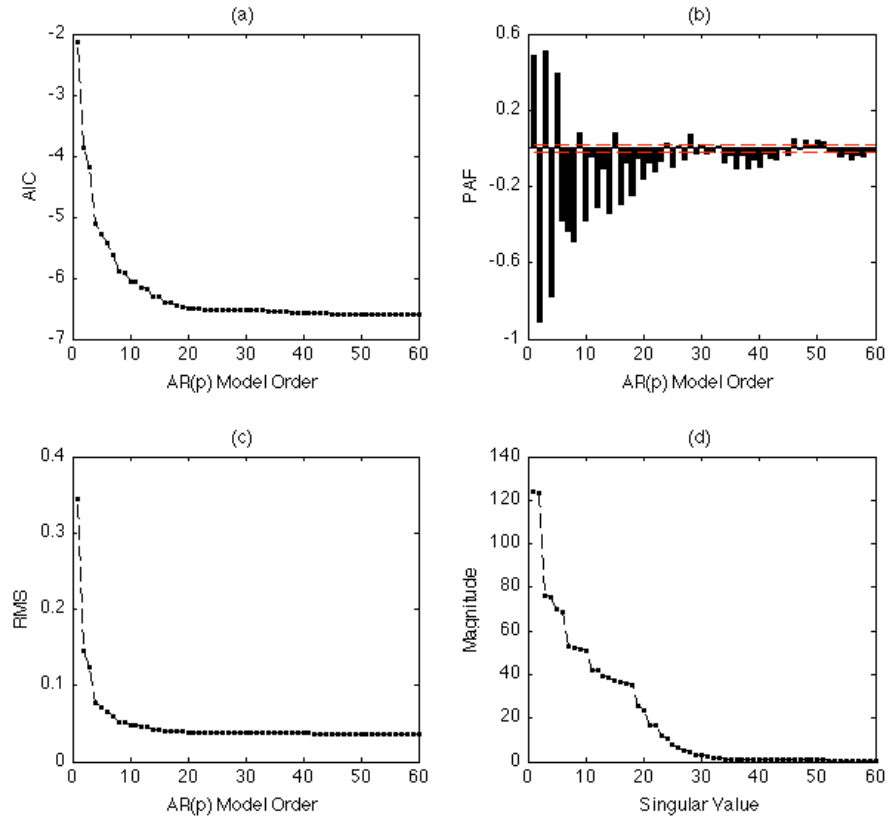


Figure 4.20. AR order estimation based on one time series of Channel 5 from the baseline condition (State#1) using four different techniques: (a) AIC; (b) PAF; (c) RMS; and (d) SVD.

A further extension of the previous study is carried out to all accelerometers using only the AIC technique. Figure 4.21 shows the AIC functions for Channels 2-5 using time series from the baseline condition. Once the functions are not minimized in the adopted range, and taking the convergence point as reference, one can see that they suggest slightly different AR model orders for each channel.

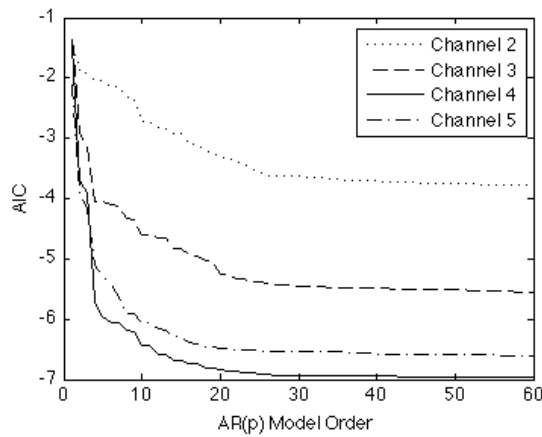


Figure 4.21. AIC functions estimated using time series from Channels 2-5.

4.5.3.2 AR Residual Errors

The first approach to SHM based on the AR model uses parameters estimated from responses measured on the structure in its baseline condition to predict the responses from the damaged condition. Herein, the AR parameters are estimated by fitting an AR model to a time series from Channel 5 using the least-squares technique. For comparison purposes, Figure 4.22 shows a 50-point window of the measured and predicted acceleration time series using the three proposed models: AR(5), AR(15), and AR(30). From a qualitative point of view, all the models have captured the underlying physical structural response; however, as expected, the higher-order models predict the data better than the AR(5) model. (One should generally observe the usual caveat that the higher-order models are potentially overfitted.)

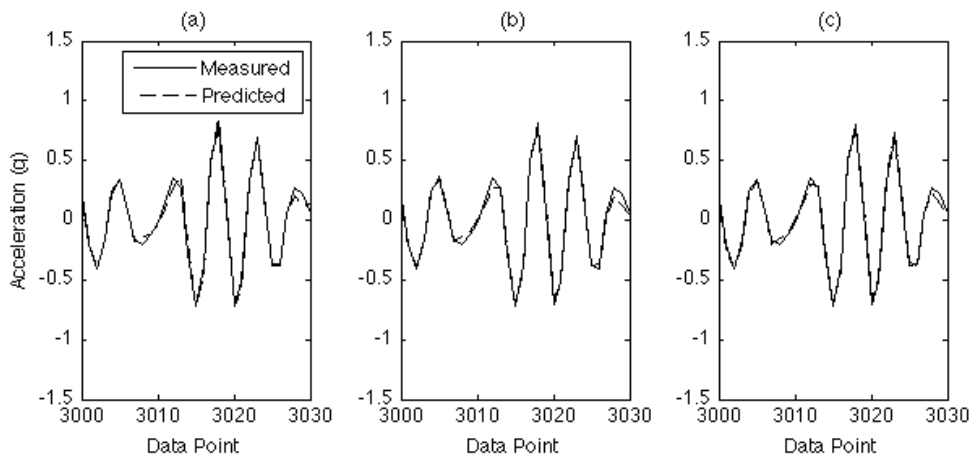


Figure 4.22. Comparison of the measured and predicted time series from the baseline condition at Channel 5 using: (a) AR(5); (b) AR(15); and (c) AR(30) models.

One indication that an AR model is fitting the data well is given by independent and normally distributed residual errors. For one time series of the baseline condition, Figure 4.23 shows histograms of the residual errors using 20 bins along with a superimposed Gaussian distribution based on the sample mean and standard deviation. Note that depending on the level of nonlinearity introduced by the bumper, the distribution of the residual errors may not be Gaussian when the AR model derived from the baseline condition is used to predict the responses of the damaged states. As expected, for the baseline condition, the histograms show that the higher the order of the AR model, the lower will be the variance of the residual errors.

Even though the residual error sequences of the three models have, apparently, an underlying normal distribution, other techniques might be used to verify the data independency. In this case, the PSD functions of the residual errors are used to find correlations or the presence of periodic signals buried under noise. Figure 4.24 illustrates the PSDs of the residual errors from the three models. The plots show that the resulting residuals from the AR(5) model are still correlated, because it is possible to identify three natural frequencies of the structure at 30.7, 54.2, and 70.7 Hz. On the other hand, the

residual errors from the AR(15) and AR(30) models seem to be uncorrelated based on the relatively flat PSDs across the entire frequency range.

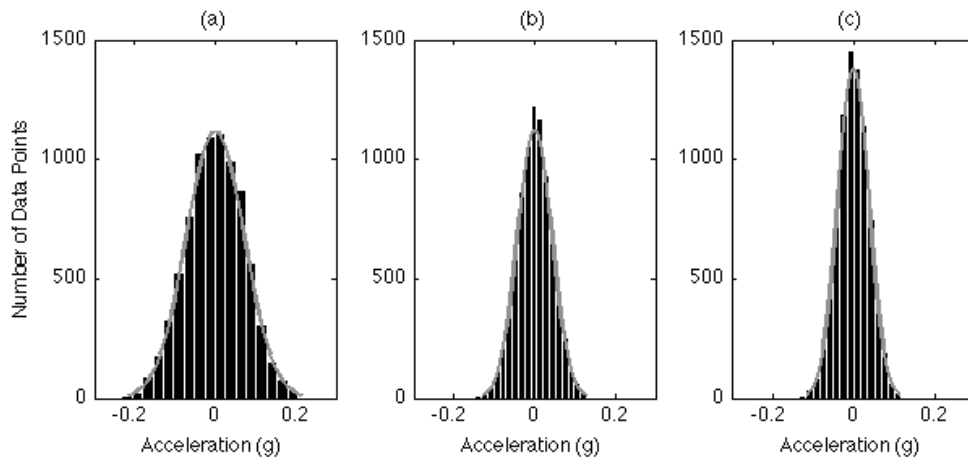


Figure 4.23. Residual-error histograms along with the superimposed Gaussian distribution based on one time series from the baseline condition at Channel 5: (a) AR(5); (b) AR(15); and (c) AR(30) models.

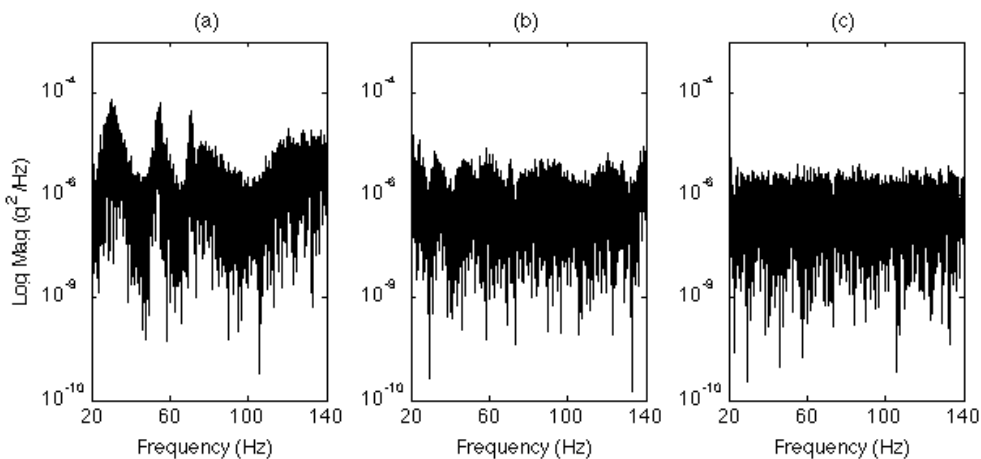


Figure 4.24. Log PSDs of the residual errors based on one time series from the baseline condition at Channel 5: (a) AR(5); (b) AR(15); and (c) AR(30) models.

As indicated above by the model order estimation techniques, the previous analysis also suggests an appropriate AR model order within the interval 15 to 30, because the residual errors are independent and normally distributed when the baseline response is calculated with parameters from the same condition. The next step is to use the AR model derived from the baseline condition to predict response data from the remainder conditions. If anomalies are present in the system, the residual error variance will generally increase. Note that this approach is based on the assumption that anomalies will introduce either linear deviation from the baseline condition or nonlinear effects in the signal; as a result, the linear baseline model will no-longer accurately predict the response of the damaged structure. With such an indication of deviation from the baseline, the next action should be to launch a

full investigation to identify the cause of the anomalies. It is critical to note that in this case, anomalies can result from either damage or from operational or environmental effects. In order to discriminate the latter anomalies from those caused by damage, this approach expects that the damage can introduce underlying non-random patterns in the measured data that will be evident from the residual errors.

The correlation analysis is one statistical technique used to find patterns within time series, such as the presence of periodic signals buried under noise due to damage. Figure 4.25 shows the normalized ACFs (for the first 200 coefficients) of the acceleration time series from Channel 5 of States#1, 7, 14 and 17. (Coefficients are scaled so that the ACF at zero time lag equals one.) The ACFs of the original time series suggest the presence of strong correlation in the time series. Moreover, it is difficult to make any inferences about the structural condition based on these plots.

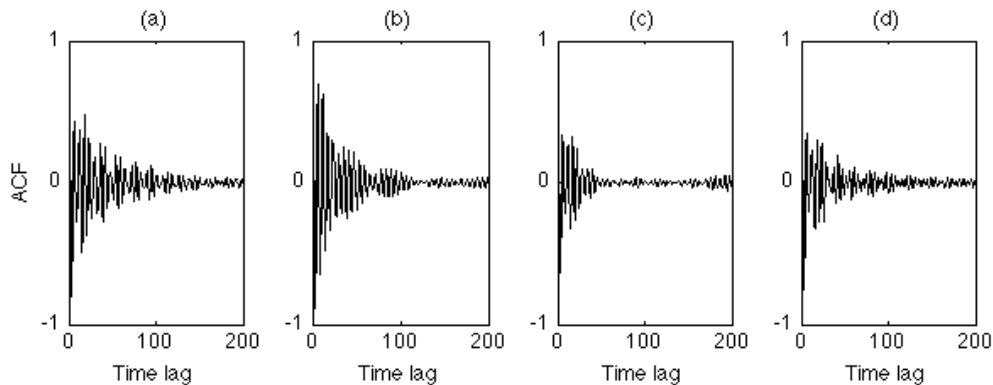


Figure 4.25. ACFs of one acceleration time series at Channel 5 from: (a) State#1; (b) State#7; (c) State#14; and (d) State#17.

Figure 4.26a shows the normalized ACFs of the residual errors from the AR(5) model for the four states mentioned above. Theoretically, if the AR model accurately represents the original time series, the residual errors should be nearly uncorrelated and the ACF should approximate a delta function. Looking at the plots, one can conclude that the residual errors from the AR(5) model are still correlated. However, Figure 4.26b and c indicate that increasing the AR model order, into an interval spanning 15 to 30, reduces the correlation among the residual errors for the undamaged conditions (States#1 and 7) and, at the same time, it shows correlations in the damaged conditions (States#14 and 17) generated by the nonlinearities introduced by the bumper and that is difficult to detect visually in the original time series. In addition, these results indicate that residual errors associated with the AR(15) and AR(30) models will be able to distinguish the damaged cases from the undamaged ones even under operational and environmental variability. Such distinctions are not as clear with the AR(5) model. This fact points out the need to choose an appropriate AR model order to capture the damage-related information buried within the response signals subjected to operational and environmental variability.

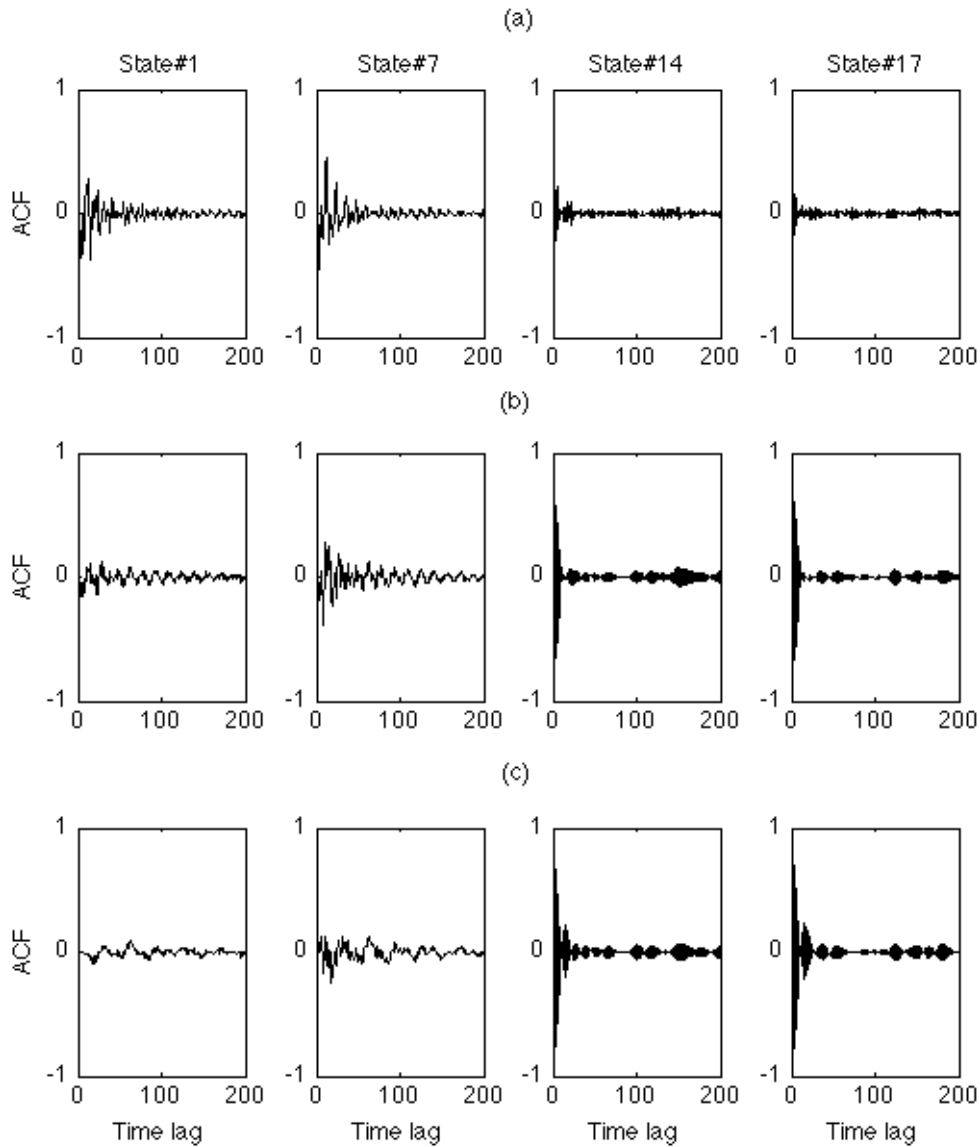


Figure 4.26. ACFs of the residual errors at Channel 5 from State#1, 7, 14, and 17 using: (a) AR(5); (b) AR(15); and (c) AR(30) models.

Lag Plots

Another manner to check the existence of patterns in the data is by means of the lag plot technique. Figure 4.27 plots the original acceleration time series from Channel 5 of State#1, 7, 14, and 17 for a lag equal to one. The damage seems to introduce slight changes into the correlation among the original data. However, these changes are amplified using the residual errors from the AR(5), AR(15), and AR(30) models, as shown in Figure 4.28, Figure 4.29, and Figure 4.30, respectively. The plots suggest that residuals from both undamaged states (State#1 and 7) are randomly distributed. However, the nonlinearities associated with damaged states (State#14 and 17) introduce some auto-correlation into the AR residual errors. Note that this analysis permits one to extract features that discriminate the undamaged and damaged states, even in the presence of operational and environmental variations.

In conclusion, as with the ACFs, the lag plots suggest that although the time series of each state condition have some auto-correlation, damage introduces strong correlation into the AR residual errors whereas there is no correlation in the residuals for undamaged states even in the presence of operational and environmental variations. This fact indicates that the AR residual errors might be used as damage-sensitive features, which confirms the previous studies in the literature [71].

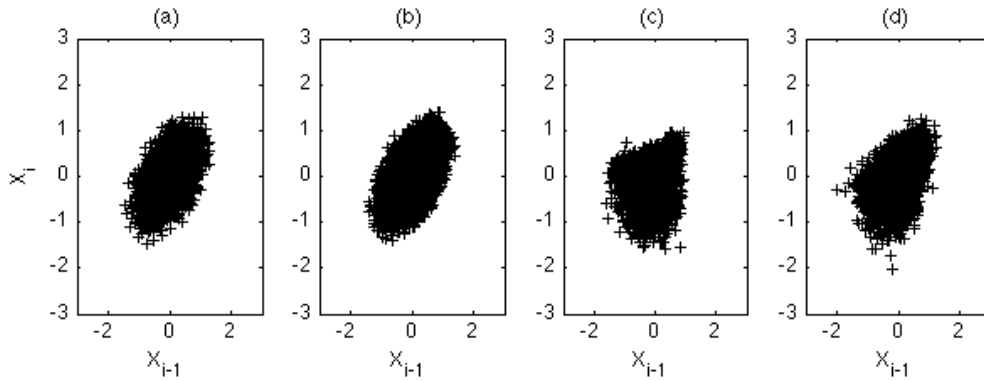


Figure 4.27. Lag plots of the original time series from Channel 5: (a) State#1; (b) State#7; (c) State#14; and (d) State#17.

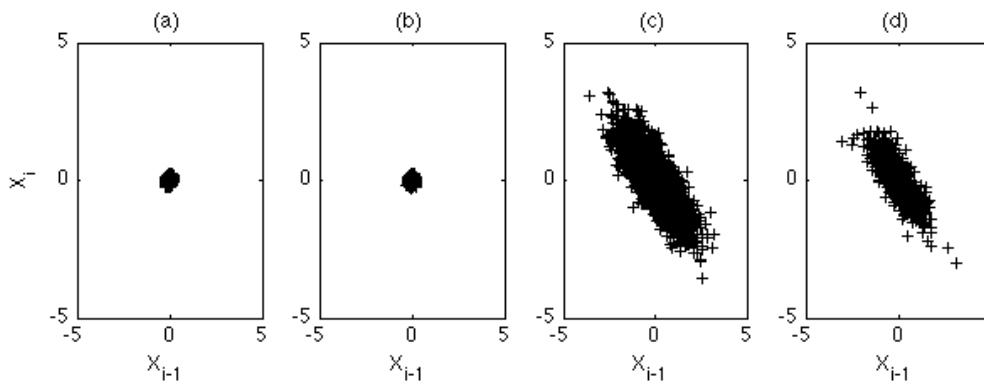


Figure 4.28. Lag plots of the AR(5) model residual errors from Channel 5: (a) State#1; (b) State#7; (c) State#14; and (d) State#17.

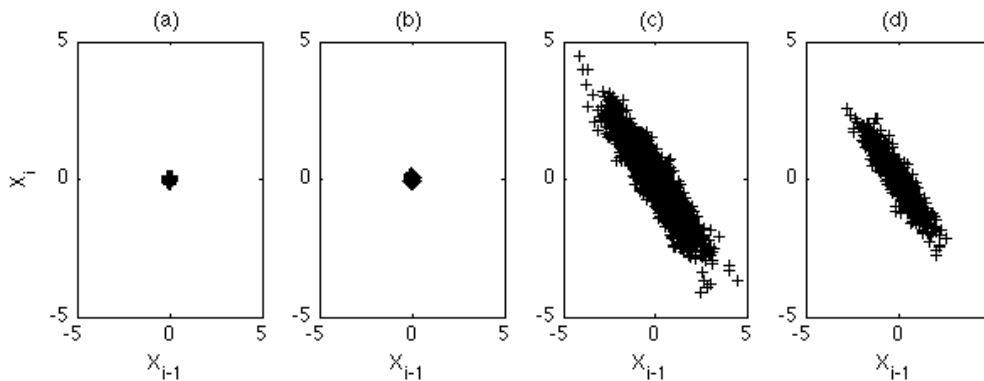


Figure 4.29. Lag plots of the AR(15) model residual errors from Channel 5: (a) State#1; (b) State#7; (c) State#14; and (d) State#17.

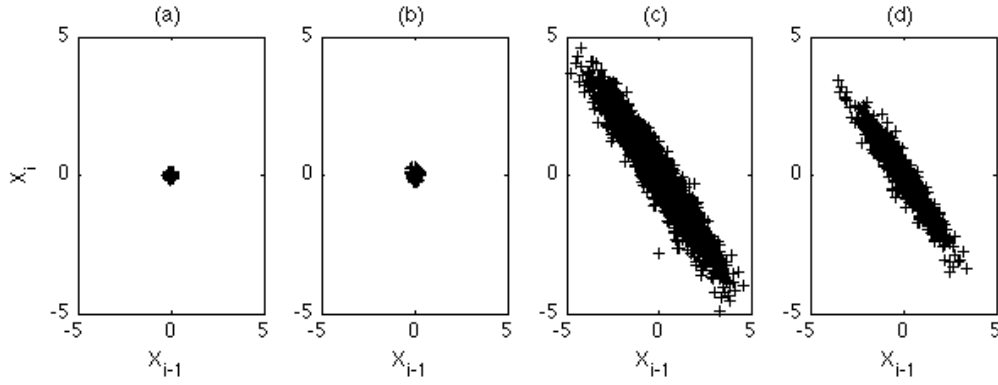


Figure 4.30. Lag plots of the AR(30) model residual errors from Channel 5: (a) State#1; (b) State#7; (c) State#14; and (d) State#17.

Dimension Reduction of the Residual Errors

In certain situations, particularly in machine learning, it might be convenient to reduce the size of the feature vectors composed of AR residual errors. The central limit theorem states that the distribution of a sum of random variables tends to be normal, even when the distributions of the individual random variables forming the sum are decidedly non-normal. Therefore, one can normalize the data by forming sums of the residual errors and examining the statistical properties of these sums. This process also reduces the number of residual errors per time series that need to be stored. The process begins by first performing a standard data normalization. For each residual error time series, the residual error mean of the baseline, \bar{x}_e , is subtracted from each value i ($i=1,2,\dots,N$) and the result is divided by the baseline residual error standard deviation, std_e , resulting in a standard normalization procedure defined as

$$z_i = \frac{e_i - \bar{x}_e}{std_e}, \quad (4.6)$$

where z_i is the normalized residual error i of the \mathbf{z} feature vector. Next, the normalized residual errors are grouped into four-point data blocks and the mean of each data block is calculated. (Note that the selected size of the data blocks will be discussed later in Section 4.6.2.) The mean values are the new damage-sensitive features. For instance, for the AR(15) model, this process permits to reduce the residual error from 8177 to 2044 residual values, with no significant loss of information as shown in Figure 4.31. The figure plots the RMS of the residuals assuming an 8177- (original) and 2044-point (grouped) residual error vectors for each state condition. The figure indicates different magnitudes but similar pattern, indicating that the 2044-point feature vector still encodes the underlying differences between states.

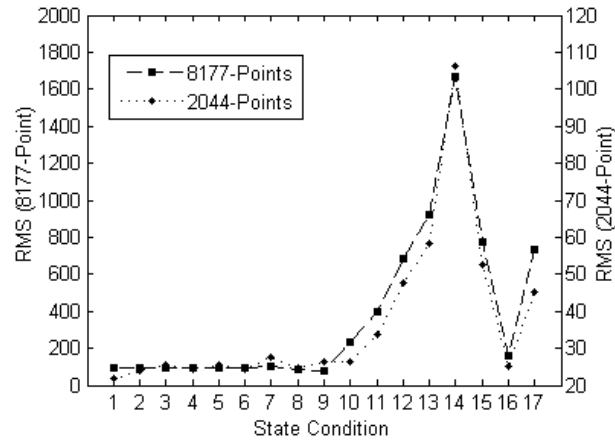


Figure 4.31. RMS of the residual errors using 8177- (original) and 2044-points (grouped).

4.5.3.3 AR Parameters

The underlying idea here is to exploit the AR parameters themselves as damage-sensitive features. One might expect changing amplitudes of these parameters in the presence of nonlinearities caused by damage even under operational and environmental variations. The underlying linear stationary assumption makes it possible to detect the presence of nonlinearities in the time series. The idea is that in a system where different dynamics are present at different times, the estimated parameters should change between intervals [130]. Figure 4.32 shows the parameters from the AR(5), AR(15), and AR(30) models estimated on one time series of each structural state condition using the least-square technique. For the sake of simplicity, the parameters are arranged into two groups; those states corresponding to the undamaged (State#1-9) and damaged (State#10-17) conditions. The figures suggest that increasing the number of impacts (by reducing initial gap at the impacting device) associated with the damaged conditions tends to decrease the AR parameter amplitudes. Furthermore, Figure 4.32 clearly shows that the model parameters associated with the AR(15) and AR(30) models obtained from the undamaged structure data are distinct from those obtained from the damaged structure even in the presence of simulated operational and environmental variability. However, there is not such a clear distinction with the corresponding parameters of the AR(5) model. To better indicate these changes, Figure 4.33 shows the amplitude of the third AR parameter under each state condition for the three models. One can clearly identify (quasi-) linear changes in the amplitude of the parameter as a function of the initial gap for the damaged states without any simulated operational and environmental variations (States#10-14). However, the parameter amplitudes for the damaged states with simulated operational and environmental variability (State#15-17) do not clearly indicate such linear changes. Furthermore, the AR(5) model cannot accurately discriminate all the damaged and undamaged states when simulated operational and environmental variability is present. For example, the AR(5) parameter amplitude corresponding to the damaged State#16 is higher than the one for the undamaged State#7. This result is a clear indication that the operational and environmental variations

can introduce changes in the structural response and mask changes in the responses related to damage when an inappropriate model order is used.

As discussed for the AR residual errors, these results highlight the importance of properly establishing the AR model order in an effort to avoid false-negative and false-positive indications of damage. In the case of the AR(15) and AR(30) models, the operational and environmental variations may only affect the nearly linear relationship between the level of damage and model parameter amplitude.

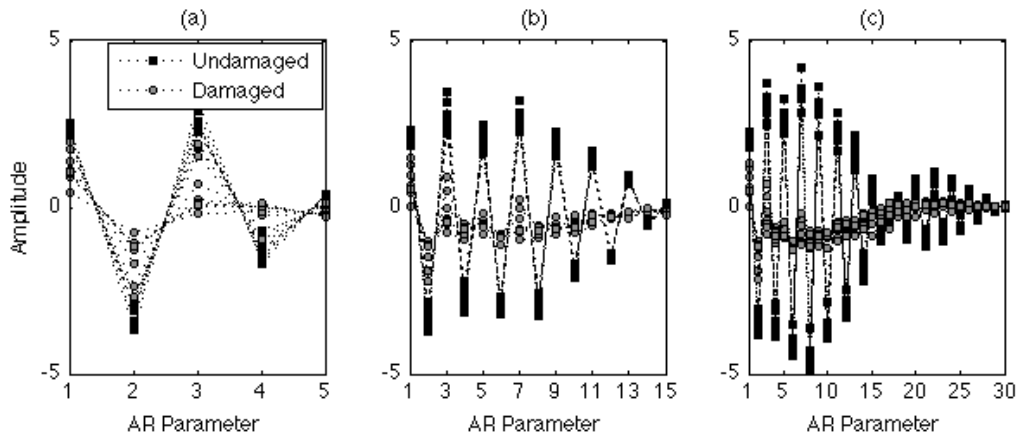


Figure 4.32. AR parameter amplitudes for all the 17 state conditions at Channel 5 using: (a) AR(5); (b) AR(15); and (c) AR (30) models.

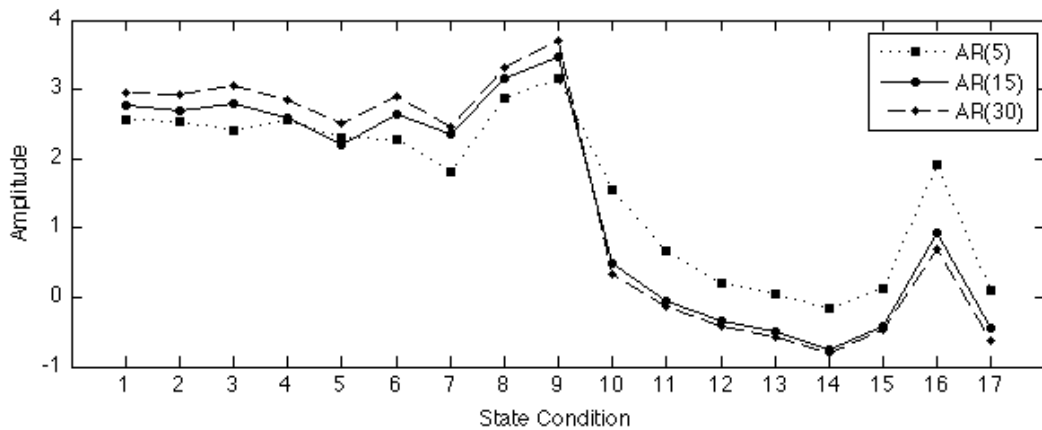


Figure 4.33. Amplitude of the third parameter of all the state conditions at Channel 5 from the three AR models.

In a further investigation, and in order to evaluate the sensitive of the AR parameters to this type of damage throughout the structure, Figure 4.34 plots the AR(15) parameters for all accelerometers (Channel 2-5), in concatenated format, based on one test of each state condition. For better visualization, once again the state conditions are grouped into undamaged and damaged conditions. Note that AR parameters should be constant when estimated based on time series data obtained from time-invariant systems. However, in the presence of operational and environmental variations as well

as damage, the parameters are expected to change, accordingly. The figure indicates particular changes in the parameters' amplitude at Channels 4 and 5 when features are from the damaged state conditions. (Note that these channels are closer to the source of damage.) Clearly, the AR parameters reveal high sensitivity to the presence of damage. This result is an indication that the AR parameters can be useful to address the two first levels in the hierarchy structure of damage identification, namely, damage detection and damage localization. However, to detect damage on a global basis, it might be necessary to perform sensor cross correlation or to install high density of sensors throughout the structure.

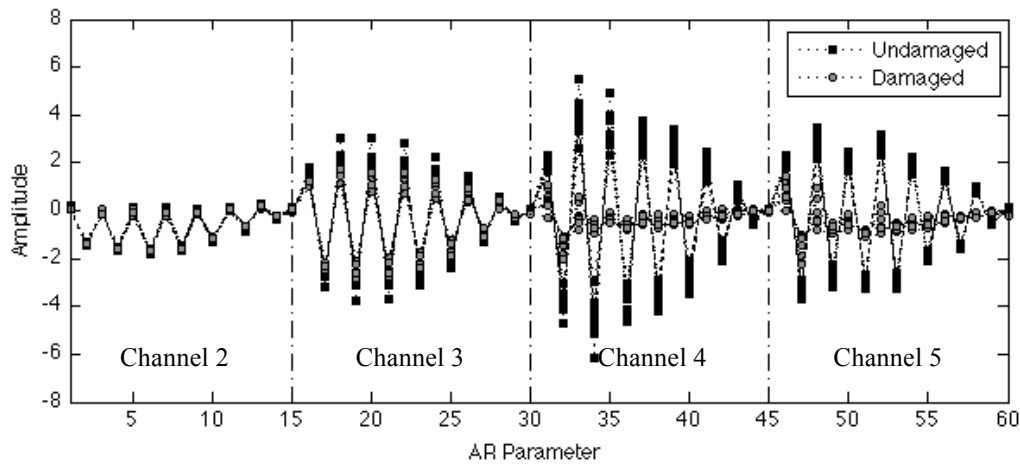


Figure 4.34. AR(15) parameters, in concatenated format, from one test (Channel 2-5) of each state condition.

4.5.3.4 Conclusions

The AR models proved to be useful feature extraction techniques for civil infrastructure SHM applications based on three main reasons: (i) they are very sensitive to damage when it manifests in the form of nonlinearities or transitions between two states; (ii) the extraction of features only depend on response time series data; and (iii) simple and easy implementation. Note that Channel 1, the input force, is not used in this feature extraction technique. Additionally, it was shown that the AR models might be useful to address the two first levels in the hierarchy structure of damage identification, namely, damage detection and localization.

4.5.4 Time-frequency Analysis

The time-frequency representation of signals is potentially a powerful technique to detect changes in system's stiffness over time. It might be particularly attractive when damage is present in the form of nonlinearities that can produce non-stationary response characteristics. Therefore, the STFT and WT are applied independently to time series from Channel 4 of State#1 (baseline), State#10 (gap = 0.20 mm), and State#14 (gap = 0.05 mm). The goal is to verify the applicability of those techniques to extract damage-sensitive features when the bumper contacts the suspended column. Note that Channel

4 was chosen because it is close to the source of damage and, consequently, its responses are more sensitive to the impacts.

The application of the STFT can be summarized as follows. First, each 8192-point acceleration time series is split into 512-point time segments with 50% overlap. Second, for each segment, a Hamming window is applied and the discrete-time Fourier transform is computed to produce an estimate of the time-varying frequency content of the signal. Finally, if a time series is representative of a stationary system, it is expected that there will be no changes in its frequency content over time. Figure 4.35, Figure 4.36, and Figure 4.37 illustrate the spectrogram (representation of the spectral density of a signal over time) for time series from Channel 4 corresponding to State#1, 10, and 14, respectively. Note that in each figure the spectrogram is plotted in time-frequency-amplitude along with time-frequency representation. Additionally, Figure 4.38 plots the concatenated format of the spectrograms, where the time domain 0-25.6 sec corresponds to the State#1, 25.6-51.2 sec to State#10, and 51.2-76.8 sec to State#14. A few observations can be made based on these spectrograms:

- (i) all three states show significant energy content around the three identified natural frequency components, at 30.7, 54.2, and 70.7 Hz (for the baseline condition), which correspond very well to the results from the analytical and experimental modal analysis results; note that the first frequency component is below 20 Hz and it is not represented as explained in Section 4.2;
- (ii) the second natural frequency component (30.7 Hz) has lower energy content than the other two natural frequencies;
- (iii) the damaged State#14 seems to distribute energy content more broadly across the spectrum by decreasing the energy at the frequency components;
- (iv) there is no significant indication that the damaged State#10 and 14 come from a non-stationary system; however, in the case of State#14, the damage seems to impose a steady increase in the natural frequencies over time when compared to the other two states.

Even though, theoretically, the stiffness of the structure should change throughout the measurement as a result of the impacts between the bumper and suspended column, the spectrograms do not clearly indicate that result. Two reasons are presented to explain it:

- (i) for low level of damage (State#10), the impacts occur relatively infrequently in time and are not sufficient to change the natural frequency components for that specific length of the moving window; however, for high level of damage (State#14), the high number of impacts makes the structure stiffer, but because many impacts occur within a given time window their effects tend to be averaged out in the spectrum estimation process and these effects are similar in every window so the system still exhibits stationary characteristics;

- (ii) the trade-off between frequency resolution and the length of the window to compute the Fourier transform can be a limitation to identify changes caused by high frequency components of short durations; the lower the length of the window in time, the poorer the frequency resolution; recall that shorter duration windows permit good time resolution but poor frequency resolution; on the other hand, longer duration windows permit good frequency resolution, but have poor time resolution.

In conclusion, the STFT analysis does not show any significant changes in the natural frequency components for the lowest damaged state (State#10). However, some minor indications of the time varying nature of the signal's frequency content can be seen for the damaged state corresponding to the most impacts (State#14), but it would be difficult to base a damage assessment on such subtle changes. Note that, within a given window, the Fourier transform represents the average properties of the signal. Furthermore, the impacts cause changes in the high-frequency components for short durations and these changes do not, in general, affect these average response properties.

As explain early in Section 3.2.7, the WT stands as an alternative approach to the well-known STFT. Therefore, in order to overcome some of the well-known frequency resolution issue with the STFT, the CWT is applied as follows. To be consistent with the previous analysis, the wavelet analysis uses the same discrete-time signals as before, i.e., the same acceleration time series from Channel 4 corresponding to State#1, 10, and 14. A complex Morlet wavelet is used to form the CWT, which consists of 143 scales. Figure 4.39, Figure 4.40, and Figure 4.41 plot the WT coefficients in both time-frequency-amplitude and time-frequency representations. The color at each point is associated with the magnitude of the WT coefficient, which represents the energy distribution of the signal. A few observations can be made based on the visual inspection of the plots:

- (i) the third and fourth natural frequency components (54.2 and 70.7 Hz for the baseline condition) are clearly observed in these plots;
- (ii) the amplitude of the WT coefficients associated with the natural frequency components at 54.2 and 70.7 Hz decrease for the damaged State#14, while other frequency components across the spectrum increase as a result of the nonlinearities associated with the impacts;
- (iii) the peaks related to the natural frequency components in Figure 4.41 for the most damaged condition (State#14) drift in frequency over time as indicated by the distribution in the higher amplitude WT coefficients at frequencies around 54.2 and 70.7 Hz; although these same bands can be seen at the lowest damage level (State#10), they are not as broad in frequency; this feature is attributed to the reduce number of impacts associated with the state condition with the lowest level of damage.

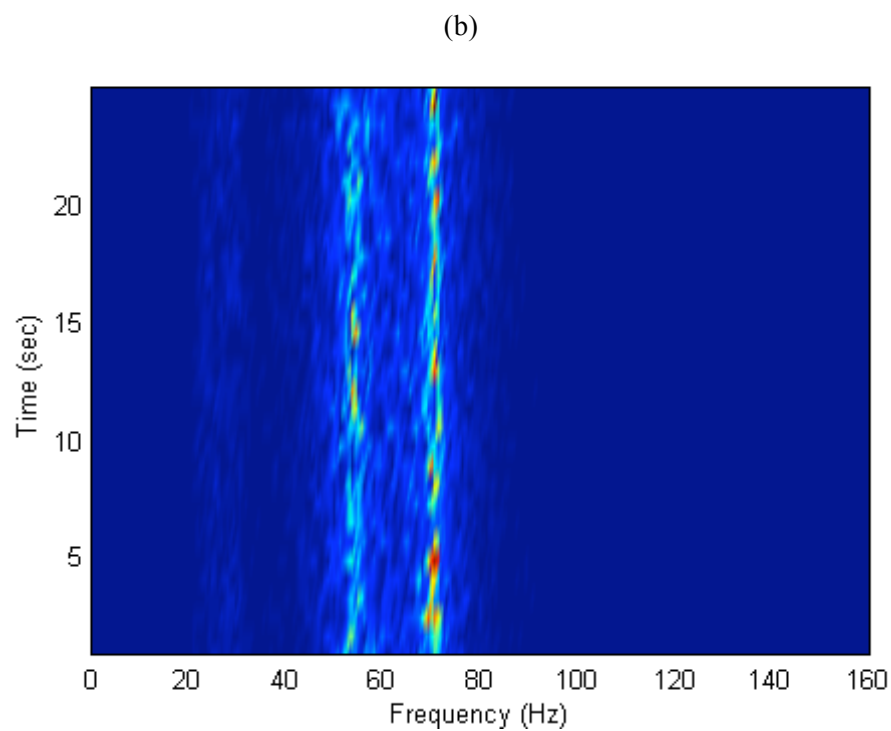
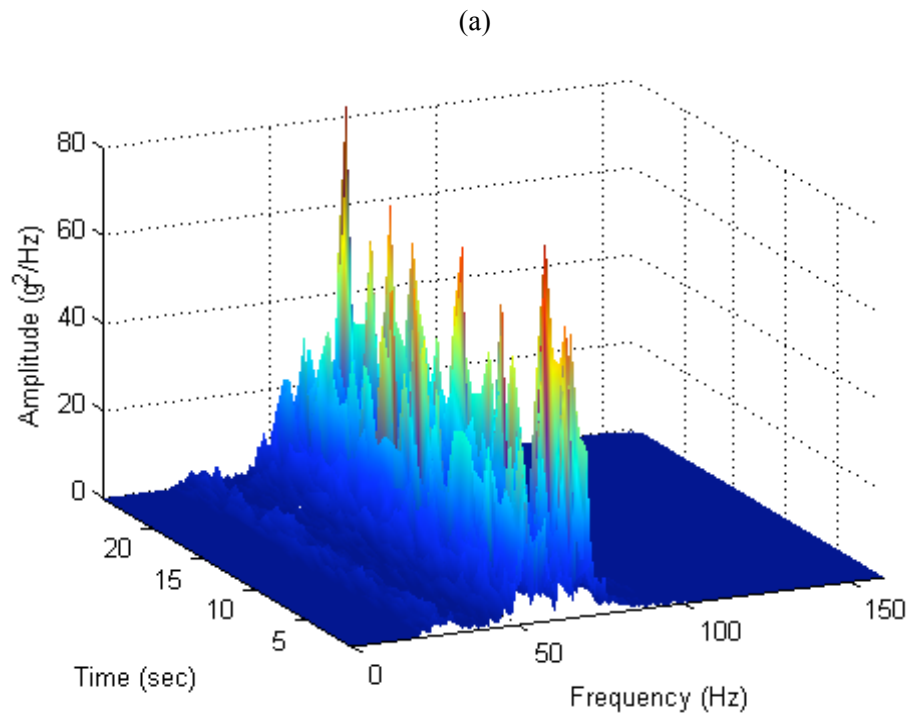


Figure 4.35. STFT analysis of signal from State#1, Channel 4: (a) time-frequency-amplitude representation; and (b) time-frequency representation.

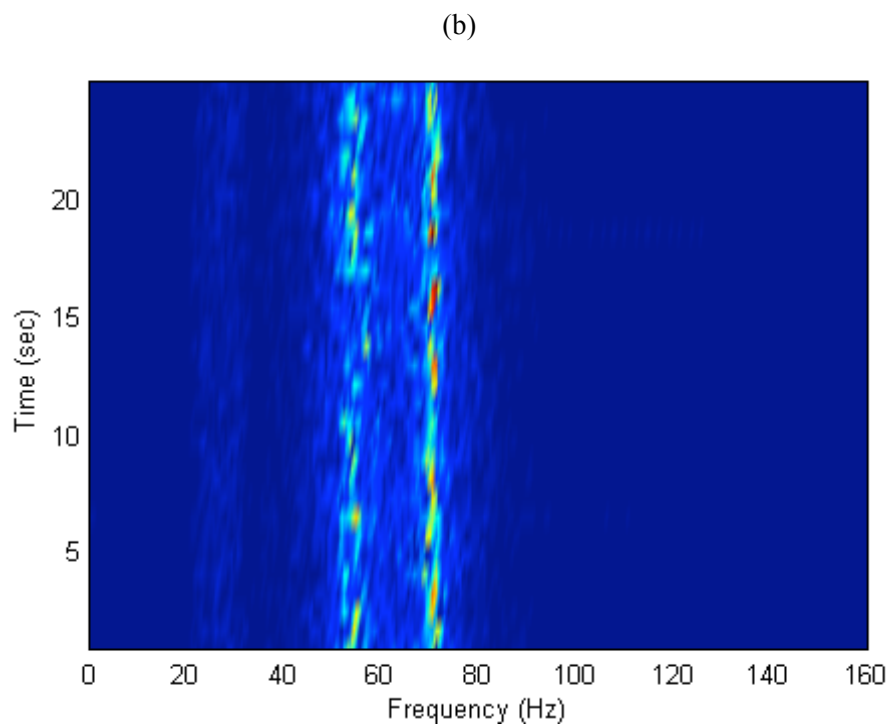
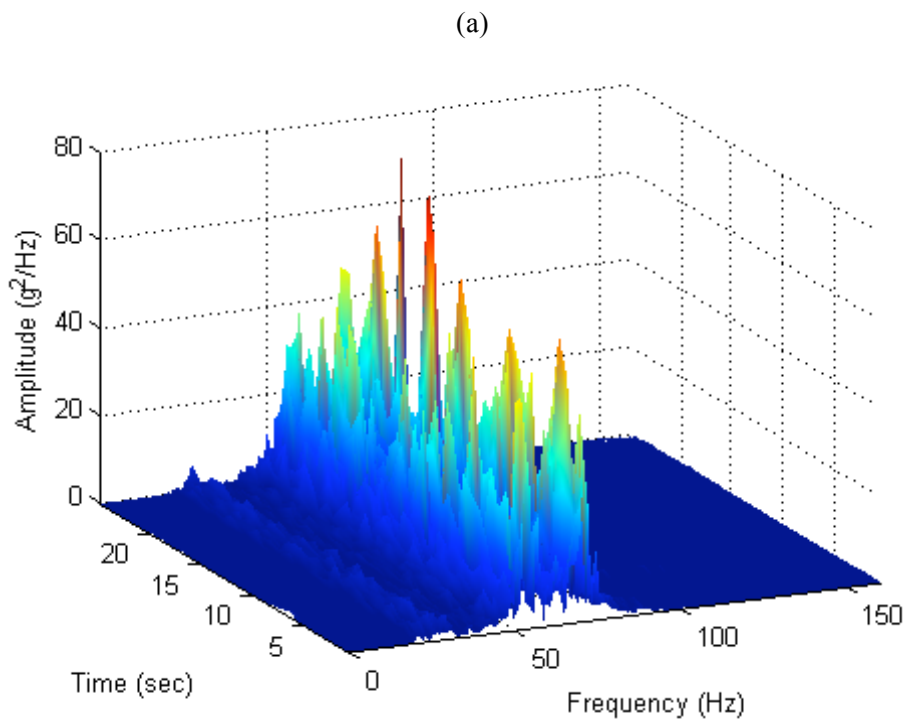


Figure 4.36. STFT analysis of signal from State#10, Channel 4: (a) time-frequency-amplitude representation; and (b) time-frequency representation.

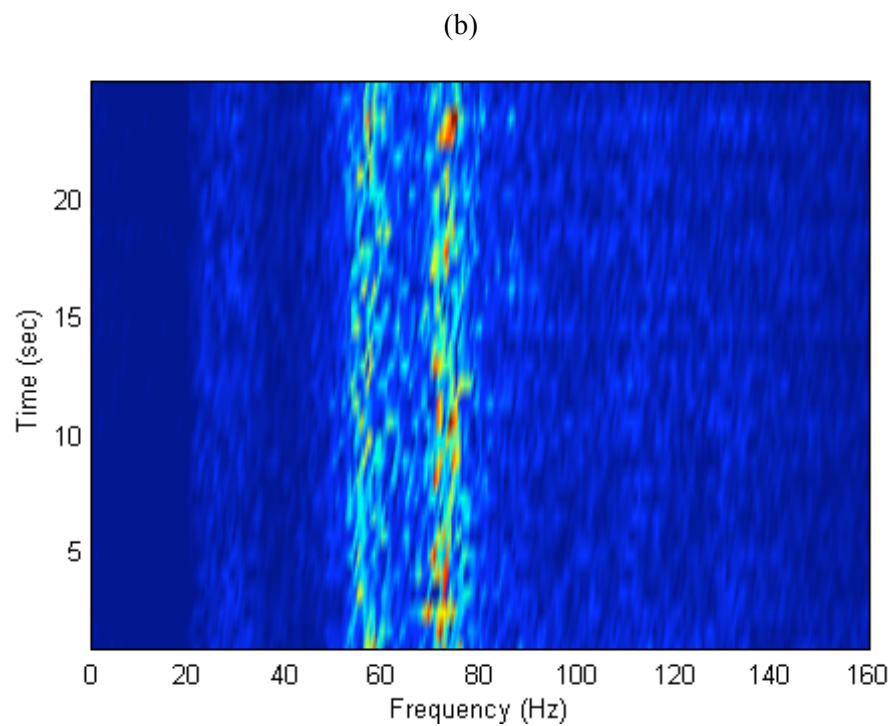
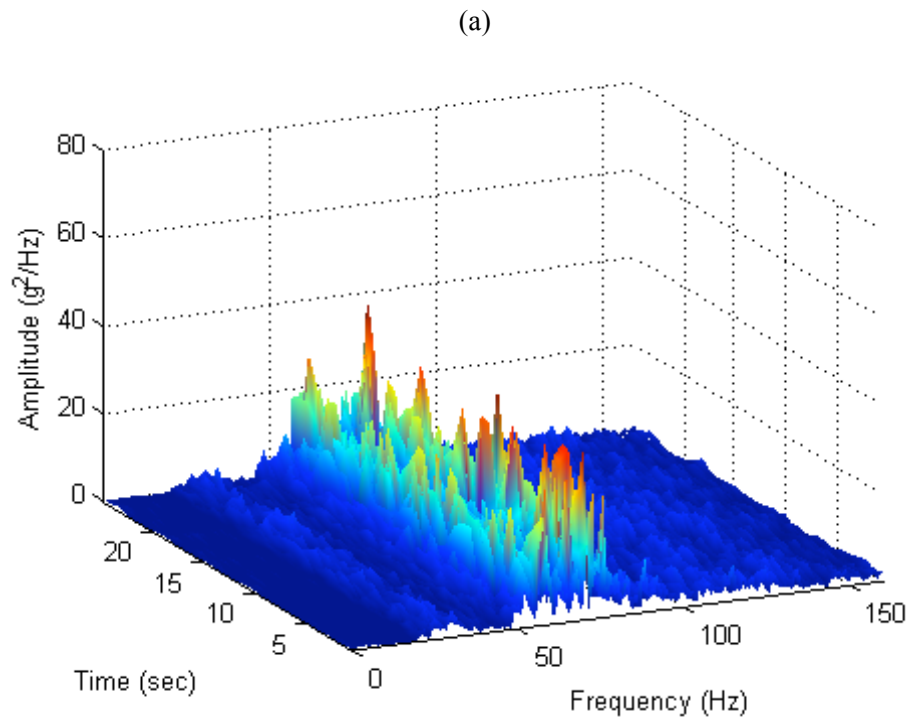


Figure 4.37. STFT analysis of signal from State#14, Channel 4: (a) time-frequency-amplitude representation; and (b) time-frequency representation.

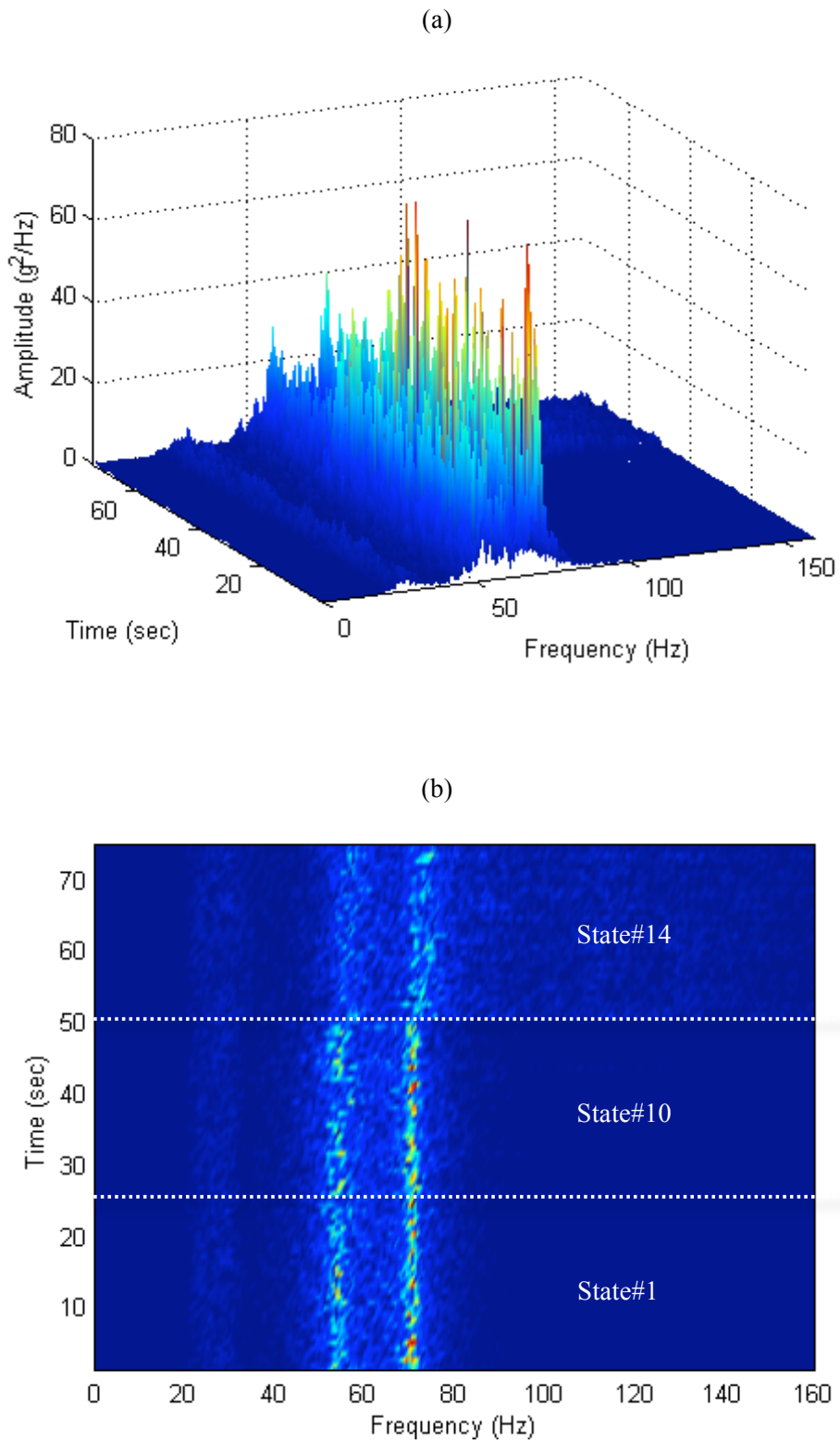


Figure 4.38. STFT analysis; individual spectrograms in concatenated format, Channel 4: (a) time-frequency-amplitude representation; and (b) time-frequency representation.

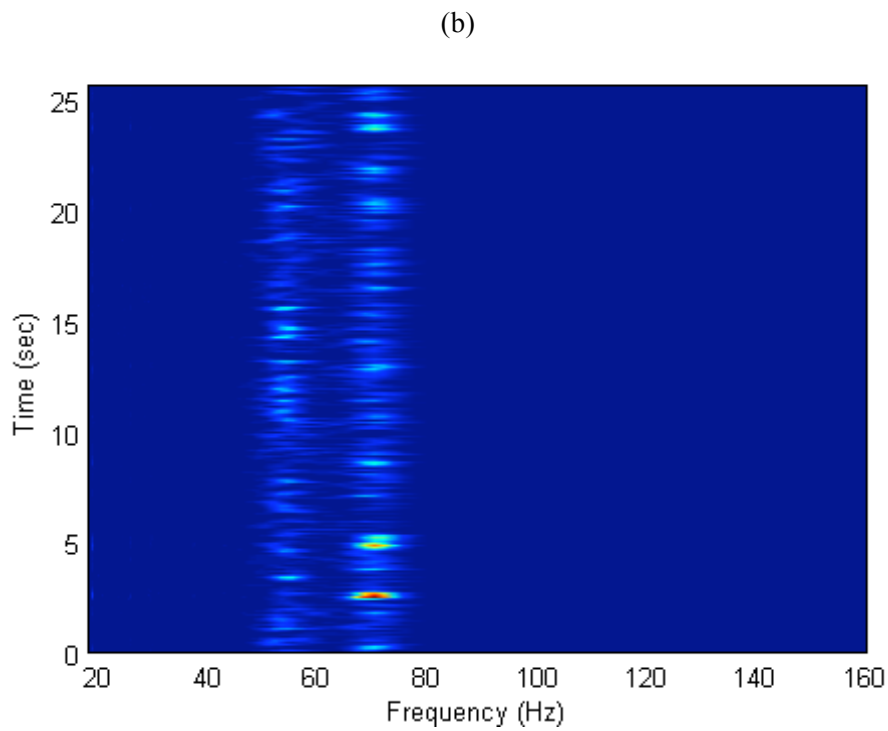
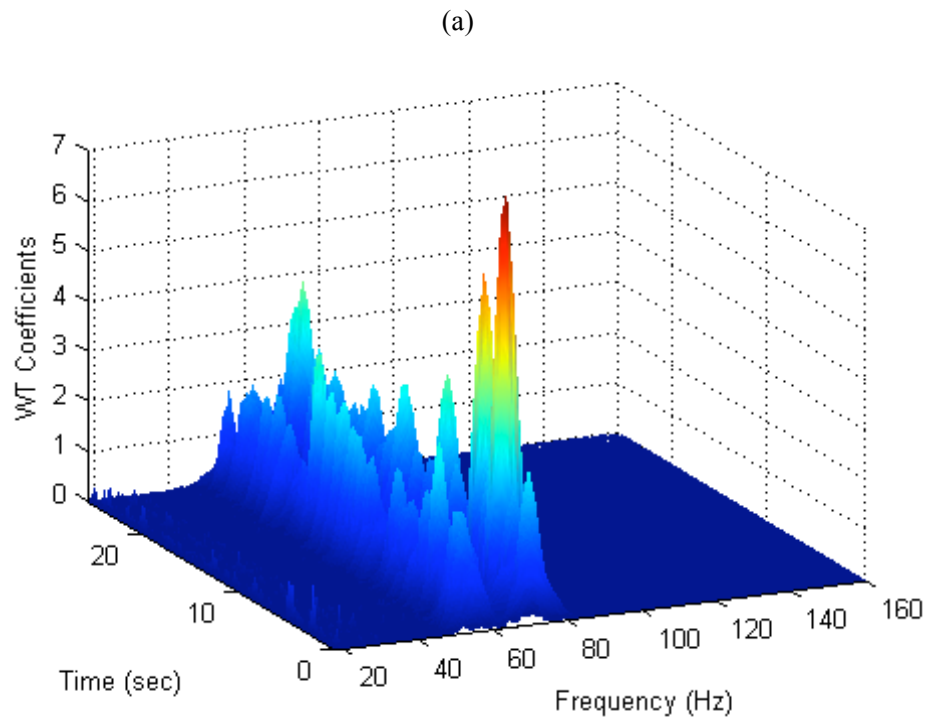


Figure 4.39. CWT of time series from State#1, Channel 4: (a) time-frequency-amplitude representation; and (b) time-frequency representation.

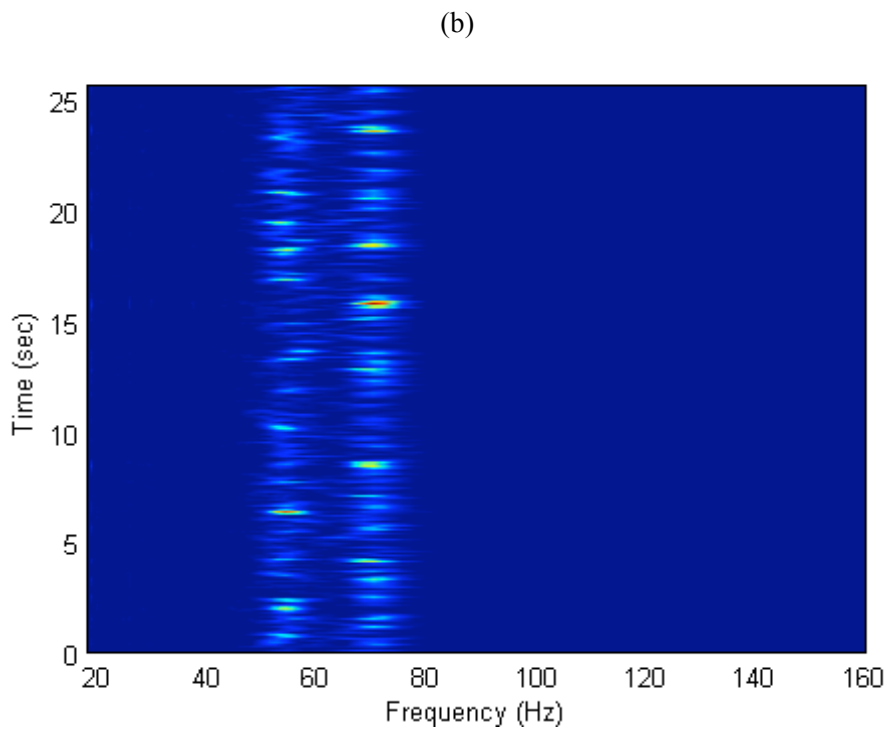
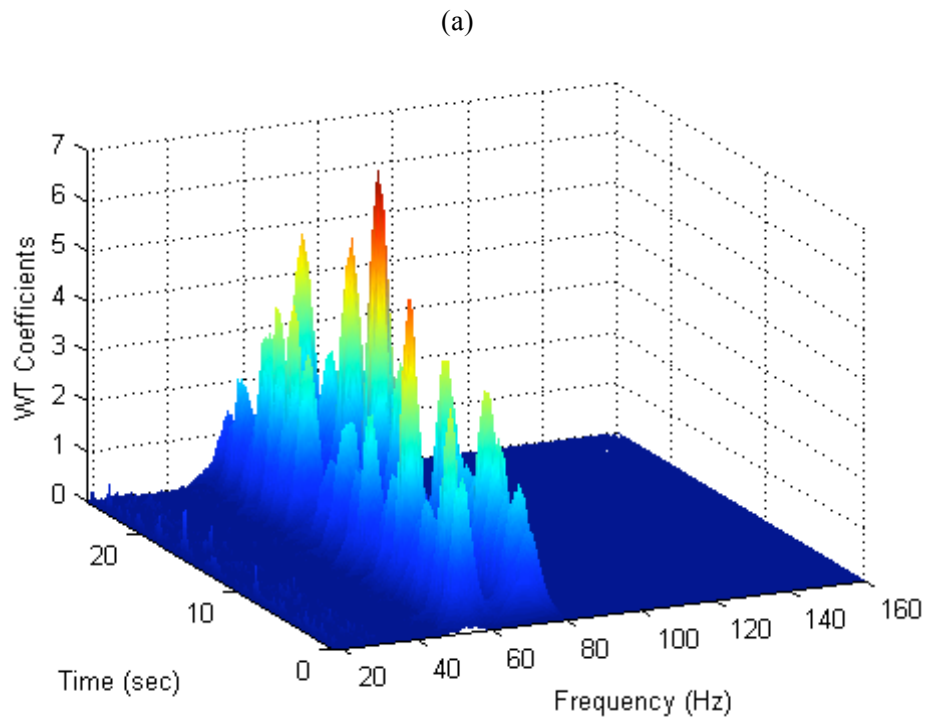


Figure 4.40. CWT of time series from State#10, Channel 4: (a) time-frequency-amplitude representation; and (b) time-frequency representation.

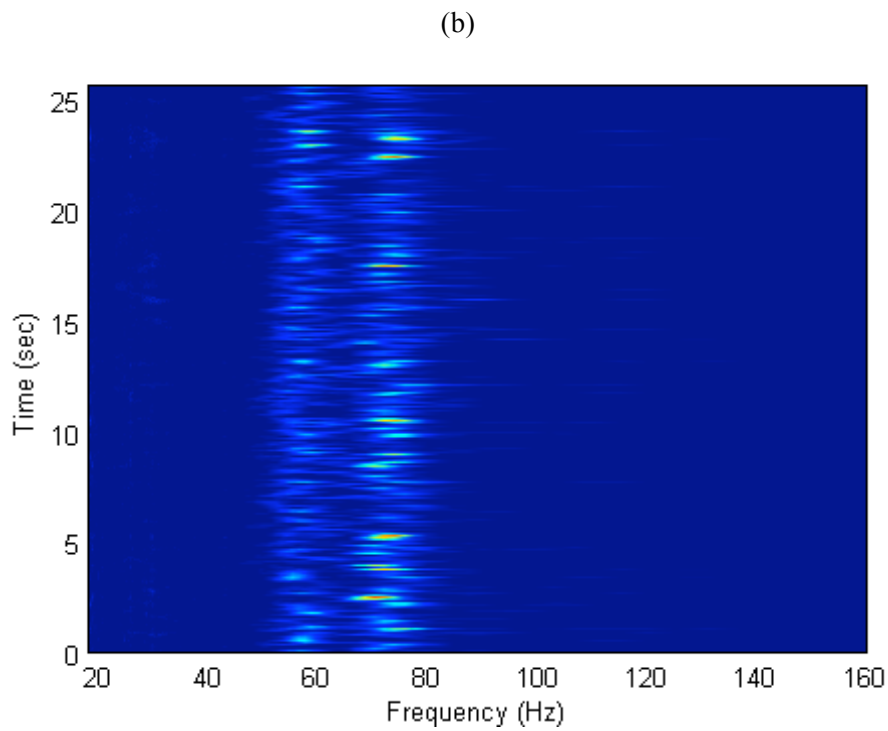
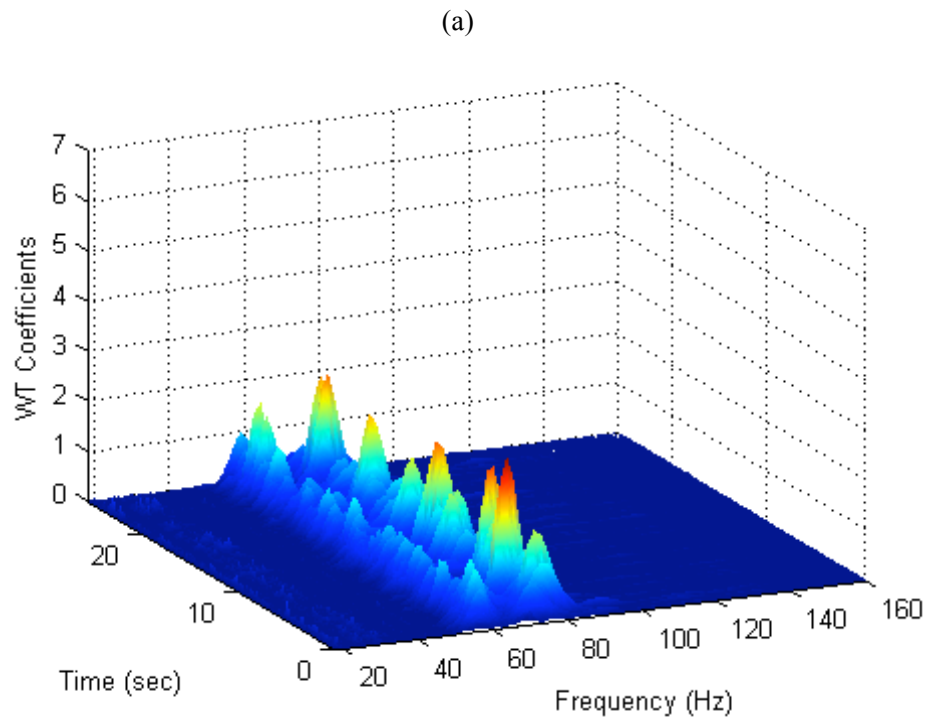


Figure 4.41. CWT of time series from State#14, Channel 4: (a) time-frequency-amplitude representation; and (b) time-frequency representation.

In order to get into details of the wavelet analysis, Figure 4.42a and b show a limited frequency bandwidth between 45 and 80 Hz from Figure 4.39 and Figure 4.41, respectively. The figures are plotted with a different scale in order to highlight changes of the frequency components over time. By looking at the time-varying nature of the peaks, there is an indication that the damaged State#14 (Figure 4.42b) corresponds to a non-stationary system because the impacts appear to cause the frequencies associated with peaks to vary in time as would be expected in a system where the stiffness alternates between two different states. Conversely, for the baseline condition (Figure 4.42a), these peaks remain relatively constant in frequency throughout the duration of the signal as would be also expected for a linear time-invariant system.

The wavelet analysis can also be used to find hidden patterns or singularities in the signal that usually last a short period of time relative to the duration of the signal. For this purpose, State#10 is used because of the reduced number of impacts between the bumper and the suspended column. (Note that for this state and when measuring the data, it was observed that the impacts occurred randomly and with no more than 10 impacts in average per time series.) As a reference, Figure 4.43a shows a time series from Channel 4 corresponding to State#10 and Figure 4.43b shows the squared AR(15) residual errors associated with the time series. (Note that the squared errors are used just to amplify the presence of singularities.) The spikes correspond to singularities imposed by the impacts that the AR(15) model cannot predict. On the other hand, singularities in the time series can also be identified by the presence of modulus maxima of the WT coefficients at specific frequency through their evolution along the time axis. For comparison, Figure 4.44 corresponds to the limited frequency bandwidth between 45 and 80 Hz in time-frequency representation of the Figure 4.40. The impacts can be identified in Figure 4.44 by comparing the spikes with those in Figure 4.43b. Moreover, one can observe that those impacts are more correlated in time with the third natural frequency component (54.2 Hz for baseline condition), suggesting that the bumper's impacts most influence the third mode. However, it should be pointed out that there is not a direct one-to-one correlation between peaks in the residual error plot and the modulus of the WT coefficients, indicating a need to validate these features with more information about the true number of impacts.

In conclusion, the CWT confirmed some of the observations made with the STFT analysis about the non-stationary nature of the response corresponding to the most damaged condition (State#14). However, even though theoretically the CWT has better time resolution at higher frequencies than the STFT, it does not have the resolution in time to clearly establish that the lower level of damaged state (State#10) corresponds to a non-stationary system. Although the results do not allow one to conclude that State#10 is from a non-stationary system, the CWT did reveal changes in the WT coefficients that can be correlated with the bumper's impacts when compared to changes in the residual errors of an AR model.

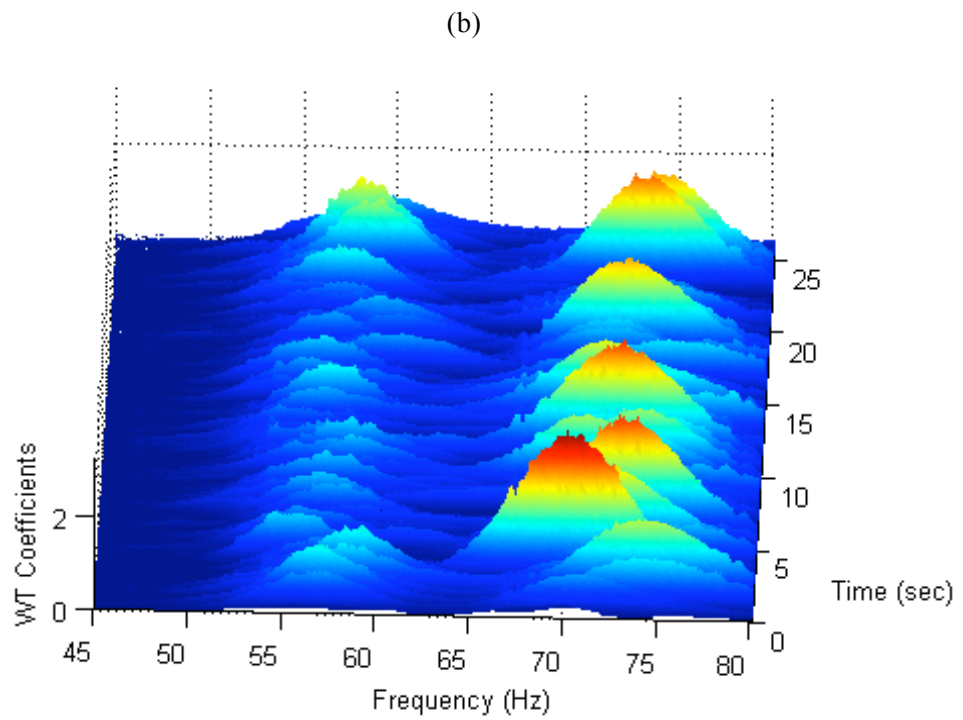
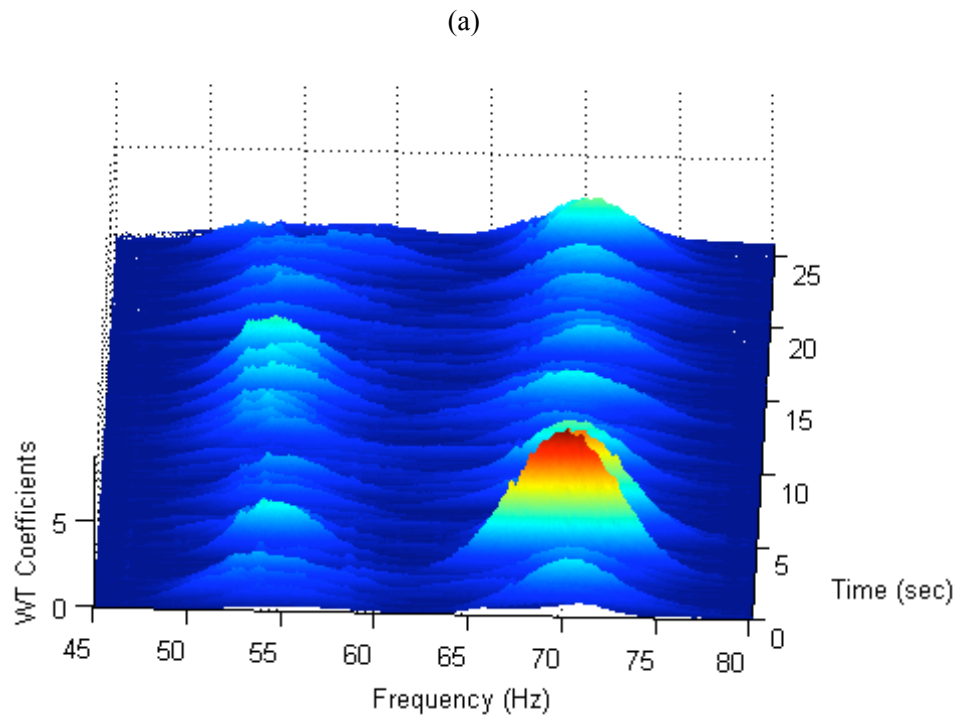


Figure 4.42. Details of the WT coefficients based on time series from Channel 4 for: (a) State#1; and (b) State#14.

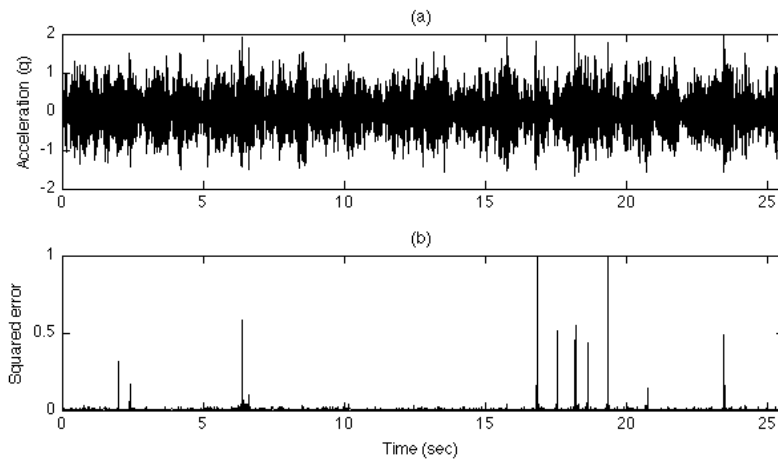


Figure 4.43. Detection of singularities: (a) original entire time series from Channel 4 of State#10; and (b) AR(15) residual errors.

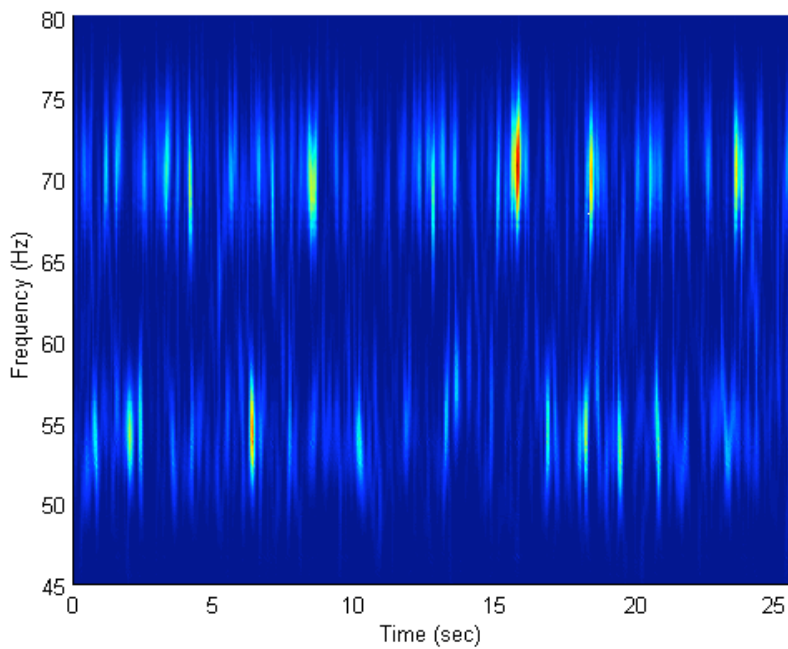


Figure 4.44. WT of the time series from State#10, Channel 4.

4.5.5 Holder Exponent

The development of techniques to detect singularities is important to detect damage in the form of discontinuities in the signal. Therefore, herein the Holder exponent is used to identify discontinuities in the time series imposed by the bumper mechanism. Figure 4.45a plots a portion of the time series from Channel 4 of State#10, previously plotted in Figure 4.43a. Note that indications of impacts

cannot be seen in that figure. However, the Holder exponent function plotted in Figure 4.45b shows significant drops that might be related to impacts imposed by the bumper. Although the drops in the Holder exponent function are fairly apparent to the naked eye, identification of them using a linear threshold is difficult because of the considerable variability associated with the Holder exponent. Additionally, recall from Figure 4.43b that also the AR(15) residual errors might be used to identify discontinuities. Thus, Figure 4.45c, d, and e plot the same portion of the AR(5), AR(15), and AR(30) residual error data, respectively. The circles mark the significant drops in Holder exponent values and the corresponding spikes in the AR residual errors associated with potential impacts.

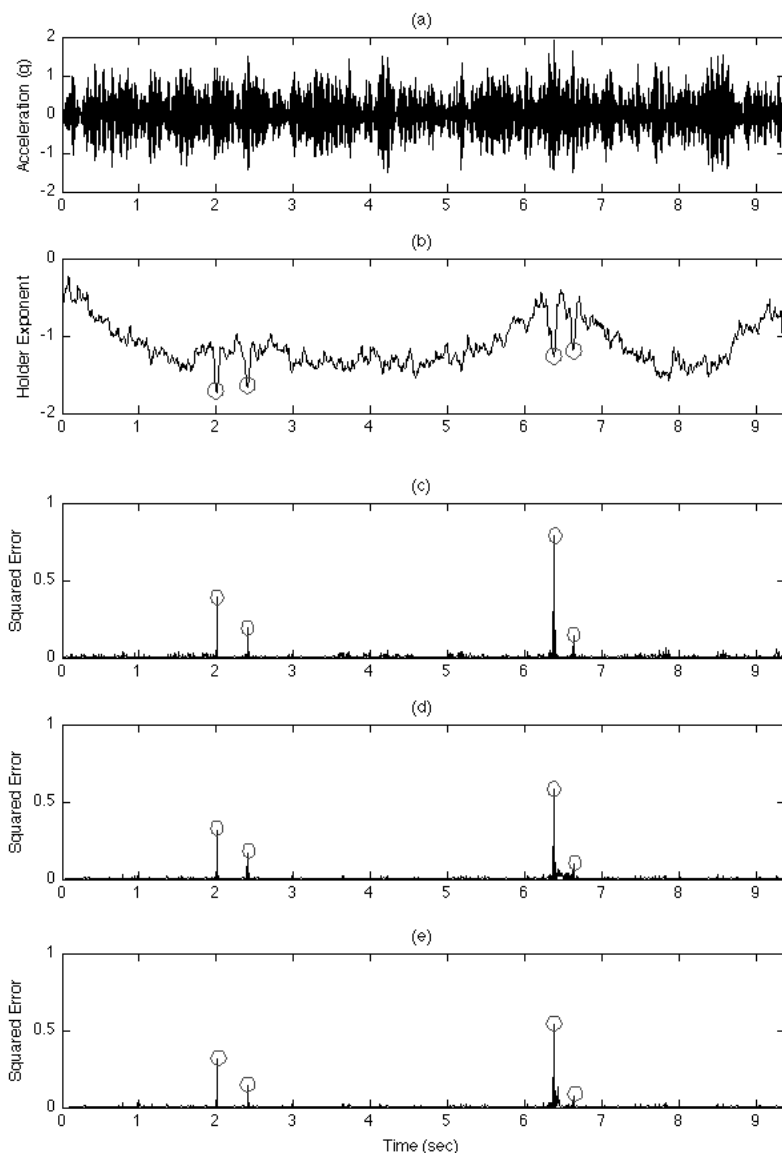


Figure 4.45. Singularity detection at Channel 4 using on time series from State#10: (a) portion of the time series; (b) Holder exponent function; (c) AR(5) residual errors; (d) AR(15) residual errors; and (e) AR(30) residual errors.

In conclusion, the Holder exponent technique proved that it might be useful to extract damage-sensitive features when damage introduces discontinuities into the measured dynamic response data. Moreover, considering the previous conclusions from the time-frequency analysis, the Holder exponent and AR residual error results showed that the impacts are better detected with a time domain approach as opposed to a frequency domain approach. The time-frequency domain approaches do not have sufficient time resolution to capture an individual impact and, as such, these effects tend to be treated only in an average sense with these methods.

4.5.6 Principal Component Analysis

The PCA have been extensively used for feature extraction and/or visualization. Herein, the PCA is used to discriminate, visually, the undamaged and damaged state conditions in the transformed feature space using, for each state condition, a feature vector composed of AR parameters estimated from one time series of Channel 5. Basically, the PCA performs a feature dimension reduction by mapping a multidimensional (original) space into a (transformed) space of fewer dimensions. Basically, the PCA is used to map feature vectors of dimension p into two- and three-dimensional Euclidean spaces.

Figure 4.46 to Figure 4.48 show the projection of the AR(5), AR(15), and AR(30) parameters (scores) onto the first two and three principal components. Although all projections seem to identify two main clusters for the undamaged and damaged conditions, the AR(15) and AR(30) parameters clearly allows one to define a hyperplane capable of discriminating all the undamaged and damaged state conditions. Actually, these results confirm the previous conclusions in 4.5.3.1 carried out to define the optimal AR model order.

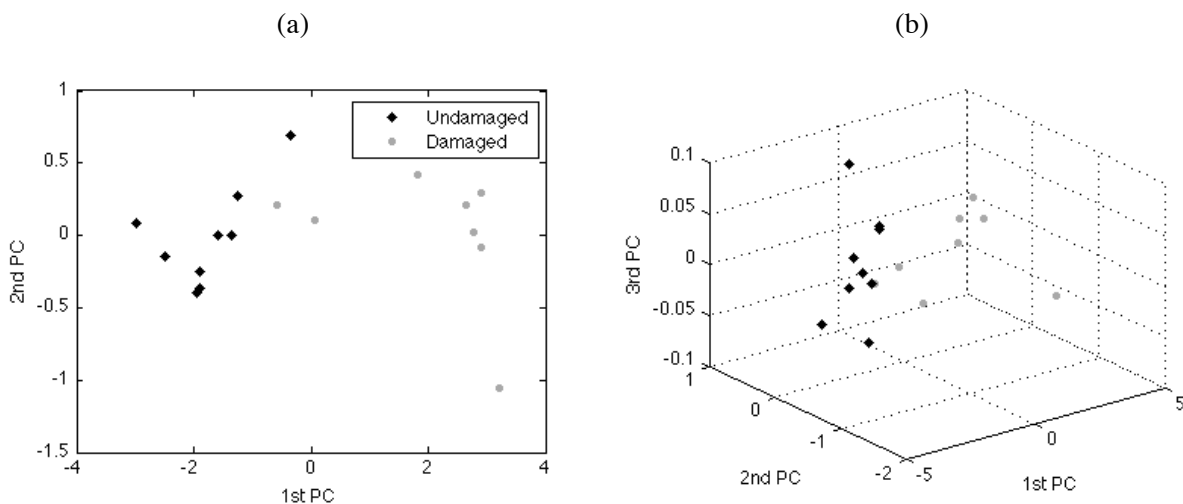


Figure 4.46. Projection of the AR(5) parameters onto the first: (a) two; and (b) three principal components.

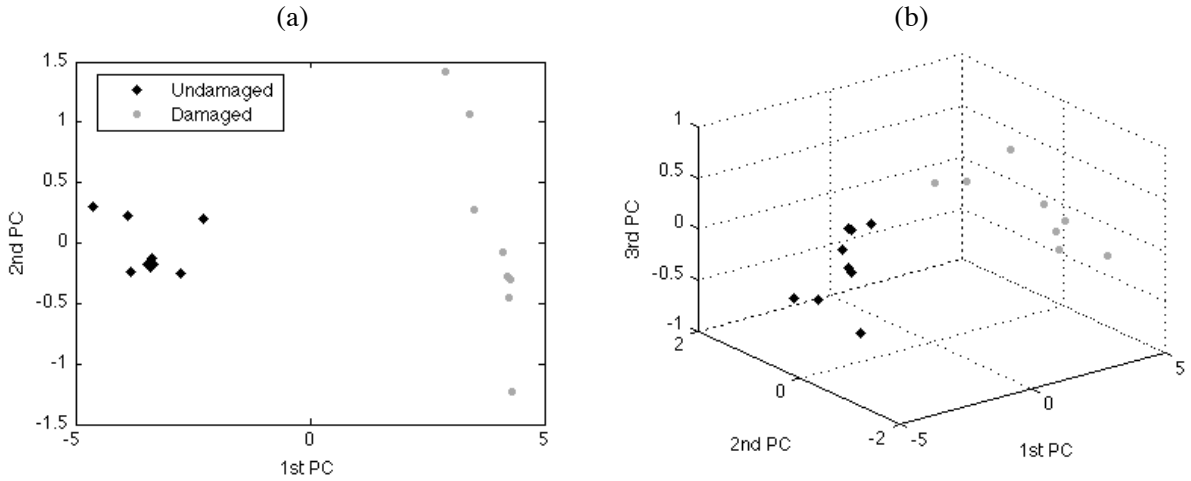


Figure 4.47. Projection of the AR(15) parameters onto the first: (a) two; and (b) three principal components.

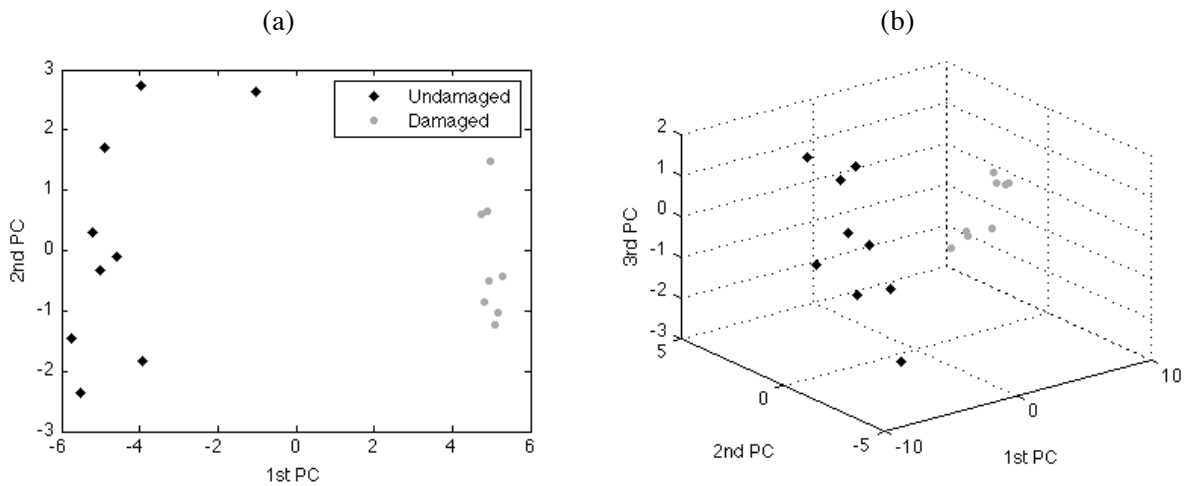


Figure 4.48. Projection of the AR(30) parameters onto the first: (a) two; and (b) three principal components.

4.5.7 Correlation Coefficients

For all time series from one test of the baseline condition (State#1), Figure 4.49 plots the correlation coefficients between Channel 1 and Channel 1-5 using Equation (3.40) along with correlation coefficients between Channel 5 and Channel 1-5. Clearly, for the former case, the figure shows that the correlation is proportional to the distance between channels, i.e., the longer the distance between Channel 1 and the remainder channels, the lower the correlation coefficient. On the other hand, for the later case, the figure highlights strong anti-correlation between Channel 5 and 4.

After understanding how the correlation varies throughout the structure for the baseline condition, the next analysis verifies if the correlation between channels can be used as a reliable damage-sensitive feature. In order to investigate possible significant correlation changes between channels when damage is present, Figure 4.50 shows the correlation coefficients between Channel 5 and Channels 1-5

using time series from one test of each of the 17 state condition. Based on the figure, one can conclude that the correlation coefficients are not able to discriminate the undamaged and damaged states or to locate the damage among the sensors, because the coefficients follow no systematic pattern that can be associated with the damaged states. Indeed, this result might be justified by considering the nature of the impacts imposed by the bumper. Notice that the impacts manifest themselves as a local phenomenon in time, which it is not enough to produce trends in the time series that can be identified by a global damage-sensitive feature such as the correlation coefficient.

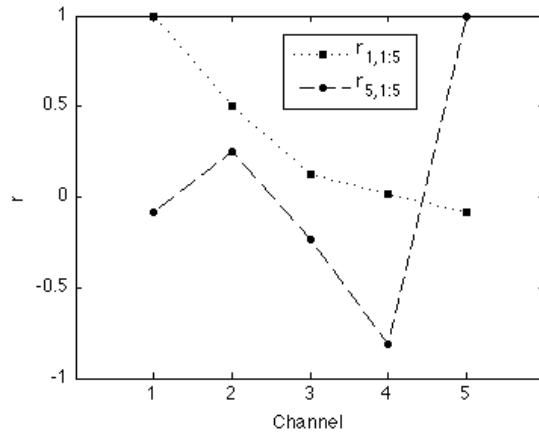


Figure 4.49. Correlation coefficients between Channel 1 and Channel 1-5 ($r_{1,1:5}$) along with correlation coefficients between Channel 5 and Channel 1-5 ($r_{5,1:5}$).

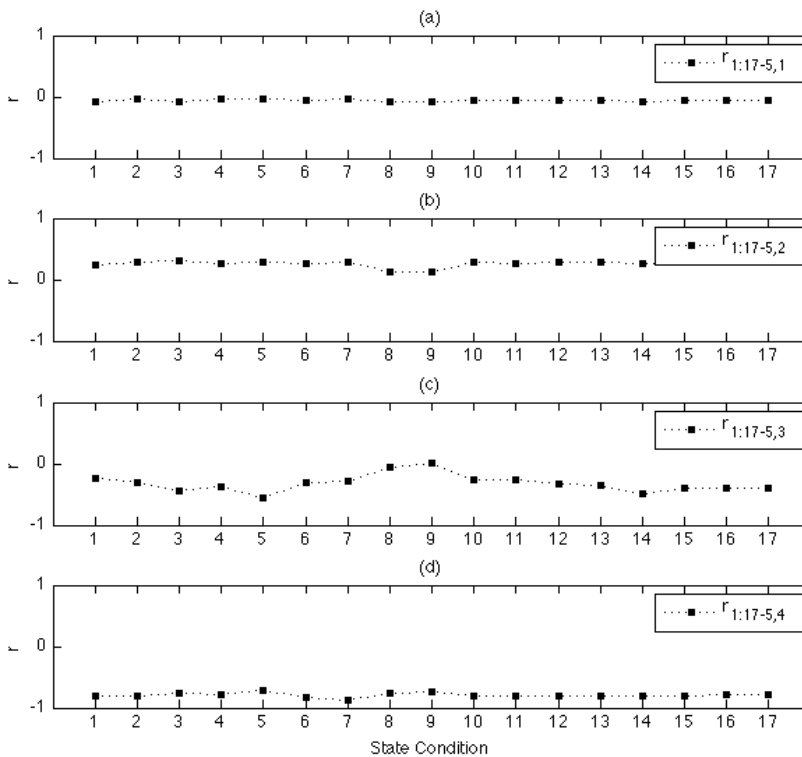


Figure 4.50. Correlation coefficients of pair of channels for all state conditions (State#1-17): (a) Channel 5 and 1; (b) Channel 5 and 2; (c) Channel 5 and 3; and (d) Channel 5 and 4.

4.6 Statistical Modeling for Feature Classification

In Chapter 1 statistical modeling for feature classification was posed as the portion of the SHM-SPR paradigm that has received the least attention in the technical literature. It was also mentioned that this step of the paradigm is concerned with the implementation of algorithms that analyze the distributions of the extracted features in an effort to determine the structural condition. Additionally, it was outlined the existence of three general categories of algorithms: (i) group classification; (ii) regression analysis; and (iii) outlier detection. However, in this section, only the first and third categories of algorithms are used. Note that all the algorithms are applied in unsupervised learning mode. Actually, these algorithms are preferred for high capital expenditure structures, such as most civil infrastructure, because often only data from the undamaged condition are available.

The cluster analysis is applied as a classical binary classification algorithm to discriminate the undamaged and damaged conditions. Note that even though this algorithm groups the data into two clusters, it is still considered an unsupervised learning algorithm because no underlying information regarding the state conditions is given when performing the analysis. Rather, the algorithm only groups the structural conditions based on the similarity of their associated feature vectors. The Shewhart X-bar control charts are applied to monitor deviations from the baseline condition. Additionally, a brief study shows how the control limits can encode the operational and environmental variations. Note that, herein, baseline refers to the condition without any operational and environmental effects. Afterwards, the performance of the novel feature extraction algorithm based on the state-space reconstruction is tested in the context of outlier detection, with the assumption that damage significantly changes the attractor of a dynamical system. In another study, the four machine learning algorithms outlined in Section 3.3 for data normalization are directly compared on the standard data sets based on the performance for outlier detection. These vibration-based algorithms are applied to create a global structural DI that is almost invariant under operational and environmental variations and sensitive to data acquired from the damaged condition. Finally, it was shown in Section 3.3 that under certain assumptions, DIs derived from the MSD-based algorithm follow a chi-square distribution when feature vectors come from the undamaged condition. Thus, a study is also carried out to show the classification performance of this algorithm on AR parameters extracted from the standard data sets under the hypothesis test that the algorithm will reject the null hypothesis (undamaged condition) if a DI does not follow a central chi-square distribution. Additionally, while the algorithm is constructed assuming multi-dimensional Gaussian distributed features, this study addresses how underlying non-Gaussian-distributed damage-sensitive features affect the results of the MSD-based algorithm and it also draws a relation between the classification performance and the optimal AR model order given by an information criterion technique.

Notice that in order to increase the statistical significance of the classification performance, for the same state conditions, in 2009 a new data set (*DataSet2009*) was acquired from the three-story

structure. However, in this case, a National Instruments (NI) PXI data acquisition system was used to collect and process the data. Analog output waveforms were generated using a PXI-4461 data acquisition module and the response signals from the five sensors were acquired using a PXI-4472B data acquisition module. A PCB 482A16 signal conditioner provided ICP conditioning to the five sensor channels. Furthermore, for each structural state condition, data were acquired from 50 separate tests instead of the 10 tests of the first data set (*DataSet2007*) collected in 2007. Therefore, all the algorithms present in this section make use of the data sets collected in 2009, with the exception of cluster analysis that was used to point out differences between those data sets. Note, however, that the data from 2009 shares the same underlying characteristics of the data from 2007.

4.6.1 Cluster Analysis

Herein the cluster analysis is used as a statistical modeling algorithm to classify the undamaged and damaged state conditions into two clusters. For the data collected in 2007, Figure 4.51 plots the binary classification for all state conditions using the AR(15) parameters extracted from times series of Channel 5 as damage-sensitive features. The Euclidean distance is the metric used to determine the similarity of the AR parameter vectors. As shown in the figure, this technique can correctly classify all the state conditions. Furthermore, Figure 4.52 plots the hierarchical cluster tree, where the states are paired into binary clusters by proximity until a hierarchical tree is formed. One can clearly observe that until the clustering reaches the top of the tree, the states are progressively grouped into two main clusters: undamaged and damaged conditions. Observe that the height of the clusters above the origin represents the Euclidean distance between the centroids of two clusters. This representation is also useful to find similarity properties among state conditions. For instance, the figure shows that State#10 and 16 are grouped together at the first level. This result is actually expected because the gap between the bumper and suspended column was set to the same value.

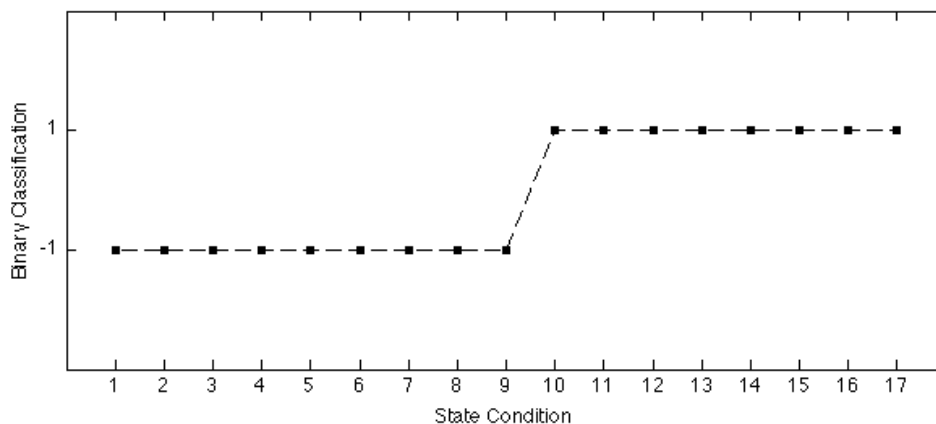


Figure 4.51. Binary classification (undamaged and damaged conditions) using AR(15) parameters from one time series of each state condition at Channel 5 (*DataSet2007*).

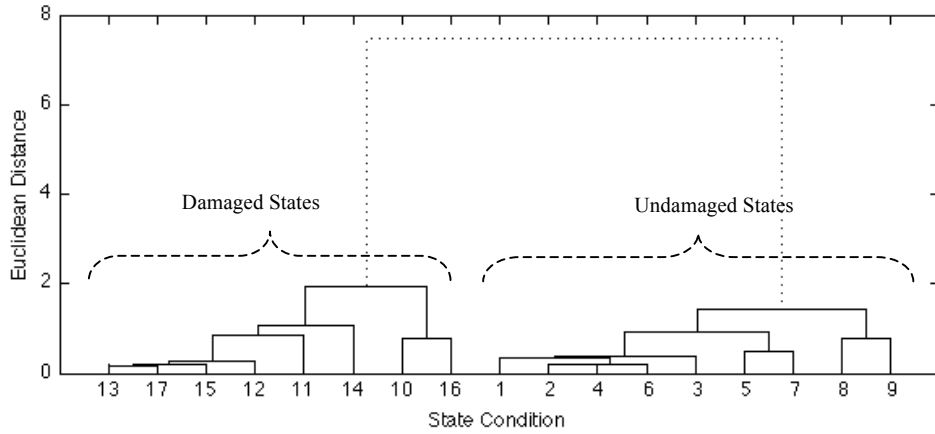


Figure 4.52. Cluster tree of the state conditions in Figure 4.51 (*DataSet2007*).

The previous cluster analysis was performed on the data sets collected in 2007. In order to evaluate the performance of this algorithm on the data collected in 2009 (*DataSet2009*), Figure 4.53 and Figure 4.54 plot the results of the cluster analysis. These figures clearly show that the algorithm has three misclassifications, namely State#10, 15, and 16. Note that those three states have in common the same gap (0.20 mm) between the bumper and suspended column. Indeed, it was verified the consistency of those results among other tests of each state condition. (This is an indication that the stationary property of the 2007 data described in Section 4.4 is still valid for the new data sets.) Based on these observations, two explanations can be pointed out: (i) the 0.20 mm gap is characterized by few impacts, and so, its influence is averaged out on the AR parameters estimation; (ii) the mechanism to set up the gap distance is not precise, and so, there is variability during the experiment that can cause slightly smaller or higher gaps than the selected ones. So, the number of random impacts per time series is the major difference between both data sets. Consequently, that difference is more relevant in the states with larger gaps and reduced number of impacts per time series. This fact provides a challenge to the damage detection process when applied to data from those states.

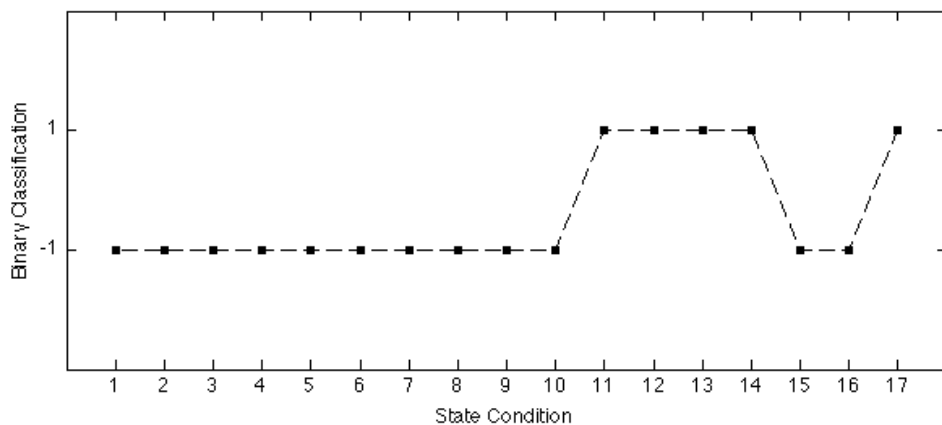


Figure 4.53. Binary classification (undamaged and damaged conditions) using AR(15) parameters from one time series of each state condition at Channel 5 (*DataSet2009*).

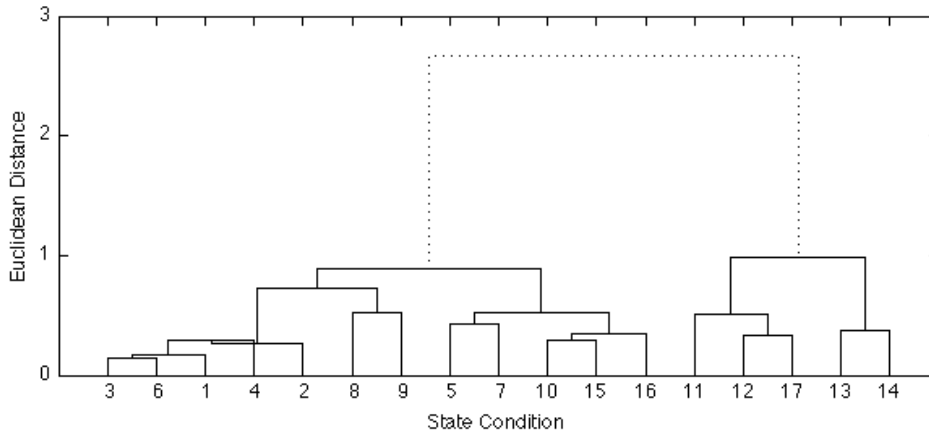


Figure 4.54. Cluster tree of the state conditions in Figure 4.53 (*DataSet2009*).

4.6.2 Statistical Process Control

The SPC techniques are useful ways to monitor processes and detect deviations from the baseline condition. In this case, the process is defined by the dynamic response characteristics of the test structure and it is expected that damage (the nonlinearities) will produce changes in the system's responses that can be identified as abnormal points in the control charts. Actually, it is expected that an out-of-control process manifests itself with changes in the mean and/or variance of time series.

However, control charts can lead to many false alarms when the observations are not independent and positively correlated [99]. Unfortunately, the assumption of independent and uncorrelated observations is not valid for the measured acceleration data, as shown in Figure 4.25a. The auto-correlation shown for the baseline condition (State#1) is certainly large enough to affect the efficacy of control charts. Therefore, the performance of the control charts can be improved when data from the observed process, and when in control, are normally and independently distributed.

One approach for dealing with auto-correlated data is to first model the data using time series models, for instance the AR models, and then to apply the control charts to the AR residual errors between the predicted and measured data (the first approach described in Section 3.2.3). This approach assumes that the residual errors are normally and independently distributed with zero mean and standard deviation σ . For instance, Figure 4.24b shows that after fitting an AR(15) model to a time series from Channel 5 of State#1, and using that model to predict the same time series, the associated AR residual errors have practically no correlation as indicated by a flat PSD. However, two final remarks are made regarding the correlation among the residual errors. First, even though there is no correlation among the residual errors associated with the AR(15) model, the same is not valid for the AR(5) model, as highlighted in Figure 4.24a. This result is an indication that the AR(15) model should have fewer outliers for the undamaged states. Second, the correlation highlighted, in the ACFs and lag plots in Figure 4.26b and Figure 4.29, shows high degree of correlation in the residual errors from the damaged states. This correlation implies that the impacts introduce some kind of pattern in the

response that can make the process appear to be out-of-control and, consequently, it can potentially increase the outlier detection performance.

To verify the performance of this statistical modeling technique for feature classification, the Shewhart X-bar control charts are constructed based on the residual errors of Channel 5 derived from an AR(15) model. The order of the model is chosen based on the assumption that the 15th order is equal to the lower bound given by the model order estimation techniques (see Section 4.5.3.1). For completeness, and as outlined in Section 3.4.2, the implementation of this algorithm can be summarized as follows. First AR parameters are estimated by fitting an AR(15) model to an acceleration time series from Channel 5 of the baseline condition (State#1). For each state condition, an AR model with parameters from the baseline condition is used to compute the residual errors between the predicted and the measured time series. Then, the residual errors are reorganized into subgroups of four. Note that subgroups of four or five data points each are recommended [99]. Prior to dividing the residuals into subgroups, they are normalized by subtracting the mean and dividing by the standard deviation of the residuals from the baseline condition. This normalization procedure is applied to all residual error data sets that are analyzed. (See *Dimension Reduction of the Residual Errors* in Section 4.5.3.2 for more details.) Second, the upper and lower control chart limits are calculated based on the sample mean and standard deviation of the baseline condition. Third, an X-bar control chart is constructed for each state condition with the subgroups of residual errors as inputs. Note that each subgroup is represented by one data point and the centerline of the charts is zero because the sample mean of the associated normalized residual errors is zero, as described above. The upper and lower control chart limits correspond to 99.73% confidence intervals, implying that approximately 0.27% of the data points from the baseline condition can be expected to fall outside the control limits. Therefore, for 2046 data points, about six points should fall outside of those limits.

Figure 4.55 plots the Shewhart X-bar control charts for all 17 state conditions using the grouped AR(15) residual errors. The figure suggests a high density of outliers among the most damaged state conditions. Additionally, Figure 4.56 summarizes the number of outliers falling beyond the control limits. Even though the limits are established based on State#1, taking as reference the horizontal dashed line set up based on the maximum number of outliers present among the undamaged states (State#1-9), which in this case is conditioned by State#5, one can conclude that this algorithm does not have enough sensitivity to discriminate those states with 0.20 mm gap between the suspended column and bumper (State#10, 15, and 16). Nevertheless, for the baseline condition (State#1), four outliers are counted beyond the control limits, which is close to the six points expected by the confidence interval. This result gives an indication that the classifier performs relatively well based on the data used to represent the process when it is thought to be in-control.

Notice that the previous analysis just used one time series from the baseline condition to establish the control limits. The following analysis takes into account time series from all the undamaged state

conditions to define those limits, i.e. the control limits are defined based on the average of the standard deviation from each undamaged state condition. Thus, the control limits encode information from all the operational and environmental conditions. Actually, as shown in Figure 4.57, this procedure permits one to reduce the overall number of outliers among the undamaged state conditions. However, the average number of outliers among the undamaged conditions (13 outliers) is slightly higher than the expected by the confidence interval (six outliers). Moreover, taking the dash line as reference, as described before, the number of outliers in the State#15 is higher than the maximum observed among the undamaged state conditions. This result clearly represents a trade-off between true detection and false alarm. Therefore, these results also highlight the applicability of this algorithm to detect damage under operational and environmental conditions as will be discussed later in the Section 4.6.4 and 4.6.5.

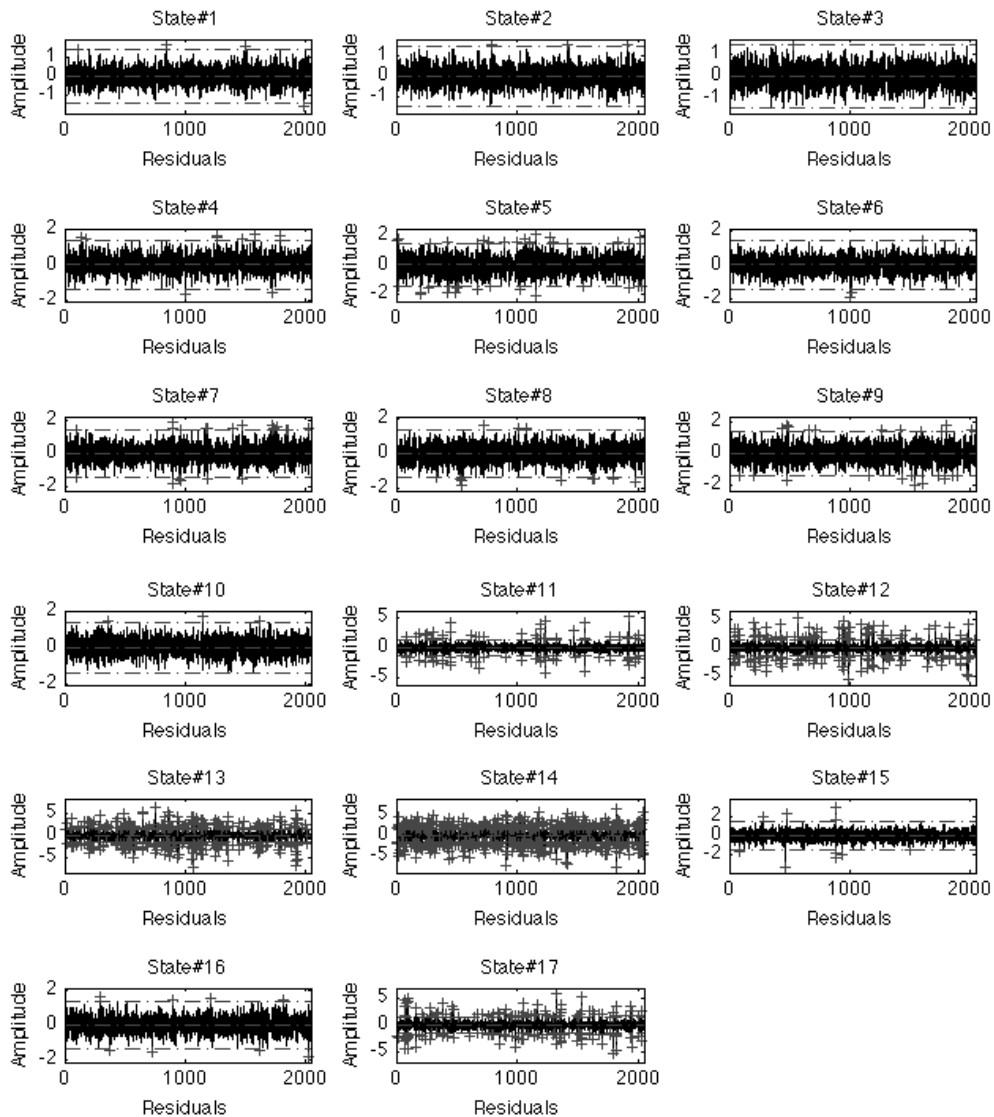


Figure 4.55. The Shewhart X-Bar control charts of the mean of the grouped AR(15) residual errors; outliers are represented by crosses.

Notice that there is still the possibility of all the points falling within the control limits but the process is not in control. This case occurs when the points exhibit some sort of systematic behavior, i.e., data points assume a non-random pattern. There are several common non-random patterns that indicate the process is out of control as documented in the references [99].

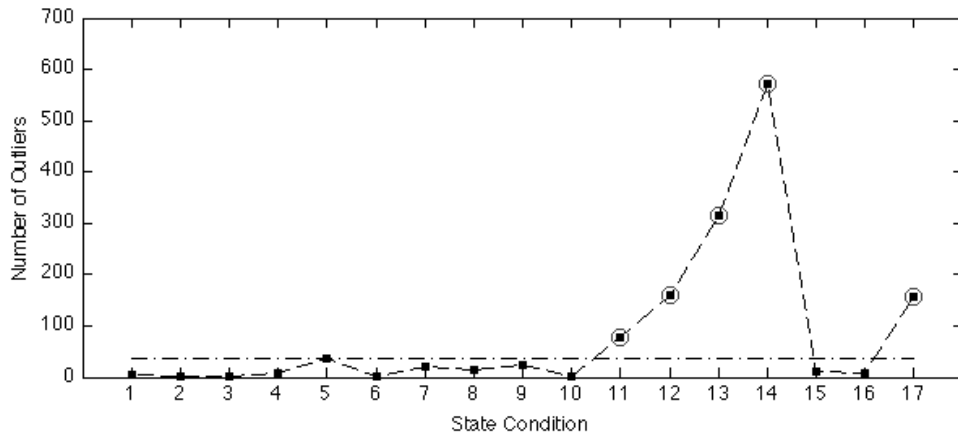


Figure 4.56. Number of outliers falling outside the control limits defined based on data from the baseline condition (State#1); the horizontal dashed line corresponds to the maximum number of outliers among the undamaged states (State#5).

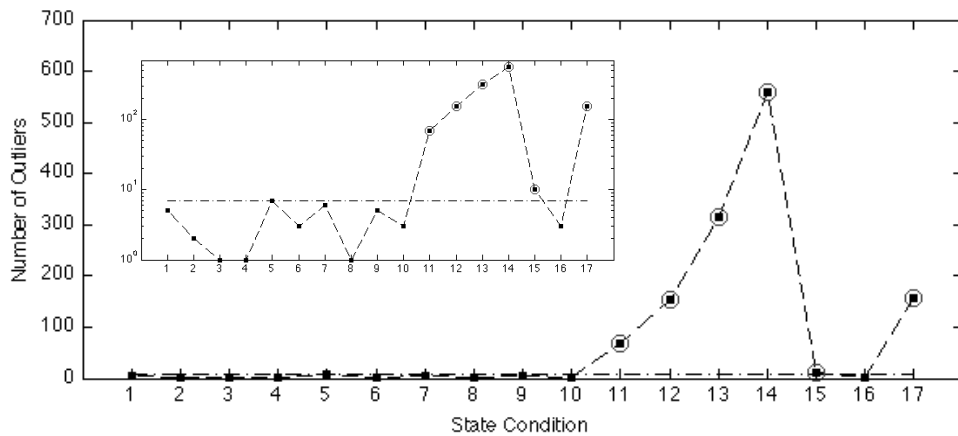


Figure 4.57. Number of outliers falling outside the control limits defined based on data from all undamaged state conditions (State#1-9); the horizontal dashed line corresponds to the maximum number of outliers among the undamaged states (State#5); in overlap format one can see the log-scale version of the figure.

4.6.3 *Outlier Detection based on State-space Reconstruction*

In this section, the outlier detection performance of the novel algorithm based on the state-space reconstruction is shown [137]. Recall that the uniqueness of this approach is the use of the MAR model to predict the state space, where the number of outlier state vectors is an indication of damage. Recall that this algorithm assumes that damage introduces changes in the form of nonlinearities into the time series and that the operational and environmental variations introduce linear changes.

The analysis carried out herein assumes the system is ergodic when in any one configuration for the undamaged condition (stationary property). This assumption permits one to simplify the analysis by using only, for each accelerometer, one out of 50 measured time series to reconstruct the state space of each of the 17 structural state conditions [138]. The following analysis is divided into two parts. First, the damage-detection MAR-based algorithm is tested, individually, using univariate embedding of time series from each accelerometer (Channel 2-5). However, for illustration purposes, the analysis is first centered on the responses from Channel 5, and then, brief results are shown to generalize it to the other accelerometers. Second, the algorithm is applied using a multivariate embedding to incorporate data measured at multiple accelerometers in order to reconstruct the global structure's dynamical state.

The embedding parameters in Equation (3.24) depend on the underlying dynamics of the structure contained in the measured data. Embedding a time series into a state space to extract the dynamic properties of the system requires suitable state-space reconstruction. A good embedding is one that compresses all the information about the future contained in the past into as few variables as possible. In this regard, the SVD technique is considered in this study to compute the suitable embedding dimension m . (Note that the dimension represents the number of variables.) Theoretically, the level of noise as well as different degrees of nonlinearities affects the dimension of the attractor. Figure 4.58 plots singular values, estimated on time series from Channel 5, for the structural conditions summarized in Table 4.1 by assuming vector spaces of dimension $w=20$. The number of singular values larger than the noise floor is an estimate of the minimal embedding dimension required to unfold the attractor. As expected, the figure highlights that the suitable embedding dimension depends on the condition of the structure and that the states with nonlinearities tend to require higher dimensions. (This result is an indication that the embedding dimension can also be a powerful way to discriminate the undamaged and damaged conditions.) For the MAR-based algorithm, the embedding dimension is picked at the convergence point of the spectrum from State#1 - the baseline condition (bold curve in the figure). Therefore, it is assumed that a suitable embedding dimension is equal to 12. Note that noise often present in the data tends to mask the deterministic behavior, and it will be dominant among the small singular values. In theory, the delay time for the attractor reconstruction from time series of infinite length can be chosen almost arbitrary [88]. However, the experimental data are limited in size and resolution and, consequently, the delay time must be estimated from the data.

Nevertheless, in this study a unit lag based on Broomhead and King [89] is assumed, with appropriately-met sampling conditions.

The MAR-based outlier detection algorithm applied to data sets from Channel 5 can be summarized as follows. First, one time series from each structural state condition is embedded into a state space using the time delay embedding in Equation (3.24) and assuming an underestimated embedding dimension $m=3$ and a lag $\tau=1$, yielding trajectory reconstructions with 8190 state vectors. Notice that an underestimated embedding dimension is assumed for the purpose of graphical representation. (Later, a parametric study is carried out to explain the influence of the embedding dimension on the outlier detection process.) In this manner, there are 17 different dynamical systems where State#1 is the baseline or the reference system.

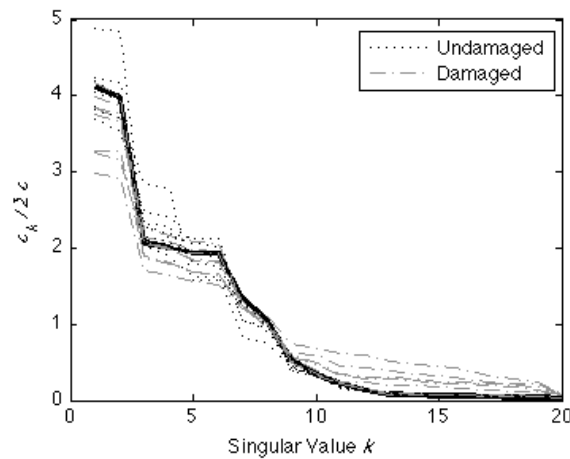


Figure 4.58. Singular values obtained from the state-space reconstructions of the undamaged and damaged structural state conditions at Channel 5, where the bold line represents the baseline condition (State#1).

The appropriate MAR model order is initially unknown. In order to establish the MAR model order, analysis of the AIC values for increasing order $p=1,2,\dots,25$ were performed with the time series from the baseline condition and using Equation (3.28). The AIC function in Figure 4.59 is minimized at $p=15$ which is subsequently used as the appropriate model order. Second, the generated trajectories are used to predict the baseline trajectory using the MAR(15) model of Equation (3.26) whose parameters were estimated from the baseline condition using the multivariate least-squares technique. (Recall that a hypothesis test is established that the MAR model will fail to predict future response if damage is present in the test condition even with operational and environmental effects.) Third, the Mahalanobis metric in Equation (3.55), with parameters estimated from the baseline, is used to detect

outliers in the predicted trajectories of the dynamical systems, with the threshold being defined based on the baseline state condition.

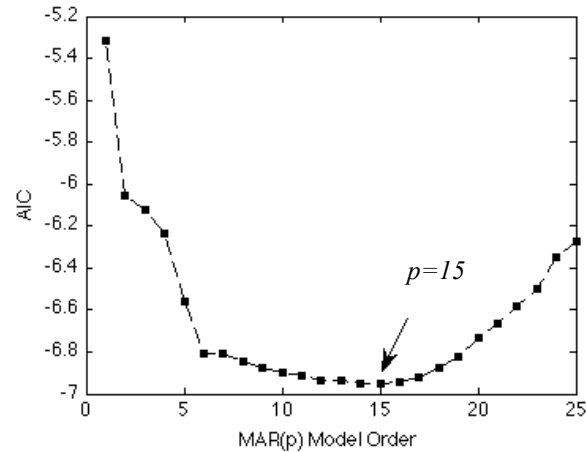


Figure 4.59. AIC function of the MAR model for increasing order $p=1,2,\dots,25$ (Channel 5).

The trajectory in the state space represents all the states that the system can assume for a specific input, and its shape can easily elucidate qualities of the system that might not be obvious otherwise. For illustration purposes, Figure 4.60 shows the predicted trajectory (or more specific the *attractor*) of the baseline condition (State#1) and the trajectories of three other conditions, namely State#7, 10, and 14 along with the baseline one in overlap format. The assumption of linear deterministic system implies that the existence of other forms of attractors indicates damage. The attractor (ellipsoid) of the baseline condition looks “noisy” and random. (Recall that it was estimated using an underestimated embedding dimension.) Even in a badly under-embedded state space, for the damaged conditions (State#10 and 17) the figure highlights state space distortions indicative of the nonlinearities induced when the suspended column hits the bumper. Furthermore, the distortions are indications that the representation seems to unfold the dynamics of the attractor even using an underestimated embedding dimension.

The MSD, or d^2 in Equation (3.55), is now used as metric to quantify the number of predicted state vectors as outliers when they belong to a class of data different from the baseline condition (State#1). First, the covariance and mean vector are computed from the baseline vector space set in order to quantify the underlying statistics of the baseline condition. Then, all potential state vectors are classified as outliers when they do not follow the baseline multi-dimensional distribution and are above of a given threshold (equals to the highest d^2 over the baseline condition). Figure 4.61a shows, in concatenated format, the d_i^2 of each state vector $i=1,2,\dots,8190$ of each structural condition. On the

other hand, Figure 4.61b plots the number of outliers for each structural condition along with the average sum-of-square MAR(15) errors (ϵ). Clearly, the figure shows significant number of outliers in the damaged conditions (State#10-17) even when damage is present along with simulated operational and environmental variations (State#15-17). For the damaged conditions without those variations (State#10-14), one can see a monotonic relationship between the level of damage and the number of outliers. Thus, the smaller the gap between the suspended column and bumper, the higher the number of outlier state vectors. Additionally, one can observe that the residual errors are correlated with the number of outliers, which gives an indication that the average sum-of-square error of the prediction can also be used as damage-sensitive feature. Note that the number of outliers as well as the residual errors can have slight differences from one test to another, because the performance of this approach depends highly on the number and intensity of random impacts that occur in each time series. These differences can be specially relevant for the low level of damage, such as State#10, 15, and 16 due to reduce number of impacts expected in each test.

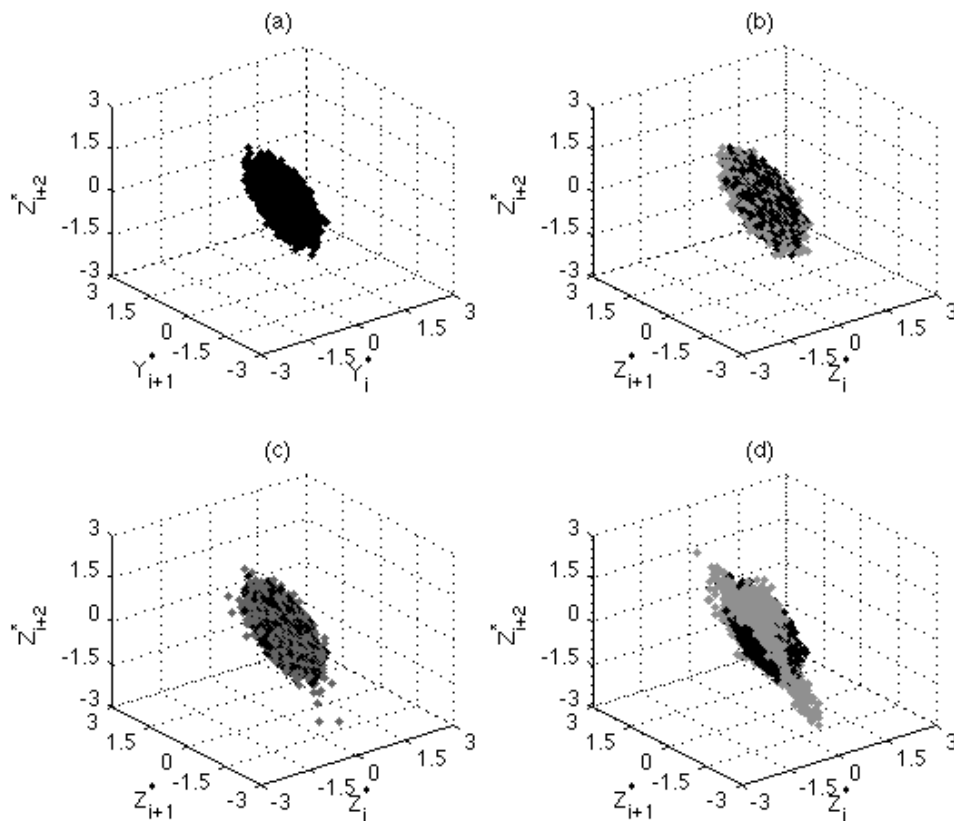


Figure 4.60. Predicted trajectory of the baseline condition (black dots) along with the predicted trajectories from test conditions (gray dots) at Channel 5 for $m=3$: (a) State#1; (b) State#1 and 7; (c) State#1 and 10; and (d) State#1 and 14.

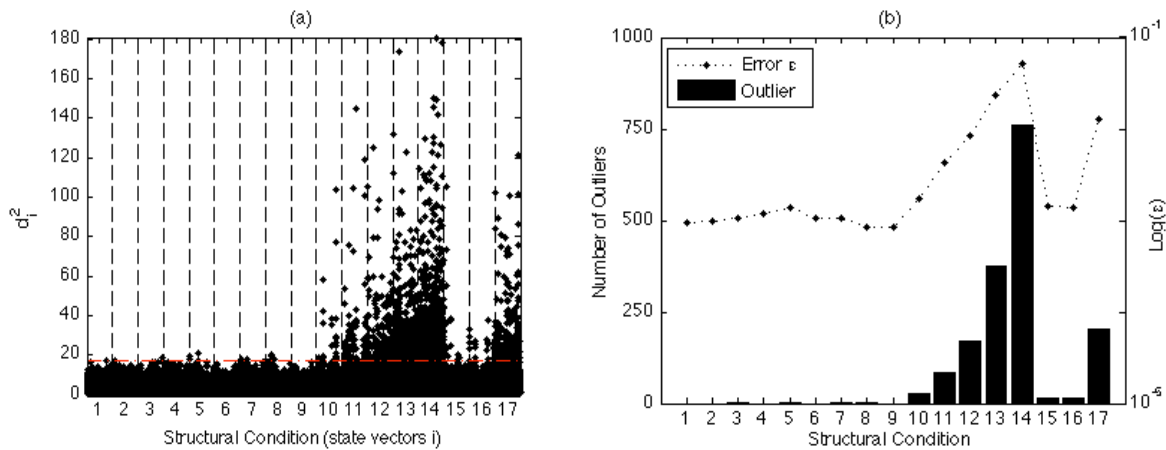


Figure 4.61. Feature extraction at Channel 5 for $m=3$: (a) plot of d^2 from all state vectors from the undamaged (State#1-9) and damaged state conditions (State#10-17), in concatenated format, along with one-sided threshold (horizontal dashed line); and (b) number of outliers, or d^2 values beyond the threshold, along with the average sum-of-square MAR errors (ε).

Figure 4.62 presents the results of a parametric study carried out to expose the influence of the embedding dimension, m , on the proper state-space reconstruction for outlier detection. In that regard, the data sets were, previously, divided into two main groups: undamaged (State#1-9) and damaged (State#10-17) conditions. The first measure is the relative distance between the mean of both d^2 values distributions – Dm . The second measure is the relative distance between the minimum number of outliers among the damaged conditions and maximum number of outliers among the undamaged conditions – $Dout$. Intuitively, the higher the distances, the better the classification performance. The figure shows Dm as a linear function of the embedding dimension, i.e., the higher the embedding dimension, the higher the distance between means of both conditions. On the other hand, the $Dout$ reveals the optimal classification at $m=20$. As the complexity of the model increases, the number of outliers among the undamaged conditions increases, and the classification performance of the classifier decreases. Furthermore, the distance $Dout$ shows that for $m>30$ there are more outliers at least in one state condition among the undamaged ones than in at least one damaged state condition. For the type of damage studied in this case, this result is an indication that the increase of dimensionality induces undesirable complexity into the models. Consequently, classifiers in high-dimensional state spaces might average out the effects of damage and, therefore, decrease their classification performance and, potentially, mask the low-level of damage, such as State#10, 15, and 16. This result permits one to conclude that the embedding dimension must be chosen carefully and kept as low as possible to avoid overfitting that occurs when the model describes random error instead of the underlying dynamical changes due to damage.

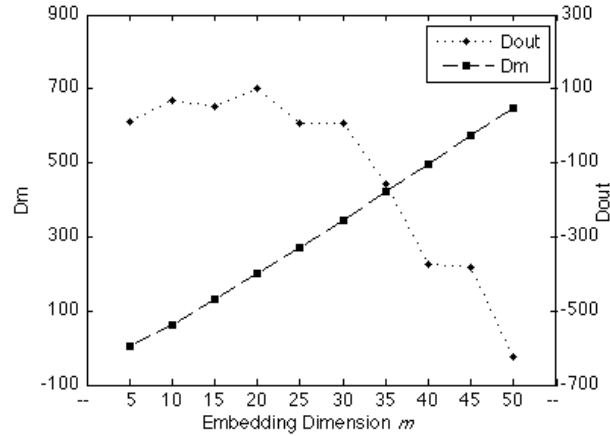


Figure 4.62. Relative distances between the undamaged and damaged conditions as a function of the embedding dimension m ; D_m is the distance between the mean of both d^2 distributions; D_{out} is the distance between the minimum number of outliers among the damaged state conditions and the maximum number of outliers among the undamaged state conditions.

In order to extend the univariate embedding to the remainder accelerometers, Figure 4.63 shows the classification performance of the algorithm for all accelerometers individually (Channel 2-5), assuming the suitable embedding dimension $m=12$ for the baseline condition, as shown in Figure 4.58. The thresholds are defined again to be equal to the highest d_i^2 among the baseline condition. Additionally, the average sum-of-square MAR(15) errors of the prediction is also plotted for each structural condition. Qualitatively, for Channel 4 and 5 one can observe an increasing of the number of outliers and errors among the damaged conditions as highlighted for $m=3$. On the other hand, one can observe a non-systematic discrimination trend for Channel 2 and 3. The insensitivity to detect damage using the responses from those sensors are related to the geometrical distance between the source of damage and output response of the structure, which implies that localization may be possible with this approach. Note that the simulated damage is a local phenomenon characterized by singular bursts in the signal and, consequently, its detection and location relies on the existence of a dense array of sensors in the structure.

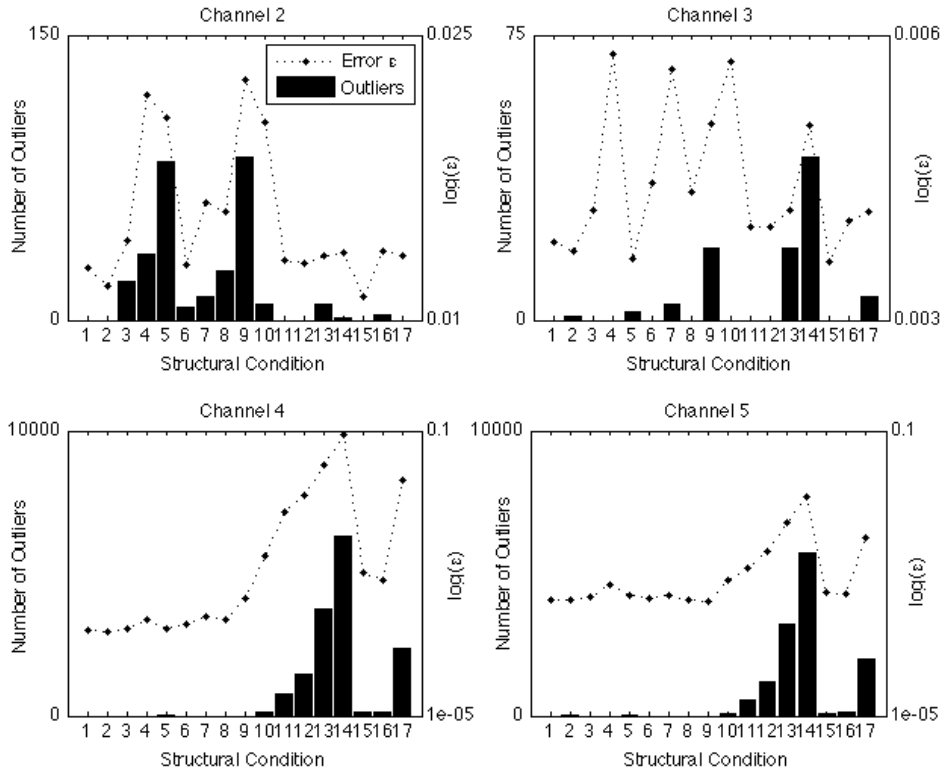


Figure 4.63. Outlier detection and feature extraction per structural condition in the four accelerometers (Channel 2-5) for $m=12$; number of outliers along with the average sum-of-square MAR errors (ϵ) in log scale.

Finally, Figure 4.64 shows the results of the state-space reconstruction in the form of a multivariate embedding presented in Equation (3.30), based on time series from multiple locations. Two multivariate embeddings are carried out to show their performance in the presence of local damage in the form of random singularities in the signal. Figure 4.64 shows for each structural condition the number of outliers along with the average sum-of-square MAR errors for a global embedding (Channel 2-5, $M=12$, and $p=7$) and a semi-global embedding (Channel 4-5 and $M=12$, and $p=8$). As in the univariate case, each embedding dimension M was estimated by performing the SVD on the multivariate trajectory matrix and assuming, for simplification, equal embedding dimension m per sensor. The AIC values were also used to estimate the appropriate $MAR(p)$ order of each embedding. Clearly, for the global embedding in Figure 4.64a, both the outlier detection and residuals show that the reconstruction of the global dynamical attractor is not statistically reliable to detect the existence of damage in the structure. On the other hand, Figure 4.64b shows that the multivariate embedding with time series from Channel 4 and 5 can be used to classify the damaged conditions, even though it shows significant number of outliers in State#8 and 9 that can lead to undesirable false-positive indications of damage. These results indicate that the multivariate embedding amplifies the linear changes due to varying mass and stiffness and, consequently, average out the effects of local damage

in the form of singularities in the signal. Therefore, for these data sets, this algorithm is more appropriate to detect local damage rather than to detect the existence of damage in a global basis.

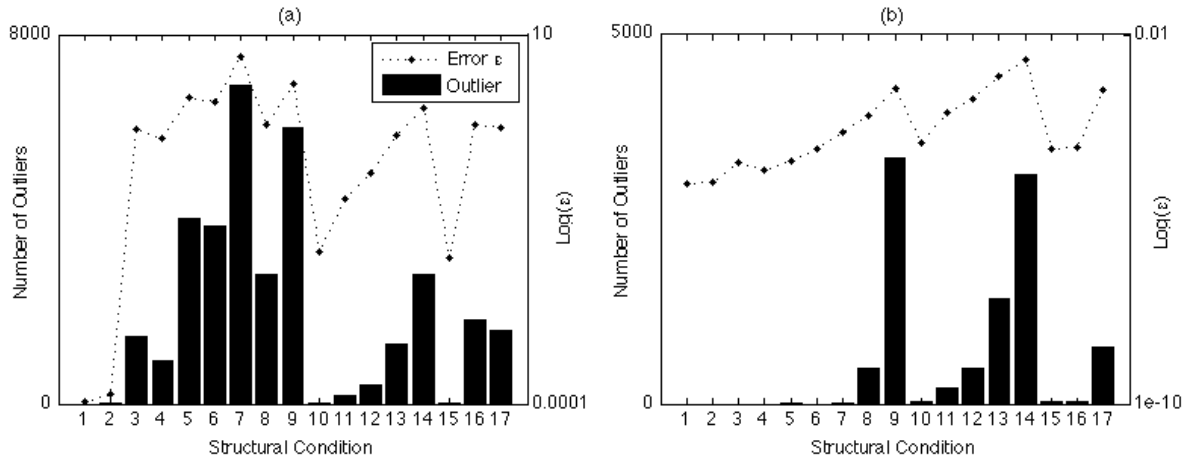


Figure 4.64. Number of outliers along with the average sum-of-square $\text{MAR}(p)$ errors (ϵ) in log scale per structural state condition: (a) based on a global embedding (Channel 2-5, $M=12$ and $p=7$); and (b) based on a semi-global embedding (Channel 4-5, $M=12$, and $p=8$).

4.6.4 Outlier Detection based on Machine Learning Algorithms

In Chapter 1 was stated that in real-world structures, the separation of changes in sensor readings caused by damage from those caused by changing operational and environmental conditions is one of the biggest challenges for transitioning SHM technology from research to practice. As such, this section applies and directly compares on the standard data sets, four machine learning algorithms for data normalization and outlier detection. These vibration-based algorithms are applied to create a global structural DI that is almost invariant under those variations and potentially sensitive to data acquired from the damaged condition. Recall that such algorithms are categorized as unsupervised learning approaches to SHM as they are used to identify deviations from the normal condition. In the hierarchical structure of damage identification, this section presents a comparative study that addresses the need for robust low-level damage detection under operational and environmental variations. Hence, this study is concerned only with identifying the existence of structural damage in a global basis.

Even though any kind of damage-sensitive feature could be used, in this case the AR parameters are used as damage-sensitive features, because, as shown in Section 4.5.3, the AR models are very sensitive to damage when it manifests in the form of nonlinearities or transitions between two states and the extraction of features only depend on response time series data. Notice that in order to increase the statistical significance of this study, each original 8192-point time series is split into two 4096-point segments. It turns out that for each state condition there are 100 tests.

For each test of each state condition, the AR parameters are estimated using the least-squares technique applied to time series from all four accelerometers (Channel 2-5) and stored into a feature vector as shown in Section 4.5.3. (Note that Channel 1, the input force, is not used in the analysis.) The appropriate order of the AR models is initially unknown. A higher order model may better match the data, but may not generalize to other data sets. In order to establish a common optimal order, analyses of the AIC values in Equation (3.28) were carried out for four individual AR(p) models of increasing order p ($p=1,2,\dots,25$). Figure 4.65 shows the average AIC function resulted from analyses performed on the 100 individual tests from the baseline time series data (State#1). (Note that for each test the number of estimated parameters is $p \times 4$ and ε is the sum of the average sum-of-square errors of Channels 2-5.) The function is not minimized in the selected range, but the linear AR models achieve enough small AIC value around $p=10$. Based on that assessment, for each test, four individual AR(10) models are used to fit the corresponding time series from the four accelerometers and their parameters are used as damage-sensitive features in concatenated format, yielding 40-dimensional feature vectors. Note that AR parameters should be constant when estimated based on time series data obtained from time-invariant systems. However, in the presence of operational and environmental variations as well as damage, the parameters are expected to change accordantly, as shown in Figure 4.34.

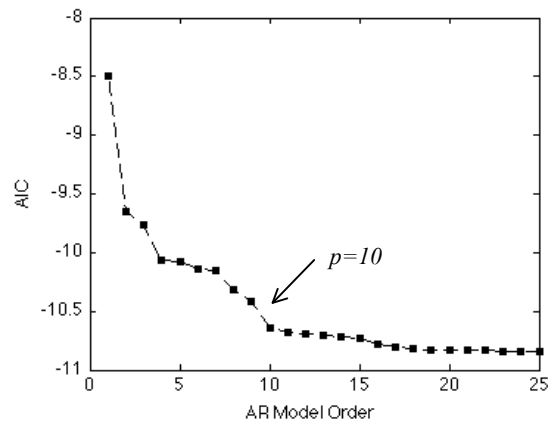


Figure 4.65. Average AIC function for four independent AR(p) models of increasing order p using baseline-based time series (State#1) from the four accelerometers (Channel 2-5).

The extraction of damage sensitive-features is the third part of the SHM process. The next step is to carry out statistical modeling for feature classification. In that regard, the AANN-, FA-, MSD-, and SVD-based algorithms outlined in Section 3.3 are implemented in an unsupervised learning mode by first taking into account features from all the undamaged state conditions. For generalization purposes, the feature vectors were split into two groups: the training and test matrices. The training matrix \mathbf{X}

permits each algorithm to learn the underlying distribution and dependency of all the undamaged state conditions on the simulated operational and environmental variability. Thus, this matrix is composed of AR parameters from 50 out of 100 tests of each undamaged state condition (State#1-9), and so it has a dimension of 40×450 . This procedure allows one to increase redundancy and to reduce the effect of noise on the data classification process. The test matrix \mathbf{Z} (40×1250) is composed of AR parameters from the remaining 50 tests of each undamaged state condition together with AR parameters from all the 100 tests of each damaged state condition (State#10-17). This procedure permits one to assess the generalization performance of the machine learning algorithms in an exclusive manner, because time series used for testing are not included in the training phase. During the test phase, the algorithms are expected to detect deviations from the normal condition when features come from damaged ones even with the presence of operational and environmental variability. Note that Equation (3.62) is used to compute the DIs from the residuals of the AANN-, FA-, and SVD-based algorithms. For every algorithm, the DIs are then stored into a 1250-length vector.

The AANN-based algorithm is built up with a feed-forward neural network to perform the mapping and de-mapping, where the network outputs are simply the reproduction of the network inputs. The network, according to Kramer's recommendations [111], has 10 nodes in each mapping and de-mapping layer and two nodes in the bottleneck layer. The nodes in the bottleneck layer intend to represent the two underlying unobserved variables driving the changes in the features: the changes in mass and stiffness. A Levenberg-Marquardt back-propagation algorithm was used to train the network. Several trainings with different initial conditions were performed with the given architecture to increase the probability that the global minimum was achieved. The FA-based algorithm assumes also two factors to represent the same number of underlying unobserved variables affecting the measured features. The Λ matrix was determined from the normal condition using the maximum likelihood estimation. Because the undamaged and damaged state conditions are known *a priori*, the MSD-based algorithm is developed in an exclusive manner by using only data from the training matrix when forming the estimates of the mean vector (40×1) and covariance matrix (40×40). In the case of the SVD-based algorithm, the state matrix \mathbf{M} for each potential damaged feature vector has a dimension of 40×451 . As a consequence, the number of singular values computed upon each matrix is equal to 40.

The ROC curves provide a comprehensive means of summarizing the performance of classifiers. Recall that the ROC curves focus on the trade-off between *true detection* and *false alarm*. Each point on the ROC curve corresponds to a specific threshold, although the values of thresholds are not evident from the plot. Figure 4.66a plots the ROC curves for all the algorithms in overlap format. The number of points to define the ROC curves is a function of the range between the maximum and minimum DI for each set of data. In this case, approximately, 800 points were used to define each

curve. Recall that the point at the left-upper corner of the plot (0,1) is called a perfect classification. To better visualize the differences in the curves, Figure 4.66b plots the ROC curves in log scale. Qualitatively, looking at the plots, one can conclude that none of the algorithms can have a perfect classification with a linear threshold because none of the curves go through the left-upper corner. Furthermore, in the whole false-alarm range and for a given threshold, it also can be seen that the AANN- and MSD-based algorithms have better true detection performance than SVD- and FA-based algorithms. Besides, for low and high probability of false alarm, the MSD-based algorithm has the best true detection performance.

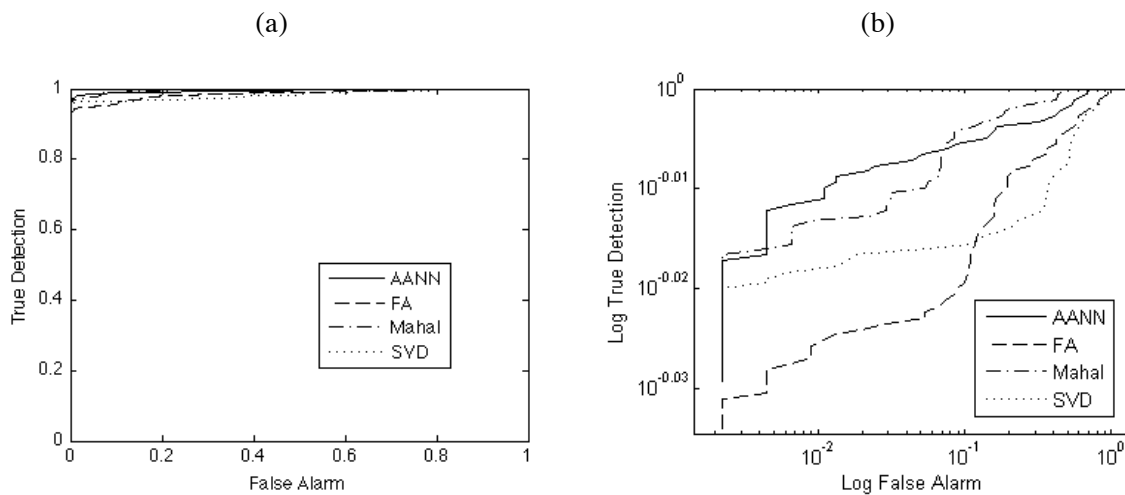


Figure 4.66. ROC curves: (a) linear scale; and (b) log scale to highlight the differences between curves.

In order to quantify the performance of the classifiers for a given threshold, Figure 4.67 plots the DI of each feature vector of the entire test data along with thresholds defined based on the 95% cut-off value over the training data. All the algorithms show a monotonic relationship between the level of damage and the amplitude of the DI, even when operational and environmental variability is present. The Type I (false-positive indication of damage) and Type II (false-negative indication of damage) errors is one common way of reporting the performance of a binary classification. This technique recognizes that a false-positive classification may have different consequences than false-negative ones. Table 4.4 summarizes the number of Type I and Type II errors for each algorithm. In an overall analysis, the table shows a clear trade-off between Type I and Type II errors, with the AANN- and MSD-based algorithms having better performance to detect damage (1.3 and 1.0%) and the FA- and SVD-based algorithms having better performance to avoid false indications of damage (2.2 and 6.2%). Actually, this result just confirms the previous observations based on the ROC curves. Nevertheless, all the algorithms perform well when compared on these standard data sets with the percentage of total misclassifications (both Type I and Type II errors) ranging between 4.0% and 4.6% of the number of tests, which can be considered a good result because it was initially assumed a level of significance equals to 5%. Note that the percentage of Type II error is related to the low level of damage states

(states with 0.20 mm gap). Therefore, for these specific data sets, one can conclude that the FA- and SVD-based algorithms are more appropriate when one wants to minimize false-positive indications of damage, with economic and reliability issues driving the SHM. On the other hand, the AANN- and MSD-based algorithms are preferred when one wants to minimize false-negative indications of damage and when life-safety issues are the primary motive for deploying the SHM system.

The classification performance of the AANN- and FA-based algorithms can potentially be improved by adjusting the number of unobserved variables, i.e., the number of factors. Note that in the previous analysis were used two unobserved factors (changes in mass and stiffness). This is actually a drawback in real-world applications, because often the number of independent operational and environmental factors driving changes in the structural responses is unknown. To highlight the influence of the number of factors assumed on both algorithms, Figure 4.68 shows the distance between the mean of the DIs from the undamaged and damaged conditions along with the number of Type II errors as a function of the number of factors. Based on the distance between means and the number of errors, the appropriate number of factors is two and three for the AANN- and FA-based algorithms, respectively. This result gives an indication that the number of factors assumed in the previous analysis is nearly the optimal solution. Note that the difference in number of factors can be related to the fact that the AANN-based algorithm is able to learn nonlinear relationships between the features. Furthermore, the number of errors also indicates that assuming higher than suitable number of factors increases the algorithm complexity and, consequently, reduces the generalization performance of the classifier. In fact, these results are of extreme importance, because they permit one to validate those algorithms for real-world applications, where the number of factors is often unknown. Note that, with the cost of more complexity, in the case of the AANN-based algorithm, the performance can also be improved by increasing the number of nodes in the mapping layers.

For general applications, one final comparison is made in terms of computational efforts. First, it was observed that the computational efforts of the algorithms might be divided in two phases: the training and test. At the training phase, it was observed that the AANN-based algorithm requires significantly more computational efforts than the other three ones in order to guarantee that the global minimum is achieved. Moreover, it is well known that the neural networks suffer from local minima phenomenon [105]. On the other hand, at the test phase, the SVD-based algorithm revealed significantly higher efforts than the others, because this algorithm requires an eigen-decomposition for each new test.

In terms of overall performance throughout this study, regardless of the fact that the AANN-based algorithm has some advantages in terms of finding nonlinear correlations among the features, the MSD-based algorithm is considered to be the best data normalization procedure in terms of classification performance, reduced computational efforts, and the fact that no assumptions are required to set its architecture. These facts, along with simplicity, make the MSD-based algorithm also a better choice for implementation on current embedded hardware.

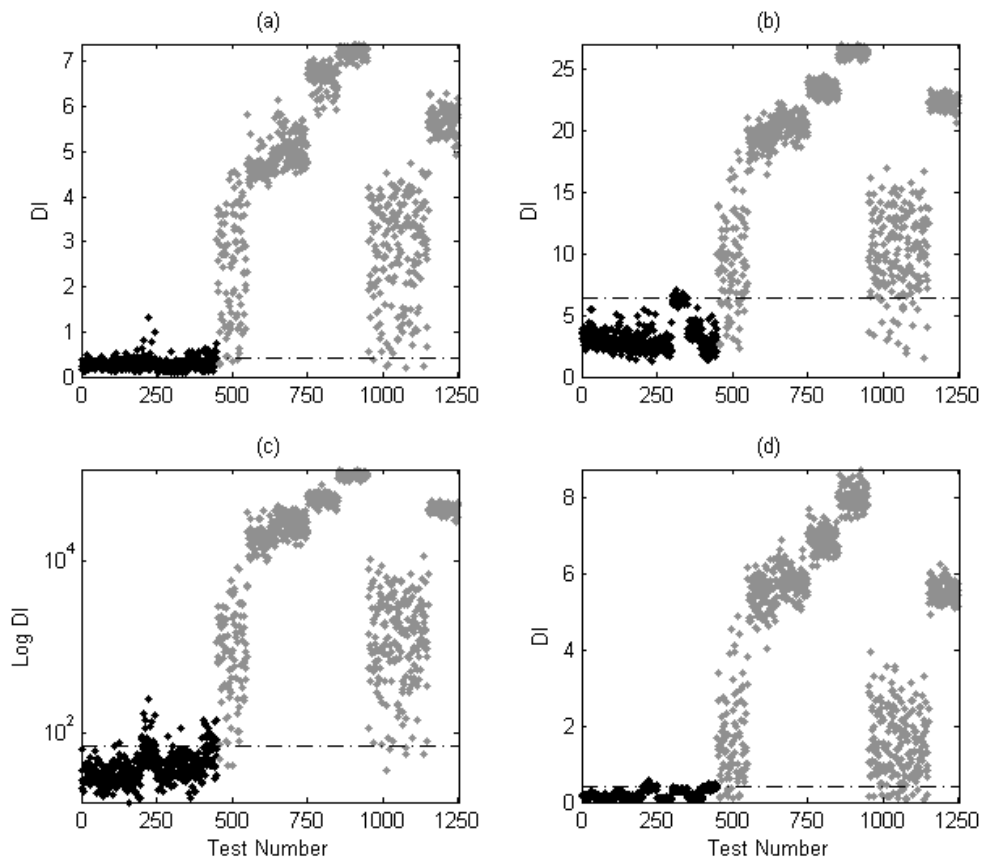


Figure 4.67. DIs calculated based on feature vectors from the undamaged (black) and damaged (gray) state conditions along with thresholds defined by the 95% cut-off value over the training data: (a) AANN-; (b) FA-; (c) MSD-; and (d) SVD-based algorithms.

Table 4.4. Number and percentage of Type I and Type II errors for each algorithm.

Algorithm	Error		
	Type I	Type II	Total
AANN	44 (9.8 %)	10 (1.3 %)	54 (4.3 %)
FA	10 (2.2 %)	43 (5.4 %)	53 (4.2 %)
MSD	42 (9.3 %)	8 (1.0 %)	50 (4.0 %)
SVD	29 (6.2 %)	29 (3.6 %)	58 (4.6 %)

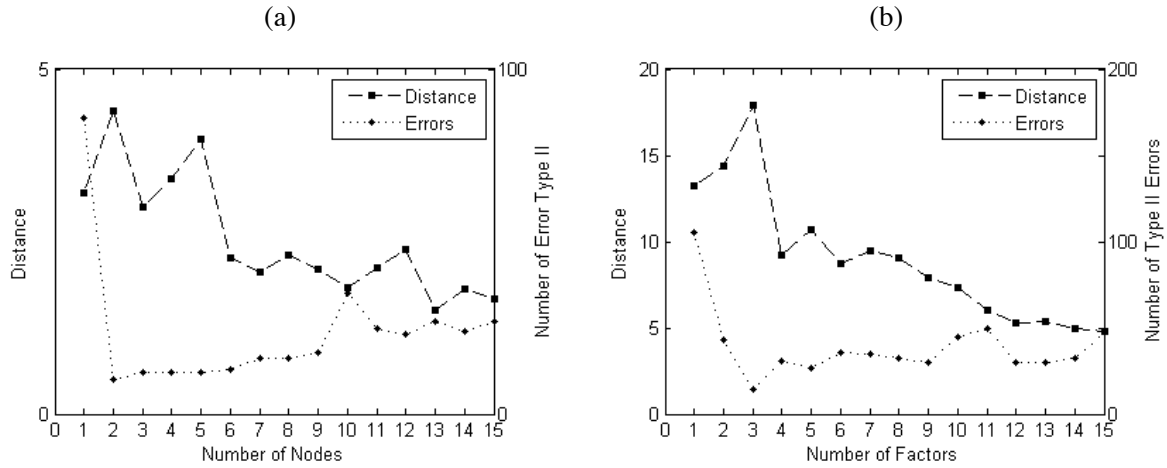


Figure 4.68. Distance between the mean of the DI distributions of the undamaged and damaged state conditions along with the number of Type II errors as a function of the number of factors: (a) AANN-; and (b) FA-based algorithms.

4.6.5 Outlier Detection based on Central Chi-square Hypothesis

In the previous section, the classification performance of the MSD-based algorithm was compared with other three machine learning algorithms, assuming a confidence interval over the DIs from the training matrix. However, as exposed in Section 3.4.3, under certain assumptions, DIs from the undamaged condition follow a parametric central chi-square distribution. This fact is relevant in SHM, because it permits to generalize the classification with confidence intervals based on a parametric distribution. This manner, the goal of this section is to classify the undamaged and damaged state conditions, individually on each accelerometer, using the MSD-based algorithm on feature vectors composed of $AR(p)$ parameters, based on the assumption that the DIs from the undamaged condition follow a parametric central chi-square distribution, χ_m^2 , with the number of degrees of freedom equal to the number of parameters p used in the AR models. Note that for each feature vector, a hypothesis test is established such that the algorithm will reject the null hypothesis (undamaged condition) if DI does not follow a chi-square distribution. Once this algorithm assumes multi-dimensional Gaussian feature vectors as inputs, the analysis also attempts to study (i) how non-Gaussian-distributed features and (ii) how the AR model order affect the distribution of the DIs from the undamaged condition as well as the classification performance. Additionally, an attempt is made to correlate the optimal AR model order with the classification performance by using the CIC technique.

The analysis is performed on the standard data sets from all four accelerometers (Channel 2-5) mounted on the three-story structure. The original data sets are composed of 50 tests from each of the 17 structural state conditions, where each of the 50 acceleration time series from each channel is composed of 8192 data points. However, in order to increase the number of time series per state condition, each time series is split into two segments, yielding time series of 4096 data points. Thus,

for each channel there are 900 and 800 acceleration time series with 4096 points from the undamaged and damaged conditions, respectively. Then, the AR parameters are estimated on each time series using the least-squares technique and stored into a feature vector, whose length is equal to the AR model order. Therefore, for each channel the data sets are composed of 1700 tests.

The dimension of the feature vector and, consequently, the appropriate AR model order is initially unknown. In Section 4.5.3.1, analysis was carried out to determine the appropriate AR model order based on the AIC. However, the AIC has been reported to be too strict in model order estimation. Therefore, in order to establish an appropriate $AR(p)$ model order for each accelerometer, independently, the CIC values in Equation (3.10) were computed as a function of the model order p ($p=1,2,\dots,50$). For the undamaged condition, Figure 4.69a plots for each channel the averaged CIC values, where the x-axis denotes the number of parameters in the AR model and the y-axis is the 900-average CIC value. The behavior of CIC as a function of model order from Channel 4 and 5 still shows a very flat minimum after convergence (note the same result was observed in Figure 4.21), which challenges the determination of the optimal model order. Clearly, in these cases, it might not be sufficient to compute $CIC(p+1) > CIC(p)$ to determine the actual absolute minimum of the CIC. As suggested by Ciftcioglu et al. [81], this might be the case when a large number of samples N_i are involved and the first term in the right-hand side of Equation (3.10) dominates. Additionally, the CIC from Channels 2 and 3 show more complexity in the time series without a clear indication of the AR model order. (This complexity might be associated to the friction between the rails and the structure.) In order to relief some emphasis on the first term and assuming stationarity in the system, Figure 4.69b shows the CIC as a function of the model order using time series of 1024-length. This procedure intends to remove redundancy in the model order determined by CIC and, consequently, yielding more accurate results in the model order estimation. Actually, it turns out that for Channels 4 and 5 the minima are much more pronounced (located between 10 and 20). However, for Channels 2 and 3, the CIC shows an oscillatory behavior that creates several local minima, roughly, at 20 and 35 and at 15 and 30, respectively. Therefore, when using smaller time series, the results seem to be conclusive only regarding Channels 4 and 5. However, these results must be seen just as a good start and further analysis is required to define the optimal number of parameters in order to discriminate, accurately, feature vectors from undamaged and damaged conditions. For this purpose, in the following analysis, a range of model orders between 1 and 50 is chosen, such that the lower bound is unequivocally too small, while the upper bound is a plausible model order.

In order to validate Equation (3.60), the original features from the undamaged condition must be nearly multi-dimensional Gaussian distributed. For illustration purposes, Figure 4.70 shows the estimated PDF from each $AR(15)$ parameter (or variable) of the entire undamaged data sets from Channel 5. Each PDF was estimated using the kernel smoothing density based on a standard Gaussian function on the 900 tests. As it is evident from the figure, some of the parameters do not follow a well-

defined Gaussian distribution. However, recall that the features are extracted from different structural state conditions whose mass and stiffness changes are made in a discrete manner, which produces multi-modal distributions that might impose distortions to the underlying distribution of the DIs from the undamaged condition.

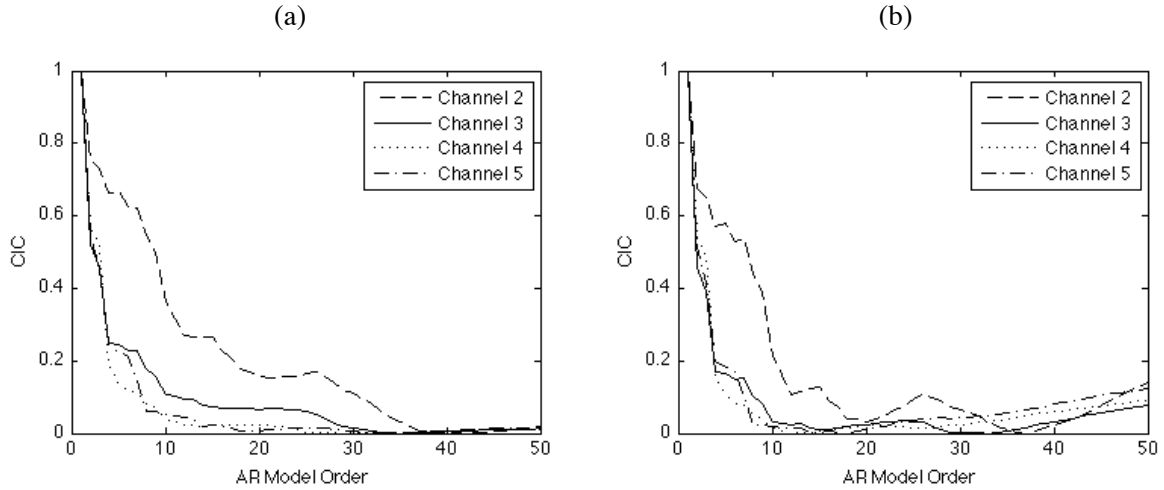


Figure 4.69. Comparison of the behavior of the CIC as a function of model order using: (a) 4096-point; and (b) 1024-point time series.

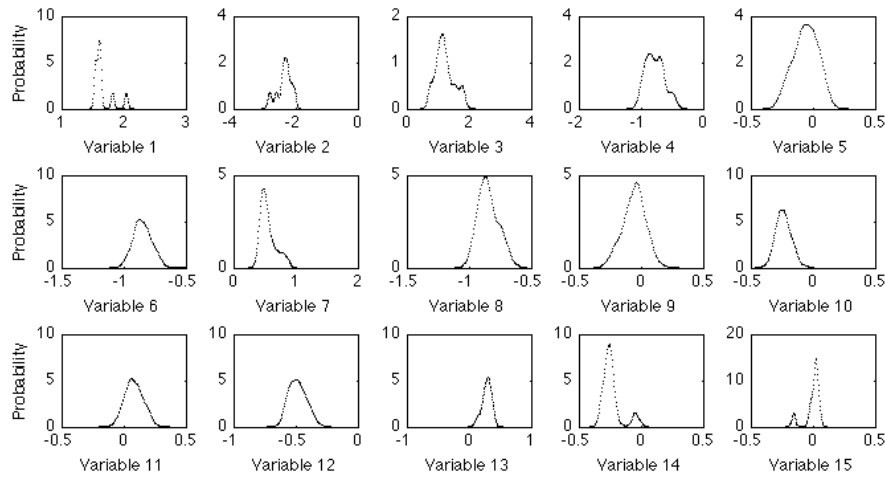


Figure 4.70. Estimated PDF for each variable, or AR(15) parameter, of the original undamaged feature vectors from Channel 5.

For each accelerometer, Figure 4.71 shows estimated PDFs along with theoretical central chi-square distributions, χ_m^2 , with m degrees of freedom for four AR(p) models of varying order $p=m=5, 15, 30$, and 50. In this case, 50% of the entire undamaged data sets are used to set the mean vector and covariance matrix of the MSD-based algorithm and the same data set is used to estimate the underlying distributions. The figure indicates that the DIs seem to have an underlying chi-square distribution even with slight visual changes. In order to better evaluate the approximation, Figure 4.72 depicts the correlation coefficients between the theoretical and estimated PDFs for AR models of

increasing order $p=1,2,\dots,50$. The results indicate close correlation in all accelerometers for p between 15 and 20, roughly. Therefore, while each individual AR parameter may not follow a Gaussian distribution, given a sufficient number of parameters, the DIs are still approximately chi-square distributed.

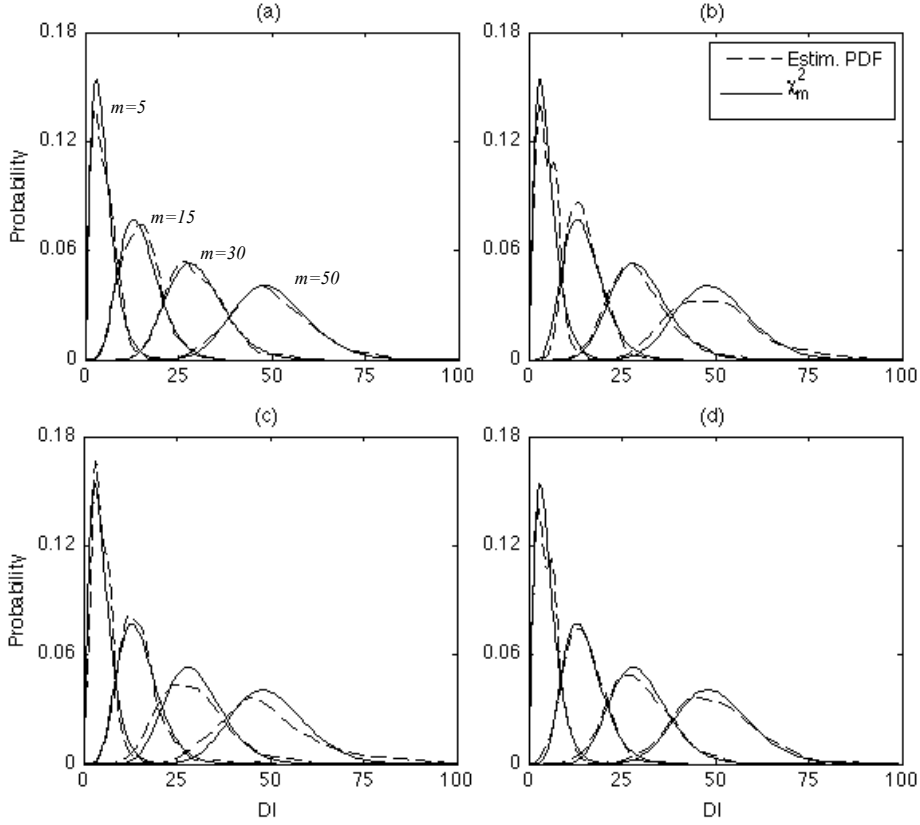


Figure 4.71. Four theoretical chi-square distributions, χ_m^2 , along with PDFs of the DIs from undamaged condition and assuming AR(p) models of increasing order $p=m=5, 15, 30,$ and 50 .

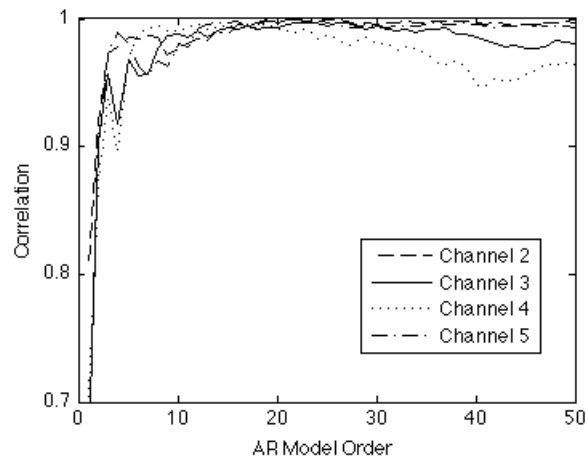


Figure 4.72. Correlation coefficients between the theoretical chi-square distributions, χ_m^2 , and PDFs of the DIs from the undamaged condition for increasing AR(p) model order $p=m=1,2,\dots,50$.

In order to evaluate the influence of the AR model order on the classification performance, the ROC curves along with the Type I and Type II errors are used. The ROC curves provide a comprehensive means of summarizing the performance of classifiers for varying threshold, by means of the trade-off between *true detection* and *false alarm*. As discussed in Section 3.4.5, each point on a ROC curve corresponds to a specific threshold, although the values of thresholds are not evident from the plot. On the other hand, the Type I/II errors provide a quantitative measure of the classification performance for a given threshold. Note that the Type I and false-alarm rate are directly correlated. On the other hand, the Type II and true-detection rate are inversely correlated.

Figure 4.73 plots, in overlap format, ROC curves of five-increment AR model order p ($p=5,10,\dots,50$). The number of points to define a ROC curve is a function of the range between the maximum and minimum DIs for each set of data. In this case, approximately, 2500 points were used to define each curve. Qualitatively, looking at the plots, one can conclude that in all accelerometers, the classification performance is a function of the AR model order. From the figures of each channel, one can visualize a convergence for given model order p . It is also possible to visualize that the AR(5) model order is clearly a common inadequate model order to discriminate the structural conditions. Note that the (0,1) point is called a perfect classification.

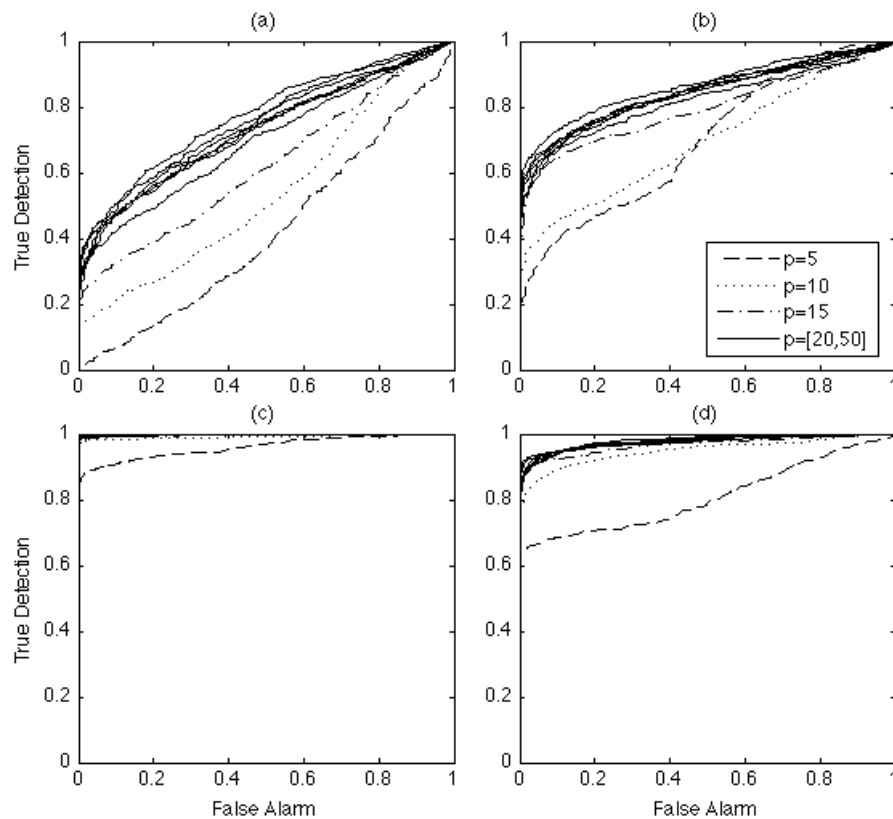


Figure 4.73. ROC curves for AR(p) models of varying order $p=5,10,\dots,50$ at: (a) Channel 2; (b) Channel 3; (c) Channel 4; and (d) Channel 5.

In order to better visualize that convergence, Figure 4.74 plots the true-detection rate, for fixed false-alarm rate of 0.1, as a function of the AR model order p . The figure shows no detection gains beyond, approximately, AR model orders of 10 (Channel 4), 15 (Channel 3 and 5), and 20 (Channel 2), confirming the previous indications given by the ROC curves in Figure 4.73. Moreover, the figure also highlights that Channels 2 and 3 are less sensitive to detect damage, because the true-detection rate cannot go beyond, roughly, 0.5 and 0.7, respectively. Actually, and when comparing with the previous results from the CIC analysis in Figure 4.69b, one can infer a close relationship between the optimal model order given by the information criterion technique and the true-detection rate in each channel. Note that due to reduce complexity, this relationship is more evident in Channels 4 and 5 than in Channels 2 and 3.

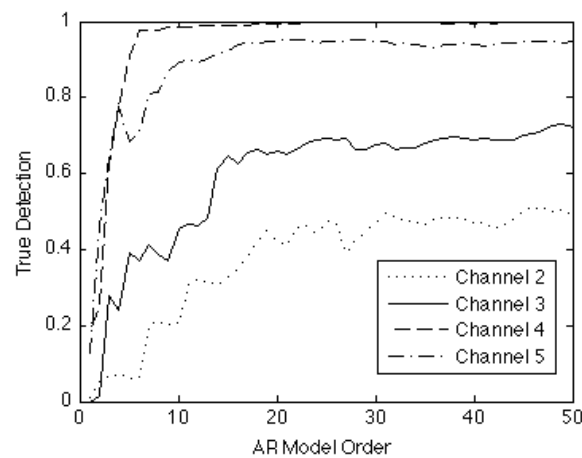


Figure 4.74. True-detection rate for fixed false-alarm rate equals to 0.1 at Channels 2-5.

Additionally, the Type I and Type II errors are computed to statistically quantify the classification performance between undamaged and damaged conditions for varying AR model order. This manner, for a given threshold, one can visualize how the AR model order influences the discrimination. Figure 4.75 plots for each accelerometer the trade-off between Type I and Type II errors for varying $p=m=1,2,\dots,50$. The threshold was found for a level of significance $\alpha=10\%$, i.e., a 90% confidence interval of the upper-tail chi-square distribution, χ_m^2 . Clearly, the results show the trade-off between fitting accuracy by increasing the order of the model and the number of misclassifications. For all channels, even those less sensitive to detect local damage, in general the higher the AR model order, the higher the number of Type I errors and the lower the number of Type II errors. Additionally, for Channel 4 and 5 one can figure out deviations from the 10% of Type I errors at $p=15$, roughly. Note that this technique recognizes that a false-positive classification may have different consequences than false-negative one, and that the optimal trade-off is application-specific. A system that is expensive to inspect typically requires a relatively low SHM false-positive rate, while systems with severe economic or life-safety risks associated with failure need to favor a low SHM false-negative rate. These considerations are essential to the proper design and thresholding of any SHM system [139].

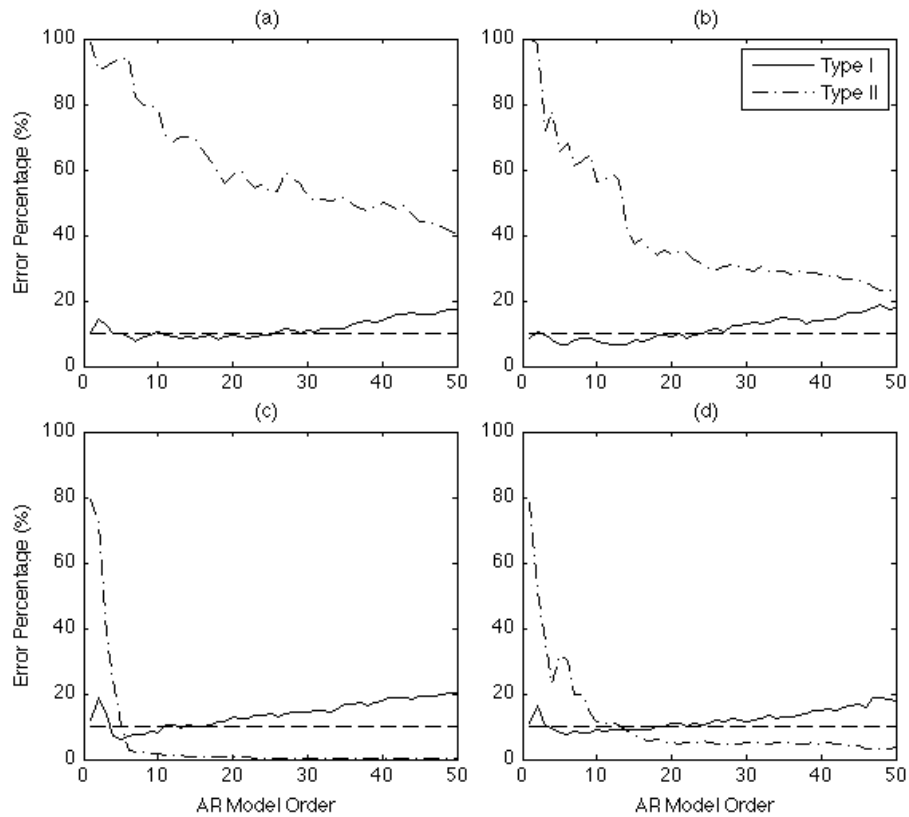


Figure 4.75. Percentage of Type I and Type II errors for varying AR model order $p=1,2,\dots,50$ assuming a level of significance equals to 10%; (a) Channel 2; (b) Channel 3; (c) Channel 4; and (d) Channel 5.

Finally, based on the previous analysis, the classification of the structural state conditions is carried out on data from each accelerometer assuming an AR(15) model, based on the assumption for simplification that the 15th order is a common AR model order. The parameters of the MSD-based algorithm are estimated based on feature vectors from the training matrix \mathbf{X} composed of 50% of the entire undamaged data. On the other hand, the test matrix \mathbf{Z} is composed of feature vectors from all the undamaged and damaged conditions, including the ones used in the training matrix. Therefore, for each channel, the test matrix is composed of 1700 feature vectors (or tests). The upper-bound threshold is found from the false alarm constraint (undamaged condition) for a level of significance $\alpha=10\%$ of a chi-square distribution with 15 degrees of freedom, χ_{15}^2 . Thus, for each accelerometer, Figure 4.76 plots the estimated PDFs based on the DIs of all tests along with the associated threshold. As expected from Figure 4.72, the figure shows that the DIs derived from the undamaged condition follow a chi-square distribution. It is also highlighted that the mean of both distributions diverge significantly for Channels 4 and 5, indicating better classification performance for those channels located near the source of damage. In order to quantify the classification performance in terms of false-positive and false-negative indications of damage, the number of Type I and Type II errors are summarized in Table 4.5, respectively. Clearly, the total number of errors increases for Channels 2 and

3 located far from the source of damage when compared to Channels 4 and 5. The percentage of Type I errors for all channels (8.3, 7.9, 10, and 9.0%) is around the 10% level of significance assumed to define the thresholds. This is a key indication that the algorithm is able to “learn” the variability due to operational and environmental conditions. Furthermore, it also indicates that the central chi-square distribution models well the underlying distribution of the DIs from the undamaged condition, and that it can be used in the proper selection of classification thresholds, despite the original feature vectors having an underlying multi-dimensional non-Gaussian distribution. Note that by changing the threshold, as shown in Figure 4.73, one might trade-off probability of false alarm and probability of true detection. Note that this algorithm has also shown to be a reliable way to identify local damage throughout the structure, as demonstrated from the low level of total misclassifications (Table 4.5) at Channel 4 and 5. However, it gives high number of Type II errors for those sensors far from the source of damage, giving an indication that real-world structures may require high density of sensors to detect damage throughout the structures.

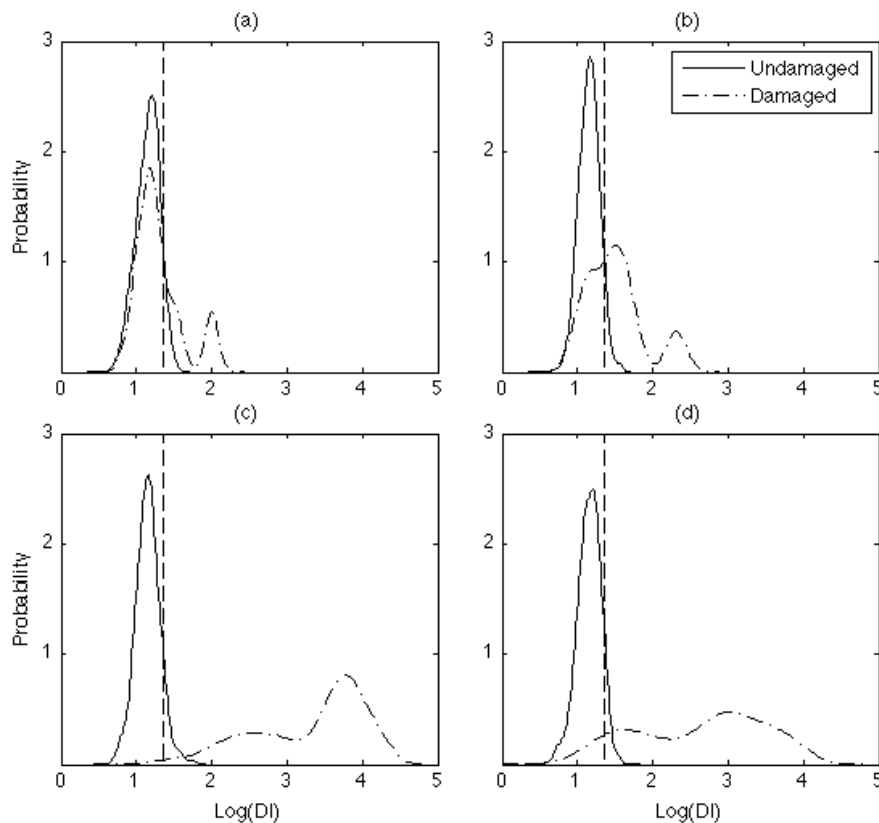


Figure 4.76. PDFs based on the DIs of all tests from undamaged and damaged conditions along with a threshold (vertical dashed line) defined by the 90% confidence interval of the χ_{15}^2 distribution when using AR(15) parameters as damage-sensitive features and 50% of the entire undamaged data sets to establish the normal condition.

Table 4.5. Number of Type I and Type II errors.

Channel	Errors		
	Type I	Type II	Total
2	75 (8.3 %)	552 (69 %)	627 (37 %)
3	71 (7.9 %)	300 (38 %)	371 (22 %)
4	90 (10 %)	7 (0.9 %)	97 (5.7 %)
5	81 (9.0 %)	62 (7.8 %)	143 (8.4 %)

4.7 Summary and Conclusions

Before applying SHM procedures to the standard data sets from the three-story base-excited frame structure, a linear physics-based numerical model of the test structure was developed in order to compare the numerical results with the measured experimental data. The structure was modeled as a shear-building model with four lumped masses at the floors. The damping matrix was obtained using the results of the experimental modal analysis. The Young's modulus was adjusted so that the numerical natural frequencies agreed with the experimental ones. The numerical model assumed negligible friction between the rails and the structure. Additionally, some statistical techniques, such as MAC, COMAC, ACF, and PSD, were used to show that the numerical model is able to predict baseline response data with high level of certainty. Finally, note that this model was just used to better understand the behavior of the test structure, rather than a damage detection tool.

In the feature extraction section, the AR models were subject to special attention. The estimated parameters as well as residual errors were tested as damage-sensitive features. The AR parameters' amplitude were shown to decrease, accordantly, for smaller gaps between the bumper and suspended column, i.e., the smaller the gap, the smaller the amplitude of the AR parameters. On the other hand, the residual errors were shown to increase significantly for those states with damage. In complementary analysis, four techniques based on AIC, PAF, RMS error, and SVD were presented for AR model order estimation. It was observed for one channel that the techniques do not give a unique solution for the AR model order when they are applied to baseline condition data. Nonetheless, the results suggest that the optimal order is in the range of 15 to 30. It was also shown that the AIC, PAF, and RMS error techniques suffer from the fact that, for each order, all model parameters must be estimated in order to calculate those values. Conversely, the SVD technique does not require prior estimation of the model parameters, which requires reduced computational efforts compared to the other three techniques. Even though the SVD technique gives the upper bound solution, the lower computational effort can be an advantage for implementation on embedded hardware. Additionally, one study was carried out to highlight the influence of the AR model order on the damage detection process. The analysis performed on the data sets showed that the lowest bound of the range of AR

model orders defined by the four techniques is capable of discriminating the undamaged and damaged state conditions, when using either the AR residual errors or parameters as damage-sensitive features, even in the presence of simulated operational and environmental variability. The analysis also showed that using an AR model of order less than that suggested by the four techniques does not allow discrimination of all the undamaged and damaged state conditions when the operational and environmental variability was included in the experiments. Finally, the results reported herein indicate that AR modeling might be an effective feature extraction technique when the damage introduces nonlinearities and the operational and environmental variations manifest themselves as linear system changes. In summary, the AR model was shown to be useful feature extraction technique for civil infrastructure SHM applications based on the three main reasons highlighted in Chapter 3: (i) they are sensitive to damage when it manifests in the form of nonlinearities or transitions between two states; (ii) the extraction of features only depends on response time series data; and (iii) simple and easy implementation. Additionally, it was shown that the AR models might be useful to address the two first levels in the hierarchy structure of damage identification, namely, damage detection and localization.

Other feature extraction techniques were tested, such as basic statistics (mean, standard deviation, skewness, kurtosis, normal probability plot, PDF), modal parameters, STFT, WT, Holder exponent, PCA, and correlation coefficients. Actually, the skewness, kurtosis, normal probability plot, and PDF were shown to be useful damage-sensitive features when damage introduces an asymmetry into acceleration response data. However, a high density of sensors throughout the structure or sensor's data fusion might be required to detect damage on a global basis, because the sensors might only be sensitive when they are located near the source of damage. Some of the limitations of using modal parameters as damage-sensitive features, specifically the natural frequencies, were demonstrated in this chapter. One could not conclude which data are from the damaged states by just examining changes in the natural frequencies when other sources of variability are present that influence the dynamic response characteristics of the structure. The Holder exponent technique proved that it might be used to extract damage-sensitive features when damage introduces discontinuities into the measured dynamic response data. Furthermore, the Holder exponent as well as AR residual errors were shown that the impacts are better detected with a time domain approach as opposed to a time-frequency domain approach (STFT and WT). The time-frequency domain approach was shown not have sufficient time resolution to capture individual impacts and, as such, these effects tend to be treated only in an average sense with these methods. On the other hand, the PCA confirmed the previous conclusions in the literature and proved to be a useful technique for feature dimension reduction by mapping a multidimensional space into a space of fewer dimensions when an appropriate feature extraction technique is used. Finally, the correlation coefficients on acceleration time series were not able to discriminate the undamaged and damaged states or to locate the damage among the

sensors, because the coefficients follow no systematic pattern that can be associated with the damaged states. Indeed, it was found that the impacts imposed by the bumper are a local phenomenon in time, which it is not enough to produce trends in the time series that can be identified by a global damage-sensitive feature such as the correlation coefficient.

In the statistical modeling for feature classification, the AR parameters were used as damage-sensitive features. The cluster analysis permitted one to conclude the existence of slight differences between the data from 2007 and 2009, in particular among the lowest level of damaged states (State#10, 15, and 16). Two explanations were pointed out: (i) the states with the lowest level of damage are characterized by few impacts between the bumper and suspended column, and so, they are averaged out on the AR parameters estimation; and (ii) the mechanism to set up the gap distance is not precise, and so, there is variability during the experiment that can cause slightly smaller or higher gaps than the theoretical ones.

The Shewhart X-bar control charts were employed in order to monitor the mean of the residual-error time series from all state conditions. Note that the mean is sensitive to the presence of outliers, so small blocks (four-length in this case) might be used for this type of damage. It was shown that the proper definition of the control limits is crucial to increase the classification performance. Results from the baseline limits showed that, in general, the number of outliers beyond the control limits increase for the damaged states even when they are affected by the operational and environmental variations. However, it was noted that this algorithm was not enough sensitive to discriminate those states with the lowest level of damage (State#10, 15, and 16). Recall that damage is introduced by the bumper mechanism in the form of singularities into the signals. Additionally, it was shown that the results might be improved by trading off true detection and false alarm when all the undamaged states with the operational and environmental variability are used to set up the control limits.

Nevertheless, in general, the control charts showed that SPC techniques might be used to detect the existence of anomalies in the acceleration responses, when a considerable number of data points fall outside the control limits. With such indications of damage, a next step might be to launch a full investigation, for example through visual inspections or local off-line NDT evaluation, to identify the cause of such anomalies. A problem that has often confronted the researchers using control charts is when to consider re-computing the control limits. Initially, the control limits need to be established assuming that both the structure and the SHM system are undamaged. However, because of normal aging of the structures, one should evaluate the need to re-calculate the control limits every time a statistically significant sign of instability is detected or when new operational and environmental conditions are encountered.

The performance of a novel algorithm, to extract damage-sensitive features under operational and environmental variability, was verified in the context of outlier detection. This algorithm uses a state-

space reconstruction to infer the geometrical and topological information about a deterministic dynamical system from observed scalar time series of the measured system response. Basically, it was proposed a MAR model of the baseline health condition to predict the state space, assuming that the model encodes the embedded vectors rather than observed time series. A hypothesis test is established that the MAR model will fail to predict future response if damage is present in the test condition and this hypothesis was investigated in the context of operational and environmental variability (non damage-related events). The applicability of this algorithm was demonstrated using univariate time delay embedding to reconstruct the structure's attractor at the individual accelerometers. An extension to a multivariate time delay embedding was performed to demonstrate the applicability of a global structure's dynamical attractor to detect damage.

For the univariate time delay embedding of time series from the accelerometers close to the source of damage, the results showed that the simulated damage, introduced in the form of nonlinearities, increase the complexity of the system as reflected by higher dimensions among the damaged structural state conditions. Actually, the author believes this increase in complexity is a common trait of almost all kinds of damage. Analysis in the predicted state spaces showed that the structural state conditions with damage assume statistically significant distortions in the trajectories compared to the baseline state condition. Furthermore, the operational and environmental effects, simulated with linear changes, do not significantly affect the underlying system's dynamical properties and, consequently, the trajectory of the system in the state space. However, a parametric study showed that embedding dimensions higher than optimum suggested by the SVD of the trajectory matrix could decrease the performance of the classifier. It is important to note that this algorithm was capable to classify the low-damaged state conditions even in an under-embedding state space. For these data sets, this fact highlights better performance than, for instance, the cluster analysis and SPC technique. On the other hand, the multivariate time delay embedding to reconstruct a global attractor was revealed to have limitations to detect nonlinearities (the damage) in a global basis in the presence of linear changes caused by operational and environmental variations. For this type of damage, this is an indication that the multivariate embedding amplifies the linear changes due to varying mass and stiffness and, consequently, averages out the effects of local damage in the form of singularities in the signal. Therefore, for these data sets, this algorithm is more appropriate to detect local damage rather than to detect the existence of damage in a global basis.

Some limitations of the state-space approach include reliance upon stationary (in a statistical sense) inputs and the need for training this algorithm with known baseline conditions (although training requirements for such algorithms have been shown to be very reasonable [110], unlike some neural network approaches). It is further noted that if a situation develops whereby the linear change effects due to operational/environmental variability completely overwhelm the nonlinear dynamic changes, then the sensitivity of this approach will be compromised; in that case, a supervised technique that

employs the MAR parameters themselves may be useful in better classification [140]. Overall, however, the generality of the MAR approach would suggest it could be quite useful for a number of time series-based predictive modeling SHM applications where networked time series comprise the fundamental raw data set and physical modeling is either too computationally burdensome or the physics are not well-known (and could have high uncertainty, such as in bolted joint connections).

In conclusion, for systems that operate in a linear manner during normal operation, the applicability of this novel nonlinear feature extractor and damage-detection approach, based on the prediction of the state space using a MAR model, has been demonstrated with experimental data and it has been shown to be a reliable way to detect local damage when it induces transitions from linear to nonlinear response, even in the presence of operational and environmental variability.

The performance of the machine learning algorithms for data normalization was also demonstrated. A study was carried out addressing the implementation and comparison of those algorithms for outlier detection that establish the normal condition as a function of the operational and environmental variability. Although several procedures for data normalization have been reported in the literature, there is no study that has compared these algorithms on a common set of data to assess their relative performance. Therefore, the study reported herein intends to provide such a comparison. It is important to note that none of these algorithms requires a direct measure of the sources of variability. Instead, the algorithms rely only on measured response acceleration time series data acquired under the varying operational and environmental conditions. The AANN-, FA-, MSD-, and SVD-based algorithms were all shown to be reliable ways to create a global DI that can separate damaged from undamaged cases, even when simulated operational and environmental variability is present in both the undamaged and damaged condition data. Furthermore, the ROC curves, along with classification performance on the basis of Type I/Type II errors, showed that FA- and SVD-based algorithms are more appropriate when one wants to minimize false-positive indications of damage with economic issues driving the SHM. On the other hand, the MSD- and AANN-based algorithms are preferred when one wants to minimize false-negative indications of damage, with life-safety issues being the primary motive for deploying the SHM system. In terms of overall performance, regardless of the AANN-based algorithm has some advantages in terms of finding nonlinear correlations among the features, the MSD-based algorithm was shown to be the best in terms of the classification performance, reduced computational efforts (during both training and test phases), and the fact that no assumptions are required regarding its architecture. Note that those facts along with the simplicity make the MSD-based algorithm also a better choice for implementation on current embedded hardware. Additionally, a parametric study carried out, to establish the relationship between the classification performance and the number of factors in the AANN- and FA-based algorithms, permitted one to conclude that those algorithms maximize the classification performance when the number of modeled factors is, approximately, equal to the number of simulated changes (mass and

stiffness) affecting the sensors readings. In fact, these results are of extreme importance, because they permit one to validate those algorithms for real-world applications, whose number of factors is often unknown.

Finally, a study was carried out to verify the applicability of the MSD-based algorithm to create a DI that takes into account the operational and environmental variations and that follow a chi-square distribution for the undamaged condition. For multi-dimensional Gaussian distributed feature vectors, a hypothesis test was established that the algorithm would reject the null hypothesis (undamaged condition) if DI does not follow a chi-square distribution. Based on the fact that data measured from real-world structures are often limited in size and the fact that it is difficult to ensure multi-dimensional Gaussian distributed feature vectors, it was shown that the underlying non-Gaussian-distributed damage-sensitive features affect the distribution of the DIs from the undamaged condition for varying AR model order. However, it was shown that the distribution of those DIs approximates a theoretical chi-square distribution and the classification is optimized when the appropriate AR model order given by the CIC is adopted. On the basis of ROC curves and Type I/II errors, with respect to the false-alarm rate, the algorithm performs within the tolerance given by the confidence interval in all accelerometers, i.e., the observed false-alarm rate is close to the chosen level of significance. For the true-detection rate, this algorithm proved to be very sensitive to the location of the damage relative to the sensors, with those sensors closer to the source of damage providing a higher true-detection performance. Once again, this fact highlighted that real-world structures may require high density of sensors to detect and/or locate damage throughout the structure.

4.8 Contributions

The main contributions of this chapter are: (i) the demonstration of the applicability of the MAR model to predict the state space of a dynamical system and to extract features sensitive to damage and relatively insensitive to operational and environmental variations; (ii) the applicability and comparison of several machine learning algorithms to remove the operational and environmental variations from the features and to detect damage; and (iii) the study that makes a correlation between the optimal AR model order given by an information criterion technique and the classification performance of the MSD-based algorithm.

5. ALAMOSA CANYON BRIDGE

5.1 Introduction and Overview

In 1996 and 1997 several dynamic tests were performed on the Alamosa Canyon Bridge, New Mexico, to quantify the variability in identified modal parameters caused by operational and environmental effects. Furthermore, several vibration-based damage detection methods were applied to the experimental modal analysis results. In the subsequent report [54], the authors highlighted two main contributions. First, an in-situ quantification of variability in measured modal parameters. Second, the extension of a strain-energy-based damage detection method to structures that exhibit plate-like bending or bending in two directions. In fact, the author believes that separating changes in sensor readings caused by damage from those caused by changing operational and environmental conditions is one of the biggest challenges for transitioning SHM from the research to practice. With this in mind, in 2008 were performed new dynamical tests to estimate the dynamic characteristics by comparing the modal parameters to the previous ones, which could be used to find out indications of possible structural degradation.

The main contribution of this chapter is the applicability of some techniques described in Chapter 3, and applied in Chapter 4, to extract damage-sensitive features and to remove the operational and environmental variability from the extracted features on data from a bridge, in order to pave the way to data-based methods to detect damage in real-world civil infrastructure. Therefore, in the feature extraction step, the modal analysis and AR models are the focus of special attention. The former because modal parameters are the features that have been most studied by the community along with the fact that they were studied in previous reports. The latter because its application in SHM has increased, significantly, in the last decade. In the statistical modeling for feature classification step, the application of the data normalization algorithms for outlier detection will be focus of special attention to evaluate their capacity to “learn” the normal condition under different types of features. It is important to note that these algorithms do not require a direct measure of the sources of variability. Instead, the algorithms rely only on response time series data acquired under varying operational and environmental conditions. Note that even though the visual inspection in 2008 showed some signs of degradation, with most of them already evident in the previous tests, these changes are not significant enough to establish that the bridge is “structurally deficient” and/or it has degraded since 1996. Thus,

this chapter applies the SHM-SPR paradigm to real-world data from one span of the bridge measured in three distinct periods with the assumption that no damage present in the structure.

The layout of this chapter is as follows. Section 5.2 provides a brief description on the test structure, experimental procedure, and collected data sets in the last 12 years. In Section 5.3 the modal parameters (natural frequencies, damping ratios, and mode shapes) as well as the AR parameters and residual errors are demonstrated as damage-sensitive features and their sensitivity to the differential temperature is also shown. In Section 5.4, four machine learning algorithms are applied to remove the operational and environmental variability from the measured data. Then, each feature vector is reduced into a DI for outlier detection. Finally, Section 5.5 concludes with a general discussion regarding the effectiveness of the four algorithms to normalize the data acquired under operational and environmental variations, and Section 5.6 summarizes the main contributions.

5.2 Operational Evaluation and Data Acquisition

The Alamosa Canyon Bridge is located adjacent to highway I-25 approximately 16 km (10 miles) north of Truth or Consequences, New Mexico, USA. This two-line bridge has seven simply supported spans with a common pier between successive spans and two abutments at both ends. Each span consists of a concrete deck supported by six steel girders and it is approximately 7.3 m (24 ft) wide and 15.2 m (50 ft) long. Figure 5.1 depicts the longitudinal side and identifies the first span of the bridge where the vibration tests were performed.



Figure 5.1. Alamosa Canyon Bridge near to Truth or Consequences, New Mexico, USA, in 2008.

The bridge was constructed around 1937 and was replaced by a new one when the Interstate Highway System was constructed in the early 1960s. Currently, the bridge is owned by the New Mexico Department of Transportation and is closed for normal traffic. It has been used as a test bed structure for several years. Under this operational state, researchers from the Engineering Institute at Los

Alamos National Laboratory have performed several dynamical tests on the bridge, namely in 1996, 1997, and 2008, to examine the variability of the deck modal parameters.

In all the three distinct periods of time, the same instrumentation architecture, namely one data acquisition system, 31 uniaxial accelerometers (including one at the driving point), and one impact hammer were used in the measurement process. Figure 5.2 shows a schematic representation of the array of sensors along with the basic structural dimensions. All sensors and the hammer were connected to the data acquisition system using coaxial wires. Even though Farrar et al. [54] have shown that in the reality the spans have some degree of structural continuity, for simplification, in this study the first span is treated as simply supported structure.

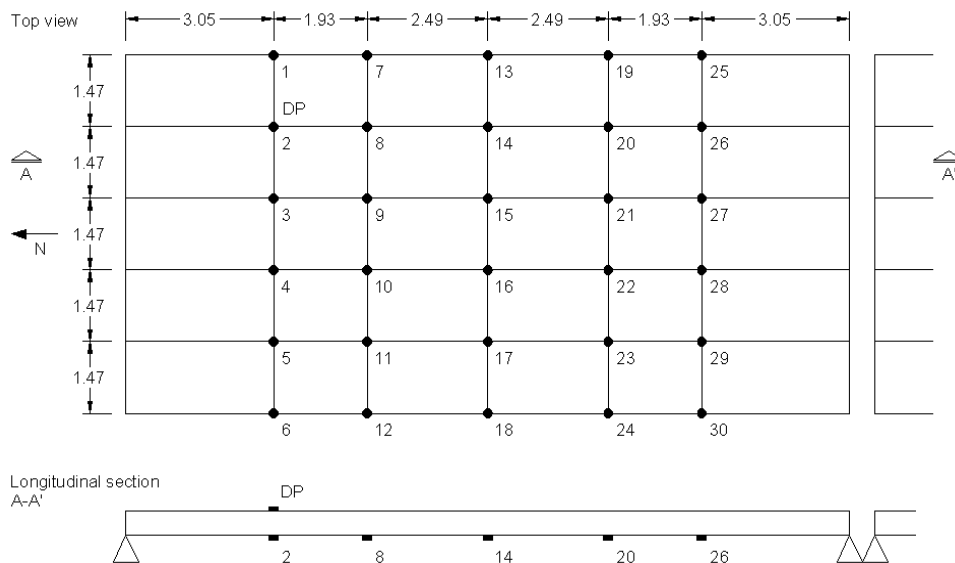


Figure 5.2. Schematic representation of the accelerometers and driving point (DP) locations.

Two different data acquisition systems were used during the tests. In 1996 and 1997 the data acquisition system consisted of a Toshiba TECRA 700 laptop computer, four Hewlett Packard (HP) 35652A input modules with 14-bit resolution and 80 dB dynamical range that provide power to the accelerometers and perform analog to digital conversion of the accelerometer signals, an HP 35651A signal processing module that performs the fast Fourier transform calculations, and a commercial data acquisition/signal analysis software package produced by HP. On the other hand, in 2008, the data acquisition system consisted of a NI PXI-1042Q with six modules NI PXI-4462. Each module has 24-bit resolution ADCs with 118 dB dynamic range and four analog input channels. The system was set up to be consistent with the parameters of the previous tests performed on the bridge, namely to yield time series and FRFs, respectively, with the same time and frequency resolution of the previous measurements. Other instrumentation was common in the three tests.

PCB model 336C piezoelectric accelerometers were used to measure the dynamic response at fixed 30 locations on the steel girders, as shown in Figure 5.2. These accelerometers have a nominal sensitivity

of 1000 mV/g, a specified frequency range of 1-2000 Hz, and an amplitude range of ± 4 g. The accelerometers were attached to the bottom flange of the steel girders using PCB model 080A27 magnetic mounts, as shown in Figure 5.3a.

A Wilcoxon Research model 736T accelerometer was used to measure the dynamic response at the driving point located on the concrete deck. This accelerometer has a nominal sensitivity of 100 mV/g, a frequency range of 5-15000 Hz, and an amplitude range of ± 50 g. The accelerometer was attached to the deck surface using aluminum mounting blocks, as shown in Figure 5.3b.

A PCB model 086B50 impact hammer with a load cell attached to its head was used to excite the deck. The load cell has a nominal sensitivity of 164.1 mV/kN (0.73 mV/lb) and a peak amplitude range of 22.24 kN (5000 lbs). A soft hammer tip was used to better excite the low frequency response of the bridge.

Five indoor-outdoor digital-readout thermometers were located across the center of the span. More details on the thermometers as well as the data acquisition system can be found in the reference [54].



Figure 5.3. Attachment of the accelerometers to the bridge: (a) on the bottom of the steel girders; and (b) on the deck surface.

Notice that during the 2008 tests, incompatibilities were detected in one module of the data acquisition system. As a result, it was decided to keep the same architecture by turning off several accelerometers (2, 5, 8, 11, 14, 17, 20, 23, 26, and 29). Figure 5.4 shows an impact being applied at the driving point and Figure 5.5 shows the area underneath the first span of the bridge, where one can see the data acquisition system and computers as well as sensors attached to the bottom flange of the girders. Notice that throughout this chapter, the sensors attached to the steel girders are also referred to nodes.

The 24-hour tests performed from July 29 to August 3, 1996 and from July 21 to 23, 1997 are summarized in Table 5.1 and Table 5.2, respectively. More details about these data sets can be found in reference [54]. On the other hand, Table 5.3 summarizes the tests performed from September 4 to 5, 2008. The data acquisition system was set up to measure acceleration and force time series as well as to compute the power spectra, FRFs, and coherence functions of the measurements. The sampling

parameters were specified to calculate FRFs from a 16-sec time window discretized with 2048 observations. The FRFs were calculated for a frequency range of 0 to 50 Hz at a frequency resolution of 0.0625 Hz. A force window was applied to the force time series and an exponential window was applied to the acceleration time series. AC coupling was specified to minimize DC offsets. For illustration purposes, one measured force at the hammer's tip and one measured acceleration time series at node 15 are shown in Figure 5.6. Additionally, Figure 5.7 shows the FRFs for time08_3.



Figure 5.4. An impact being applied adjacent to the driving point (in 2008).



Figure 5.5. Picture of the area underneath the first span with the data acquisition system (in 2008).

Table 5.1. Summary description of the data sets from the 24-hour test in July/August, 1996.

Test Label	Date	Time	Number of Channels	Number of Impacts
sp1_hm07	1996/07/31	09:15	32	1
sp1_hm08		11:30		
sp1_hm09		13:12		
sp1_hm10		15:13		
sp1_hm11		17:52		
sp1_hm12		20:09		
sp1_hm13		21:20		
sp1_hm14		23:29		
sp1_hm15	1996/08/01	01:21		
sp1_hm16		03:19		
sp1_hm17		05:19		
sp1_hm18		07:03		
sp1_hm19		09:22		

Table 5.2. Summary description of the data sets from the 24-hour test in July, 1997.

Test Label	Date	Time	Number of Channels	Number of Impacts
time97_1	1997/07/21-23	04:00	32	5
time97_2		06:00		
time97_3		08:00		
time97_4		10:00		
time97_5		12:00		
time97_6		14:00		
time97_7		16:00		
time97_8		18:00		
time97_9		20:00		
time97_10		22:00		
time97_11		24:00		

Table 5.3. Summary description of the data sets measured in September, 2008.

Test Label	Date	Time	Number of Channels	Number of Impacts
time08_1	2008/09/04	15:12	22	5
time08_2		15:17		
time08_3	2008/09/05	10:00	22	10
time08_4		17:20		

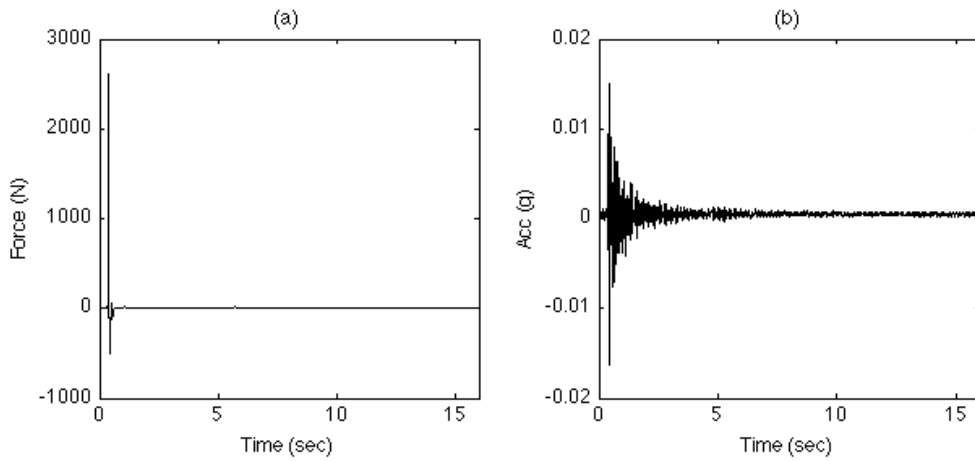


Figure 5.6. Response caused by a hammer impact (time08_3): (a) force; and (b) acceleration time series at node 15.

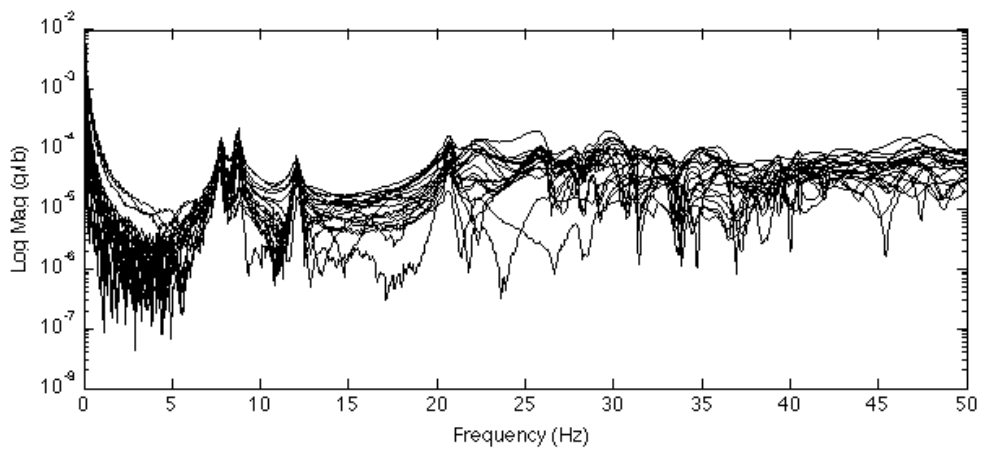


Figure 5.7. FRFs in overlaid format (time08_3).

Once the bridge is closed to traffic, it will only be possible to identify sources of operational and environmental variability from the data acquisition systems, inconsistencies in the excitation (hammer), temperature variations, and adverse weather conditions. However, the unique source of variability measured was the difference temperature across the deck in 1996 and 1997 tests. Nevertheless, for completeness, Table 5.4 summarizes the daily average air temperature and humidity at Truth or Consequences for one day of each period of tests [141]. The higher percentage of humidity (64%) in 1997 might be associated to rain observed on the days before the tests. This table permits one to conclude that the percentage of humidity of the tests in 2008 is closer to the tests in 1996 than in 1997. However, in terms of temperature variation, the tests in 1997 are closer to 1996 than 2008 to 1996. Nevertheless, note that the differences in the air temperature do not imply that the difference temperature across the deck is different.

Table 5.4. Daily average temperature and humidity records at Truth or Consequences, New Mexico.

Year	Temperature °C (°F)			Humidity %
	Mean	Maximum	Minimum	
1996/08/01	27 (80)	31 (88)	18 (65)	44
1997/07/22	24 (76)	32 (90)	18 (65)	64
2008/09/04	22 (72)	30 (86)	16 (60)	41

Finally, during the tests performed in 2008, some indications of structural degradation were observed, mainly the joints were filled with debris and the pavement showed some signs of transverse surface cracking, as show in Figure 5.8. However, similar observations had been made in 1996 and 1997. Therefore, the 2008 visual inspection of the bridge was not conclusive regarding the existence of accumulated structural degradation when compared to the previous tests.

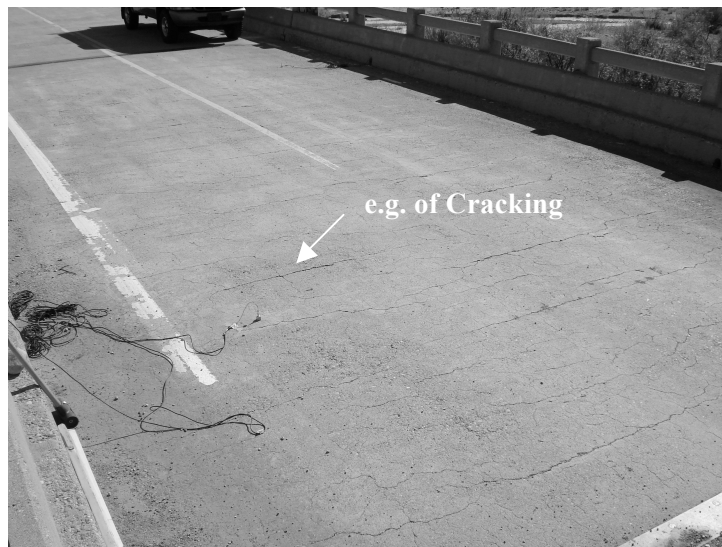


Figure 5.8. Transverse cracking on the surface of the deck pavement (in 2008).

5.3 Feature Extraction

The goal of this section is to use the modal analysis and AR models to extract damage-sensitive features from time series, namely the modal parameters (i.e. natural frequencies, damping ratios, and mode shapes) as well as AR parameters and residual errors. A study is conducted to show the sensitivity of those features on the temperature using the data from the 24-hour tests performed in 1996 and 1997. Additionally, the dimension of a dynamical system is tested as damage-sensitive feature.

5.3.1 Modal Parameters

The current way to better understand the dynamics characteristics of the structures is to define the modal parameters. Some SHM procedures rely on the modes to detect damage, because it is expected that changes in either material properties or boundary conditions might change the modes. However, as shown in Section 2.2, the operational and environmental variability can impose changes in the dynamical properties of a system and mask changes in the modal parameters related to damage. Therefore, the modal parameters will be extracted for two reasons (i) to highlight the variability on the modal parameters caused by thermal effects using the 24-hour tests performed in 1996 and 1997 and (ii) to verify the existence of changes in the modal parameters estimated in 2008 by comparing with the modal parameters estimated in 1996 and 1997.

The modal parameters were estimated by curve fitting the FRFs from each test, i.e., the natural frequencies, damping ratios, and mode shapes of the deck were estimated using a RFP global curve-fitting algorithm [100, 136]. The RFP is a frequency domain curve-fitting algorithm that operates directly on the complex FRF and it performs a least square error curve fit to all FRFs. The first six modes are concentrated in two distinct frequency ranges. Therefore, in order to improve the results, the FRFs were curve fitted in two frequency bands (6.00-14.0 Hz and 19.0-28.0 Hz). The bands for the RFP algorithm were determined by examining the CMIF using the imaginary part of the FRFs. Notice that the fit function outside the band assumes zero value.

In order to show the dependency of the modal parameters on the temperature, Figure 5.9a and b plot, respectively, the variability of the first natural frequency and damping ratio along with the differential temperature across the deck for the 24-hour test performed in 1996. The figures suggest that the variability of the natural frequency is proportional to the differential temperature across the deck. Furthermore, the corresponding damping ratios seem to be inversely proportional to the temperature (and so to the first natural frequency). The same trend is valid in the 24-hour test performed in 1997 as shown in Figure 5.10.

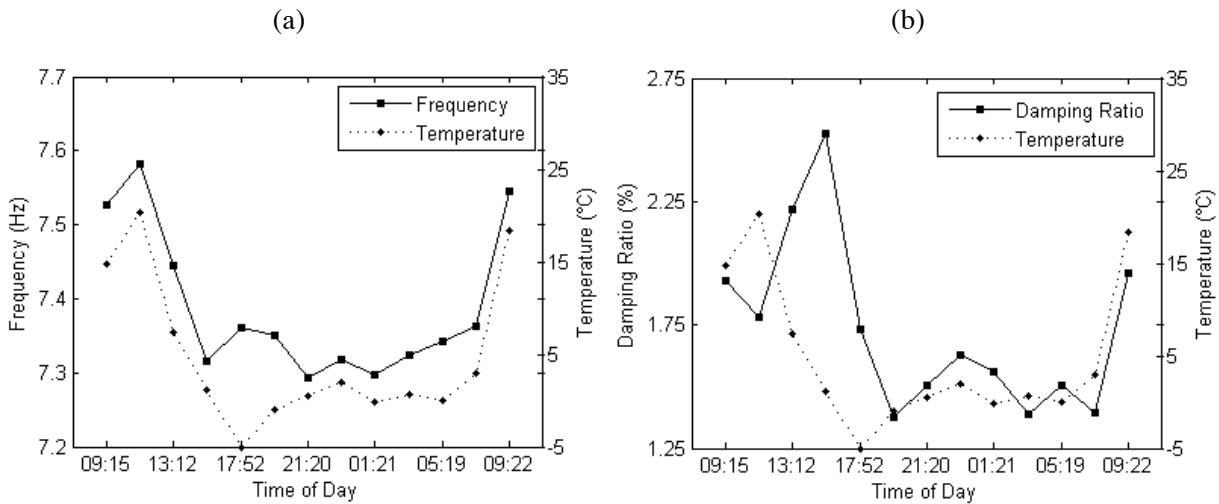


Figure 5.9. Variability in the modal parameters along with the differential temperature across the deck during the 24-hour test in 1996: (a) first natural frequency; and (b) first damping ratio.

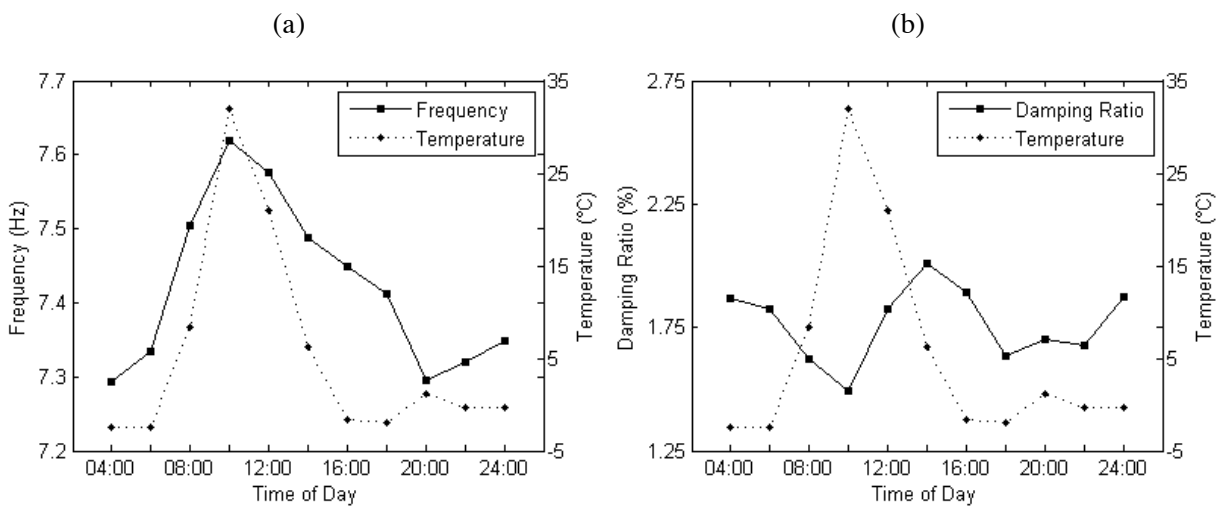


Figure 5.10. Variability in the modal parameters along with the differential temperature across the deck during the 24-hour test in 1997: (a) first natural frequency; and (b) first damping ratio.

Table 5.5 summarizes the maximum values obtain in the first natural frequency and damping ratio during the 24-hour tests in 1996 and 1997 as well as the estimated values in 2008 for time08_3 (10:00) and time08_4 (17:20). Taking the difference between the extreme values and dividing by the maximum value, in 1996 one can observe variations of -3.8% and -46%, respectively, in the first natural frequency and damping ratio. In 1997, approximately the same magnitude of variability was observed, respectively, -4.3% and -26%. The comparison between 1996-1997 and 2008 dynamical tests permits one to conclude that the variability in the first natural frequency is of the same magnitude (-4.3%) and the variation in the damping ratio (-17%) confirms the previous indications. Although the

differential temperature was not measure in 2008, based on the close correlation (especially the natural frequencies) with previous results, where the differential temperature was measured, the differences between time08_3 and time08_4 are most likely related to the differential temperature across the deck. Additionally, Table 5.6 summarizes the first natural frequency and damping ratio for the three periods of tests at 10:00 (morning) and 17:20 (afternoon). Note that the interpolation is used when no measurement is available at the specific time. The simple comparison of the natural frequency's amplitude does not permit one to draw any conclusions on the presence of damage. Actually, in the afternoon one can observe frequency variations of less than 1%. Furthermore, and assuming that the structure is undamaged, the damping ratios show high variability along the day (over 30% in 1997).

Table 5.5. Maximum and minimum values of the first natural frequency and damping ratio observed in 1996, 1997, and 2008.

Year	Maximum		Minimum	
	Frequency (Hz)	Damping Ratio (%)	Frequency (Hz)	Damping Ratio (%)
1996	7.58	2.5	7.29 (-3.8%)	1.4 (-46%)
1997	7.62	2.0	7.29 (-4.3%)	1.5 (-26%)
2008	7.75	1.5	7.41 (-4.3%)	1.3 (-17%)

* Percent change between maximum and minimum is shown in parentheses

Table 5.6. Values of the first natural frequency and damping ratio observed in 1996, 1997, and 2008 at 10:00 (morning) and 17:20 (afternoon).

Year	10:00		17:20	
	Frequency (Hz)	Damping Ratio (%)	Frequency (Hz)	Damping Ratio (%)
1996	7.56 (-2.5%)	1.8 (20%)	7.35 (-0.8%)	1.4 (7.7%)
1997	7.62 (-1.7%)	1.5 (0.0%)	7.42 (0.1%)	1.7 (31%)
2008	7.75	1.5	7.41	1.3

* Percent change between 2008 and 1996/1997 is shown in parentheses

To summarize, the first six natural frequencies and modal damping ratios from the 24-hour tests of 1996 and 1997, along with the ones from the time08_3 and time08_4 in 2008, are plotted in Figure 5.11. Even though the relative variation between natural frequencies could have changed, the figure shows that all the natural frequencies from 2008 are within the variation measure in 1996 and 1997 over a 24-hour period. However, the same conclusion is not valid for the damping ratios. Indeed, one

out of two damping ratios of the sixth mode shape are significantly far from the 1996-1997 mean. Therefore, assuming that the structure is undamaged and taking into account the variability observed in the damping ratio estimates for varying number of extra terms in the RFP method along with the variability found in the three periods, one can conclude that this is a further indication of the challenge to use this feature for damage detection.

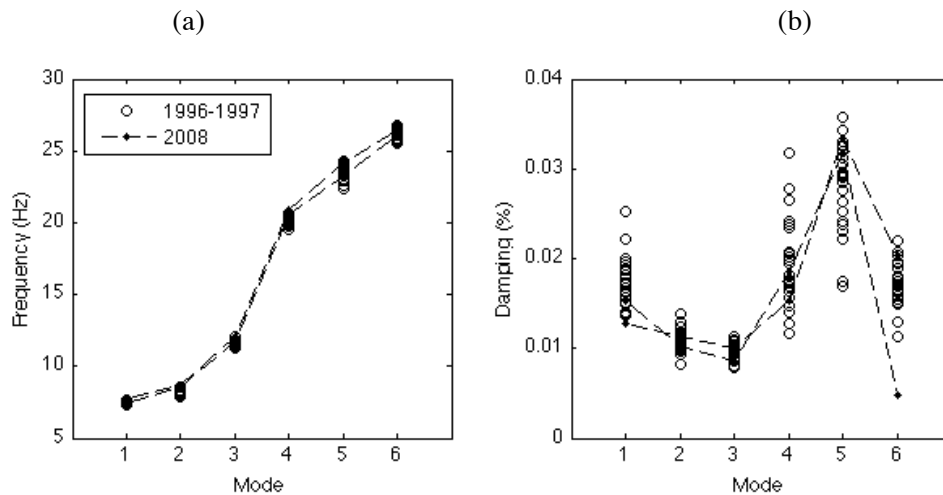


Figure 5.11. Modal parameters of all tests in 1996, 1997, and 2008: (a) natural frequencies; and (b) damping ratios.

Figure 5.12 plots the first mode shape for two independent tests during the 24-hour vibration tests performed in 1996, 1997, and 2008, corresponding to the modal parameters summarized in Table 5.5. The first mode shape is related to plate-like bending. Although the structure is symmetric about its longitudinal centerline axis, an asymmetrical variation in the first mode shape that changes throughout the day is evident from the plots. This asymmetry along the longitudinal axis is correlated with the time of day and associated to solar heating. The thermal effects are more pronounced because of the north-south orientation of the bridge. Therefore, if not properly accounted in the damage detection process, such changes in the dynamics response characteristics can potentially result in false indications of damage. For instance, in Figure 5.12a if the mode at 11:30 was considered to be the baseline condition, a classification algorithm would identify the mode at 21:20 as some form of an outlier. This outlier could inappropriately be labeled as damaged if the environmental variability associated with this feature was not taken into account in the damage detection process.

In conclusion, throughout this section, it was shown that variations in the modal parameters exist and these variations are primarily attributed to thermal effects. Indeed, this fact reinforces the need to use data normalization algorithms that are capable of removing the effects of the operational and environmental variations from the measurements, as will be discussed later in Section 5.4.

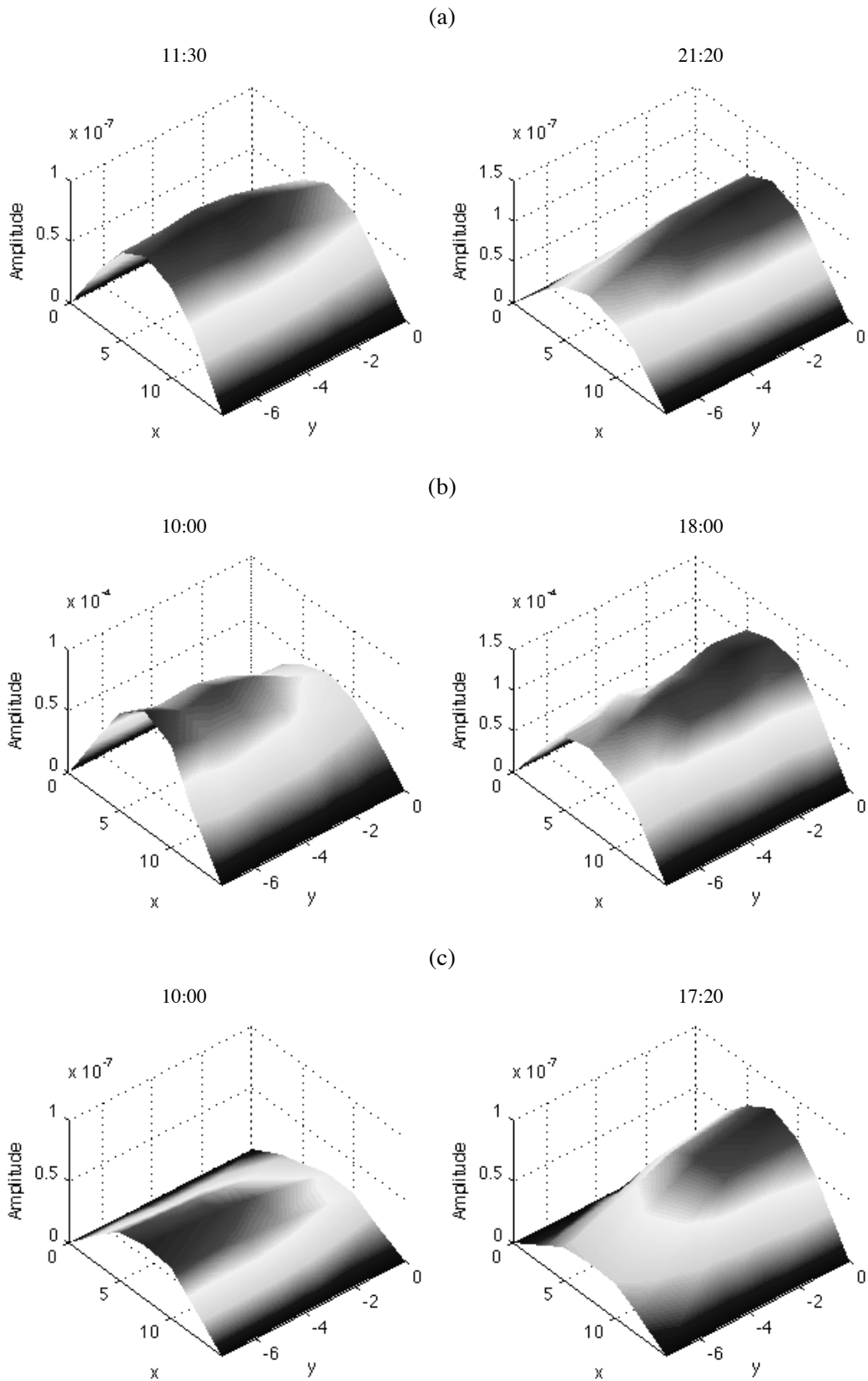


Figure 5.12. First mode shape for the maximum and minimum natural frequencies observed in: (a) 1996; (b) 1997; and (c) 2008.

5.3.2 Auto-regressive Models

In the last chapter, the applicability of the AR parameters and residual errors to detect damage under simulated operational and environmental variability was demonstrated. Herein, this section intends to evaluate the applicability of those damage-sensitive features to real-world data. Note that for illustration purposes the following analysis is focused only on data sets from the mid-span node 15.

5.3.2.1 Linear Assumption

The AR models have been used for modeling the response of the structure to random inputs. However, in this case and as shown in Figure 5.6, the input is in the form of a impulse force and the sensor response is in the form of a decaying transient response that oscillates until finally approaching zero after a certain time. A brief explanation using a linear system is given below to justify the applicability of the AR models to predict transient responses.

The simplest vibration system can be represented by a single mass m connected to a spring with stiffness k , damping mechanism with viscous damping d , and an external excitation source $f(t)$. The mass is allowed to move only along the spring elongation direction. This system is currently called single-degree-of-freedom (SDOF) system and it is shown in Figure 5.13. Mathematically, the input-response relationship can be described as

$$m\ddot{s} + d\dot{s} + ks = f(t). \quad (5.1)$$

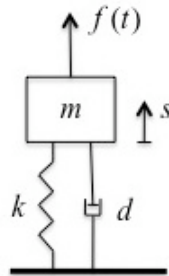


Figure 5.13. SDOF system.

As derived in Worden and Tomlinson [142], the output of this system can be described at a sequence of regularly spaced times t_i . Using the *backward* finite difference method and after some rearrangement, a discrete-time representation of Equation (5.1) can be given by

$$s_i = \phi_1 s_{i-1} + \phi_2 s_{i-2} + \beta_1 f_{i-1}, \quad (5.2)$$

where ϕ_1 , ϕ_2 , and β_1 are constant parameters. Assuming an impulse response, the force term f_{i-1} in Equation (5.2) is zero and, consequently, the response turns out to be a regression in the form of the AR model in Equation (3.5).

In order to illustrate the applicability of the AR model to fit transient time series responses in a simple example, two different impact forces are applied on the SDOF system, namely $I_1 = 100 \times 10^3 N$ and $I_2 = I_1 \times 2$. The system is assumed to have the following properties: $m = 300 kg$, $d = 1095 N - s / m$, and $k = 400 \times 10^3 N / m$. Figure 5.14 plots both three-sec free vibration responses in overlap format. Figure 5.15a plots the AR(5) parameters estimated based from both time series responses and Figure 5.15b shows the predicted responses, along with the AR residual errors, using an AR model with parameters estimated from the response caused by I_1 . As one can visualize, the AR parameters from both responses overlap and the residual errors are negligible. Therefore, for linear systems, one can clearly verify the applicability of the AR models to estimate transient response data.

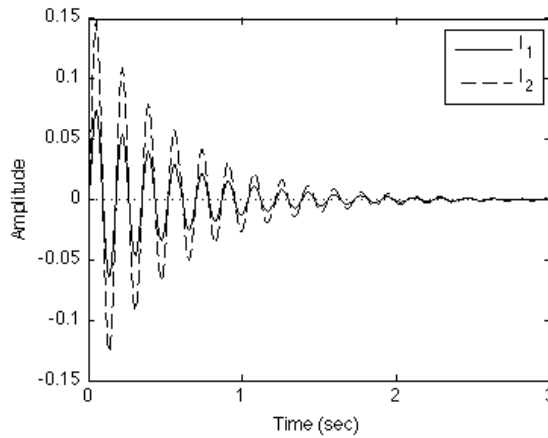


Figure 5.14. Free vibration responses caused by two impulse forces (I_1 and $I_2 = I_1 \times 2$).

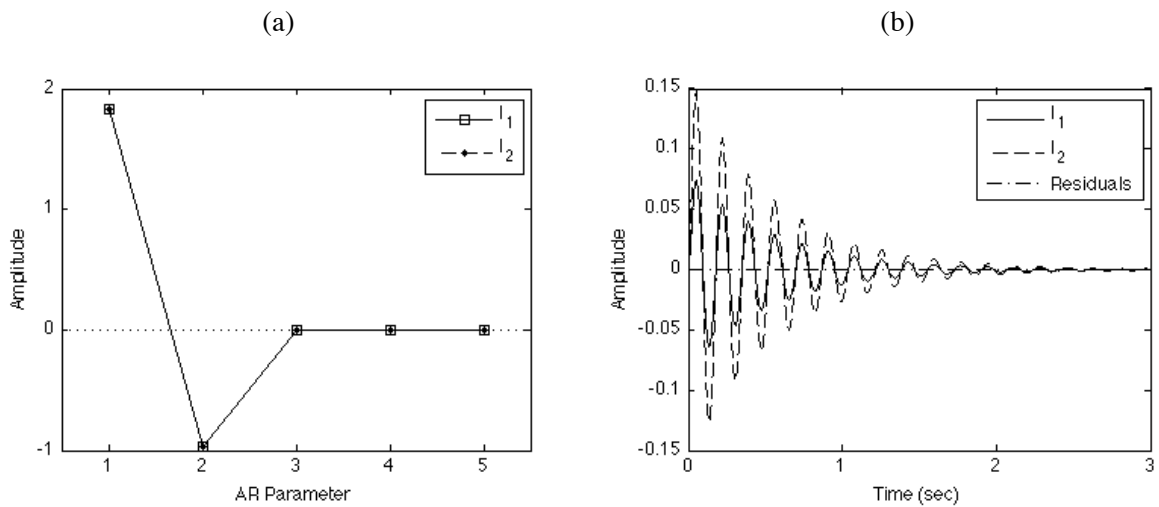


Figure 5.15. AR model analysis: (a) estimated parameters based on responses caused by I_1 and I_2 ; and (b) responses estimated using parameters from the response caused by I_1 .

5.3.2.2 Appropriate Model Order

As shown in Chapter 4, the proper definition of the AR model order is a key step to detect damage. In order to identify the appropriate order at node 15, the four techniques described in Section 3.2.3 are applied to data sets from 1996, 1997, and 2008. Figure 5.16, Figure 5.17, and Figure 5.18 plot the normalized average values as a function of the model order p ($p=1,2,\dots,100$), using the four proposed techniques, namely, AIC, RMS, SVD, and PAF. Note that the plotted curves are the average of curves estimated on 13, 11, and 20 time series from the three periods, respectively. From a global perspective, some observations can be pointed out: (i) the AIC function is not minimized in the selected range; (ii) all four techniques do not give a unique solution when looking at the convergence point of each curve; and (iii) the converge order for RMS and SVD techniques is around 25. Therefore, in order to keep the AR model order as low as possible and using the same procedure as in Chapter 4, throughout this chapter, an AR(25) model will be used as the basis to extract damage-sensitive features.

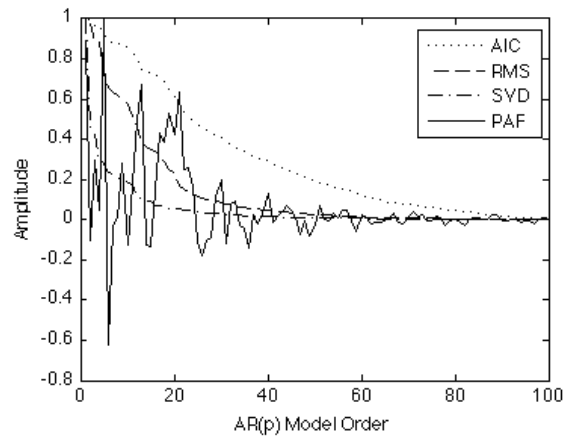


Figure 5.16. Normalized 13-average AIC, RMS, SVD, and PAF functions during the 24-hour test in 1996 (node 15).

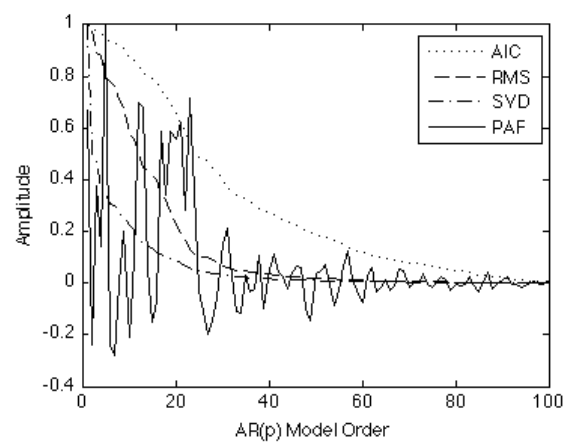


Figure 5.17. Normalized 11-average AIC, RMS, SVD, and PAF functions during the 24-hour test in 1997 (node 15).

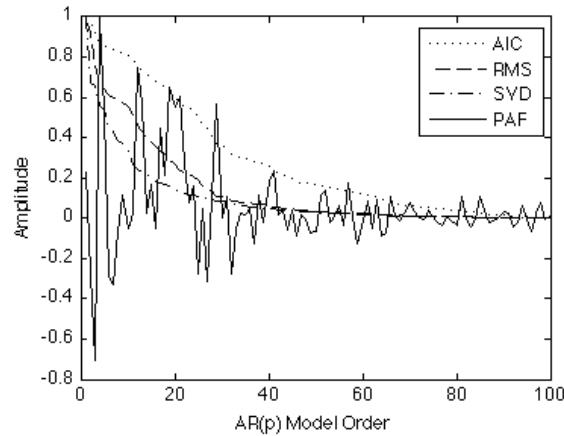


Figure 5.18. Normalized 20-average AIC, RMS, SVD, and PAF of the tests performed in 2008 (node 15).

5.3.2.3 AR Parameters

When measuring data from real-world structures, the researcher frequently faces challenges in the parameter estimation caused by the operational and environmental effects. Note that besides the temperature, traffic, and humidity, another sources of variability need to be addressed. As highlighted in Section 2.2, it is also well known that the modal testing procedures might produce variable results, because of inevitable noise caused by electrical disturbance, operator errors, and variable testing environment. In order to produce estimators that are not affected by the presence of outliers, the concept of robust statistics [143] is considered to obtain averaged AR parameters. The procedure can be described in the following steps. First, AR parameters (or variables) are estimated on time series from each data set using the least-squares technique. Second, the mean and standard deviation of each parameter is computed. Afterwards, assuming a normal distribution function for each variable, the parameters beyond two standard deviations of the mean (i.e. 95% confidence) are considered outliers and discarded from the data sets. Finally, a new outlier-free mean of each parameter is computed. Obviously, the new mean represents a better estimation of the population mean, because it does not take into account the deviations caused by non-frequent parameters. This procedure can then be illustrated using the so-called error bars.

For node 15, Figure 5.19, Figure 5.20, and Figure 5.21 depict the error bars related to the AR(25) parameters estimated on time series from 1996, 1997, and 2008, respectively. For each parameter, the plots show the range with the mean (cross sign), and the upper and lower limits (dash) corresponding to two standard deviations from the original mean. Additionally, one can observe the new outlier-free mean of the parameters (dot). Note that outliers correspond to parameters falling beyond the upper and lower limits.

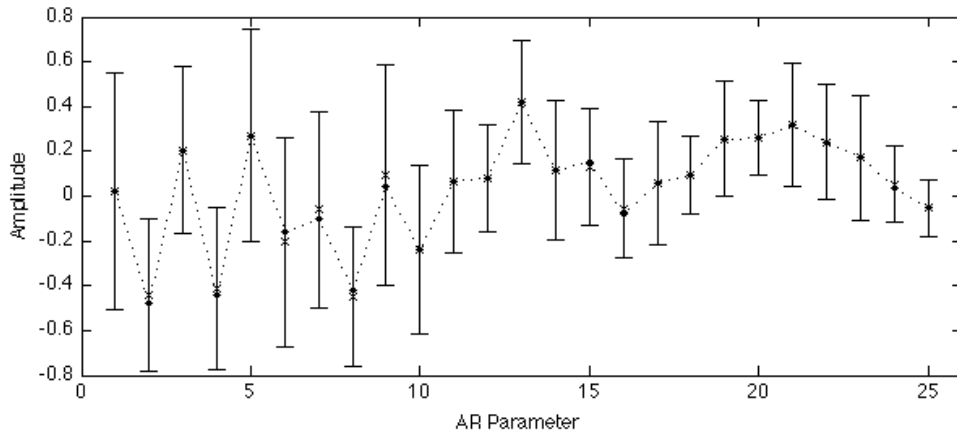


Figure 5.19. Error bar (two standard deviations) with AR(25) parameters estimated at node 15 during the 24-hour test in 1996 along with the outlier-free means (dots).

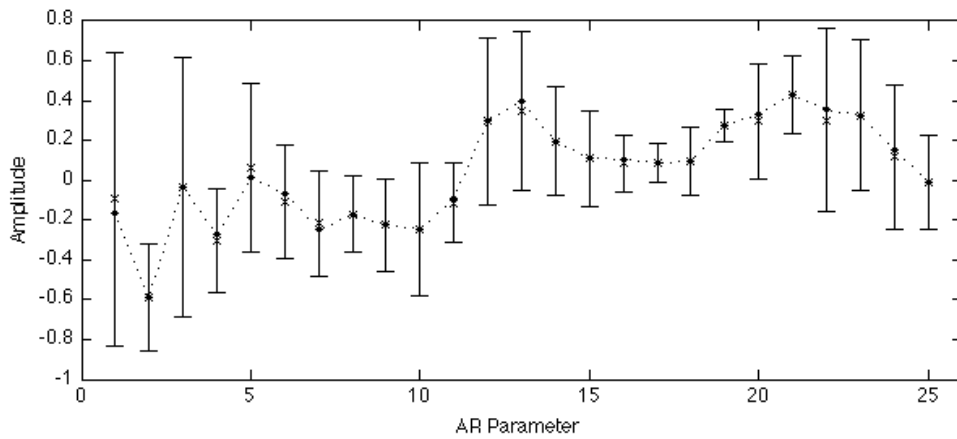


Figure 5.20. Error bar (two standard deviations) with AR(25) parameters estimated at node 15 during the 24-hour test in 1997 along with the outlier-free means (dots).

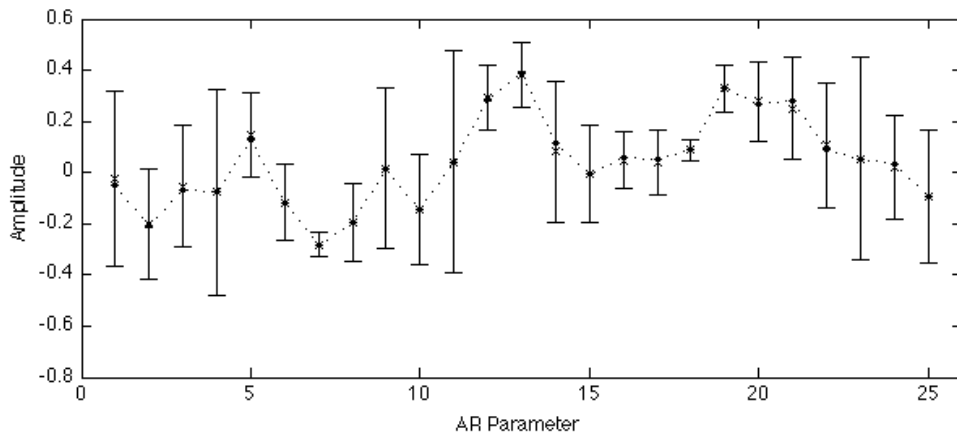


Figure 5.21. Error bar (two standard deviations) with AR(25) parameters estimated at node 15 during the tests in 2008 along with the outlier-free means (dots).

In order to compare the AR parameters from the three periods, Figure 5.22 plots the outlier-free means of the AR parameters for the three periods. Even though one can detect slight local changes in the parameters from 1996 and 1997, they appear to have a similar global pattern. Table 5.7 summarizes the correlation coefficients of the AR parameter curves from 1996, 1997, and 2008. The correlation analysis indicates that all three curves are highly positive correlated. However, clearly one can conclude that the AR parameters from 1996 are better correlated with 1997 ($r = 0.82$) rather than 2008 ($r = 0.78$).

Note that even though there exists differences in the AR parameters from 1996 to 2008, it is not clear that those changes might be associated to the existence of damage in the structure. Rather, this is just an indication that the system generating the time series shows some statistical differences. Note that these changes might be associated to the fact that the comparison was carried out in a discrete manner, using measurements from three different days.

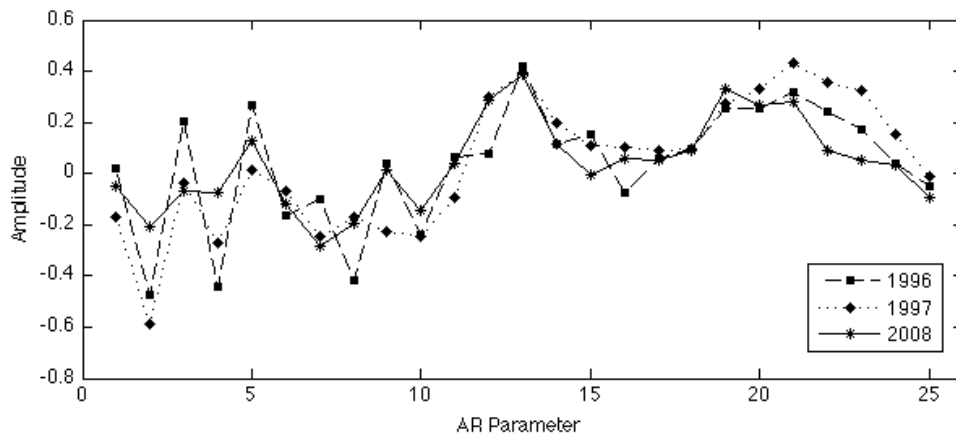


Figure 5.22. Outlier-free means of the AR parameters estimated in 1996, 1997, and 2008.

Table 5.7. Correlation coefficients of the AR parameter curves in Figure 5.22.

Year	1996	1997	2008
1996	1.00	0.82	0.78
1997	0.82	1.00	0.83
2008	0.78	0.83	1.00

Linearity Check of the AR Parameters

In real-world structures, the excitation (i.e. the hammer impacts in this case) might be one source of variability encountered among the AR parameters. Even though for linear systems the AR parameters should be constant over varying impact intensity, the operational and environmental effects along with structure's inertia in certain ranges, especially at low force level, can input variability into the AR

parameters. In order to check the linearity of the structural response and the consistency of the AR parameter estimation, in 2008 two tests were performed (time08_1 and time08_2) for two different levels of hammer-impact forces. As shown in Figure 5.23, the low-level impact force has 2669 N (600 lbs) peak and the high-level one has 5340 N (1200 lbs). Figure 5.24 depicts the average of the AR parameters estimated on five time series of each test. In an average-sense, the plot highlights an overall similar pattern with some local differences. Therefore, as suggested by the SDOF system in Figure 5.15a, this is an important indication that the structure responds in a (quasi-) linear manner and that the AR parameter estimation does not depend on the intensity of the impacts.

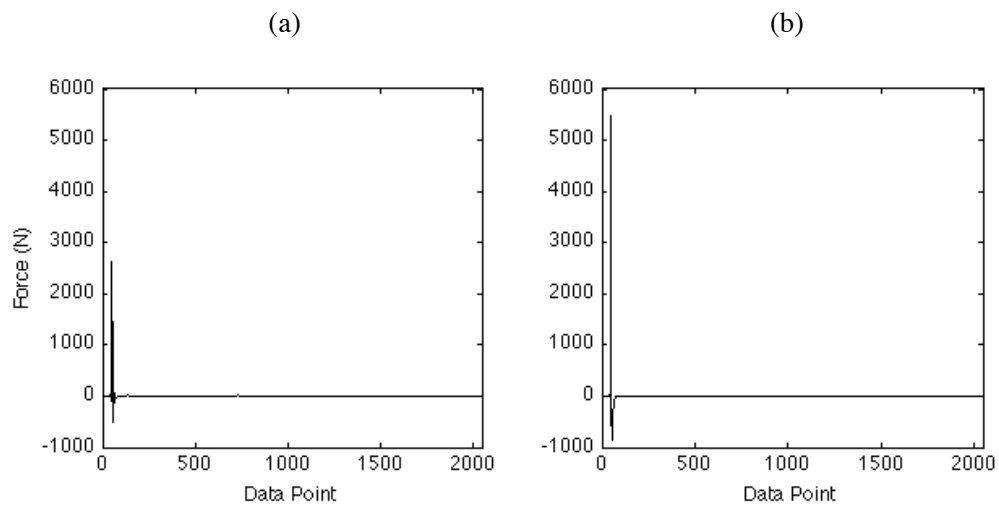


Figure 5.23. Force time series for linearity check using tests performed in 2008: (a) low force level, time08_1; and (b) high force level, time08_2.

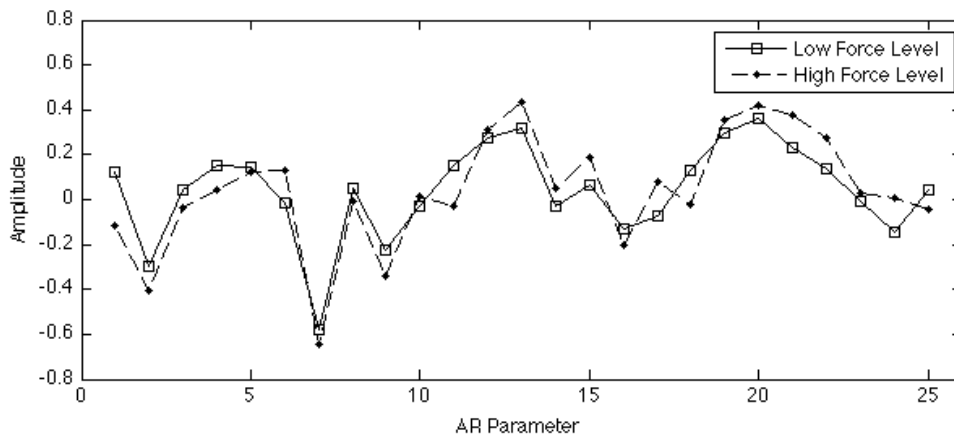


Figure 5.24. Average of the AR(25) parameters for linearity check using time08_1 and time08_2 tests performed in 2008 at node 15.

5.3.2.4 AR Residual Errors

Along with the AR parameters, the AR residual errors are also currently used in SHM as damage-sensitive features. In order to show, qualitatively, the performance of the AR(25) model, with outlier-

free 24-hour-average parameters of 1996, to predict the measured response time series, Figure 5.25 to Figure 5.27 plot the measured and predicted acceleration time series at 17:52, 18:00, and 17:20, for 1996, 1997, and 2008, respectively. Based on a global observation, one can conclude that the average of the AR(25) parameters from the 24-hour test in 1996 seems to encode the structural dynamics, even when using this AR model to predict time series from 1997 and 2008. Nonetheless, in order to quantify those differences, Figure 5.28 plots the RMS of AR residual errors of the prediction for 34 (13+11+5+5) time series. If the structure's properties have not changed since 1996, it is expected that the residuals will have the same magnitude. However, the figure highlights increasing residuals since 1996 as an indication that the responses from 1997 and 2008 have some statistical differences. Notice that the RMS errors of the tests from 1996 follow a nearly straight line because the 24-hour-average parameters at same year were used to define the AR model.

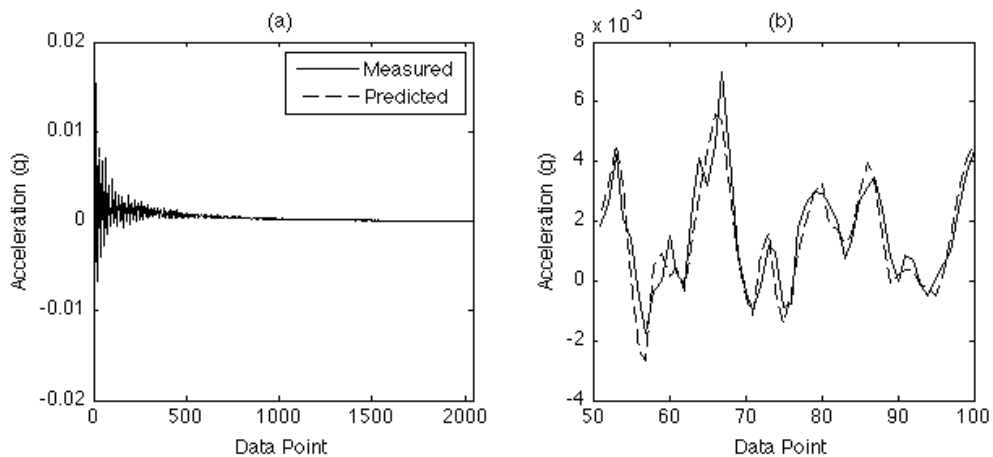


Figure 5.25. Measured and predicted acceleration time series at 17:52 (1996) using an AR(25) model with the 24-hour-average parameters of 1996: (a) full time series; and (b) windowed time series.

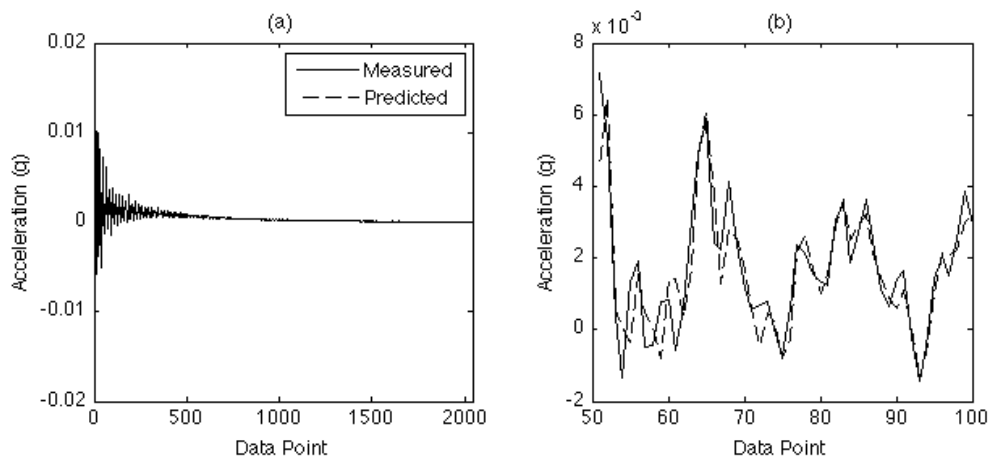


Figure 5.26. Measured and predicted acceleration time series at 18:00 (1997) using an AR(25) model with the 24-hour-average parameters of 1996: (a) full time series; and (b) windowed time series.

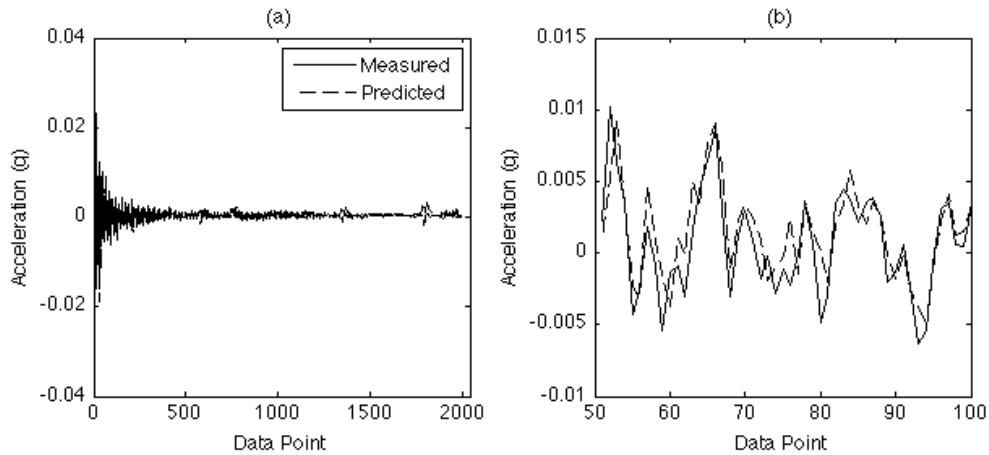


Figure 5.27. Measured and predicted acceleration time series at 17:20 (2008) using an AR(25) model with the 24-hour-average parameters of 1996: (a) full time series; and (b) windowed time series.

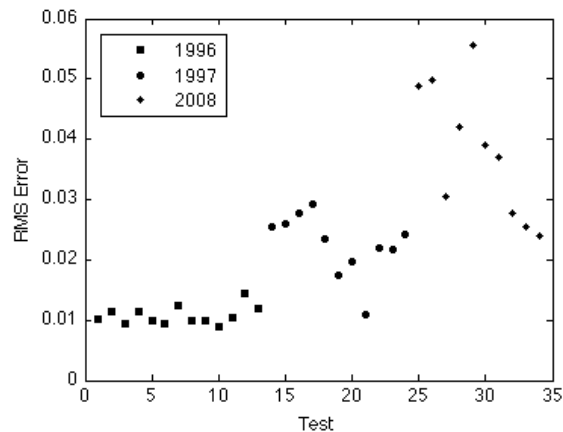


Figure 5.28. RMS of the AR(25) residual errors from the tests performed in 1996, 1997, and 2008.

As an extension of the results depicted in Figure 5.28, the two-step AR-ARX prediction model proposed in [71] is applied on the data from 1996, 1997, and 2008. Note that this model is similar to the one described in Section 3.2.4, where the input time series corresponds to the residual errors from the AR model. Basically, the two-step model can be summarized as follows. First, AR($p=25$) models are constructed for all time series. Second, the ARX($a=15, b=10$) model is constructed to predict each output time series using the residual errors estimated from the previous AR model as the input. As discussed in [85], it is suggested to keep the sum of a and b smaller than p ($a + b \leq p$). The parameters used in the ARX model correspond to the outlier-free 24-hour-average parameters of 1996. Finally, for the same raw data of the previous analysis, the RMS of the AR-ARX residuals are computed and plotted in Figure 5.29. However, the figure does not show significant relative improvements over Figure 5.28.

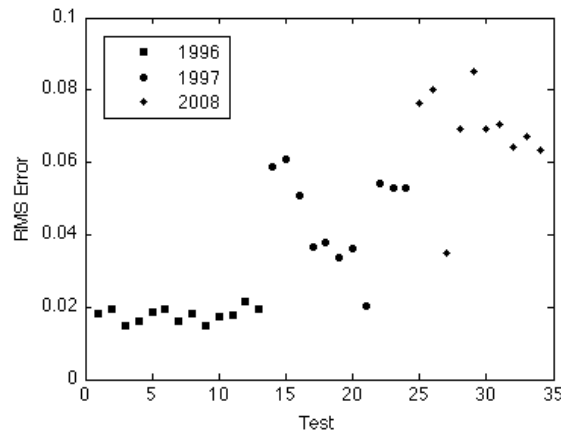


Figure 5.29. RMS of the AR(25)-ARX(15,10) residual errors from the tests performed in 1996, 1997, and 2008.

Look-up Table Approach

Throughout this section, the AR residuals were obtained using the 24-hour-average parameters from 1996. However, in order to better identify the source of variability that is influencing the process, a look-up table approach is formed. Basically, each time series is predicted using an AR model with parameters from 1996 assigned based on the closest differential temperature between 1996 and the one being predicted. In theory, this procedure permits one to take into account the variability, in particular that caused by differential temperature, because the time series from 1996 that originate AR parameters share some similarity with the time series being tested. Figure 5.30 and Figure 5.31 plot the RMS of the AR(25) and AR(25)-ARX(15,10) residuals using the described approach. The thresholds correspond to the highest RMS error among the observations of 1997. Once the temperature was not measured in 2008, the observations of the 2008 tests correspond to the minimum RMS obtained for each set of parameters, i.e., the assumption is that the RMS error is minimized for the parameters extracted from time series of 1996 in similar temperature conditions of the 2008 data. The results show that using the look-up table approach, the data from 2008 is relatively similar to the data from 1997 using either the AR or AR-ARX models.

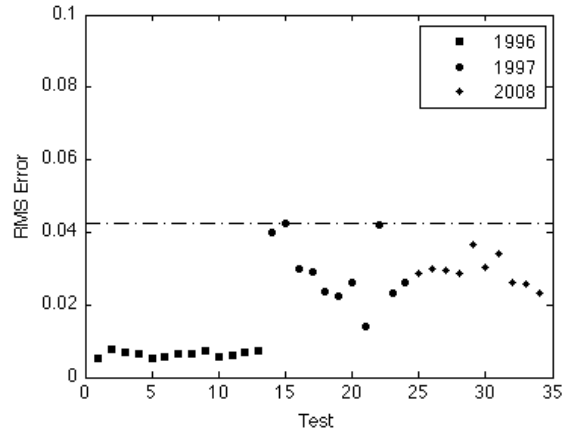


Figure 5.30. RMS of the AR(25) residual errors from the tests performed in 1996, 1997, and 2008; horizontal dashed line corresponds to the maximum value of 1997.

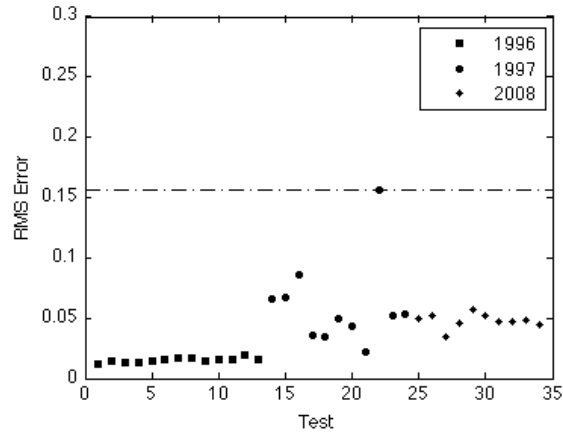


Figure 5.31. RMS of the AR(25)-ARX(15,10) residual errors from the tests performed in 1996, 1997, and 2008; horizontal dashed line corresponds to the maximum value of 1997.

Influence of the Differential Temperature on the AR Residual Errors

It was already shown in Section 5.3.1 the influence of the differential temperature across the deck on the modal parameters. Furthermore, it was shown that the responses from 1997 and 2008 have some statistical differences from the ones of 1996. Additionally, the look-up table approach suggested that the differential temperature might have considerable influence on the prediction. The next study intends to highlight the influence of the temperature on AR parameters and residual errors throughout the day. Following the procedure adopted to the modal parameters, for the 24-hour tests in 1996 and 1997, the influence of the temperature is checked at node 15 by computing the RMS error of the prediction based on an AR model set up with parameters from a particular time of day. For the 24-hour test in 1996, Figure 5.32 plots the RMS error of each test obtained based on an AR(25) model with parameters estimated at 21:20 along with the differential temperature across the deck. In the same

manner, for the 24-hour test performed in 1997, Figure 5.33 plots the RMS error for each test obtained based on an AR(25) model with parameters estimated at 22:00. Clearly, both figures highlight positive correlation between the residuals and the differential temperature throughout the day.

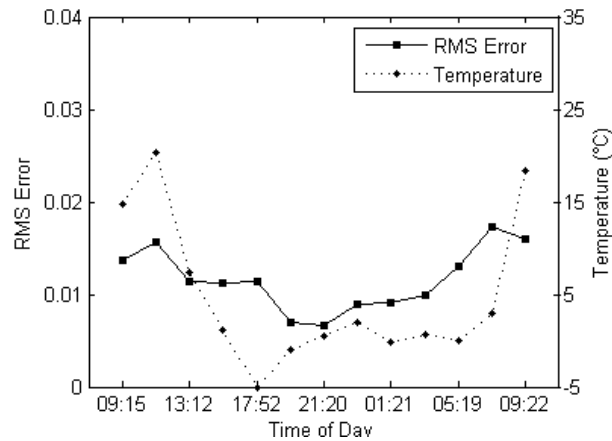


Figure 5.32. Differential temperature across the deck along with the RMS of the AR(25) residuals, with parameters estimated at 21:10, for each test at node 15 during the 24-hour test in 1996.

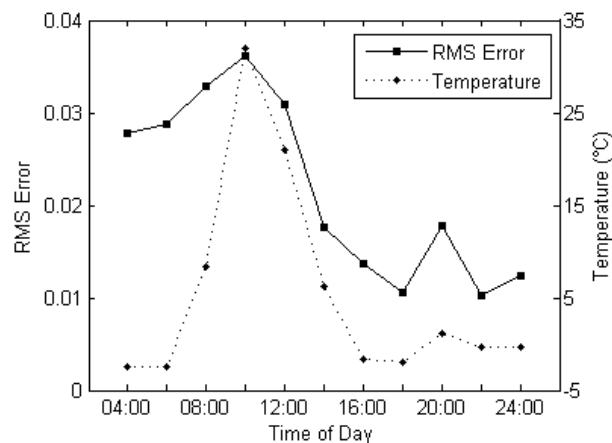


Figure 5.33. Differential temperature across the deck along with the RMS of the AR(25) residual errors, with parameters estimated at 22:00, for the 24-hour tests in 1997 at node 15.

5.3.3 Dimension of a Dynamical System

As shown in Section 4.6.3 on state-space reconstruction, the dimension of a system, borrowed from the dynamical systems field, under special conditions, can be a powerful manner to discriminate time series from different structural conditions, because damage might affect the dimension of the attractor. Even though it is not known *a priori* the existence of a specific type of damage, Figure 5.34 shows three averaged singular spectra of vector spaces of dimension $w=60$, composed of time series from node 15. The number of singular values larger than the noise floor is an estimate of the minimal embedding dimension required to unfold the attractor. The figure is not conclusive about significant changes in the system's dimension since 1996. Note that often when structures age and even with

visual degradation, the system can still exhibit linear behavior. Moreover, as shown in Figure 4.58, linear changes do not introduce sufficient complexity to increase, significantly, the dimension of a dynamical system. Thus, it is the author's speculation that those slight differences observed in the plot might be associated with the operational and environmental variability.

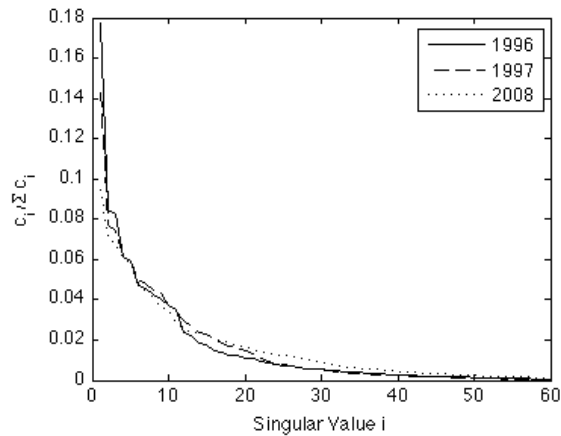


Figure 5.34. Averaged singular spectra at node 15 in 1996, 1997, and 2008.

5.4 Statistical Modeling for Feature Classification

In the last feature-extraction section, the modal analysis as well as the AR models were studied to extract features and to highlight their sensitivity to operational and environmental variations, especially the differential temperature across the deck. The following analysis intends to perform outlier detection using feature vectors composed of the first six natural frequencies and the AR(25) parameters from node 15. Additionally, the four machine learning algorithms for data normalization described in Section 3.3, namely, the AANN-, FA-, SVD-, and MSD-based algorithms, are applied in order to remove the effects of the operational and environmental variations on the features. The normal condition of the structure is established using the data from the 24-hour tests in 1996 and 1997. Then, the concept of DI is used to reduce each feature vector into a unique value. Thus, the AANN-, FA-, and SVD-based algorithms use the methodology described in Section 3.4.4 to reduce each residual feature vector into a score. On the other hand, for each feature vector, the DI derived from the MSD-based algorithm is equal to the d^2 in Equation (3.55).

Basically, the analysis in this section intends to verify: (i) the performance of the machine learning algorithms to remove the operational and environmental variability from the features in the context of outlier detection; (ii) if feature vectors from 2008 are classified as inliers or outliers; and (iii) the importance of the number of unobserved variables (or factors) modeled in the AANN- and FA-based algorithms.

Note that a feature vector will be considered a multi-dimensional inlier when its features share similarities with the ones used to establish the normal condition. Furthermore, as discussed in Section

5.2, there is not a clear indication that the structure has suffered significant structural degradation from 1996 to 2008. Therefore, the author does not speculate that an outlier is derived from the damage condition, rather the author poses outliers as derived from tests that have underlying statistical differences from the ones used to set the normal condition. These outliers might be associated with operational and environmental variations not included in the training data.

5.4.1 Modal Parameters

The modal parameters have been used as damage-sensitive features since the first studies on SHM. However, as described in Section 2.2 and as shown in Section 5.3.1, the temperature normally plays the major role on the modal parameters variation. In order to account to those variations, statistical modeling is often required. In this case, only the natural frequencies are used as damage-sensitive features, because as shown in Section 5.3.1, the damping ratios show relatively large variability when compared to the natural frequencies, and so they are discarded from this analysis. Note that for each time of the day, the natural frequencies are estimated from the average of the FRFs.

The normal condition of the structure is established using the estimated natural frequencies of the 24-hour tests from 1996 and 1997. Therefore, the training matrix, $\mathbf{X} \in \mathfrak{R}^{6 \times 24}$, corresponds to 24 feature vectors, composed of the first six natural frequencies. The test matrix, $\mathbf{Z} \in \mathfrak{R}^{6 \times 26}$, is composed of the entire training data plus two feature vectors from the tests performed in 2008 at 10:00 and 17:20.

The AANN-based algorithm is built up with a feed-forward neural network. According with Kramer's recommendations [111], the network has three nodes in each mapping and de-mapping layers. A Levenberg-Marquardt back-propagation algorithm was used to train the network. Several trainings with different initial conditions were performed with the given architecture to increase the probability that the global minimum was achieved. The number of nodes at the bottleneck layer for the AANN-based and the number of factors in the FA-based algorithm were varied to study their relevance on the classification performance. The threshold for the MSD-based algorithm is based on 99% confidence interval of a chi-square distribution with six degrees of freedom, χ_6^2 . On the other hand, the thresholds for the SVD-, AANN-, and FA-based algorithms are based on 99% cut-off value over the training data.

Figure 5.35 to Figure 5.38 plot the DIs derived from all four machine learning algorithms for outlier detection. In terms of overall analysis, all the algorithms seem to normalize the data from the normal condition. However, the algorithms do not output consistent results regarding the classification of the two feature vectors from 2008. (Note that data from 2008 were not used in the training phase.) With exception of the FA-based algorithm with one modeled factor, all the algorithms classify at least one of the feature vectors as an outlier.

As discussed in Section 4.6.4, the classification performance of the AANN- and FA-based algorithms depends on the number of unobserved variables, i.e., the number of modeled factors. As shown in Figure 5.37, the AANN-based algorithm classifies the tests from 2008 as outliers using both one and two nodes. However, as shown in Figure 5.38, the FA-based algorithm outputs distinct results using one or two factors. Actually, as indicated in Section 4.6.4, this inconsistency might be a drawback in real-world applications, because often the number of operational and environmental factors driving changes in the structural responses is unknown. Therefore, assuming one factor to encode the temperature variation, for instance, the algorithm classifies both feature vectors from 2008 as inliers, i.e., they are representative of the normal condition. However, if one assumes two factors (e.g. temperature and humidity variations), the same algorithm classifies the feature vector from 17:20 as an outlier. This result is an indication that for real-world SHM applications, the performance of these algorithms requires an insight on the number of operational and environmental factors driving changes in the structural responses.

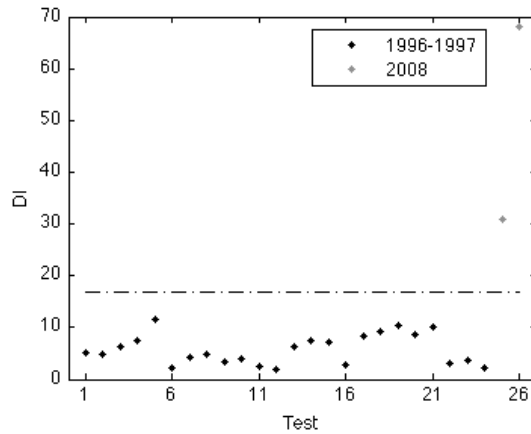


Figure 5.35. Outlier detection of feature vectors composed of natural frequencies using the MSD-based algorithm; threshold defined based on 99% confidence interval of a χ_6^2 .

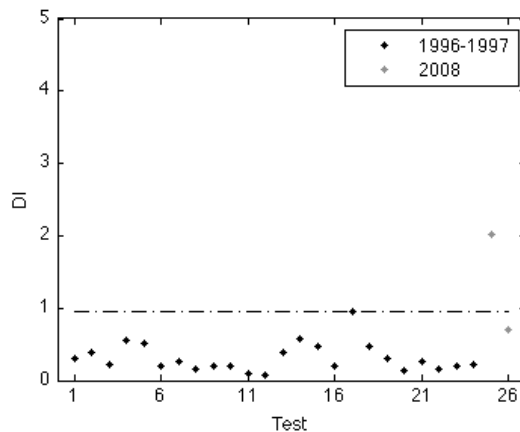


Figure 5.36. Outlier detection of feature vectors composed of natural frequencies using the SVD-based algorithm; threshold equals to 99% cut-off value over the DIIs from the training data.

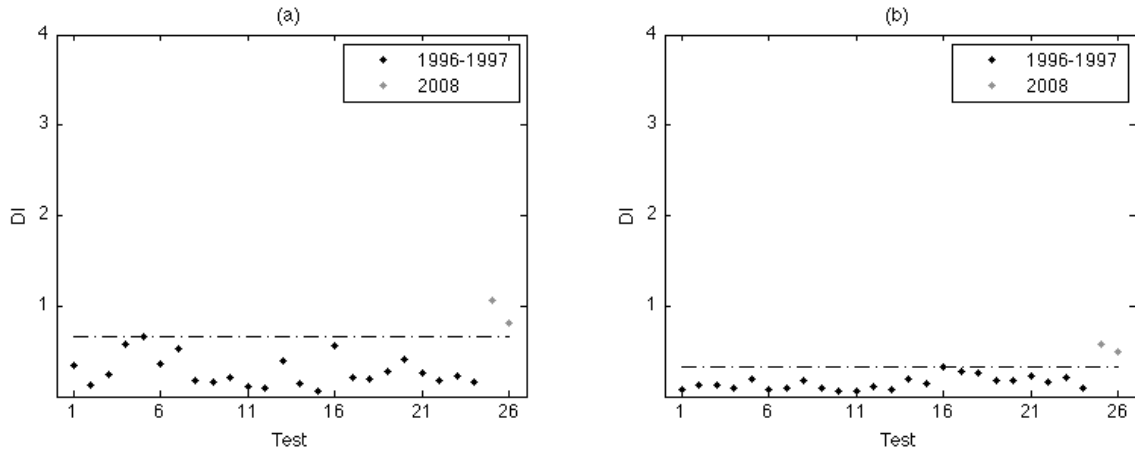


Figure 5.37. Outlier detection of feature vectors composed of natural frequencies using the AANN-based algorithm; threshold equals to 99% cut-off value over the DIs from the training data assuming: (a) one factor; and (b) two factors.

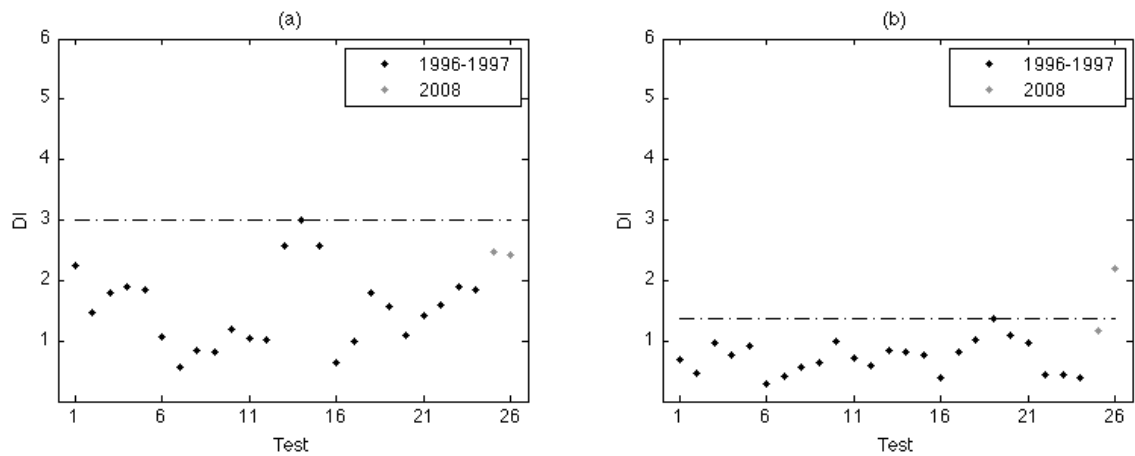


Figure 5.38. Outlier detection of feature vectors composed of natural frequencies using the FA-based algorithm; threshold equals to 99% cut-off value over the DIs from the training data assuming: (a) one factor; and (b) two factors.

5.4.2 AR Parameters

Herein, the four machine learning algorithms are used to normalize the normal condition data, i.e., to remove the effects of the operational and environmental variations on the AR(25) parameters from node 15. Afterwards, the transformed features are reduced to a DI for outlier detection. In this case, all the 13 tests from 1996 and 44 tests from 1997 are used to establish the normal condition. The test data

is composed of the entire training data plus the remainder 11 tests from 1997 and all 20 tests from 2008. Notice that the tests from 1997, used in the test phase and not included in the training phase, intends to evaluate the robustness of each algorithm to normalize the data from the normal condition. To summarize, the data is split into the training matrix, $\mathbf{X} \in \mathfrak{R}^{25 \times 57}$, and the test matrix, $\mathbf{Z} \in \mathfrak{R}^{25 \times 88}$.

The AANN-based algorithm is built up with a feed-forward neural network. After several runs based on the error minimization, it was observed that three nodes is the optimal number of nodes in each mapping and de-mapping layer. A Levenberg-Marquardt back-propagation algorithm was used to train the network. Several trainings with different initial conditions were performed with the given architecture to increase the probability that the global minimum was achieved. The threshold for the MSD-based algorithm is based on 99% confidence interval of a chi-square distribution with 25 degrees of freedom, χ_{25}^2 . On the other hand, the thresholds for the SVD-, AANN-, and FA-based algorithms are also based on 99% cut-off value over the DIs from the training data.

Figure 5.39 to Figure 5.42 plot the DIs, in concatenated format, from all four machine learning algorithms. In a general observation, all the algorithms seem to normalize well the data from the normal condition, even when data from the normal condition is not used in the training phase. Therefore, it is an indication that the algorithms encode the normal condition and correctly classify new feature vectors when they share similarities with the data used in the training. However, some discrepancies are observed for the 2008 tests. While the MSD-based algorithm clearly classifies all feature vectors from 2008 as outliers, in a broad sense the other three algorithms classify those feature vectors as inliers. The results from the MSD-based algorithm suggest more sensitivity of this algorithm to classify data from the undamaged condition when they are not represented in the training phase. Actually, this sensitivity might be a limitation in real-world applications, because it is unlikely to obtain the same responses twice under similar operational and environmental conditions due to the uncertainty of several unmeasured factors present in the structures.

In order to evaluate the importance of the modeled factors in the AANN- and FA-based algorithms, Figure 5.41 and Figure 5.42 plot the DIs for one and two factors. Both algorithms generally tend to classify the tests from 2008 in the same manner when using one or two factors, giving an indication that the temperature might be the major source of variability in the structural response at node 15.

Finally, for better understanding on the MSD-based algorithm performance, Figure 5.43 plots the estimated PDF based on the training data and theoretical chi-square distribution for 25 degrees of freedom, χ_{25}^2 . The smoothed PDF was obtained using the kernel density estimator based on a standard Gaussian function. Even though the distributions do not overlap, the author poses those differences due to chance. Recall that temporal discrete and reduced amount of data from 1996 and 1997 were used to set the normal condition. Note that the “bump” on the right-hand side results from the data collected in 1996.

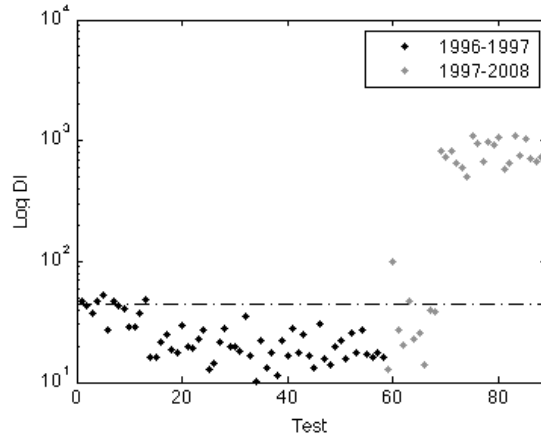


Figure 5.39. Outlier detection of feature vectors composed of AR(25) parameters using the MSD-based algorithm; threshold defined based on 99% confidence interval of a χ^2_{25} .

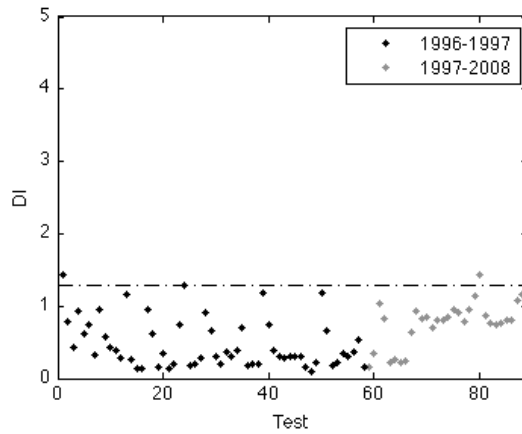


Figure 5.40. Outlier detection of feature vectors composed of AR(25) parameters using the SVD-based algorithm; threshold equals to 99% cut-off value over the DIs from the training data.

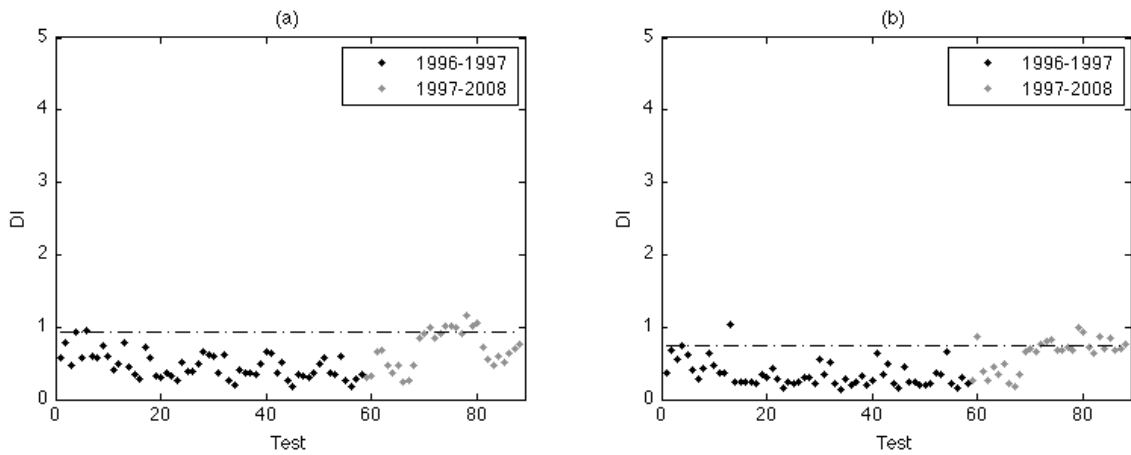


Figure 5.41. Outlier detection of feature vectors composed of AR(25) parameters using the AANN-based algorithm; threshold equals to 99% cut-off value over the DIs from the training data assuming: (a) one factor; and (b) two factors.

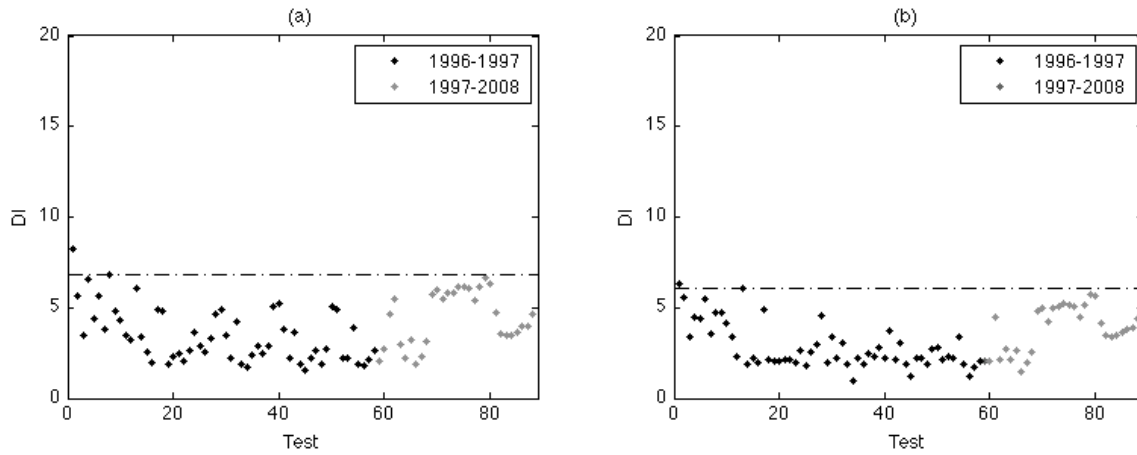


Figure 5.42. Outlier detection of feature vectors composed of AR(25) parameters using the FA-based algorithm; threshold equals to 99% cut-off value over the DIs from the training data assuming: (a) one factor; and (b) two factors.

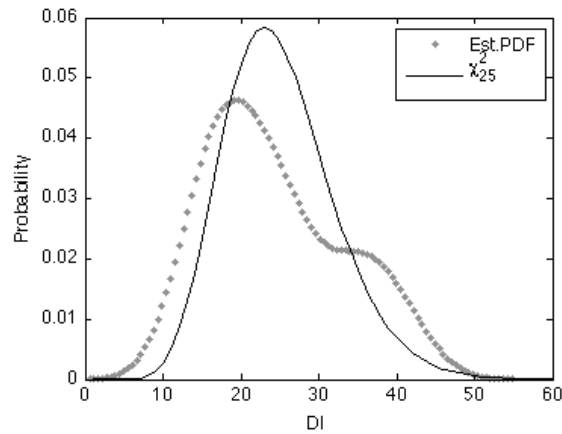


Figure 5.43. Estimated PDF of the DIs from the training data along with the theoretical χ_{25}^2 , when using the MSD-based algorithm.

5.5 Summary and Conclusions

In an attempt to transiting SHM technology from research to practice, the analysis presented in this chapter applied the SHM-SPR paradigm to data from a real-world structure, namely, the Alamosa Canyon Bridge. Basically, the analysis was centered on the feature extraction and statistical modeling for feature classification steps of the paradigm. Special emphasis was given to the modal analysis and AR models to extract damage-sensitive features as well as to the four machine learning algorithms to separate changes caused by operational and environmental conditions from changes caused by damage. The analysis made use of the 24-hour test data collected in 1996 and 1997 (to characterize the normal condition) along with data acquired in 2008.

In the feature extraction step, it was shown that the modal parameters as well as AR parameters and residuals are very sensitive to the differential temperature across the bridge deck. In the case of the

modal parameters, it was shown that the first natural frequency is proportional to the differential temperature. A maximum of 4.3% change in the fundamental natural frequency was observed throughout the day. Moreover, the first modal damping ratio is inversely proportional to the differential temperature (and also to the natural frequency), particularly, during the 1996 and 1997 tests. It was verified that those changes might reach 46% in one day. However, it was noted that the computation of the damping ratios is very sensitive to the estimation method used and so their application for damage detection might be limited. Additionally, the extraction of the mode shapes showed an asymmetrical variation in the first mode that changes throughout the day. This asymmetry, along the longitudinal axis, was correlated with the time of day and solar heating. The thermal effects were more pronounced because of the north-south orientation of the bridge. Therefore, this is an indication that if not properly accounted for in the damage detection process, such changes in the dynamics response characteristics can potentially result in false indications of damage.

Regarding the applicability of the AR models as feature extraction approach, four techniques were used to determine the appropriate model order. All techniques did not give an unique solution when looking at the convergence point of each curve; however, by taking the SVD and PAF as reference, it was shown that the data measured in 2008 seem to require slightly higher AR model orders than the data from 1996 and 1997; nevertheless, for simplification an AR(25) model was adopted as the basis to extract damage-sensitive features. Then, analysis was carried out to understand the variability in the estimation of the AR parameters. Significant variability in the AR parameters was observed throughout the day. However, by discarding the outliers and taking the average of the parameters, it was shown that the 24-hour-average parameters of 1996 and 1997 are similar with a correlation coefficient $r=0.82$. Additionally, even though the average of 2008 data only corresponds to tests performed in the morning and in the afternoon, it was possible to show that the parameter average is also correlated with the 24-hour-average of 1996 ($r=0.78$). Along with the AR parameters, the AR residual errors were also tested as damage-sensitive features. An AR(25) model, with 24-hour-average parameters of 1996, was used to predict time series from 1996, 1997, and 2008. It was observed a reasonable prediction as an indication that the 24-hour-average parameters of 1996 encode the structural dynamics. However, the RMS of the residuals indicates increasing magnitude since 1996 as an indication that the responses from 1997 and 2008 have some statistical differences. Additionally, for the 24-hour tests of 1996 and 1997, it was shown that the RMS of the AR residuals also have significance dependence on the differential temperature.

In the statistical modeling for feature classification step of the SHM-SPR paradigm, the machine learning algorithms for data normalization, namely, the MSD-, SVD-, AANN-, and FA-based were used to test their applicability on real-world data. Note that it was observed some signs of structural degradation in 2008, mainly the joints were filled with debris and the pavement showed some signs of surface cracking. Nonetheless, the data from 1996 and 1997 were considered to represent normal

condition of the structure and the machine learning algorithms were used to verify (i) if the algorithms are able to remove the changes of the operational and environmental conditions from the features and (ii) if the tests from 2008 are statistically different to be considered outliers. To achieve that, the natural frequencies and AR parameters were tested as damage-sensitive features, because the former is still the most used one and the latter have been proposed as an alternative to detect damage in civil infrastructure. The main conclusions of this study can be summarized as follows. In terms of an overall observation, the analysis showed that the algorithms are able to normalize the normal condition data, even when data from 2007 are not included in the training phase. However, in terms of classification performance of the 2008 data, the results were not consistent within each type of feature and algorithm used. Nevertheless, it was observed a tendency among the algorithms to classify the 2008 data as outliers when using the natural frequencies and inliers when using the AR parameters. Assuming that the structure is undamaged, for the AR parameters, those results are an indication that the algorithms are able to remove the variability caused by the operational and environmental variability from the extracted features. However, the results from the MSD-based algorithm suggest more sensitivity of this algorithm to give false-positive indications of damage when data from the undamaged condition are not represented in the training phase. Actually, this sensitivity might be a limitation in real-world applications, because it is unlikely to obtain the same responses twice under similar operational and environmental conditions due to the uncertainty of several unmeasured factors present in the structures. Additionally, a study carried out to evaluate the performance of the AANN- and FA-based algorithms, for varying number of modeled factors, showed that the AANN-based algorithm performed consistently when using one or two nodes in the bottleneck layer to ideally represent the temperature or temperature and humidity. However, the FA-based algorithm (using natural frequencies) outputted different results when using one or two nodes, raising challenges of setting the appropriate number of factors for real world applications.

This study intended to highlight the applicability of the feature extraction techniques and machine learning algorithms on real-world data rather than to be used as a comparative study. Note that the damage-sensitive features might not be directly compared, because the natural frequencies are a global damage-sensitive feature that were estimated using response time series at several locations. Conversely, the AR parameters are local damage-sensitive features that characterize the response at one node. Recall that, and as suggested by this chapter, these algorithms have potential problems if the training data are only representative of a limited range of operational and environmental variability. Thus, one should note that with these algorithms there is no guarantee that they will work effectively when new data corresponds to operational and environmental conditions not used in the training phase. Regardless of the classification carried out in this chapter, one should be aware that the data used in the training and test phases were not sufficient to establish with high confidence that the statistical changes in the data from 2008 are correlated with damage. Moreover, the main purpose of

this application was to show the limitations and challenges of the machine learning algorithms applied to real-world data, rather than effectively classify the data from 2008 as damaged.

Finally, based on the experience gained in Chapter 4 and 5, the author herein outlines a possible procedure to design the training process in future data normalization processes:

- (i) measurement of response data (e.g. accelerations and strains) at several locations in the structure;
- (ii) measurement of operational and environmental factors (e.g. temperature and humidity) at several locations; this procedure is important to better take into account the variability that influences the process; it can potentially be used to form look-up tables and/or to quantify the number of independent factors affecting the structural responses;
- (iii) the measurements should be representative of several cycles; at least two cycles are recommended, which one might be used to establish the normal condition (training phase) and another to verify the existence of damage or structural degradation (test phase); note that, the data should be collected when the structure is thought to be undamaged; when possible, it is recommended that data should be collected in the early times of operation; this step is extremely important to establish the normal condition of the structure; recall that the damage detection implicit in the SHM-SPR paradigm is based on comparison between two states;
- (iv) the definition of thresholds is of extreme importance for reliable classification; a problem that often confronts the researchers is when to consider re-computing the thresholds; initially, the thresholds need to be established assuming that both the structure and the SHM system are undamaged; however, because of normal aging of the structures and systems, one should evaluate the need to re-calculate the thresholds every time a statistically significant sign of instability is detected; however, this decision needs to be backed with exhaustive visual inspections and/or appropriate NDT.

5.6 Contributions

The main contribution of this chapter is the extension of the SHM-SPR paradigm to real-world data collected when the structure is thought to be undamaged, namely (i) applicability of the AR model to extract damage-sensitive features; and (ii) applicability of the machine learning algorithms to remove the effects of the operational and environment variations from the sensors readings without direct measurement of those variations.

6. CONCLUSIONS, CONTRIBUTIONS, AND FUTURE RESEARCH

6.1 Conclusions and Contributions

In any real-world structure, the separation of changes in sensor readings caused by damage from those caused by changing operational and environmental conditions is one of the biggest challenges for transitioning SHM technology from research to practice. To address that issue, herein the SHM process was posed in the context of the SPR paradigm. In the hierarchical structure of damage identification, this dissertation was motivated by the need for robust incipient vibration-based damage detection methods. Therefore, it is mainly concerned with detection of damage in the structures.

Recognizing the applicability of the SHM-SPR paradigm for civil infrastructure, this dissertation presented statistical methods adopted from the machine learning field and tested their applicability to data measured on civil structures. Even though this procedure might be applied to structures of arbitrary complexity, the procedures are especially posed for SHM bridge applications. The AR model was the focus of special attention. The machine learning algorithms for data normalization (based on AANN, FA, MSD, and SVD) were also the focus of special attention because they permit one to separate changes in the structural responses caused by the operational and environmental variations from changes caused by damage, without the need to measure the operational and environmental variations such as temperature and humidity. At the same time, a new algorithm was proposed for feature extraction that uses the state-space reconstruction from response time series. Basically, this algorithm compares predicted attractors using a MAR model whose parameters encode the baseline condition of the structure.

The applicability of the SHM-SPR paradigm for damage detection was first tested on standard data sets from a laboratory base-excited three-story frame structure. Essentially, this analysis was important to bridge the gap between laboratory-based applications to data from real-world structures. The analysis on data from both conditions (undamaged and damaged) confirmed the usefulness of the AR models to extract damage-sensitive features and the machine learning algorithms to remove the effects of the operational and environmental variations from the extracted features. The AR model was shown to be useful feature extraction technique for civil infrastructure SHM applications based on three main reasons: (i) they are sensitive to damage when it manifests in the form of nonlinearities or transitions

between two states; (ii) the extraction of features only depend on response time series data; and (iii) simple and easy implementation. Additionally, it was shown that the AR models might be useful to address the first two levels in the hierarchy structure of damage identification, namely, damage detection and localization. The comparison of the machine learning algorithms in the context of outlier detection highlighted the MSD-based algorithm as the best in terms of the classification performance, reduced computational efforts (during both training and test phases), and the fact that no assumptions are required regarding its architecture. Note that those facts, along with the simplicity, make the MSD-based algorithm also a better choice for implementation on current embedded hardware. Additionally, a study carried out permitted to draw a direct correlation between the optimal AR model order given by an information criterion technique and the classification performance of the MSD-based algorithm, even when using non-Gaussian multi-dimensional feature vectors to set the normal condition. The analysis on the standard data sets also validated the applicability of the MAR model to predict the state space of a dynamical system and to extract damage-sensitive features using a local embedding. The performance of this algorithm was also tested in the context of outlier detection. Actually, when using these features for outlier detection, they were shown to be more sensitive to damage than other well-known methods. Finally, note that this analysis on standard data sets highlighted that real-world structures might require a high density of sensors to detect and/or locate damage throughout the structure.

To the extent possible, all SHM research should be validated using data from real-world structures. Therefore, the applicability of the SHM-SPR paradigm on a real-world structure was demonstrated on data from one span of the Alamosa Canyon Bridge assuming that the structure was in its undamaged condition, nonetheless in the presence of operational and environmental variability. The differential temperature across the deck was shown to be one of the factors driving changes in the structural properties. In this case, the modal analysis and the AR model were used to extract damage-sensitive features. The applicability of the AR models on impulse responses was successfully demonstrated. The machine learning algorithms were also applied to remove the effects of the temperature on the extracted features. The results were shown to be a function of the type of the damage-sensitive feature used. Actually, the classification performance for a given level of significance showed the tests from 2008 as outliers when using the natural frequencies. However, in the case of the AR parameters, although the parameters from 2008 highlighted some statistical changes compared with 1996 and 1997, after normalization, a tendency to classify the tests from 2008 as inliers was observed. However, the results from the MSD-based algorithm suggest more sensitivity of this algorithm to give false-positive indications of damage when data from the undamaged condition are not represented in the training phase. Actually, this sensitivity might be a limitation in real-world applications, because it is unlikely to obtain the same responses twice under similar operational and environmental conditions due to the uncertainty of several unmeasured factors present in the structures. Furthermore, in terms of

a global observation for both features, all the machine learning algorithms were shown to have a good performance to normalize the data from the normal condition. This result shows the applicability of these machine learning algorithms for real-world applications when the training data is representative of the operational and environmental variability present in the structures.

6.2 Future Research

The challenges posed by the Silver Bridge collapse are not dissimilar to the issues facing present day bridge owners. In the case of the USA, how should the owners manage an aging Interstate system, when roughly 30% of its bridge inventory is rated as “structural deficient”? In the case of Portugal, should the owners invest in monitoring systems to avoid fatalities like in the Hintze Ribeiro Bridge collapse in 2001? How should future research on SHM be used to address the inevitable degradation of existing bridges around the world?

The current practise of visual inspection has been identified as a shortcoming in bridge asset management. At the 50th anniversary of the Interstate Highway System, Walther and Chase [8] stated that despite the advances in BMS modeling, the condition assessment activities associated with NBIS and BMS still rely heavily on visual inspections, which inherently produces widely variable results. The same authors stressed that the challenge would be to develop better assessment methodologies that can generate better prediction models to support the owners’ decisions regarding bridge safety assessment and maintenance. Moreover, research findings from a comprehensive study conducted by the FHWA, on the reliability of the visual inspection method of highway bridges, found significant variability of the condition rating assignments. For instance, the condition rating system requires that inspectors assign a rating from zero to nine, with zero representing a failed condition and nine representing excellent condition. The study concluded that 95% of the primary element condition ratings for individual bridges would vary within two rating points of the average. Moreover, the inspectors normally hesitate to assign “low” or “high” condition ratings and, consequently, the rating tend to be grouped around the middle of the scale [144]. Visual inspections also cannot detect hidden deterioration or damage. For instance, it is difficult to simply look at the bridge and say that one pier has settled unless the damage is severe. Additionally, frequently the inspections are restricted to some parts of the bridges due to access constraints. Therefore, how can new SHM research introduce quantitative data for bridge management?

Improvements in damage detection and quantitative measures are needed to optimize BMS [8]. It is the author’s belief that any proposal for bridge safety and maintenance, and therefore asset management, should be based on results from long-term monitoring as well as visual inspections along with NDT. This approach will contribute to a much more reliable asset management. Notice that the subjective knowledge of practicing engineers will be always present at two levels: visual inspection

and data analysis. However, the engineers and/or owners will be provided with more quantitative information to support their decisions.

Over the last decade, the research conducted in the SHM and asset management fields has been conducted separately. Therefore, it is the author's belief that both fields should be joined together to develop a more reliable bridge safety and maintenance process. As a future research topic, the SHM results should be incorporated into the sufficiency rating (SR) given by the BMS.

In the USA, states annually submit to the FHWA all the required information for each bridge based on the visual inspections results. Then, the FHWA uses those results to calculate the SR and determine which bridge may need repair or replacement. Basically, the SR formula described in [145] takes into account four separate factors to obtain a score, indicative of bridge sufficiency to remain in service, which ranges between 0% (entirely insufficient or deficient bridge) and 100% (entirely sufficient bridge)

$$SR = S_1 + S_2 + S_3 - S_4, \quad (6.1)$$

where S_1 is the Structural Adequacy and Safety (0-55%), S_2 is the Serviceability and Functional Obsolescence (0-30%), S_3 is the Essentiality for Public Use (0-15%), and S_4 corresponds to Special Reductions (0-13%, only when $S_1+S_2+S_3 \geq 50\%$).

In order to incorporate the quantitative information from SHM systems, a correction factor η can be introduced into Equation (6.1) to increase the reliability of S_1 and when the bridge safety is the main concern for deploying a SHM system. Thus, a new health sufficiency rating (HSR) formula can be derived in the form of

$$HSR = S_1(1 - \eta) + S_2 + S_3 - S_4. \quad (6.2)$$

Note that the correction factor might be tailored to better gather damage-related information or to address the specific reasons for deploying SHM systems. For instance, another correlation factor might be used to correct S_2 , when the goal of the SHM system is to preserve the serviceability of the bridge. Based on the experience gained in statistical modeling for feature classification, an approach for the correction factor might be based on the machine learning algorithms described in Section 3.3. For the MSD-based algorithm, the factor might be given by

$$\eta = f(DI, pvalue). \quad (6.3)$$

The weight of this correction, or the maximum reduction rate, would depend on the reliability of the SHM system and on the type of structure.

In addition to the coupling of SHM-BMS described above, it is the author's belief that, in order to transpose SHM process from research to practice, it is crucial to address specifically the following issues:

- create an international task force on a project to develop a full-scale test-bed structure to validate current SHM technology and their ability to address data storage, maintenance, and bridge-type damage; for instance, it can potentially be performed on bridges about to be demolished;
- design should promote a holistic approach to SHM that includes optimal sensor placement and sensor validation [15, 146], implying an all-inclusive design perspective where the structure and sensors must be seen as a whole;
- promote multi-disciplinary teams to truly integrate hardware and software SHM solutions; few research programs have addressed both the hardware and software components of the SHM process; additionally, the sensing systems have not been developed addressing issues related to SHM, rather the community usually adapts commercial off-the-shelf sensing systems; so, hardware and embedding software must be developed in an integrated manner;
- integrate NDT technology (sensors and/or actuators) to detect growing damage;
- address the lifespan of the bridges and SHM systems; a current lifespan of a bridge is over 100 years; the lifespan of a data acquisition system might be 1/10 of the bridge structure; additionally, often the first signs of structure degradation might only be visualized 20 years after construction; thus, sensors for long-term SHM must be of high durability to cover at least one rehabilitation cycle;
- need of densely distributed sensor networks to better cover a relatively large area of the structure; traditionally, the SHM process is performed in a global basis with a reduce number of sensors distributed over a relatively large area of the structures; however, many studies have reported that in civil engineering infrastructure such a strategy does not detect local damage at an early stage; this early damage detection is crucial to avoid damage accumulation; at the same time smaller and more cost competitive sensors need to be developed;
- establish the baseline of each new bridge to assess the structural integrity over time; it is a rule of thumb that the baseline condition must be established based on monitoring from at least one year to capture seasonal variability [62];
- assume a probabilistic approach over a deterministic one, because there are many uncertainties in current procedures at both software and hardware;

- and finally, combine different machine learning algorithms to detect damage in the structures; furthermore, cross-diagnosis using multiple algorithms is important to increase the likelihood to detect damage in the structures.

REFERENCES

1. Farrar, C. R., Doebling, S. W., & Nix, D. A. (2001). Vibration-based Structural Damage Identification. *Philosophical Transactions of the Royal Society: Mathematical, Physical & Engineering Sciences*, 356 (1778), 131-149.
2. Farrar, C., & Worden, K. (2007). An Introduction to Structural Health Monitoring. *Philosophical Transactions of the Royal Society*, 365, 303-315.
3. Doebling, S. W., Farrar, C. R., Prime, M. B., & Shevitz, D. W. (1996). *Damage Identification and Health Monitoring of Structural and Mechanical Systems from Changes in their Vibration Characteristics: A Literature Review*. Los Alamos National Laboratory Report: LA-13070-MS.
4. Sohn, H., Farrar, C. R., Hemez, F. M., Shunk, D. D., Stinemates, D. W., Nadler, B. R., et al. (2004). *A Review of Structural Health Monitoring Literature from 1996-2001*. Los Alamos National Laboratory: LA-13976-MS.
5. Randall, R. B. (2004). State of the Art in Monitoring Rotating Machinery - Part 1. *Sound and Vibration*, 38, 14-21.
6. Randall, R. B. (2004). State of the Art in Monitoring Rotating Machinery - Part 2. *Sound and Vibration*, 38, 10-17.
7. Pawar, P. M., & Ganguli, R. (2007). Helicopter Rotor Health Monitoring - A Review. Proceedings of the Institution of Mechanical Engineers, Part G: *Journal of Aerospace Engineering*, 221 (5), 631-647.
8. Walther, R. A., & Chase, S. B. (2006). *Condition Assessment of Highway Structures: Past, Present, and Future*. Transportation Research Circular - 50 Years of Interstate Structures: Past, Present, and Future (E-C104), 67-78.
9. Kessler, S. S., Spearing, S. M., & Soutis, C. (2002). Damage Detection in Composite Materials using Lamb Wave Methods. *Smart Materials and Structures*, 11 (2), 269-278.

-
10. Park, G., Soon, H., Farrar, C. R., & Inmar, D. J. (2003). Overview of Piezoelectric Impedance-based Health Monitoring and Path Forward. *Shock and Vibration Digest*, 35 (6), 451-463.
 11. Ihn, J. B., & Chang, F. K. (2004). Detection and Monitoring of Hidden Fatigue Crack Growth using a Built-in Piezoelectric Sensor/actuator Network: II. Validation using Riveted Joints and Repair Patches. *Smart Materials and Structures*, 13 (3), 621-630.
 12. Sohn, H., Park, G., Wait, J. R., Limback, N. P., & Farrar, C. R. (2004). Wavelet-based Signal Processing for Detecting Delamination in Composite Plates. *Smart Materials and Structures*, 13 (1), 153-160.
 13. Farrar, C. R., Sohn, H., & Worden, K. (2001). Data Normalization: A Key to Structural Health Monitoring. *Proceedings of the 3th International Workshop on Structural Health Monitoring* (pp. 1229-1238). Stanford, Palo Alto, CA: DEStech Publications, Inc.
 14. Rytter, A. (1993). *Vibration Based on Inspections of Civil Engineering Structures*. PhD Dissertation, Department of Building Technology and Structural Engineering, Aalborg University, Denmark.
 15. Worden, K., & Duijvelde, J. M. (2004). An Overview of Intelligent Fault Detection in Systems and Structures. *International Journal of Structural Health Monitoring*, 3 (1), 85-98.
 16. Farrar, C. R., & Lieven, N. A. (2006). Damage Prognosis: The Future of Structural Health Monitoring. *Phil. Trans. R. Soc. A*, 365, 623-632.
 17. Inaudi, D., Manetti, L., & Glisic, B. (2009). Integrated Systems for Structural Health Monitoring. *Proceedings of the 4th International Conference on Structural Health Monitoring on Intelligent Infrastructure*, 22-24 July, Zurich, Switzerland.
 18. Ko, J. M., & Ni, Y. Q. (2005). Technology Developments in Structural Health Monitoring of Large-scale Bridges. *Engineering Structures*, 27, 1715-1725.
 19. Lynch, J. P., & Loh, K. J. (2006). A Summary Review of Wireless Sensors and Sensor Networks for Structural Health Monitoring. *The Shock and Vibration Digest*, 38 (2), 91-128.
 20. Glaser, S., Li, H., Ou, J., & Lynch, J. (2007). Sensor Technology Innovation for the Advancement of Structural Health Monitoring: A Strategic Program of US-China Research for the Next Decade. *Smart Structures and Systems*, 3 (2), 221-244.
 21. Wenzel, H. (2007). SHM at the Civil Infrastructure: Applications, Recent Progress and Future Demands. *Proceedings of the 6th International Workshop on Structural Health Monitoring* (pp. 56-64), September 11-13, Stanford, CA: DEStech Publications, Inc.

-
22. Phares, B. M., Wipf, T. J., Greimann, L. F., & Lee, Y.-S. (2005). *Health Monitoring of Bridge Structures and Components Using Smart Structure Technology, Volume 1*. Wisconsin Highway Research Program, Center for Transportation Research and Education, Iowa State University.
 23. Pines, D., & Aktan, E. (2002). Status of Structural Health Monitoring of Long-span Bridges in the United States. *Progress Structural Engineering and Materials*, 4, 372-380.
 24. Kattell, J., & Eriksson, M. (1998). *Bridge Scour Evaluation: Screening, Analysis, & Countermeasures*. United States Department of Agriculture.
 25. Placzek, G., & Haeni, F. P. *USGS Water-Resources Investigations Report 95-4009*. Retrieved January 10, 2010, from USGS, Science for a Changing World: http://water.usgs.gov/ogw/bgas/scour/#*.
 26. Richardson, E. V., & Lagasse, P. F. (1999). Stream Stability and Scour at Highway Bridges. Compendium of papers from the 1991 to 1998 *proceedings of the ASCE Water Resources Engineering*. ASCE.
 27. Melville, B. W., & Coleman, S. E. (2000). *Bridge Scour*. Water Resources Publications, LLC.
 28. NTSB. (2008). *Collapse of I-35W Highway Bridge, Minneapolis*, Minnesota, August 1, 2007. National Transportation Safety Board, Accident Report, NTSB/HAR-08/03, November 14.
 29. Transportation, M. D. Retrieved December 30, 2009, from: http://www.dot.state.mn.us/i35wbridge/pdfs/bridge_inspection_report_06-15-06.pdf.
 30. Inaudi, D., Bolster, M., Deblois, R., French, C., Phipps, A., Sebasky, J., et al. (2009). Structural Health Monitoring System for the New I-35W St Anthony Falls Bridge. *Proceedings of the 4th International Conference on Structural Health Monitoring on Intelligent Infrastructure*, 22-24 July, Zurich, Switzerland.
 31. Kleinhans, D. D. (2008). Monitoring System on Huey P. Long Bridge Will Track Load Transfer. *Roads & Bridges*, 46 (5).
 32. Aktan, A. E., Catbas, F. N., Pervizpour, M., Kulcu, E., Grimmelsman, K., Barrish, R., et al. (2000). Real-Time Bridge Health-Monitoring for Management. *Proceedings of the 2nd Workshop on Advanced Technologies in Urban Earthquake Disaster Mitigation*, July 9-14, Kyoto University.
 33. Time. Retrieved January 18, 2010, from Time Photo Gallery: http://www.time.com/time/photogallery/0,29307,1649646_1421726,00.html.

-
34. OU, J., & LI, H. (2009). Structural Health Monitoring in the Mainland of China: Review and Future Trends. *Proceedings of the 7th International Workshop on Structural Health Monitoring*. Vol. I, pp. 29-41. September 9-11, Stanford, CA: DEStech Publications, Inc.
 35. Wong, K. Y. (2004). Instrumentation and Health Monitoring of Cable-supported Bridges. *Structural Control and Health Monitoring*, 11, 91-124.
 36. PBase.com. Retrieved January 10, 2010, from:
http://www.pbase.com/alex1030/tsing_ma_bridge.
 37. Ou, J. P., & Li, H. (2006). The State-of-art and Practice of Structural Health Monitoring for Civil Infrastructures in the Mainland of China. *Structural Health Monitoring and Intelligent Infrastructure*. Vol. 1, pp. 69-94. London, UK: Taylor & Francis Group.
 38. Zhang, G., Zhang, Z., & Fischer, C. (2007). Structural Health Monitoring of a Long-Span Cable-stayed Bridge. *Journal of Intelligent Material Systems and Structures*, 18, 835-843.
 39. Civil Engineering Portal. Retrieved January 10, 2010, from:
<http://www.engineeringcivil.com/theory/civil-engineering-disasters/>.
 40. Johnson, P. M., Couture, A., & Nicolet, R. (2007). *Commission of Inquiry into the Collapse of a Portion of the de la Concorde Overpass*. Gouvernement du Québec, October 3, 2006 - October 15, 2007.
 41. ISHMII. Retrieved January 04, 2010, from Case Studies Collection:
<http://www.ishmii.org/Literature/CaseStudiesMain.html>.
 42. Glisic, B., Inaudi, D., & Casanova, N. (2009). SHM Process - Lessons Learned in 250 SHM Projects. *4th International Conference on Structural Health Monitoring on Intelligent Infrastructure*. 22-24 July, Switzerland.
 43. Lauridsen, J., & Lassen, B. (1999). The Danish Bridge Management System DANBRO. In P. C. Das, *Management of Highway Structures* (pp. 61-70). Thomas Telford Publishing.
 44. Mendonça, T. P., & Vieira, A. (2004). Bridge Management System - GOA. *Proceedings of the 2nd International Conference of the International Association for Bridge Maintenance and Safety*. 18-22 October, Kyoto, Japan: Routledge USA.
 45. U.S. Department of Transportation. (1999). *Asset Management Primer*. Federal Highway Administration Office of Asset Management, December.
 46. U.S. Department of Transportation. (2007). *Asset Management Overview*. Federal Highway Administration Office of Asset Management, December.

-
47. Chang, P. C., Flatau, A., & Liu, S. C. (2003). Review Paper: Health Monitoring of Civil Infrastructure. *Structural Health Monitoring*, 2 (3), 257-267.
 48. Kim, C.-Y., Jung, D.-S., Kim, N.-S., Kwon, S.-D., & Feng, M. Q. (2003). Effect of Vehicle Weight on Natural Frequencies of Bridges Measured from Traffic-induced Vibration. *Earthquake Engineering and Engineering Vibration*, 2 (1), 109-115.
 49. Zhang, Q. W., Fan, L. C., & Yuan, W. C. (2002). Traffic-induced Variability in Dynamic Properties of Cable-stayed Bridge. *Earthquake Engineering and Structural Dynamics*, 31, 2015-2021.
 50. Soyoz, S., & Feng, M. Q. (2009). Long-term Monitoring and Identification of Bridge Structural Parameters. *Computer-Aided Civil and Infrastructure Engineering*, 24, 82-92.
 51. Rohrmann, R. G., Baessler, M., Said, S., Schmid, W., & Ruecker, W. F. (2000). Structural Causes of Temperature Affected Modal Data of Civil Structures Obtained by Long Time Monitoring. *Proceedings of the IMAC XVIII* (pp. 1-7). February 7-10, San Antonio, Texas.
 52. Roberts, G. P., & Pearson, A. J. (1998). Health Monitoring of Structures - Towards a Stethoscope for Bridges. *Proceedings of ISMA 23, International Conference on Noise and Vibration Engineering*. Leuven, Belgium, September.
 53. Askegaard, V., & Mossing, P. (1988). Long Term Observations of RC-bridge using Changes in Natural Frequency. *Nordic Concrete Research*, 7, pp. 20-7.
 54. Farrar, C. R., Cornwell, P. J., Doebling, S. W., & Prime, M. B. (2000). *Structural Health Monitoring Studies of the Alamosa Canyon and I-40 Bridges*. Los Alamos National Laboratory Report: LA-13635-MS.
 55. Xia, Y., Hao, H., Zanardo, G., & Deeks, A. (2006). Long Term Vibration Monitoring of an RC Slab: Temperature and Humidity Effect. *Engineering Structures*, 28, 441-452.
 56. Sohn, H., & Farrar, C. R. (2000). Statistical Process Control and Projection Techniques for Damage Detection. *Symposium on Identification of Mechanical Systems: International Mechanical Engineering Congress and Exposition*. November 11-16, New York.
 57. Farrar, C. R., Baker, W. E., Bell, T. M., Cone, K. M., Darling, T. W., Duffey, T. A., et al. (1994). *Dynamic Characterization and Damage Detection in the I-40 Bridge Over the Rio Grand*. Los Alamos National Laboratory Report: LA-12767-MS.
 58. Peeters, B., & De Roeck, G. (2001). One-year Monitoring of the Z24-Bridge: Environmental Effects versus Damage Events. *Earthquake Engineering and Structural Dynamics*, 30, 149-171.

-
59. Peeters, B., Maeck, J., & De Roeck, G. (2001). Vibratio-based Damage Detection in Civil Engineering: Excitation Sources and Temperature Effects. *Smart Materials and Structures*, 10, 518-527.
 60. Z-24 Bridge. (1999, April 28). (H. Verbraken, Producer) Retrieved January 18, 2010, from <http://www.kuleuven.be/bwm/Z24/>.
 61. Alampalli, S. (2000). Effects of Testing, Analysis, Damage, and Environment on Modal Parameters. *Mechanical Systems and Signal Processing*, 14 (1), 63-74.
 62. Alampalli, S. (1998). Influence of In-serive Environment on Modal Parameters. *Proceedings of IMAC XVI* (pp. 111-116). February 2-5, Santa Barbara, California.
 63. Woon, C. E., & Mitchell, L. D. (1996). Variations in Structural Dynamic Charateristics Caused by Changes in Ambient Temperature: I. Experimental. *Proceedings of the IMAC XIV* (pp. 963-971). February 12-15, Dearborn, Michigan.
 64. Cawley, P. (1997). Long Range Inspection of Structures using Low Frequency Ultrasound. Structural Damage Assessment using Advanced Signal Processing Procedures, *DAMAS* (pp. 1-17). University of Sheffield.
 65. Farhey, D. N. (2006). Instrumentation System Performance for Long-term Bridge Health Monitoring. *Structural Health Monitoring*, 5 (2), 143-153.
 66. Worden, K., Farrar, C. R., Manson, G., & Park, G. (2007). The Fundamental Axioms of Structural Health Monitoring. *Proceedings of the Royal Society A: Mathematical, Physical and Engineering Sciences*, 463 (2082), 1639-1664.
 67. Chopra, A. k. (2001). *Dynamics of Structures: Theory and Applications to Earthquakes Engineering*. Prentice Hall, Second Edition.
 68. Salawu, O. S. (1997). Detection of Structural Damage Through Changes in Frequency: A Review. *Engineering Structures*, 19 (9), 718-723.
 69. Wirsching, P. H., Paez, T. L., & Ortiz, H. (1995). *Random Vibrations: Theory and Practice*. John Wiley & Sons, Inc.
 70. Farrar, C. R., Worden, K., Todd, M. D., Park, G., Nichols, J., Adams, D. E., et al. (2007). *Nonlinear System Identification for Damage Detection*. Los Alamos National Laboratory Report: LA-14353-MS.
 71. Sohn, H., Farrar, C., Hunter, N., & Worden, K. (2001). *Applying the LANL Statistical Pattern Recognition Paradigm for Structural Health Monitoring to Data from a Surface-effect Fast Patrol Boat*. Los Alamos National Laboratory Report: LA-13761-MS.

-
72. Mattson, S. G., & Pandit, S. M. (2006). Statistical Moments of Autoregressive Model Residuals for Damage Localization. *Mechanical Systems and Signal Processing*, 20, 627-645.
 73. Box, G. E., Jenkins, G. M., & Reinsel, G. C. (1994). *Time Series Analysis: Forecasting and Control* (3rd Edition ed.). New Jersey: Prentice-Hall, Inc.
 74. Cassar, T. A., Camilleri, K. P., & Fabri, S. G. (2009). Order Estimation of Computational Models for Dynamic Systems with Application of Biomedical Signals. *Proceedings of the 3th International Conference on Advanced Engineering Computing and Applications in Sciences* (pp. 163-168).
 75. Parzen, E. (1974). Some Recent Advances in Time Series Modeling. *IEEE Transactions Automatic Control*, 19, 723-730.
 76. Al-Smadi, A., & Wilkes, D. M. (2002). Robust and Accurate ARX and ARMA Model Order Estimation of Non-Gaussian Processes. *IEEE Transactions on Signal Processing*, 50 (3), 759-763.
 77. Akaike, H. (1974). A New Look at the Statistical Model Identification. *IEEE Transactions on Automatic Control*, AC-19 (6), 716-723.
 78. Kedem, B., & Fokianos, K. (2002). *Regression Models for Time Series Analysis*. Hoboken, New Jersey: John Wiley & Sons, Inc.
 79. Hurvich, C. M. (1991). Bias of the Corrected AIC criterion for Underfitted Regression and Time Series Models. *Biometrika*, 78 (3), 499-509.
 80. Ciftcioglu, O., Hoogenboom, J. E., & van Dam, H. (1988). Studies on Multivariate Autoregressive Analysis using Synthesized Reacor Noise-like Data for Optimal Modelling. *Progress Nuclear Energy*, 21, 687-696.
 81. Ciftcioglu, O., Hoogenboom, J. E., & van Dam, H. (1994). A Consistent Estimator for the Model Order of an Autoregressive Process. *IEEE Transactions on Signal Processing*, 42 (6), 1471-1477.
 82. Box, G., & Jenkins, G. (1976). *Time Series Analysis: Forecasting and Control*. Englewood Cliffs, New Jersey: Prentice Hall.
 83. Liang, G., Wilkes, D. M., & Cadzow, J. A. (1993). ARMA Model Order Estimation Based on the Eigenvalues of the Covariance Matrix. *IEEE Transactions on Signal Processing*, 41 (10), 3003-3009.
 84. Sohn, H., & Farrar, C. (2001). Damage Diagnosis using time series analysis of vibration signals. *Smart Materials and Structures*, 10, 446-451.

-
85. Worden, K., Allen, D. W., Sohn, H., Stinemates, D. W., & Farrar, C. R. (2002). *Extreme Value Statistics for Damage Detection in Mechanical Structures*. Los Alamos National Laboratory Report: LA-13903-MS.
 86. Takens, F. (1981). *Detecting Strange Attractors in Turbulence*. Springer, 898, 366-381.
 87. Fraser, A. M., & Swinney, H. L. (1986). Independent Coordinates for Strange Attractors from Mutual Information. *Physical Review A*, 33 (2), 1134-1140.
 88. Buzug, T., & Pfister, G. (1992). Optimal Delay Time and Embedding Dimension for Delay-Time Coordinates by Analysis of the Global Static and Local Dynamical Behavior of Strange Attractors. *Physical Review A*, 45 (10), 7073-7084.
 89. Broomhead, D. S., & King, G. P. (1986). Extracting Qualitative Dynamics from Experimental Data. *Physica D*, 20, 217-236.
 90. Bishop, C. M. (1995). *Neural Networks for Pattern Recognition*. Oxford: University Press.
 91. Jolliffe, I. T. (2004). *Principal Component Analysis*. Springer, Second Edition.
 92. Yan, A. -M., Kerschen, G., Boe, P. D., & Golinval, J. -C. (2005). Structural Damage Diagnosis under Varying Environmental Conditions - Part I: A Linear Analysis. *Mechanical Systems and Signal Processing*, 19, 847-864.
 93. Yan, A. -M., Kerschen, G., Boe, P. D., & Golinval, J. -C. (2005). Structural Damage Diagnosis under Varying Environmental Conditions - Part II: Local PCA for Non-Linear Cases. *Mechanical Systems and Signal Processing*, 19, 865-880.
 94. Giraldo, D. F., Dyke, S. J., & Caicedo, J. M. (2006). Damage Detection Accommodating Varying Environmental Conditions. *International Journal of Structural Health Monitoring*, 5 (2), 155-172.
 95. Hogan, J. A., & Lakey, J. D. (2005). *Time-Frequency and Time-scale Methods*. Boston: Birkhauser.
 96. Misiti, M., Misiti, T., Oppenheim, G., & Poggi, J. M. (2007). *Wavelet Toolbos 4: User's Guide*. The MathWorks.
 97. Polikar, R. Retrieved September 15, 2007, from The Wavelet Tutorial: The Engineer's Ultimate Guide to Wavelet Analysis: <http://user.rowan.edu/~polikar/wavelets/WTtutorial>.
 98. Robertson, A. N., Farrar, C. R., & Sohn, H. (2003). Singularity Detection for Structural Health Monitoring using Holder Exponents. *Mechanical Systems and Signal Processing*, 17 (6), 1163-1184.

-
99. Montgomery, D. C. (2007). *Introduction to Statistical Quality Control*. New York: John Wiley & Sons, Inc.
 100. Maia, N. M., & Silva, J. M. (1997). *Theoretical and Experimental Modal Analysis*. NY: John Wiley & Sons Inc.
 101. Ndambi, J. -M., Vantomme, J., & Harri, K. (2002). Damage Assessment in Reinforced Concrete Beams using Eigenfrequencies and Mode Shapes Derivatives. *Engineering Structures*, 24, 501-515.
 102. Silverman, B. W. (1986). *Density Estimation for Statistics and Data Analysis*. New York: Chapman and Hall.
 103. Browman, A. W. (1984). An Alternative Method of Cross-validation for the Smoothing of Density Estimates. *Biometrika*, 71, 352-360.
 104. NIST/SEMATECH. *e-Handbook of Statistical Methods*. Retrieved in September 8, 2008, from: <http://www.itl.nist.gov/div898/handbook/>.
 105. Sohn, H., Worden, K., & Farrar, C. (2001). Novelty Detection under Changing Environmental Conditions. *SPIE's 8th Annual International Symposium on Smart Structures and Materials*. 4-8 March, Newport Beach, CA, USA.
 106. Worden, K., Sohn, H., & Farrar, C. R. (2002). Novelty Detection in a Changing Environmental: Regression and Interpolation Approaches. *Journal of Sound and Vibration*, 258 (4), 741-761.
 107. Sohn, H., Worden, K., & Farrar, C. R. (2002). Statistical Damage Classification under Changing Environmental and Operational Conditions. *Journal of Intelligent Material Systems and Structures*, 13 (9), 561-574.
 108. Figueiredo, E., Figueiras, J., Park, G., & Farrar, C. (2008). Data Normalization and Nonlinear Damage Identification using Auto-associative Neural Networks and Factor Analysis. *Proceedings of the 4th European Workshop on Structural Health Monitoring* (pp. 1017-1024). Krakow, Poland.
 109. Sohn, H. (2006). Effects of Environmental and Operational Variability on Structural Health Monitoring. *Phil. Trans. R. Soc. A*, 365, 539-560.
 110. Worden, K., & Manson, G. (2007). The Application of Machine Learning to Structural Health Monitoring. *Phil. Trans. R. Soc. A*, 365, 515-537.
 111. Kramer, M. A. (1991). Nonlinear Principal Component Analysis using Autoassociative Neural Networks. *AIChE Journal*, 37 (2), 233-243.

-
112. Worden, K., Manson, G., & Allman, D. (2003). Experimental Validation of a Structural Health Monitoring Methodology: Part I. Novelty Detection on a Laboratory Structure. *Journal of Sound and Vibration*, 259 (2), 323-343.
 113. Li, H., Li, S., Ou, J., & Li, H. (2009). Modal Identification of Bridges under Varying Environmental Conditions: Temperature and Wind Effects. *Structural Control and Health Monitoring*, 10.1002/stc.319.
 114. Oh, C. K., Sohn, H., & Bae, I.-H. (2009). Statistical Novelty Detection within the Yeongjong Suspension Bridge under Environmental and Operational Variations. *Smart Materials and Structures*, 18, 1-9.
 115. Kullaa, J. (2003). Is Temperature Measurement Essential in Structural Health Monitoring? *Proceedings of the 4th International Workshop on Structural Health Monitoring 2003: From Diagnostic & Prognostics to Structural Health Monitoring* (pp. 717-724). DEStech Publications, Inc.
 116. Ruotolo, R., & Surage, C. (1999). Using SVD to Detect Damage in Structures with Different Operational Conditions. *Journal of Sound and Vibration*, 226 (3), 425-439.
 117. Elsner, J. B., & Tsonis, A. A. (1996). *Singular Spectrum Analysis: A New Tool in Time Series Analysis*. New York: Plenum Press.
 118. Jain, A. K., Murty, M. N., & Flynn, P. J. (1999). Data Clustering: A Review. *ACM Computing Surveys*, 31 (3).
 119. Matlab. (2008). *Statistical Toolbox, User's Guide*. The MathWorks, Inc.
 120. Sohn, H., Kim, S. D., & Harries, K. (2008). Reference-Free Damage Classification Based on Cluster Analysis. *Computer-Aided Civil and Infrastructure Engineering*, 23 (5), 324-338.
 121. Grant, E. L., & Leavenworth, R. S. (1988). *Statistical Quality Control* (Vol. Sixth Edition). McGraw-Hill Publishing Company.
 122. Gupta, B. C., & Walker, H. F. (2007). *Statistical Quality Control for the Six Sigma Green Belt*. Milwaukee, Wisconsin: ASQ Quality Press.
 123. Sohn, H., Czarnecki, J. A., & Farrar, C. R. (2000). Structural Health Monitoring using Statistical Process Control. *Journal of Structural Engineering*, 126 (11), 1356-1363.
 124. Fugate, M. L., Sohn, H., & Farrar, C. R. (2001). Vibration-based Damage Detection using Statistical Process Control. *Mechanical Systems and Signal Processing*, 15 (4), 707-721.

-
125. Worden, K., & Manson, G. (2000). Damage Detection using Outlier Analysis. *Journal of Sound and Vibration*, 229 (3), 647-667.
 126. Fawcett, T. (2004). *ROC Graphs: Notes and Practical Considerations for Researchers*. HP Laboratories, Palo Alto, USA.
 127. Figueiredo, E., Park, G., Figueiras, J., Farrar, C., & Worden, K. (2009). *Structural Health Monitoring Algorithm Comparisons using Standard Data Sets*. Los Alamos National Laboratory Report: LA-14393.
 128. Bornn, L., Farrar, C. R., Park, G., & Farinholt, K. (2009). Structural Health Monitoring with Autoregressive Support Vector Machines. *Journal of Vibration and Acoustics*, 131 (2), 021004-1-9.
 129. Hernandez-Garcia, M. R., Masri, S. F., Ghanem, R., Figueiredo, E., & Farrar, C. R. (2010). An Experimental Investigation of Change Detection in Uncertain Chain-like Systems. *Journal of Sound and Vibration*, 329, 2395-2409.
 130. Kantz, H., & Schreiber, T. (1997). *Nonlinear Time Series*. Cambridge University Press.
 131. Pimentel, M., Santos, J., & Figueiras, J. (2008). Safety Appraisal of an Existing Bridge via Detailed Modelling. *International FIB Symposium 2008: Tailor Made Concrete Solutions, New Solutions for our Society*. Amsterdam, Netherlands.
 132. Naeim, F., & Kelly, J. (1999). *Design of Seismic Isolated Structures: From Theory to Practice*. USA: John Wiley and Sons, Inc.
 133. Chopra, A. K. (2006). *Dynamics of Structures: Theory and Applications to Earthquake Engineering*. Third Edition.
 134. Bendat, J. S., & Piersol, A. G. (2000). *Random Data: Analysis and Measurement Procedures* (3rd Edition). John Wiley and Sons, Inc.
 135. Richardson, M. H., & Formenti, D. L. (1982). Parameter Estimation from Frequency Response Measurements using Rational Fraction Polynomials. *1st IMAC Conference*. Orlando, Florida.
 136. Ewins, D. J. (1984). *Modal Testing: Theory and Practice*. Research Studies Press.
 137. Figueiredo, E., Todd, M. D., Farrar, C. R., & Flynn, E. (2010). Autoregressive Modeling with State-space Embedding Vectors for Damage Detection under Operational Variability. *International Journal of Engineering Science*, 48, 822-834.
 138. Galka, A. (2000). *Topics in Nonlinear Time Series Analysis with Implications for EEG Analysis*. Singapore: World Scientific.

-
139. Eric B. Flynn, Michael D. Todd (2009). A Bayesian Approach to Optimal Sensor Placement for Structural Health Monitoring with Application to Active Sensing. *Mechanical Systems and Signal Processing*, ISSN 0888-3270, DOI: 10.1016/j.ymssp.2009.09.003.
 140. Salamone, S., Fasel, T. Bartoli, I., Srivastava, A., Lanza di Scalea, F., & Todd, M. D. (2009). Structural Health Monitoring of Adhesively Bonded Joints. *Materials Evaluation*, 67(7), 828-836.
 141. Weather Underground. Retrieved March 28, 2010, from <http://www.wunderground.com>.
 142. Worden, K., & Tomlinson, G. R. (2001). *Nonlinear in Structural Dynamics: Detection, Identification and Modelling*. IOP Publishing.
 143. Huber, P. J. (2004). *Robust Statistics*. New Jersey: John Wiley & Sons, Inc.
 144. US Department of Transportation. (2001). *Reliability of Visual Inspection for Highway Bridges*. Final Report, Federal Highway Administration, FHWA-RD-01-020.
 145. US Department of Transportation. (1995). *Recording and Coding Guide for the Structure Inventory and Appraisal of the Nation's Bridges*. Federal Highway Administration, Office of Engineering Bridge Division, FHWA-PD-96-001.
 146. Brownjohn, J. M. (2006). Structural Health Monitoring of Civil Infrastructure. *Phil. Trans. R. Soc. A*, 365, 589-622.

APPENDIX A

SHMTools Software

A.1. Introduction and Overview

SHMTools is a Matlab package to support the SHM process. The package provides a set of functions organized into modules according to the three primary steps of the SHM statistical pattern recognition paradigm: data acquisition, feature extraction, and statistical modeling for feature classification (or damage detection). A modular function design and a set of standardized parameter formats make it easy to assemble and test customized SHM process. *SHMTools* is made available for free by the Engineering Institute at Los Alamos National Laboratory in collaboration with University of California in San Diego. It is the beginning of a larger effort to collect and archive proven approaches to SHM for re-use by the research community. Therefore, the package includes various statistical techniques and algorithms with source codes, along with structural data sets to serve as benchmarks for the evaluation of algorithms.

The software package can be downloaded from <http://institute.lanl.gov/ei>. The package includes function library, documentation, and standard data sets as shown in Figure A.1.

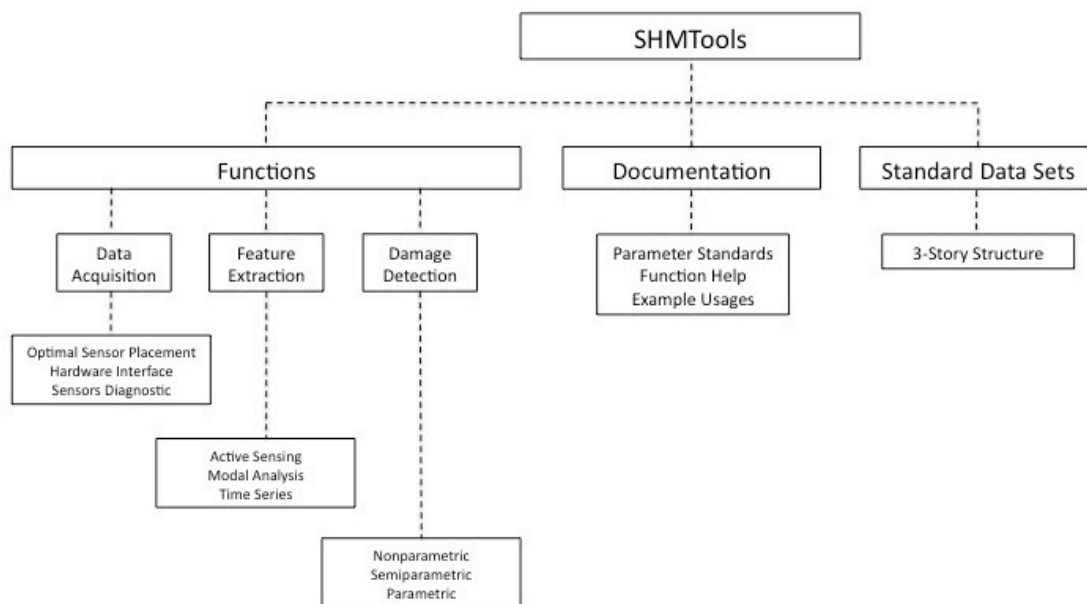


Figure A.1 Organizational chart of the *SHMTools* package.

A.2. Function Library

All SHM functions are under the Functions directory at the root level. These functions are divided into three groups as follows.

A.2.1 Data Acquisition

These functions provide basic services for common SHM related data acquisition tasks. These functions are divided into three categories:

- Optimal Sensor Placement – functions for designing modal analysis-based sensing networks;
- Hardware Interfacing – functions for interfacing with and acquiring data from common data acquisition hardware;
- Sensor Diagnostics – functions for assessing sensor conditions through impedance-based methods.

A.2.2 Feature Extraction

The functions in this group take the data (generally in the form of time series) and extract features that can be used in the detection phase. The feature extraction algorithms are divided into three groups:

- Active Sensing – a set of functions for managing, visualizing, and extracting features for ultrasonic wave propagation-based active sensing;
- Modal Analysis – these functions take in either a matrix of time series, or frequency response functions, and return modal properties such as mode shapes, natural frequencies, and damping ratios;
- Time Series – these functions take in a matrix of time series, and return a matrix of feature vectors.

A.2.3 Statistical Modeling for Feature Classification

The damage detection algorithms work in two phases. The training phase takes feature vectors from the normal condition (state conditions under operational and environmental effects when the structure is undamaged), and builds a model of the undamaged condition. This model is subsequently used in the detection phase to classify future feature vectors as normal/undamaged or abnormal/damaged conditions. The detection algorithms are organized in three groups:

- Nonparametric – no distributional assumption is made about the phenomena generating the undamaged data;
- Semiparametric – here the data space is partitioned into multiple cells (group of feature vectors) using any of many possible procedures, and a parametric model (e.g. a Gaussian) is learned for each cell;
- Parametric – the algorithms are built with an underlying assumption about the phenomena generating the data.

The algorithms from each group come in pairs of “learn” and “score” functions. For instance, in the parametric group, the *learnMahalanobis_shm* function learns the parameters of a Mahalanobis distance function from the training data provided; then, the *scoreMahalanobis_shm* function uses those parameters to evaluate the similarity of future feature vectors with the original training data.

As a convention, the scores returned by a “score” function are interpreted as follows: the higher the score of a sample, the closer the sample is to the normal condition. This way detection simply consists of thresholding the score values, i.e. every score under a certain threshold is indicative of damage. (However, throughout this dissertation the higher the scores are indicative of abnormal condition.)

The detection routines are customizable in that the user could pick from various sub-routines to implement a detection algorithm. For instance a semiparametric routine can be assembled by picking from a choice of partitioning functions, a choice of parametric models (such as a Gaussian) to obtain a detector that consists of first partitioning the data space, then learning the particular parametric model on each cell of the partition.

By default mechanism, the user calls *assembleOutlierDetector_shm* which will navigate the various options available and produce a training routine called *trainOutlierDetector < ... >* (with appended time stamp). This training routine will take in the training data and learn a model of the normal conditions according to the various choices made during assembly, and also produces a threshold for future detections. The learned model and threshold are subsequently used by *detectOutlier_shm* to classify future feature vectors as undamaged or damaged. A training routine (*trainOutlierDetector_shm*) is also available by default, which implements a semiparametric detector consisting of fitting a Gaussian mixture model to the training data after partitioning with the *kmeans_shm* function.

A.3. Documentation

All documentation can be found in the Documentation directory at the root directory level. The three main documents are:

- Parameter Standards – this document provides general parameter standards to facilitate communication between functions;
- Function Help – it provides full details about all the available functions;
- Example Usages – extensive documentation that drives the user through various ways to assemble functions using standard data sets (Figure A.2).

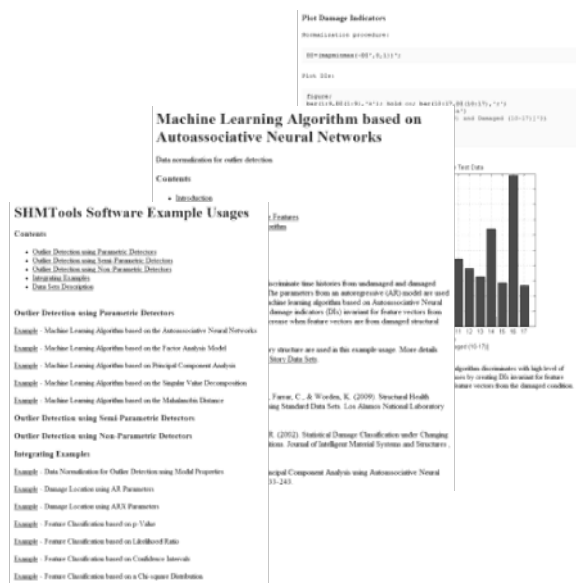


Figure A.2 Encyclopedia of documented example usages.

A.4. Standard Data Sets

The software is prepared to have as many as desirable standard data sets. However, the data sets from the base-excited three-story frame structure are the default available ones.